Imperial College London

Department of Materials

Performance and Stability of Nanostructured Solid Oxide Fuel Cell Cermet Electrodes

Jingyi Chen

Jan 2019

Supervised by Prof. Alan Atkinson

Prof. Nigel Brandon

Submitted in part fulfilment of the requirements for the degree of Doctor of Philosophy in Materials of Imperial College London and Diploma of Imperial College London

Declaration

I hereby declare that this thesis is a presentation of my original research. Information derived from the published and unpublished work of others has been appropriately acknowledged and referenced.

Jingyi Chen (2019)

The copyright of this thesis rests with the author and is made available under a Create Commons Attribution Non-Commercial No Derivatives license. Researchers are free to copy, distribute or transmit the thesis on the condition that they attribute it, that they do not use it for commercial purposes and that they do not alter, transform or build upon it. For any reuse or redistribution, researchers must make clear to others the license term of this work.

Acknowledgement

I would like to thank, first of all, my supervisors Professor Alan Atkinson and Professor Nigel Brandon for their guidance and support in both my scientific research and personal development throughout my PhD.

I would like to thank Imperial College London and the Chinese Scholarship Council for funding my PhD and the CDT in the Advanced Characterisation of Materials, led by Professor Stephen Skinner, for providing many training courses. I would like to acknowledge Dr. Paul Boldrin and Dr. Chris Starkey for synthesising the nanocomposite powder used in this study.

I would also like to thank Dr. Enrique Ruiz-Trejo for teaching and guiding me through fuel cell fabrication and testing during the first year of my PhD, Dr. Antonio Bertei and Dr. Xin Wang for many meaningful discussions and sharing with me their expertise in electrochemical and microstructural modelling throughout my PhD.

Also, I would like to express my gratitude to Dr. Stevin Pramana and Mr Chen-yu Tsai for their help with analysing XRD data, Dr. Oluwadamilola O Taiwo, Dr Samuel Cooper, Dr. Moshiel Biton and Dr. Farid Tariq for their guidance in image processing and Dr. Kristina Kareh for her guidance in FIB-SEM.

I really appreciate the support from my friends and colleagues in the Electrochemical Science and Engineering and the Electro-ceramics groups throughout my PhD, especially my 'neighbours' in office and laboratory and Miss Bo Chen for listening to interesting stories of my daily life (and a bit of science). I also greatly appreciate the time and efforts Mr. Qianfan Jiang has spent with me in solving mathematical problems.

Finally, I would like to thank my dear parents and grandparents for their encouragement and believes in science which morally support me in the good and bad times.

Abstract

Nickel-ceramic cermets are the most industrial relevant materials in solid oxide fuel cell (SOFC) anode and solid oxide electrolyser cell (SOEC) cathode today. Nano-structure engineering of the electrode provides the benefits of high electrochemical activity, but the electrode's stability has been questionable. For commercial applications, SOFC cells should sustain good performance for 40,000 hours of high temperature operations. Nickel coarsening between 500 °C to 1000 °C for high temperature SOFCs leads to both a reduction in the triple phase boundary (TPB), which is the electrochemical reaction site and a reduction in network connectivity, which is essential for current collection. In this work, particular attention is paid to the evolution of nickel nanoparticles in the cermet and its structural relationship with the ceramic phase.

Impregnation is one of the most popular techniques to incorporate nanoparticles in SOFC electrodes. In this study, nickel-impregnated scandia stabilised zirconia (ScSZ) electrodes were annealed isothermally at 650, 800 and 950 °C in 3% H_2O-5% H_2-N_2. An initial degradation of the electrodes was observed during the first 17 h of annealing. At 800 °C, the in-plane conductivity degraded from 1000 S cm^{-1} to 700 S cm^{-1} and the area specific resistance (ASR) for electrochemical reaction from 0.17 to 1.15 Ω cm^2 seen in electrochemical impedance spectra (EIS). Post-mortem scanning electron microscopy (SEM) images revealed an increase in particle size of the impregnated nickel nanoparticles, which caused a reduction in both active electrode area and TPB density.

The nickel-impregnated electrode showed good performance initially but degraded in a relatively short time as a result of nickel coarsening. Alternatively, the bottom-up manufacturing which uses nanoparticles from the beginning of powder mixing has great industrial potential. Composite nanoparticles of nickel oxide-yttria stabilised zirconia (YSZ)

fabricated by continuous hydrothermal flow synthesis (CHFC) were processed into solid oxide cell (SOC) electrodes. The nanocomposite powders have a high surface area of 189 m^2 g^{-1} and form 1 – 10 µm agglomerates after freeze-drying and ball milling. Focused ion beam (FIB)-SEM images and 3-D reconstruction revealed the electrode had a dual porosity microstructure with micron-size agglomerates, containing inter-penetrating networks of Ni (180 nm), YSZ (170 nm) and pores (310 nm), separated by micron-sized pores. The electrode has a high TPB density of 11.1 μm^{-2}. The electrodes aged at 800 °C in 3% H_2O-5% H_2-N_2 for 600 h showed excellent stability. The electrochemical reaction resistance was stable at 0.15 Ω cm^2. FIB-SEM 3-D reconstruction suggested that after aging, the TPB density was still high at 10.0 μm^{-2} and the particle size of Ni and YSZ remained approximately 100 nm.

Similarly, nanoscale nickel gadolinia-doped ceria (CGO) electrodes were fabricated from similar nanocomposite powders. The electrodes have high TPB density of 8.4 μm^{-2} and double phase boundary (DPB) density of 1.91 μm^{-1}. During isothermal aging at 800 °C in 3% H_2O-5% H_2-N_2, the total polarisation resistance was stable at 0.20 Ω cm^2. During the aging, the TPB density decreased but the DPB density remained relatively constant. In the Ni-CGO electrodes, the electrochemical reactions primarily take place on the surface of CGO and the nickel network mainly serves as current collector.

The excellent stability of nanostructured electrodes made by hydrothermal synthesis, in comparison to nickel impregnation, indicated that the microstructural relationship between the nickel and the ceramic phase is important to its stability. The ceramic phase can effectively inhibit the coarsening of nickel, especially when their particle sizes are comparable and when they form networks intertwined with each other.

Contents

Declaration I

Acknowledgement II

List of Figures IX

List of Tables XVII

List of Acronyms XVIII

1 Background and Motivation 1

1.1 Solid Oxide Cells 1

1.2 Working Principles of SOFC 2

1.2.1 Electrochemistry 4

1.2.1.1 Nernst Potential 4

1.2.1.2 Polarisation 5

1.3 Current State of SOFC Development 11

1.4 Fuel Electrode Materials 15

1.5 Objectives of the Thesis 20

2 Literature Review 22

2.1 Fabrication Techniques of Nanostructured Anodes and Their Electrochemical Performance 22

2.2 The Stability of Nickel in Nanostructured Electrodes 29

2.2.1 Nickel Coarsening and its Thermodynamics 30

2.2.2 Mechanisms of Nickel Coarsening 31

2.2.3 Influencing Factors for Nickel Coarsening 33

2.3 Impact of Nickel Coarsening on Electrochemical Performance 35

2.4 Method to Inhibit Nickel Coarsening 37

2.5 Conclusions 42

3 Methodology 44

3.1 Electrochemical Impedance Spectroscopy 44

3.1.1 Theory 44

3.1.2 Rig Design 47

3.1.3 Transmission Line Model 51
3.1.4 Distribution of Relaxation Times 52
3.2 Focused Ion Beam- Scanning Electron Microscopy 53
3.2.1 Theory 53
3.2.2 Sample Preparation 60
3.2.3 Milling and Imaging 61
3.2.4 Image Processing 62
3.3 Other Characterisation Methods 65
3.3.1 Brunauer-Emmett-Teller Surface Area and t-Plot 65
3.3.2 Laser Diffraction Particle Sizing 68
3.3.3 X-ray Diffraction and Rietveld Refinement 69
3.3.4 Van Der Pauw Conductivity 70
3.4 Summary 71
4 Nickel Impregnated Scandia-Stabilised Zirconia Electrode 72
4.1 Experimental 72
4.2 Results and Discussion 74
4.2.1 Electrode Electronic Conductivity 74
4.2.2 Electrochemical Impedance Spectroscopy 77
4.2.3 Microstructure Characterisation 87
4.2.4 Physical Model of Electrode ASR 92
4.3 Conclusions 98
5 Fabrication of Nanoscale Nickel Yttria-Stabilised Zirconia Electrode from Nanocomposite Powder 100
5.1 Experimental 101
5.1.1 Nanoparticle Synthesis 101
5.1.2 Fabrication of the Electrode 101
5.1.3 Powder Characterisation 102
5.1.4 Electrode Characterisation 102
5.2 Results and Discussion 104
5.2.1 NiO-YSZ Nanocomposite Powder Characterisation 104

5.2.2 Ni-YSZ Nano-Composite Electrode Physical Characterisation 107
5.2.3 Electrochemical Characterisation and Modelling 113
5.3 Conclusions 119
6 Microstructural Evolution of the Nanostructured Co-sintered Nickle Yttria-Stabilised-Zirconia Cermet Electrode 120
6.1 Experimental 121
6.2 Results and Discussion 121
6.3 Conclusions 134
7 Co-sintered Nanoscale Nickel Gadolinia-Doped-Ceria Electrode 136
7.1 Experimental 136
7.2 Results and Discussion 137
7.3 Conclusions 160
8 Conclusion 162
9 Future Work 168
10 Publications and Presentations 170
11 Bibliography 172

List of Figures

Figure 1.1 Schematics illustrating the operation of SOFC with oxygen ion conducting electrolyte. Modified from [8]..... 3

Figure 1.2 Planar design of the SOFC stack, after [11]..... 4

Figure 1.3 voltage vs. current density curve for (a) a low temperature fuel cell (70 °C) and (b) a typical SOFC at high temperature (800 °C or above). Modified from [15]..... 8

Figure 1.4 gas concentration profiles for the limiting behaviours of gas transport on top of the SOFC electrode [19]..... 9

Figure 1.5 The Hype Cycle illustrating the maturity of SOFC technology and its alternatives..... 13

Figure 2.1 Nyquist plots for the hydrogen oxidation on Pd-infiltrated Ni-CGO cermet anode at different PdO loading in 97% H_2 and 3% H_2O [75]..... 24

Figure 2.2 SEM image of the Ni-YSZ anode made from the co-precipitated nano-sized composite NiO-YSZ powder, reproduced from [94]..... 27

Figure 2.3 Transmission electron microscopy (TEM) images of the hydrothermally synthesized nanoparticles of CGO (a) [99] and 70 mol% Ni- 30 mol% SDC (b) [100]..... 29

Figure 2.4 Vapour equilibrium diagram of nickel species with excess solid nickel [109]..... 32

Figure 2.5 Electrical conductivity of the nickel nano-coating anode synthesized by Pechini process and the conventional Ni-YSZ anode after thermal cycling [148]..... 41

Figure 2.6 Secondary electron images on the cross section of a sintered Ni-YSZ anode before reduction (top row) and after reduction (bottom row) showed large zirconia particles about 20 µm in diameter and small nickel particles about 1 µm in diameter surrounded by a fine zirconia framework [149]..... 42

Figure 3.1 An example of a cathode-supported thin-film electrolyte cell with platinum as the counter electrode. Modified from [150]..... 46

Figure 3.2 The closed-chamber rig design for symmetrical cell measurement. The symmetrical cell sits inside a pyrophyllite sample holder which is clamped by springs..... 48

Figure 3.3 The open gas flow rig design for SOFC measurement. The symmetrical cell sits on a groove in a cylindrical alumina platform. The inlet gas blows directly at the edge of the symmetrical cell. 49

Figure 3.4 Cross-sectional SEM image of the interface between the silver paste and the porous Ni-YSZ electrode. On the left of the image is the silver paste (white) and pore (black), and on the right of the image is the Ni-YSZ electrode. 50

Figure 3.5 schematics of a transmission line used in this study with parallel lines representing the electronic conductor and the ionic conductor respectively. 51

Figure 3.6 The Nyquist plot of a Ni-YSZ electrode at 800 °C in humidified 5% H2- N2 (on the left) and its corresponding DRT plot (on the right). 53

Figure 3.7 Schematic of the FIB-SEM set up for imaging SOFC electrode. Modified from [162]... 54

Figure 3.8 The interaction zone of electrons and the specimen under the surface of impact [163]. 55

Figure 3.9 Schematics showing the electron collection by an E-T detector. Modified from [164]... 57

Figure 3.10 Operations and positions of the in-lens and BsE detectors in the Zeiss Auriga Dual Beam system. Modified from [165]. 58

Figure 3.11 Interaction volume of electrons in carbon at 1, 3 and 10 keV energy beams from Monte Carlo simulation [168]. 59

Figure 3.12 SEM image on top of the cross-sectional area of a porous Ni-YSZ electrode after FIB milling, showing the protective gold coating and the curtaining effect. The SEM image below shows a stronger effect of curtaining of a poorly milled cross section. 60

Figure 3.13 Schematics of the whole specimen for FIB-SEM imaging (left) and a SEM image of the specimen after the U-shape trench is dug out before imaging. 61

Figure 3.14 An example of the representative volume check done on the FIB-SEM 3D volume with a porous Ni-YSZ electrode. The volume fractions (on the left) are calculated from a fraction of the sampling volume to the whole sampling volume and converge after 0.2. Similarly, the TPB density converges after 0.4. 64

Figure 3.15 The five types of adsorption isotherm [175]. 67

Figure 3.16 Van der Pauw DC measurement was carried out by four point contacts on the electrode plane. A small current of 0.01A was passed through probe 1 and probe 3 while the potential was measured between probe 2 and probe 4. A repeated measurement was done by swapping 1 and 3 and swapping 2 and 4. R_1 represents the resistance averaged from these two measurements. Similarly, R_2 is calculated from the two measurements with current passing through probe 2 and 4 and the potential measured between 1 and 3 70

Figure 4.1 In-plane conductivities of the Ni-impregnated ScSZ electrode were measured with time as the electrodes were being annealed isothermally in humidified 5% H_2-95% N_2. 75

Figure 4.2 Nyquist plot and Bode plot for a symmetrical infiltrated cell aged at 650 °C for 30 min. The dots represent the experimental data and the solid lines represent the equivalent circuit fitting. The equivalent circuit model is shown in the inset. 78

Figure 4.3 Nyquist plot and Bode plot for a symmetrical infiltrated cell aged at 950 °C for 70 min 79

Figure 4.4 The area specific resistance contributions as a function of time at different annealing temperatures. The measurement was made at 10 min intervals during the first 120 min and then at 60 min interval thereafter 80

Figure 4.5 Ohmic resistance, electrochemical reaction resistance and diffusion resistance of the infiltrated electrode at 10 min, 1030 min and 3010 min of annealing. 82

Figure 4.6 The time evolution of the contributions to ASR from the ohmic, oxygen ion transfer, electrochemical reaction and the gas diffusion processes. Measurement was made at 650 °C in two gas compositions 1) humidified 5% H_2 and 95% N_2 (above), 2) humidified 95% H_2 and 5% N_2 (below), with a flow rate of 100 ml min^{-1}. Silver paint was applied onto the surface of the electrodes in addition to the Pt mesh contact to improve current collection. 84

Figure 4.7 Values of the three contributions to the ASR at 10 min, 1030 min and 3010 min at 650 °C with a silver paint coating on the cell to improve current collection. 85

Figure 4.8 Nyquist plots for a symmetrical cell, with silver paint current collection, measured at different temperatures, fuel gas composition and gas flow rate (indicated in the legend). 86

Figure 4.9 SEM micrographs of a) the ScSZ porous scaffold after sintering, b) the ScSZ scaffold after impregnating with nickel, c) the fracture cross section of nickel-ScSZ electrode after being reduced at 950 °C and held for 3010 min. 88

Figure 4.10 The secondary electron cross-sectional image of the image sliced and polished by focused ion beam shows three different phases with different colour contrast. The darkest phase is the epoxy resin that fills the pores. The brightest phase is nickel, which appears as nearly spherical particles. The grey phase in-between is ScSZ, forming a support network. The electrode has been reduced and aged at 950 °C in wet 5% hydrogen and 95% nitrogen for 30 min. 89

Figure 4.11 Secondary electron images of an electrode reduced and aged at 950 °C for 30 min a1) and 3010 min b1). The images were processed for image analysis by enhancing the contrast and edge threshold level to emphasise the circular objects (nickel particles) in a2) and b2). 90

Figure 4.12 The diameter-weighted particle size distributions of nickel in the infiltrated electrode after 30 min (above) and 3010 min (below) of annealing 91

Figure 4.13 Schematic of the electrode microstructure between two Pt mesh contact points (no additional silver current collection) showing the inactive regions due to break up in percolation of the nickel network upon degradation (note: figure not drawn to scale). Electrochemical reaction takes place at the percolating triple phase boundaries and the electrons released from hydrogen oxidation flow along the nickel path (in black) to the Pt mesh current collector 93

Figure 4.14 The time evolution of active area fraction of electrodes at 650 °C, 800 °C and 950 °C. 94

Figure 4.15 The evolution of active triple phase boundary densities with annealing time at 950 °C, 800 °C and 650 °C derived from the electrode model. 95

Figure 5.1 Thermal properties of the NiO-YSZ powder. (a) dilatometry of the freeze-dried NiO-YSZ green pellet: linear shrinkage and shrinkage rate vs. temperature (b) DSC and TGA of the freeze-dried NiO-YSZ powder from room temperature to 950 °C 105

Figure 5.2 NiO-YSZ powder size distribution and surface area measurements. (a)The particle size distribution measured by laser scattering as-dried and after calcination and milling. (b) Adsorption and desorption isotherm of N_2 at 77 K of the NiO-YSZ nano-composite powder after calcination and ball milling. 106

Figure 5.3 SEM image of a typical agglomerate particle of the NiO-YSZ nano-composite powder after calcination 107

Figure 5.4 Morphology and composition of the Ni-YSZ electrode (a) SEM image of the top surface of the Ni-YSZ electrode. The particle circled in dotted line is YSZ and the particle circled in solid

line is Ni. (b) XRD pattern and Rietveld refinement of the Ni-YSZ electrode c) SEM cross section of the Ni-YSZ electrode on the YSZ substrate. 108

Figure 5.5 The dual porosity microstructure (a) EDX mapping on the top surface of the Ni-YSZ electrode combined with back-scattered electron image. The green region represents where Ni is detected and red region, Zr. (b) schematic showing the evolution of the microstructure in the fabrication route after 1) calcination and ball milling 2) sintering and 3) reduction. 109

Figure 5.6 3-D reconstruction from FIB-SEM image sequence. (a) 3-D reconstructed volume of the Ni-YSZ electrode. The red region represents Ni and the yellow region YSZ. Porosity is represented as transparent hollow space. (b) Percolated TPB network inside the 3-D reconstructed volume. (c) Cumulative frequency curves for the equivalent diameter for the three phases, Ni, YSZ and pores measured from the 3-D reconstructed volume. The average particle sizes are determined from the 50^{th} percentile (indicated by the dotted line). (d) Frequency distribution of the pore size, showing a major peak at approximately 200 nm and a raised tail at 1000 nm. 111

Figure 5.7 Impedance spectra of the nano-composite electrode after being exposed to humidified 5% H_2-N_2 for 60 min at 800 °C and at open circuit, measured from 10 kHz to 0.01 Hz. (a) Nyquist plot compared with the equivalent circuit model (inset) fitting and the physically-based model simulation (b) the Bode plot of the imaginary component (c) the Nyquist plot after ageing for 10 h and for 100 h in humidified 5% H_2-N_2. 115

Figure 6.1 Cross-sectional SEM image of the nanostructured Ni-YSZ after 60 min of reduction and aging at 800 °C. The region includes micron-sized clusters of intertwined nanoscale Ni and YSZ network and pores in-between the clusters. 122

Figure 6.2 The Nyquist plots of the impedance of the symmetrical cell with nano-composite electrodes at 800 °C under open circuit voltage (left) at different aging time and their corresponding distributions of relaxation times (right). 123

Figure 6.3 DRT of the EIS measurement with varying hydrogen partial pressure (a) and at different temperatures. The Arrhenius plot of the medium-frequency response R_{med} is plotted and its activation energy calculated (c). The impedance spectrum of the symmetrical cell aged for 6100 min at 800 °C in humidified 5% H_2-N_2 in fitted with complex nonlinear least square (CNLS) fitting with the equivalent circuit in the inset (d). 125

Figure 6.4 The ASR for R_{med} with time for an electrode aged in the short term for 60 h and another aged in the long term for 600 h. The FIB-SEM reconstructions of E1 and E100 electrodes correspond to the high temperature aging time indicated by the arrow. 127

Figure 6.5 Distribution of the particles' equivalent spherical diameters for Ni, YSZ and Pore, with the particles identified by the watershed algorithm. The 3-D volume illustrates the particles identified in the Ni network in E100. Each particle is represented by a different colour to its neighbouring particles..... 128

Figure 6.6 Distribution of the neck diameter for the three networks, Ni, YSZ and pore in E1 after 1h aging and E100 after 100 h aging. The necks are the areas shared by neighbouring particles. The 3-D volume visualises the necks, indicated by different colours, in the Ni network in E100. 129

Figure 6.7 The morphology of the electrode E100 after 100 h of aging. The FIB-SEM image in (a) shows nickel as the bright phase, YSZ as the grey phase and pore as the dark phase. The contact angles between Ni and YSZ at TPBs within the region reframed in red are measured. The 3-D reconstruction of a selected region in the electrode is shown in (b), with the nickel network in red and YSZ network in yellow. The first 3-D image on the left shows both phases, while the second image shows primarily the Ni network (with the YSZ phase made translucent) and the third image the YSZ network..... 133

Figure 7.1 thermal properties of the composite NiO-CGO powder. The sintering behaviour is shown in (a) the shrinkage and rate of shrinkage during constant-rate heating measured in dilatometer of a pressed green pellet using the as-dried powder. The mass change and the endothermic reaction were shown in (b) by DSC and TGA..... 138

Figure 7.2 particle size and surface area measurement. The volume-weighted particle size distributions (in diameter) in (a) are plotted for the initial powders as-dried and the final powders after calcination and ball milling. The adsorption and desorption isotherms on N_2 for the final powder is plotted in (b). The SEM image in (c) shows a typical particle of the final powder sprinkled on the conductive carbon tape..... 140

Figure 7.3 The XRD pattern corresponds to the Ni-CGO electrode cast on a YSZ substrate after the electrode was sintered at 1300 °C and reduced at 800 °C. The Bragg reflections belong to Ni (Cubic) marked in the first row of peak positions and $Ce_{0.9}Gd_{0.1}O_{1.95}$ (Cubic) in the second row. The measured data are drawn with black dots, the calculated profiles in red lines and the difference between the two in blue lines..... 141

Figure 7.4 FIB-SEM 3-D reconstruction of the porous Ni-CGO electrode. The original FIB-SEM image taken by back-scattered electrons in (a) shows the phase contrast for Ni, CGO and the resin-filled pore. The CGO appears to be very bright, followed by Ni and lastly the resin is the darkest. The image histogram indicates three distinct peaks for the three phases. The consecutive images following (a) were collected and the image stack was reconstructed to the 3-D structure of

the electrode in (b). The reconstructed volume on the left shows the intertwined Ni (in red) and CGO (in yellow) in the porous structure. The volume on the right shows the interface between CGO and pore, i.e. the DPBs. The grey network represents percolated DPBs. The blue parts are the DPBs disconnected from the network and become inactive..... 143

Figure 7.5 Impedance spectra and the corresponding DRT graphs of the symmetrical cells under open circuit conditions at a flow rate of 100 ml min^{-1}. In (a), at 800 °C, the H_2 partial pressure was changed from 5% to 95% and the DRT graphs were plotted accordingly. The temperature of the measurement furnace was varied between 800 °C to 700 °C in humidified 5% H_2-N_2 and the corresponding DRTs plotted in (b). The Arrhenius plot derived from (b) is plotted in (c) and the activation energy of the two different processes taking place at different characteristic frequencies, one between 0.1 and 0.5 Hz as R_{low} and the other between 2 and 10 Hz as R_{high}. In (d), an impedance spectrum (Nyquist plot) at 800 °C in humidified 5% H_2-N_2 is plotted together with the equivalent circuit model (ECM) fitting. The equivalent circuit is shown in the inset in (d). 146

Figure 7.6 Variation of the polarisation resistances at high frequency and low frequency during annealing at 800 °C..... 148

Figure 7.7 The variations of the polarisation resistances at high and low characteristic frequencies with the annealing time is depicted here. The symmetrical cell was reduced at 650 °C for 1 h and heated up to 800 °C for the annealing and impedance measurements in humidified 5% H_2-N_2. ... 150

Figure 7.8 SEM images of the electrode after 60 min and 4000 min of annealing at 800 °C in humidified 5% H_2-N_2. The almost pristine electrode with 60 min annealing and in-situ reduction is presented in (a). The image on the left is the cross section of the electrode and on the right is the top surface of the electrode with EDX mapping, where orange indicates Ce and green indicates Ni. In (b) are the cross-sectional images for the electrode with 4000 min annealing and in-situ reduction. 152

Figure 7.9 Microstructural comparisons between the electrodes aged for 60 min and for 4000 min at 800 °C. The active TPB network in the 3-D volume is shown in (a) as the blue lines and the particle diameter distributions of Ni and CGO for the two reconstructed volumes are shown in (b). 154

Figure 7.10 Magnified views of the electrode aged for 4000 min at 800 °C in humidified 5% H_2-N_2. Nickel is presented in red and CGO in yellow. In the images on the left, Ni was made translucent to highlight the CGO network structure and vice versa for the images on the right. On one side of the zoom-in region (a), Ni coarsening is appreciable and a few agglomerated particles are labelled.

On the other side of the region (b), Ni coarsening is much less severe and many Ni particles remained very fine..... 159

Figure 8.1 SEM images of the three types of microstructures investigated a) nickel-impregnated ScSZ, b) co-sintered Ni-YSZ nanocomposite powder and c) co-sintered Ni-CGO nanocomposite powder..... 162

Figure 8.2 Trends of the electrochemical polarisation resistances of the three different electrodes during aging at 800 °C in humidified 5% H_2 – N_2..... 164

Figure 8.3 The active (percolated) TPB densities of the three electrode as-reduced and after aging. The TPB densities for co-sintered electrodes are measured from FIB-SEM 3D reconstructions and for Ni-impregnated ScSZ electrodes are calculated from the electrochemical polarisation resistances using the physical TLM model..... 166

List of Tables

Table 1.1 The properties of common SOFC electrode materials 18

Table 4.1 Comparison between the model predicted electrochemical reaction ASR and the measured ASR at 650 °C with silver paste in moist (3 vol% water vapour) 5 vol% hydrogen-nitrogen 97

Table 5.1 TPB densities of Ni-based porous cermet electrode 112

Table 5.2 Physical and microstructural parameters used in the Transmission Line Model of the nano-composite Ni-YSZ electrode 117

Table 6.1 Values from complex nonlinear least square (CNLS) fitting on the impedance spectrum in Figure 6.3d with the equivalent circuit of two R-CPEs and one Gerischer. 126

Table 6.2 Microstructural parameters and electrochemical resistance for electrodes E1 after 1 h of aging and E100 after 100 h of aging. 130

Table 7.1 Microstructural parameters of the 3-D reconstruction for the electrodes aged for 60 and 4000 min 155

List of Acronyms

ALS Adler Lane Steel

APU auxiliary power unit

ASR area specific resistance

BET Brunauer-Emmett-Teller

BEV battery electrical vehicle

BSE backscattered electron

CGO gadolinium-doped ceria

CHFS continuous hydrothermal flow synthesis

CHP combined heat and power

CNLS complex non-linear least square

CPE constant phase element

CSTR continuous stirrer tank reactor

CTE coefficient of thermal expansion

CVD chemical vapour deposition

DPB double phase boundary

DRT distribution of relaxation times

DSC differential scanning calorimetry

EDX energy dispersive X-ray

EIS electrochemical impedance spectroscopy

EsB energy selective backscattered

E-T Everhart-Thornley

EVD electrochemical vapour deposition

FCHJC Fuel Cells and Hydrogen Joint Undertaking

FCEV fuel cell electrical vehicle

FEG field emission gun

FIB focused ion beam

FRA frequency response analyser

GT gas turbine

IPO initial public offering

IT intermediate temperature

MIEC mixed ionic and electronic conductor

OCV open circuit voltage

PEMFC proton exchange membrane fuel cell

ScSZ scandia-stabilised zirconia

SE secondary electron

SEM scanning electron microscopy

SIMS secondary ion mass spectrometer

SOC solid oxide cells

SOEC solid oxide electrolyser cell

SOFC solid oxide fuel cell

STP standard temperature and pressure

TEM transmission electron microscopy

TGA thermogravimetric analysis

TLM transmission line model

TPB triple phase boundary

XRD X-ray Diffraction

YSZ yttria-stabilised zirconia

1 Background and Motivation

In this chapter, an overview of the solid oxide fuel cells (SOFCs) and solid oxide electrolyser cells (SOECs) is presented. The role of SOFCs and SOECs in today's energy market and its future potential are summarised. The different fuel electrode materials are compared, with a focus on Ni-yttria-stabilised zirconia. Finally, the motivations of this thesis are explained, together with details of each chapter.

1.1 Solid Oxide Cells

The solid oxide cell (SOC), which refers to both the SOFC and the SOEC, is a key component in realising the hydrogen economy. Hydrogen gas (H_2) as a fuel is environmentally benign, with water vapour as its oxidation product. H_2 gas has a high energy content per unit weight of 120.7 kJ g^{-1} and is abundantly available [1]. Hence, H_2 gas is of interest as an energy carrier in a low carbon energy infrastructure. Today, it is produced mainly by steam reforming of fossil fuels and natural gas, and occasionally by electrolysis or photochemical reactions [2] which has a much higher production cost. SOFC generates electricity from hydrogen, giving out water, and SOEC uses electrical energy to produce hydrogen from water. Conceptually, they are the same cell running in reverse modes. When combined with a gas turbine, SOFC power systems are capable of reaching a very high electrical efficiency of 70% and heat-and-power efficiency of 90% [3], [4]. While SOFC development has been ongoing for the last decades, interest in SOECs has recently been revived for renewable hydrogen production from wind and solar power. High temperature

water electrolysis using SOECs is considered the cleanest and most efficient technology available to store energy from intermittent and site-specific renewable power generation to match supply with demand [5].

1.2 Working Principles of SOFC

The SOC comprises three layers, namely, the fuel electrode, the electrolyte and the air electrode. For SOFCs, the fuel electrode is the anode where the oxidation of fuel takes place and the air electrode is the cathode where the oxygen gas is reduced to ions. The electrolyte is a dense layer, sandwiched by porous electrode layers. Though some interest has been shown in proton conducting oxides, especially the $Ba(Zr,Ce,Ln,Y)O_{3-\delta}$ perovskite, to lower the operating temperature, the majority of SOFCs still use an oxygen ion conductor, YSZ for example, as the electrolyte.

Typically SOFCs operate between 500 °C and 1000 °C [6]. Nowadays, SOFCs can be efficiently powered by natural gas, bio-gas and other hydrocarbon fuels, with internal reforming [7]. As shown in Figure 1.1, syngas (H_2 and CO) flows through the anode side and is oxidised to water vapour and CO_2. Meanwhile, air on the cathode side provides oxidant when the oxygen gas is being incorporated into the cathode lattice as oxygen ions O^{2-}. Electrons are released during the oxidation of syngas and passed through to current collector to power an external load. The electrons then flow back to the cathode to drive the reduction reaction. The electrodes are porous to maximise the electrochemical reactions on the solid-gas interface. However, the electrolyte needs to be impermeable to achieve high fuel utilisation. When running on H_2, the reactions taking place in a SOFC are

H_2 (gas) + O^{2-} (electrolyte) ⇆ H_2O (gas) + $2e^-$ (current collector) at the anode; (1.1)

$\frac{1}{2}O_2$ (gas) + $2e^-$ (current collector) ⇆ O^{2-} (electrolyte) at the cathode; (1.2)

H_2 (gas) + ½ O_2 (gas) ⇆ H_2O (gas) overall (1.3)

.

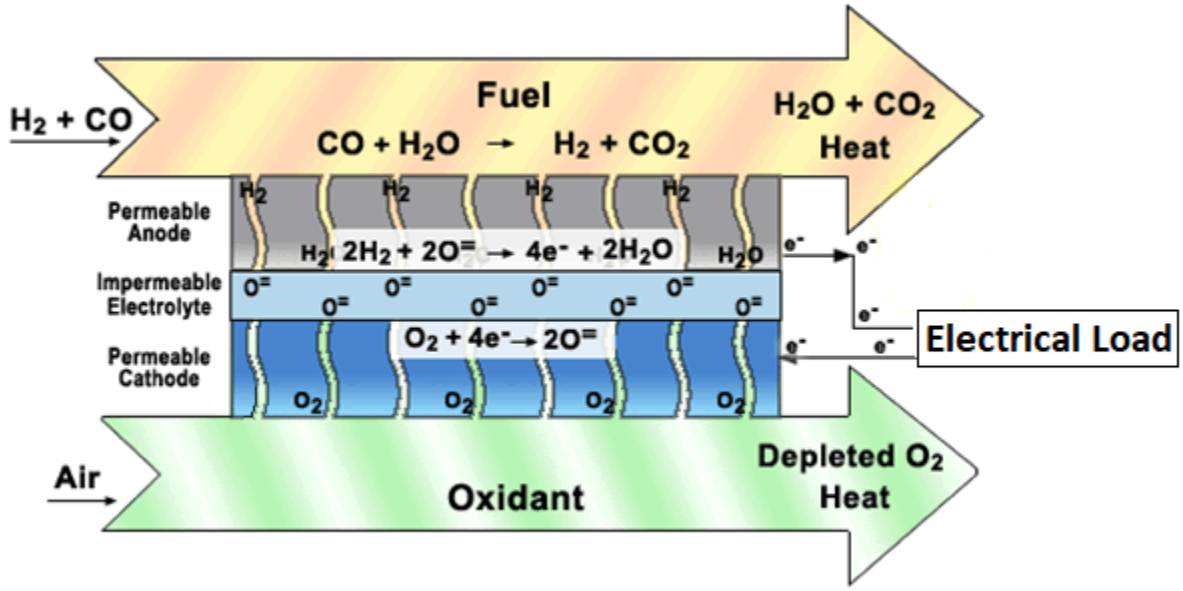


Figure 1.1 Schematics illustrating the operation of SOFC with oxygen ion conducting electrolyte. Modified from [8].

In practice, fuel cell units are connected in series to build a stack for the desired voltage. Tubular and planar cells are the two common SOFC designs. While tubular cells offer better thermal cycling stability and easier sealing, planar cells have higher power densities and simpler manufacturing by tape casting and screen printing [9]. The planar design in Figure 1.2 shows different layers within a repeating unit. A layer of current collector is applied on both the anode and cathode sides. Popular choices for current collector are Ni felts, chromia forming metal plates with or without doped $LaCrO_3$ coatings [10].

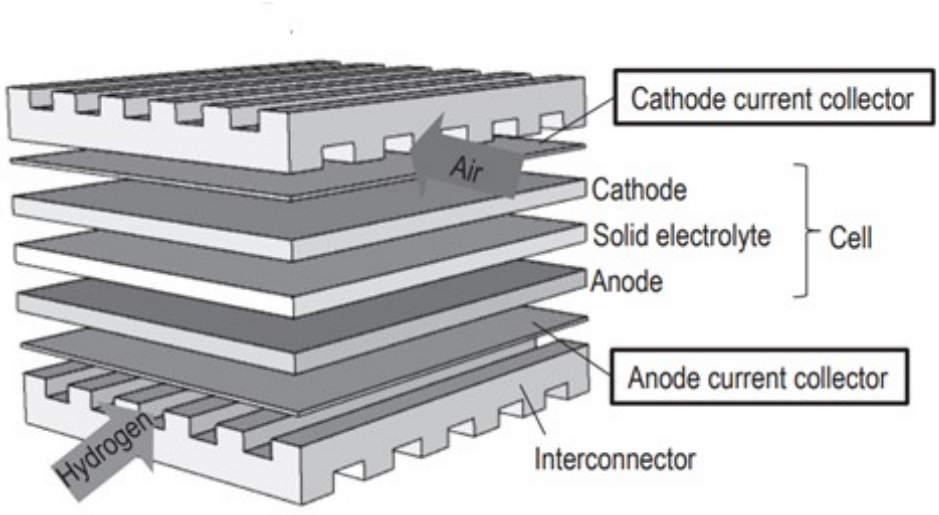


Figure 1.2 Planar design of the SOFC stack, after [11].

1.2.1 Electrochemistry

1.2.1.1 Nernst Potential

In thermodynamics, the change in Gibbs free energy ΔG of a reaction is given by the interaction between enthalpy change ΔH and entropy change ΔS,

$$\Delta G = \Delta H - T\Delta S = -nFE \qquad (1.4)$$

The overall reactions in SOFCs at the operating temperatures have negative ΔG and negative ΔS. The electromotive force E in Equation 1.4 is determined from ΔG, n the number of electrons transferred in the balanced equation and F the Faraday's constant. Increasing the temperature T will decrease the equilibrium cell potential E [12], which is often called the open circuit voltage (OCV).

With hydrogen fuel, the overall reaction as described in Equation 1.3 has a Nernst potential E_{nernst} influenced by the partial pressures of the hydrogen, water vapour at the anode and oxygen at the cathode P_{H2O}, P_{H2} and P_{O2}.

$$E_{Nernst} = -\frac{\Delta G^o}{2F} + \frac{RT}{2F} ln \frac{P_{H_2} P_{O_2}^{\frac{1}{2}}}{P_{H_2O}} \qquad (1.5)$$

where ΔG° is the change in Gibbs free energy under standard state and R the universal gas constant. ΔG° is -229 kJ mol^{-1} at 25 °C for Equation 1.3 and hence the standard potential is 1.18 V [13]. Because water vapour is indispensable in this reversible reaction, in the laboratory setting the fuel gas is usually humidified and modelling studies normally assume a 3% atm steam, which is the saturated vapour pressure at room temperature (25 °C). From Equation 1.5, it is shown thermodynamically, that increasing system pressure or increasing the concentrations of reactant gases will lead to an increase in the equilibrium cell potential.

1.2.1.2 Polarisation

When a current is drawn from a SOFC, the actual cell potential is lower than its equilibrium potential due to irreversible losses. These voltage drops are termed polarisations or overpotentials. Three polarisations in fuel cell operations are the activation polarisation, the ohmic polarisation and the concentration polarisation as shown in Figure 1.3.

Activation polarisation is pronounced in the low current region. It reflects the kinetics of the reactions on the electrode surface, where some of the emf is lost in overcoming the activation barrier for the reaction. The activation polarisation η_{act} manifests itself in Figure 1.3a as the initial rapid fall in voltage and can be expressed as

$$i = i_o \left[\exp\left(\alpha_a \frac{nF\eta_{act}}{RT}\right) - \exp(-\alpha_c \frac{nF\eta_{act}}{RT})\right] \qquad (1.6)$$

where n is the number of electrons transferred, i the current density, i_o the exchange current density, α_a and α_c the asymmetry factors for anodic and cathodic reactions [14]. Equation 1.6 is also known as the Butler-Volmer Equation. This low current region initial fall in voltage with current is often observed in proton exchange membrane fuel cells (PEMFCs) but less significant for high temperature SOFCs because the fast kinetics at high temperature facilitates charge transfer. At low over potential ($\eta_{act} < 0.1$ V) [14], the Butler-Volmer equations can be simplified as Equation 1.7, which is approximately linear.

$$\eta_{act} = i \frac{RT}{i_o nF} \qquad (1.7)$$

The ohmic polarisation η_{ohm} is from the resistance to the ion flow in the electrolyte mainly and the electron flow through the electrodes and the external circuit [13]. It is the linear region on the V-I curves in Figure 1.3 and follows a linear relationship

$$\eta_{ohm} = iR_{tot} \qquad (1.8)$$

where R_{tot} is the total cell resistance comprising of resistances of anode, cathode, electrolyte and the contact resistance between the layers.

At a higher current density, the concentration polarisation becomes dominant when the diffusion of the gaseous reactants to/from the electrochemical reaction sites becomes rate-determining. The concentration polarisation η_{conc} can be calculated as[15]

$$\eta_{conc} = \frac{RT}{nF}\ln\left(\frac{P}{P_o}\right) = \frac{RT}{nF}\ln\left(1 - \frac{i}{i_{lim}}\right) \qquad (1.9)$$

where P is the pressure at the reaction site at the actual current density and P_o is the pressure when the current density is zero. i_{lim} is the limiting current at which the fuel is used

up at a rate equal to its maximum supply speed. It should be noted that Equation 1.9 is only true for a thick electrode in which the transport to the electrode plane is in series with the electrode reaction. In a "volume" electrode such as porous mixed conductor or a fine composite, the gas diffusion behaviour is more complex.

In a porous composite SOFC electrode, the concentration polarisation depends largely on the electrode microstructure, especially the porosity and tortuosity. During fuel cell operation, the concentration of the reactant gases near the surface reaction sites decreases, and the higher the current, the greater the decrease. The replenishment of the reactant gases depends on the microstructure of the pore network and the diffusivity of the gases. Toshio and colleagues reported an increase in power density in anode-supported tubular SOFCs at 600 °C from 0.2 W cm^{-2} to 1.1 W cm^{-2} when the porosity of the anode was increased from 37% to 54% [16]. A smaller mean pore radius and a lower porosity were also found to lower the fuel conversion in a one-dimensional numerical simulation of a methane-fuelled SOFC [17]. In another simulation a pore size of 3 µm and porosity of 40% was found to minimise the concentration over-potential [18]. Porosity and pore size of the electrode are important as gas diffusion in the pores can influence the kinetics of the reaction.

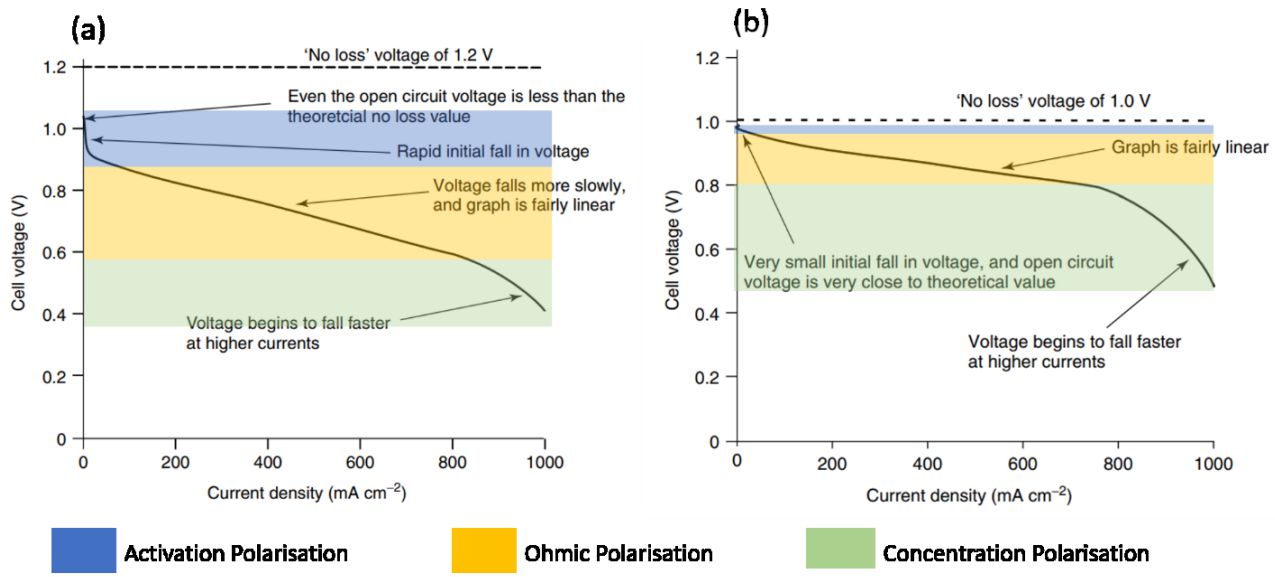


Figure 1.3 voltage vs. current density curve for (a) a low temperature fuel cell (70 °C) and (b) a typical SOFC at high temperature (800 °C or above). Modified from [15].

In summary the actual cell voltage is determined as

$$V = E_{nerst} - \eta_{act,a} - \eta_{act,c} - \eta_{ohm} - \eta_{conc,a} - \eta_{conc,c} \qquad (1.10)$$

where $\eta_{act,a}$ is the activation polarisation at anode, $\eta_{act,c}$ the activation polarisation at cathode and likewise $\eta_{conc,a}$ and $\eta_{conc,c}$. The operating voltage is determined by both the Nernst potential and the sum of different overpotentials. Though high temperature SOFCs have lower Nernst potential than PEMFCs or other low temperature counterparts, SOFCs have smaller overpotentials which leads to a generally higher operating voltage (Figure 1.3).

Besides the three main polarisation processes mentioned above, additional polarisation losses can happen for the gas transport above the electrodes. This is the case when the gas supply to the electrode surface becomes limiting and the scenarios are illustrated in Figure 1.4.

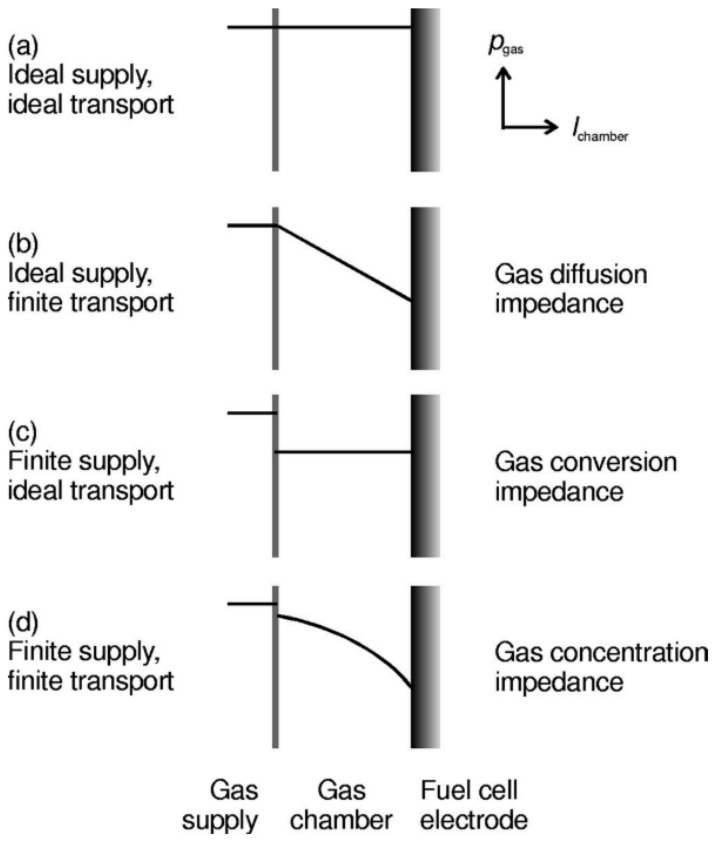


Figure 1.4 gas concentration profiles for the limiting behaviours of gas transport on top of the SOFC electrode [19].

In Figure 1.4, the inlet gas concentration at the electrode surface is influenced by the transport behaviour in the gas layer outside the electrode. Figure 1.4a is the ideal case when the gas concentration at the electrode is always constant to the inlet concentration because there is infinitely fast transport inside the gas chamber. In Figure 1.4b, the gas layer near the electrode has finite transport and the concentration profile decreases linearly from the inlet to the electrode. The gas transport inside this layer is governed by diffusion. The stagnant layer model proposed by Primdahl and Mogensen describes this phenomenon as the "gas diffusion impedance" [20]. In Figure 1.4c, the electrochemical reaction creates an abrupt concentration change in the gas chamber. The test rig geometry has an effect and

the inlet gas flow rate determines the extent of polarisation. This effect was first analysed by Primdahl and Mogensen as the "gas conversion impedance" using a Continuous Stirrer Tank Reactor (CSTR) model [21]. Figure 1.4d is a combined effect of Figure 1.4b and Figure 1.4c, when the concentration gradient is influenced by both diffusion and convection.

Alternatively, the total polarisation can be quantified by the area specific resistance (ASR) in Equation 1.11**,** when the VI characteristic is approximately linear. On a stack level, a fuel cell unit runs on hydrogen and air to generate electricity. There is a potential difference between the electromotive force emf of the inlet gases and the cell voltage V. The slope on the I-V curve in Figure 1.3b is the ASR. ASR is less sensitive to small fluctuation in cell voltage and fuel utilisation than power density and hence it is often used as a performance measure in fuel cell tests [22].

$$\mathrm{ASR} = R_{ohm} + R_{electrochem} + R_{conc} + R_{diff} + R_{conver} \qquad (1.11)$$

The total polarisation ASR is the sum of the ohmic resistance R_{ohm} mainly from the electrolyte and the electrical contact, $R_{electrochem}$ the resistance from the electrochemical reactions taking place in SOFCs, R_{conc} the gas concentration resistance arising from the transport inside the porous electrode, R_{diff} the gas diffusion impedance and R_{conver} the gas conversion impedance. While the former three are originated from the properties of the SOFC cells, the latter two are associated with the structure of the current collector layer [23]and the dynamics of the gas flow surrounding the cell.

1.3 Current State of SOFC Development

In the global energy market, SOFC technology holds promise in Combined Heat and Power (CHP), Long-range Transportation, Auxiliary Power Units (APU) and Stationary power generation. The EU, the USA, China and Japan have long been the major players in SOFC development, with Korea recently entering the market with strong policies [24]. In July 2018, Bloom Energy Corporation, a leading company in SOFC technology, launched its initial public offering (IPO) at $15 a share, after its SOFC-based server platforms seizing a considerable share from the data centre market for reliable on-site power supply [25]. In California, international companies like Apple, eBay, IKEA and Coca-Cola have installed more than 200 MW of SOFC-based systems. The Ene-Farm project in Japan has installed 180,000 SOFC and PEMFC-based CHP units till 2016 and has successfully lowered the system cost to less than $10,000 per 1kW unit [26]. In 2018 SOFC stacks operated for more than 35,000 h have been analysed [27]. The fuel flexibility of SOFCs with the possibility to run on a wide range of hydrocarbon fuels makes it easier to integrate them into the established gas grid [28]. The fuel flexibility of SOFCs make them ideal electricity generation devices for a smooth transition from the current fossil fuel to the future renewable hydrogen economy.

In the transportation sector, NISSAN revealed the first concept car called e-Bio Fuel Cell during the Olympic Games in Brazil in 2016. The SOFC range extender operates on bio-ethanol and recharges the high voltage battery, extending the driving range from 150 km to 600 km with a 30 L ethanol tank [29]. The SOFC stack has a high stack volumetric power density of 10 W cm^{-3} and gravimetric power density of 3 kW kg^{-1}, exceeding that of an internal combustion engine. With hydrocarbon refuelling, SOFCs and internal

combustion engines have similar specific energy of 1 kWh kg^{-1} [30] . It is clearly a promising alternative for combustion engines to reduce noise and pollution. In the UK, there are a few hydrogen refuelling stations today, with the plan to expand to 65 stations under the H2ME project co-funded by the European Union's Horizon 2020 programme through the Fuel Cells and Hydrogen Joint Undertaking (FCHJC) [31]. Ceres Power in the UK successfully doubled its revenue in 2018 to 6300 k£, after releasing its 5kW stack with increased power density, reduced start-up time and vibration tolerance for automotive applications [32]. The gradual improvement in hydrogen fuel supply infrastructure will allow fuel cell electrical vehicles (FCEV) to rival battery electrical vehicles (BEV), as well as increase the efficiency and reduce emission of greenhouse gases with FCEVs running on hydrogen fuel.

CHP and Stationary application are particularly well suited for SOFCs based on its high temperature operation and high efficiency. For operations $>$ 5 h, the energy density of fuel cell far outweighs its lead-acid battery counterpart [33]. LG Fuel Cell systems successfully demonstrated over 1000 h operating time for a 200 kW-class SOFC system fed by natural gas from the grid, with multiple start-ups and shutdowns [26] in 2016. In the EU, the first industrial size biogas-fed SOFC system was installed in 2017 under the DEMOSOFC project, integrating a biogas system, a 58 kWe SOFC module and a heat recovery system. Worldwide, a great number of SOFC units ranging from 1 kW for household usage to 1 MW for international data centre have been installed in the last five years. Those distributed generation applications demonstrate the potential in SOFC's initial market entry and will validate the stack reliability for larger stationary systems in the near future.

Though the recent five years saw a positive commercial uptake in SOFC technology, the current state of development in SOFCs is still behind PEMFC and lithium batteries. PEMFCs do not have the long start-up time as SOFCs due to its much lower operating

temperature. Li-ion batteries, with a more advanced global supply chain and hence lower cost, are dominant as the energy system in green vehicles [34].

The Gartner Hype Cycle [35] in Figure 1.5 illustrates the current development phase of SOFC technology, in comparison to PEMFC and Li-ion battery. Today, the inflated hype for SOFCs has been dismissed with the realisation of the low cost-competitiveness of this technology. SOFC has entered a stage when both the benefits and the issues of the technology have been made widely aware and the technological challenges in commercialisation are being addressed. For example, Japan's Ene-Farm 0.3-1 kW residential systems and FCEV products are being highly subsidised by government programmes [36]. The UK Research Council has been maintaining or reducing the grants for fuel cell and relevant field since 2015 [37]. Meanwhile US companies manufacturing stationary fuel cell systems supported by various state incentive programmes, including Bloom Energy, are still struggling to make a net profit in the competition with grid electricity [38].

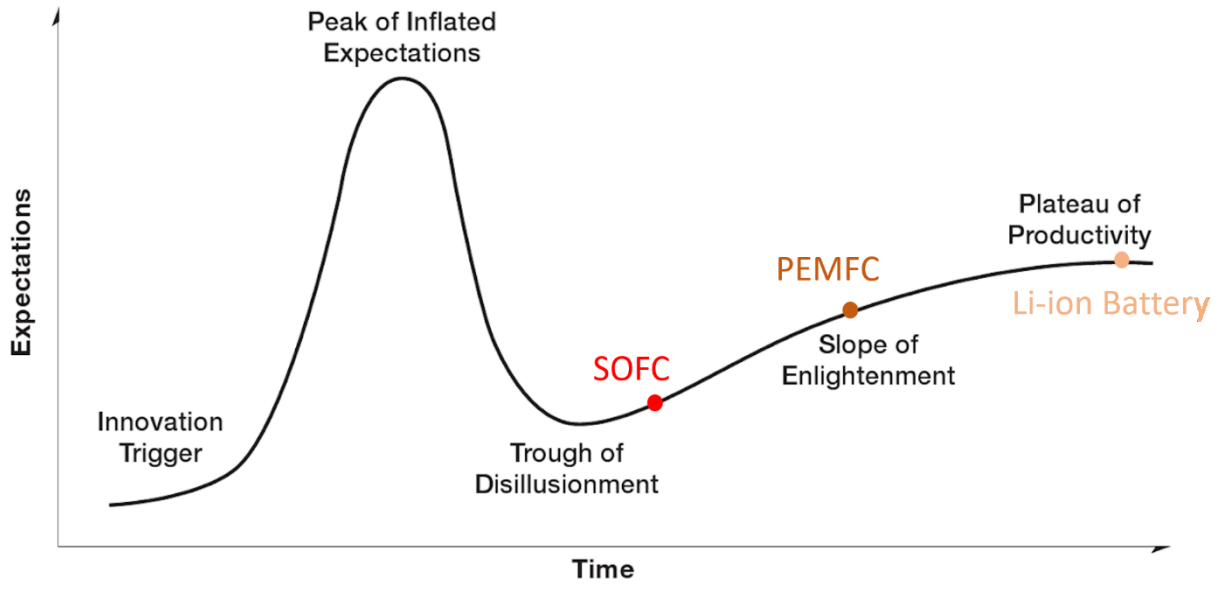


Figure 1.5 The Hype Cycle illustrating the maturity of SOFC technology and its alternatives

Till now the major fuel cell companies are still making net losses in the financial year 2018, including Bloom Energy, Ballard Power and Ceres Power. Bloom Energy, one of the leaders in SOFC technologies, was on a loss of $ 135M out of its total revenue of $ 528M [39]. The companies have niche markets, for example reliable non-stop electrical power for data centres and hospitals and are relying on significant government subsidies. To boost market impact, The U. S. Department of Energy set a cost reduction target for fuel cell systems to $ 40 kW^{-1} in 2020 from the current cost of $ 53 kW^{-1} [40].

The high cost for SOFCs is a great hurdle for market penetration. The Japan Ene-Farm residential micro CHP unit cost \$0.26 kWh^{-1}, still slightly more expensive than grid electricity after government subsidy [38]. On the cell level, cost reduction will come from materials optimisation. SOFCs do not use precious metals as catalyst due to their high operating temperature. Therefore, enhancing the reaction rate in the electrode and electrolyte materials is the best option to increase the power density of the cell and consequently bring down the cost per kW. After accounting for the efficiency and heat generation, the target power density of the cell is approximately 0.5 W cm^{-2} [41], which translates to 0.15 Ω cm^2 for the electrode polarisation resistance.

Another critical challenge for SOFC technology is to sustain a long operation life-time. Several stacks operated for over 10,000 h have been monitored and post-test diagnosed, some showed low voltage degradation rate of 0.2 % per 1,000 h [27]. The Durability target set by the U.S. Department of Energy for fuel cell stack is 0.3 % of voltage degradation per 1000 h. in 2020 [42]. The current laboratory standard for fuel cell stack degradation rate was also reported to be approximately 1% per 1000 h for stationary application and per 400 – 600 h for automotive. Degradation originating from the cell component include, coarsening of nickel particles and carbon deposition in the anode(when operating on hydrocarbon fuel)

at the anode, Sr segregation and Cr poisoning at the cathode, as well as delamination between layers [43]. Until now, there are no perfect solutions to those issues, though the understanding on degradation mechanisms have improved and some methods to mitigate the deterioration found over the last five years.

1.4 Fuel Electrode Materials

The fuel electrodes for SOCs need to be stable in the high-temperature reducing atmosphere and electronically conducting. Additionally, the mismatch in coefficient of thermal expansion (CTE) in the electrode and the electrolyte should be minimised to avoid mechanical delamination.

The fuel electrode materials being studied nowadays are in two categories: 1) the composite of two electronic and ionic conducting phases and 2) a single phase of mixed ionic and electronic conductor (MIEC). The fuel electrodes are made porous to maximise the anode-gas interface and hence fuel access. In category 1), the electrochemical reaction takes place at the region where the pore, the electronic conductor and the ionic conductor meet, called the triple phase boundary (TPB). At the TPB, the oxygen ions from the ionic conductor oxidise the fuel gases from the pore, releasing electrons that travel along the electronic conductor. The product gases then flow out of the pores. Similarly, the electrochemical reaction zone is at the double phase boundary (DPB) between the pore and the MIEC phase for category 2), with both the ions and the electrons are transported along the MIEC network [44]. It is also common to have the combination of 1) and 2), because the DPB electrode has large electrochemical reaction zone but can be further improved with the

addition of another phase to enhance its conductivity (either ionic or electronic) and catalytic activity.

The most conventional fuel electrode material is Ni-YSZ cermet. Ni serves as both a good electronic conductor and a catalyst for hydrogen oxidation. Meanwhile, the YSZ network in the fuel electrode maintains the mechanical compatibility with the YSZ electrolyte by reducing the CTE of composite as compared to pure Ni [3] to minimised the mismatch with the electrolyte [45] and supplies the required ionic conductivity. 8 mol% YSZ has an oxygen ionic conductivity of 0.164 S cm^{-1} at a temperature of 1000 $^{\circ}$C [46]. The processing route for porous Ni-YSZ electrode has been well-researched and is widely utilised in industry. The processing involves homogeneous mixing of NiO and YSZ powder, firing at high temperature and finally the reduction of NiO to Ni during the operation of SOFC to create the porosity required. Nevertheless, Ni-YSZ electrodes suffer from carbon deposition where there is insufficient steam and sulfur poisoning when operating on natural gas, which drastically reduce its electrochemical activity. It is hence essential to pre-process the natural gas when using SOFCs with Ni-YSZ anode [47]. Due to the high electrochemical activity, mechanical stability and its simple and mature manufacturing, Ni-YSZ remains very relevant today despite emerging new materials.

For intermediate temperature (IT)-SOFC at 500-600 °C, Ni-gadolinia doped ceria (CGO) anode and CGO electrolyte are popular choices. CGO is a MIEC at the reducing and high temperature atmosphere. It becomes a MIEC at above 450 °C in reducing atmosphere and shows a high ionic conductivity of approximately 0.5 S cm^{-1} at 800 °C [48]. Also a catalyst for carbon oxidation, CGO has been found, in combination with Ni as a cracking catalyst, as a good anode for direct oxidation of dry methane [49]. The addition of Ni as the metallic phase in the cermet compensates for the low electronic conductivity of CGO. Some studies

also suggest that Ni promotes the uptake of hydrogen from the gas phase, enhancing the surface limitations of CGO [1]. Despite its low mechanical strength, CGO reduces the carbon deposition when using hydrocarbon fuels [50]. The extended reaction zone from TPBs to DPBs in Ni-CGO fuel electrodes result in faster kinetics and hence Ni-CGO electrodes have demonstrated excellent electrochemical performance. Steele [51] predicted a peak power density of 400 mW cm^{-2} at 500 °C for a cell with 25 µm $Ce_{0.9}Gd_{0.1}O_{1.95}$ (GDC10) electrolyte. Many single cell measurements with Ni-CGO electrode and CGO electrolyte show promising power density, 386 mW cm^{-2} at 600 °C by Zhen et al. [52], 335 mW cm^{-2} at 550 °C by Fu et al. [53]. In an anode-supported cell test, the polarisation resistance of the cell with Ni-YSZ anode is 0.158 Ω cm^2 at 800 °C in humidified H_2, which is higher than 0.072 Ω cm^2 for the cell with a Ni-CGO anode [54].

Table 1.1 summaries the pros and cons of other common anode materials.

Table 1.1 The properties of common SOFC electrode materials

Property	Material	Advantage	Drawback	Reference
Ionic Conductor	ScSZ	High ionic conductivity (~ 0.1 S cm^{-1} at 850 °C for 10 mol% ScSZ)	Phase transitions accompanied by volume changes between 400 and 600 °C	[55]
	$La_{1-x}Sr_xGa_{1-y}Mg_yO_{3-0.5(x+y)}$ (LSGM)	High ionic conductivity and chemical compatibility with MIECs	Formation of resistive phase due to chemical reactions between LSGM and NiO	[56]
Electronic Conductor	Cu	High electronic conductivity and reduced carbon deposition as a poor catalyst for C-H bond activation	Conventional cermet fabrication is not applicable due to low melting point of 1083 °C	[57]
	Ru	Good catalyst for hydrocarbon reforming to prevent carbon deposition	Expensive precious metal (used as a catalyst layer with a low loading of 2 mg cm^{-2})	[58]
MIEC	Doped $SrTiO_3$	Stable towards redox cycling and good electronic conductivity in reducing atmosphere	Low ionic conductivity	[59]

Nanoscale engineering of the microstructure is a promising method to improve the fuel electrode performance as a result of the increase in TPB density. Kishimoto et al. observed a significant increase in TPB density to 18.4 μm^{-2} for a nanoscale Ni-CGO electrode as compared to 2.5 μm^{-2} for conventional Ni-YSZ [60]. A mathematical model by Janardhanan et al. based on particle geometries also predicted a TPB density increase by 10 times when the particle size of the ionic and electronic conducting phases were reduced from 5 µm to 1 µm, with a fixed porosity of 35% [61]. Also, adding nanoparticles with large catalytic surface area inside the fuel electrode leads to additional catalytic activity. Adding ceria nanoparticles in a traditional Ni-YSZ SOFC anode was found to enhance the sulphur tolerance of the electrode, sustaining a power density of 220 mW cm^{-2} at 0.6 V in humidified H_2 containing 40 ppm H_2S at 700 ^oC for 500 h [62].

Operating in the temperature range from 500 °C and 1000 °C poses many challenges in materials selection in order to ensure long-term stability of the system. For Ni-YSZ electrodes, the high sinterability of Ni is undesirable as it reduces the contact area between Ni and YSZ, and therefore the TPB density. Ni coarsening at high temperature can also cause a reduction in the connectivity of Ni network and consequently the conductivity. Simwonis et al. reported a conductivity decrease of porous Ni-8 mol% YSZ anode cermet from 3900 S cm^{-1} to 2600 S cm^{-1} after exposure in Ar-4% H_2-3% H_2O at 1000 °C for 4000 h, which is directly linked to a shift in the Ni particle size distribution towards larger particles [63]. With nanostructured SOFC anode, the coarsening is expected to be worse due to the high surface energy of nanoparticles.

1.5 Objectives of the Thesis

Enhancing electrochemical performance is an important aspect for cost reduction in SOFC units and introducing nanoscale electrode features offers a practical solution to this. Ensuring a long life-time for SOFCs is another key aspect for commercialisation. Fundamentally, at the SOFC cell or stack level, it requires retention of the integrity of the structure during long exposure to high temperatures. The project seeks to investigate the microstructure of high-performance nanostructured Ni-based cermet electrodes and nickel coarsening in the electrode.

To understand the high performance and degradation behaviours of the nanostructured Ni cermet electrode, three research questions are raised.

1) What are the impacts of nickel nanoparticle coarsening in the electrode's electrochemical performance?
2) Will the nanoparticles be preserved in the high temperature operating conditions between 600 to 1000 °C for SOC applications?
3) Does the microstructure of the cermet influence the coarsening behaviours of the nanoparticles?

To find the answers for the questions above, which are the general objectives of this thesis, the specific objectives are set as follows.

1) To study nickel coarsening at high temperatures (600 °C to 1000 °C), by looking into the morphology of nickel after aging;

2) To compare nickel-zirconia and nickel-ceria composite anodes fabricated using impregnation and co-sintering of composite nanoparticles;

3) To monitor the real-time electrochemical performance of the nano-structured Ni cermet electrodes with non-destructive measurements;

4) To relate the electrochemical performance of nano-structured Ni cermet electrodes with the microstructure and clarify the different mechanisms contributing to the ASR.

In the thesis, the literature on nanostructured Ni-based cermet electrode and nickel coarsening is reviewed in Chapter 2. Chapter 3 elaborates the main characterisation methods used in the project. Chapter 4 studies the degradation in Ni-impregnated Scandia-stabilised Zirconia (ScSZ) electrodes at three different aging temperatures. Chapter 5 focuses on the fabrication and performance of nanoscale Ni-YSZ electrodes using nanocomposite powders made by continuous hydrothermal flow synthesis (CHFS). Chapter 6 investigates the high temperature degradation behaviour of the nanoscale Ni-YSZ electrodes described in Chapter 5. Chapter 7 applies the fabrication route developed in Chapter 5 to nanoscale Ni-CGO electrodes and looks briefly into the stability of the electrodes. Chapter 8 draws a conclusion on performance and stability of nanostructured Ni-based cermet electrode for SOFC applications and Chapter 9 outlines the future work.

2 Literature Review

This chapter reviews the properties of the nanostructured Ni-based SOFC anode, comparing the anode microstructures resulted from different fabrication techniques. The electrochemical performances of the anodes are discussed in line with their microstructures. The mechanisms of Ni coarsening and the various methods to minimise Ni coarsening are summarised.

2.1 Fabrication Techniques of Nanostructured Anodes and Their Electrochemical Performance

Nanostructured electrodes have much larger active surface area as compared to the conventional micron-scale electrodes for SOFCs. Simulations have proved that reducing the particle size of the nickel and ceramic phases leads to an increase in TPB densities. A geometrical model adopted by Janardhanan et al. for porous composite electrodes predicted that with 50% porosity, the TPB density increases from 1 to 15 μm^{-2} when the particle size of the mono-dispersed particles reduces from 5 to 1 µm [61].

Impregnation is a promising fabrication route to enhance the electrochemical performance of SOFCs. It is one of the most widely-used laboratory methods to introduce nanoparticles in the electrode structure. Impregnation, sometimes referred to as infiltration, is carried out by dripping metal nitrate solutions onto porous scaffolds and allowing the nitrate to spread into the scaffold by capillary action. The infiltrated electrodes are then heat treated to

decompose the nitrate to oxide. The above-mentioned process is then repeated until a sufficient loading of the impregnated oxides is achieved [64]. The size of impregnated Ni particles on CGO scaffold was reported in the range of 100 – 300 nm [60]. The size of impregnated CGO and YSZ particles on Ni was also reported in the range of 100 – 300 nm [65]. The impregnated particles have uniform size distribution and are well dispersed [66]. Impregnation is a very versatile fabrication method and because it does not require high temperature sintering, it opens up the possibility to incorporate catalytic particles with low melting points such as Cu [67][68]. However, the process is time-consuming as it requires several infiltration-calcination cycles to achieve percolation of the phase, because the porosity in the SOFC electrode is much lower than the porous support used in catalysis [64].

Impregnation has been shown to produce electrodes with superior electrochemical performance compared to the conventional route. For example, impregnating $La_{0.9}Sr_{0.1}Ga_{0.8}Mg_{0.2}O_{3-d}$ with nickel produced an electrode with ASR of only 0.008 Ω cm^2 at 650 ^{o}C [69], much lower than the ASR of 0.05 Ω cm^2 for a similar electrode produced by the conventional route. With nano-YSZ impregnation in nickel-cermet anode, the overpotential reduced from 195 mV to 63 mV at 200 mA cm^{-2} at 900 °C and the polarisation resistance from 1.9 Ω cm^2 to 0.5 Ω cm^2 [70]. Impregnation of copper and cerium nitrate into Ni-based cermet anodes suppressed carbon deposition when the cell was fed with methane [71]. Infiltrating palladium reduces the area specific resistance of Ni/CGO anode as shown in Figure 2.1. The catalytic activity of infiltrated palladium at different loadings indicated on the Nyquist plots was found to promote the hydrogen oxidation reaction. Rh, Ni and Fe were also found to act as catalysts for anode reactions [72]. Moreover, infiltrated nickel particles showed no dimensional change after one redox-cycle, suggesting enhanced redox

stability [73]. The impregnated electrodes also have a better thermal expansion coefficient match to the dense electrolyte which reduces the risk of electrode delamination [74].

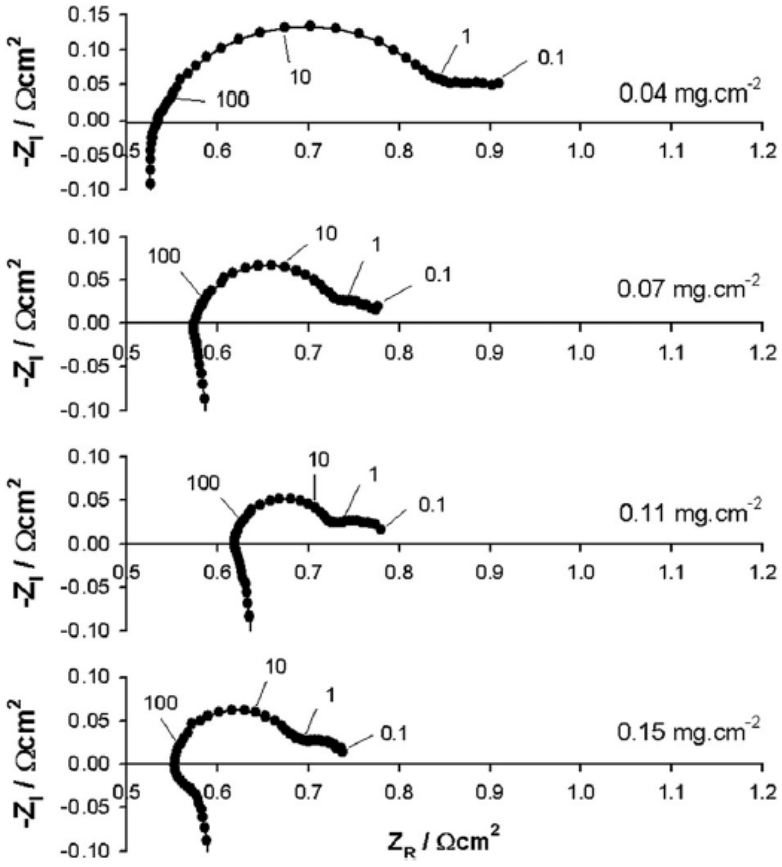


Figure 2.1 Nyquist plots for the hydrogen oxidation on Pd-infiltrated Ni-CGO cermet anode at different PdO loading in 97% H_2 and 3% H_2O [75].

Over the last few years, studies have been done to study the optimisation of microstructures in infiltrated electrodes. Yuan et al. reported that replacing YSZ scaffold with Sr-doped $LaFeO_3$ (LSF) and YSZ composite scaffold reduced the infiltration cycles from 8 to 2 to reach the target ASR 0.1 Ω cm^2 at 700 °C [76]. Atomic layer deposition was also used to deposit La_2O_3 in infiltrated LSF-YSZ electrode, which improved the ASR from 0.4 to 0.2 Ω cm^2 at 600 °C [77]. Gorte summarised their research and pointed out the ALD coating needs to be of the correct thickness to stabilise the infiltrated nanostructure

and single infiltrations as surface modification with low loading (e.g. 3 wt%) of infiltrate can significantly reduce polarisation resistance [78]. Gao et al. found that the nickel loading is optimal at 12.3 vol% which gives the maximum power density for a cell with Ni-infiltrated LSGM anode [79]. The density of infiltrated Ni nanoparticles needs to be high enough to form good particle-particle contact but not too high to completely cover the surface of the ionic conductor. Nicholas and Barnett also developed a geometry model as an SOFC infiltrated cathode design tool which calculates the infiltration loading (vol%) to achieve the lowest polarisation resistance in MIEC-infiltrated on ionically conducting scaffold [80], [81]. In the meantime, Shah and Barnette proposed power low models for predicting the degradation in infiltrated CGO air electrode [82]. Overall, the microstructure of infiltrated electrodes has been better understood and simulation tools have also been developed to facilitate the infiltration techniques.

Thin film techniques such as chemical vapour deposition (CVD) and electrochemical vapour deposition (EVD) are sometimes used in making Ni-based nanoscale electrodes for SOFC applications as well. In the vapour deposition process, a reactive gas carries the precursors of the materials to the substrate and reacts with other gases or decomposes to deposit the precursor materials onto a substrate in the form of a film [83]. Ying et al. [84] developed a combustion CVD route to make Ni-CGO electrodes with 50 nm particle size and the polarisation resistance of the cell with Ni-CGO anode and $Sm_{0.5}Sr_{0.5}CoO_{3\pm\delta}$ (SSC)-$Sm_{0.1}Ce_{0.9}O_{3\pm\delta}$ (SDC) cathode is as low as 0.17 Ω cm^2 at 600 °C.

Exsolution of metal particles has recently attracted much attention in generating nanoparticles on oxide surfaces, especially nickel particles deposited on perovskite oxides. The exsolution takes place when the catalytically active transition metals substituted on the B-sites of perovskite oxides (ABO_3) in oxidising conditions was exposed to reducing

condition. The metal particles are released onto the surface and partially embedded. They appear as periodic array of metal nanoparticles [85]. The exsolved Ni particles are typically several 10 nm in size and the interactions between the metal particle and the parent oxide limit coarsening and coking during SOFC operations [86]. The polarisation resistance of $PrBaMn_{1.7}Ni_{0.3}O_{5+\delta}$ with exsolved Ni nanoparticles on the oxide surface is 0.099 Ω cm^2 at 800 °C in humidified H_2 and constant current density under a constant voltage of 0.6 V at 700 °C in H_2 for over 200 h [87]. Though the exsolved Ni particles are not percolating, they are promising as good catalytic materials in SOFC anode due to the high stability of the exsolved nanoparticles [88].

It is worth mentioning that tape casting and screen printing are the two most common manufacturing process for SOC electrodes and are well-established in industrial fabrication [89] [90]. They are easy to implement and cost effective. Both fabrication methods involve mixing the powders of NiO and the ionic conductor phase and formulating the powder into an ink with sufficient solid loading and suitable viscosity. The ink was then cast or printed onto the electrolyte substrate and fired at a high temperature (above 1000 °C). Most of the screen-printed and tape-cast SOFCs reported in literature have particles in the micrometre range [91][92]. The challenge to fabricate nanoscale electrode materials using tape casting and screen printing is the low green density of the cast/printed film and the different sintering kinetics of the nano-sized particles as compared to conventional micron-sized particles [93].

Despite the difficulties in ink formulation, attempts have been made to fabricate composite nanopowders for SOFC anodes. Nanosized Ni-YSZ composite particles were synthesised by co-precipitation of the constituent metal hydroxides. $ZrOCl_2 \cdot 8H_2O$, $Y(NO_3)_3 \cdot 6H_2O$ and $Ni(NO_3)_2 \cdot 6H_2O$ were used as precursors in de-ionised water and added dropwise to NaOH

solution to make the precipitate. The precipitates were then washed, dried, pulverised and calcined at 1000 °C. In the screen-printed Ni-YSZ anodes made from the co-precipitated powders, the particle sizes were between 200 – 400 nm as shown in Figure 2.2 and the polarisation resistance of the anode was 0.36 **Ω** cm^2 at 800 °C in 3% H_2O-H_2 under OCV [94]. NiO-YSZ nanocomposite powders made using different precursors shows similar grain size of 200 – 400 nm and polarisation resistance of 0.23 Ω cm^2 at 800 °C in the resultant Ni-YSZ electrode [95]. Song et al. also showed that the co-precipitated NiO-YSZ nanocomposite increase the maximum power density of 0.87 W cm^{-2} at 750 ° in comparison to 0.73 W cm^{-2} of the conventional composite power [96].

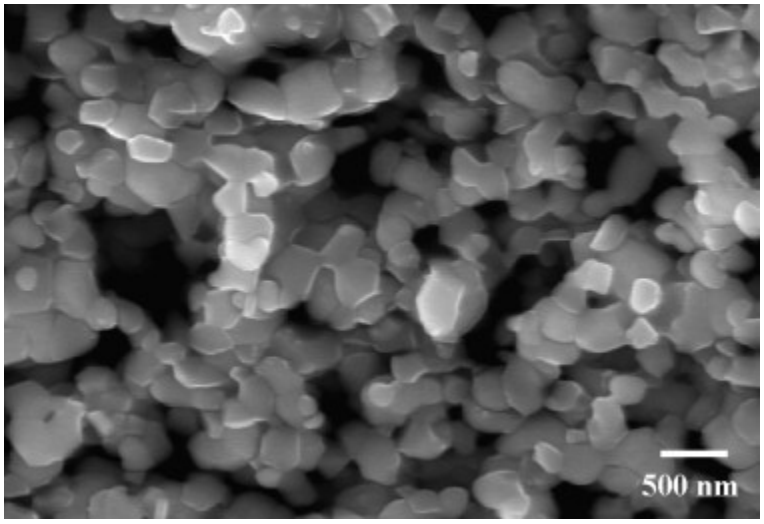


Figure 2.2 SEM image of the Ni-YSZ anode made from the co-precipitated nano-sized composite NiO-YSZ powder, reproduced from [94].

Another chemical fabrication route for nanocomposite powder is the hydrothermal method. The reactants are placed into an autoclave filled with water and the reactions are carried out under high temperature and pressure. This method utilises the solubility of the precursors at high temperature (~ 200 °C). For example, $Ni(NO_3)_3 \cdot 6H_2O$ and urea were dissolved in water and ethanol and heated in a sealed autoclave to 90 °C to produce $Ni(OH)_2$.

The product was then calcined at 450 °C to yield submicron flake-like agglomerates with nanocrystal NiO of 2-3 nm [97]. The advantage of the hydrothermal synthesis as compared to the co-precipitation route is the oxides can possibly be directly precipitated from the heated solution without drying and calcination. This prevents excessive agglomeration caused by heat treatment. Typical hydrothermally synthesized oxide nanoparticles have high surface area approximately 100 $m^2 g^{-1}$ and grain size approximately 10 nm [98] as shown in Figure 2.3. A single cell with Ni-CGO nanocube composite anode synthesised hydrothermally showed a higher power density of 97 mW cm^{-2} at 600 °C compared to the 67 mW cm^{-2} for a conventional Ni-CGO powder and a decrease in anode's polarisation resistance from 0.58 to 0.14 Ω cm^2 [99]. Similar improvement in power density was also observed in Ni-$Ce_{0.8}Sm_{0.2}O_{1.9}$ (SDC) electrode synthesised hydrothermally in comparison to the conventional solid mixing route [100]. Combining both the co-precipitation and hydrothermal processes will give the benefits of yielding oxide directly in a continuous reactor. The hydrothermal flow system will also enable thorough mixing of the different oxide precipitates [101].

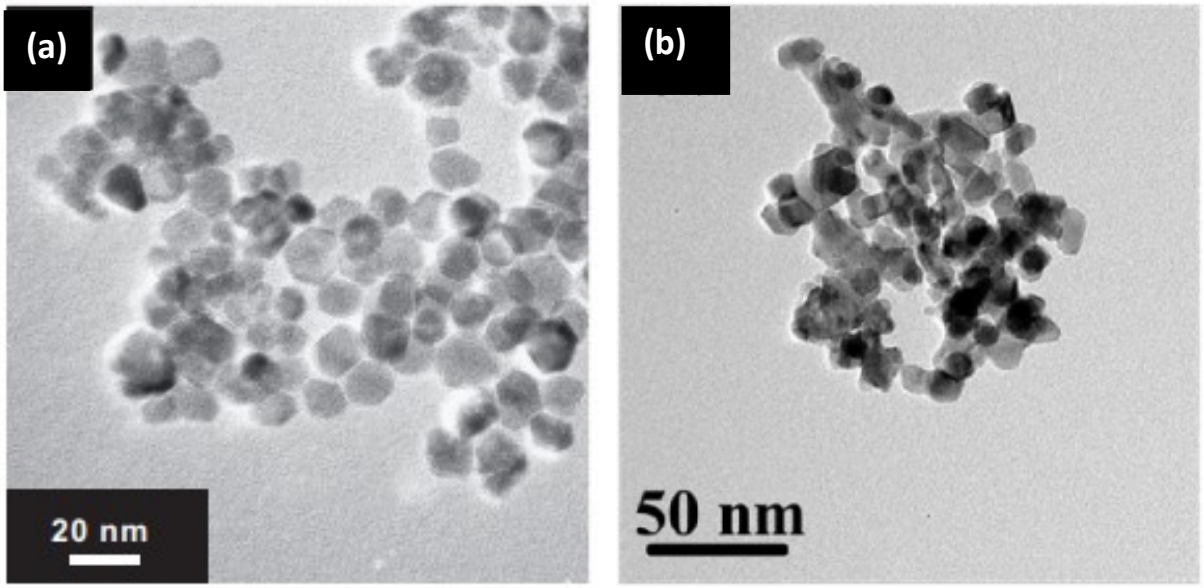


Figure 2.3 Transmission electron microscopy (TEM) images of the hydrothermally synthesized nanoparticles of CGO (a) [99] *and 70 mol% Ni- 30 mol% SDC (b)* [100].

2.2 The Stability of Nickel in Nanostructured Electrodes

The morphology of the nickel and ceramic composite plays a significant role in SOFC's electrochemical performance. Bieberle and Gaukler [102] showed that Nyquist plots of Ni-YSZ anode fabricated using screen printing, nickel sputtering and electrostatic spraying were very different. The different impedance data were a result of different nickel-ceramic morphologies. Adding to the complication is the evolution of the nickel phase with time during high temperature operations. It is hence important to study the structural relations between nickel and ceramic phase, which will in term determine many microstructural features such as TPB length, tortuosity and porosity. Ultimately, the morphology and its evolution in the anode influence the cell's power density and stability.

2.2.1 Nickel Coarsening and its Thermodynamics

Nickel coarsening in a composite anode structure is the growth of larger nickel grains at the expense of small grains driven by the reduction of the Gibbs free surface energy. The Gibbs-Thomson equation [103] shows that the chemical potential is inversely related to the radius of the particle and therefore large particles are energetically favourable. The partial derivative of Gibbs free energy G is related to the radius of the particle r by:

$$\frac{\partial G}{\partial n} = G_n + \frac{2\gamma v}{r} \qquad (2.1)$$

with n representing the number of atoms in a particle, G_n the Gibbs free energy per atom, γ the surface energy and v the average atomic volume. Thermodynamically, Nickel atoms tend to move from high curvature regions to low curvature region to reduce the chemical potentials.

In a nickel-ceramic composite, the coarsening of nickel is also related to the interfacial energy between the nickel and ceramic phase. Phase field simulation has shown that lowering the interfacial energy between nickel and YSZ from 1.8 J m^{-2} to 1.2 J m^{-2} prevented about 10% TPB length reduction over the initial 100 hours of coarsening [104]. The contact angle between nickel droplets on YSZ in a 4% H_2-Ar atmosphere at 1500 ^{o}C is 112-117^{o} [104][105], which is undesirably large. The poor wettability between the Ni and the ceramic phase adds onto the effect of Ni coarsening in the cermet structure as simulated by a continuum diffuse-interface model [106].

2.2.2 Mechanisms of Nickel Coarsening

Three possible transport mechanisms have been proposed for nickel coarsening: evaporation-condensation, bulk diffusion and surface diffusion.

Evaporation-condensation is expected with a high nickel vapour pressure [107]. Studies have revealed local enrichment accompanied by local depletion of nickel content in cermet anodes [108][109]. Transmission electron microscopy images of Ni/YSZ anode thin foils showed that the exposure to 98% H_2 and 2% H_2O, as compare to pure H_2, exacerbated the nickel agglomeration to an extent that nickel grains came detached from the cermet backbone [110]. The vapour equilibrium diagram [109] showed that $Ni(OH)_2$ is the most volatile nickel species in a mixture of hydrogen and water vapour and the gaseous nickel-containing vapour pressure increases rapidly by a magnitude of 10^4 when the H_2O content increases from 0 to 20 % (Figure 2.4).

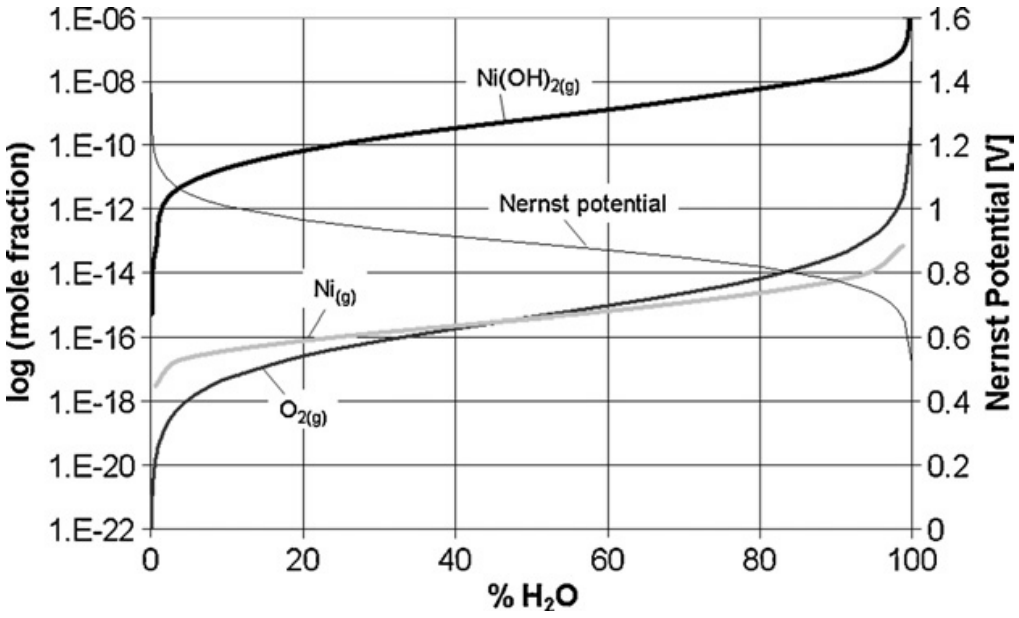


Figure 2.4 Vapour equilibrium diagram of nickel species with excess solid nickel [109].

Water is commonly present in the anode gas as a product of the oxidation reaction. Adsorption of OH^- on the nickel surface and subsequent diffusion from the surface to the bulk was recognised as anodic hydroxylation [111]. Hydroxide ions at the hot surface of nickel are present due to water dissociation at high temperatures. Adsorbed OH^- forms nickel hydroxide with nickel, which then likely to evaporate at a location, being transported and condense at a different location in the cermet structure.

Surface diffusion is defined as movement of atoms in the top few lattice layers within a thickness of 1nm [104]. Nickel surface diffusivity is of the order of $10^{-10}\,m^2\,s^{-1}$, nearly six order of magnitude greater than its bulk diffusivity at 1100 °C [112][33][34]. Nickel hence preferentially diffuses over the surface than through the bulk. The difference in curvature between large and small particles gives rise to a difference in vacancy concentration ΔC [115]. This concentration gradient results in a vacancy flow according to Fick's law. Hence, surface diffusion j between two particles with distance Δx can be expressed as:

$$j = D_v \frac{\Delta C}{\Delta x} \qquad (2.2)$$

Where D_v is the diffusion coefficient of vacancy. The model from Vassen et al. [116] based on Fick's law and surface diffusion predicted a 23% growth of nickel particle size after 10,000 h of operation at 800 °C. This great extent of growth assumed that surface diffusion is the dominant coarsening mechanism.

Recent observations in microstructural evolution of Ni by 3-D imaging indicated that Ni coarsening takes place in the time scale of a few hours and is less prominent after the particles become isolated [117]. The findings suggest surface diffusion is the dominant mechanism for nickel coarsening, as compared to the evaporation-condensation mechanism, especially when the partial pressure of water vapour is not significant.

2.2.3 Influencing Factors for Nickel Coarsening

Growth of nickel grains becomes noticeable above a threshold temperature, which was found to be 473K by Ebrahimi and Li [118], and 593K by Thuvander et al. [119]. Both temperatures fall below the usual operational temperatures of SOFCs and thus grain growth is expected in nickel ceramic composite anodes.

Previous studies indicated nickel agglomeration is related to the operation temperature and reduction temperature. Reduction of nickel oxide for the anode cermet at 550 °C and 750 °C produced nickel clusters due to reassembly of nickel after reduction was completed. The cermet reduced at 650 °C, on the contrary, produced a homogeneously distributed nickel phase and a high power density of 0.5 W cm^{-2} and a low area specific resistance of 0.5 Ω cm^2 at 850 °C [120]. 180 nm-thick nickel thin films sputtered onto TiO_2-doped YSZ

substrates agglomerated when annealed at 1173K but stayed in its original state at 773K. When the nickel films were reduced to 80nm in thickness, agglomeration was observed at 773K as well [121]. Coarsening is suggested to be a thermally activated process and transport on the surface is faster than in bulk. Attempts have been made to fit the nickel particle growth with an Arrhenius equation [120]–[124]. Iwanschitz et al. [122] proposed a modified Arrhenius relationship between the nickel particle radius r in nm and the reduction temperature T in Kelvin from a 24 h isothermal aging experiment.

$$r = r_o + Ae^{\frac{-E_a}{RT}} \qquad (2.3)$$

Equation 2.3 was fitted to the measured radii of nickel particles from 50 wt% Ni-CGO and 70 wt% Ni-CGO anode reduced and annealed for 24 h at different temperatures from 500 °C to 1000 °C. The fitted and measured data are in good agreement.

Based on the theory of a vacancy gradient due to curvature, coarsening is expected to be more severe when the particle size distribution is wide. When exposed to humid gas for 2286 h, the particle size distribution of nickel in a Ni-CGO anode showed a fast shift towards larger particle size during the first 200 h and the rate of change slowed down afterwards due to disappearance of particles smaller than 300nm [125]. Observations by X-ray nano-tomography also shows a similar aging trend by measuring the mean nickel phase diameter, suggesting the large size difference between the particles promotes nickel coarsening [126]. Additionally, the amount of nickel in the cermet can also affects the rate of coarsening. Klemensø et al. [127] showed the nickel content is a decisive factor in determining the extent of degradation over time.

The presence of water vapour not only enhances the formation of volatile nickel species but also might increase the surface diffusion coefficient of nickel [128][124]. Porous Ni-CGO

anodes in humid atmosphere with 60 vol% H_2O showed a high nickel particle growth of 280% during the first 200 h whereas the equivalent anode under dry conditions with 97 vol% N_2 and 3 vol% H_2 showed a much lower growth of 2% over the same period of time [125].

2.3 Impact of Nickel Coarsening on Electrochemical Performance

The direct impact of nickel coarsening is the reduction of TPB density. X-ray tomography images reported by Kennouche et al. [129] showed a continuous decrease in active TPB density in a Ni-YSZ anode as the average nickel particle size increased from 650 nm to 950 nm. Simulations of ASR have shown that the ASR is mainly determined by the triple phase boundary density [60], [130]. As a result of coarsening, a reduction of TPB length from 1.84 μm^{-2} to 1.34 μm^{-2} was observed in Ni-YSZ anode after the cell stack operated for 1900 h at 800 ˚C, accompanied by a stack degradation rate of -54.0 $\mu V\ h^{-1}$ [131] at constant current density. A metal-supported SOFC with Ni-$Ce_{0.8}Sm_{0.2}O_{2-\delta}$ (SDC) infiltrated anode showed a rapid voltage decrease from 0.804 V to 0.645 V at 700 °C with a current density of 0.86 Acm^{-2} but was stable at 600 °C and 0.4 Acm^{-2} [132]. A further 175 h stability test at 700 °C led to an increase in polarisation resistance from 0.24 to 0.36 Ωcm^2, which was associated with TPB reduction in the infiltrated anode coatings.

Nickel coarsening also causes a drop in electronic conductivity due to the interruption of nickel connectivity. Nickel coarsening led to a decrease of 33% of the initial electrical conductivity after exposing porous Ni-8YSZ anode cermet to wet hydrogen at 1000 °C for 4000 h [63]. In the study of Simwonis et al. [130], nickel particle size increased by 26.0%

while the number of particles decreased by 37.1% after coarsening. The loss of nickel-nickel contact cut off some electronic paths. The increase in particle size due to nickel coarsening reduces the contact area between the nickel and the electrolyte, and also the percolated TPB length.

Nickel agglomeration is expected to be more prominent in nickel impregnated electrodes due to the presence of small particles and therefore larger thermodynamic driving force. Impregnation introduces nano-sized particles into a porous YSZ scaffold due to a lower heat treatment temperature. The impregnated particles were in the range of 100-300 nm for Ni-impregnated YSZ scaffold, much smaller than the typical 1-2 µm in a typical cermet [70]. In the studies of U.P. Muecke et al. [133], while nickel-CGO with 16 nm nickel particle size exhibited a degradation of electrical conductivity of about an order of magnitude when dwelling at 560 ^{o}C for 1630 h, an equivalent film with 53 nm nickel particle size showed stable electrical conductivity throughout. The tendency to agglomerate for nanoparticles to reduce surface energy[192] also makes it difficult to preserve the nano-scale microstructure during the high temperature sintering in conventional SOFC electrode fabrication.

Interestingly, X-ray tomography analysis on a Ni-YSZ electrode at its pristine and annealed state showed that the pore connectivity improved as a result of nickel coarsening. This opening-up of new accessible pore space connected some originally isolated TPBs and mitigated the effect of TPB reduction[117]. Mogensen and Skaarup suggested the rate determining step of electrochemical reaction in SOFC occurs at the TPBs or the adjacent YSZ surface [134]. 3-D tomography of Ni-YSZ composite electrodes with varying YSZ content showed that even though electrodes with 30 wt% and 40 wt% YSZ showed similar active TPB density, their polarisation resistance differed by approximately a factor of 2 and this was associated to the difference in YSZ tortuosity [135]. The connectivity of the YSZ

phase is hence found to be critical in determining the electrochemical performance. Though the ceramic phase in the cermet is generally regarded as stable during the high temperature operations, some studies indicate coarsening can happen in the nanoscale ceramic phase as well, which can influence the electrochemical performance.

Long-term SOFC cell tests(>1,000 h) have been mostly carried out on cells consisting of micrometre-sized Ni-YSZ particles [27], and the limited number of studies on the stability of nanoscale Ni-cermet electrodes necessitates further investigations.

2.4 Method to Inhibit Nickel Coarsening

The ceramic phase is often regarded as rigid because of its low mobility[117], with its surface diffusion coefficient approximating to 3×10^{-16} m^2 s^{-1} at 1100 °C[114]. The ceramic phase therefore functions as a fixed scaffold in the composite structure. The ceramic matrix is expected to have a pinning effect on nickel grains. When annealed at 1000 °C for 10 hours, the average particle size of nickel was 350 nm for 20 wt% Nickel in CGO and 730 nm for pure nickel. An increasing trend of average particle size was observed when the nickel content increased from 20 wt% to 100 wt% [133]. A two particle model [136] with an additional term accounting for the limited growth space for nickel in the anode predicted a surface diffusion coefficient of 1.3 x 10^{-12} m^2 s^{-1} at 800 °C, which is much smaller than the surface diffusion coefficient with an order of 10^{-10} m^2 s^{-1} determined by Blakely et al. [137] for pure nickel. The discrepancy is attributed to the introduction of the maximum particle radius as a result of pore volume constraint. Hence, the ceramic phase is believed to provide microstructural stability by reducing the sintering and coarsening of the nickel metal phase [67][138][126]. Study on mesoporous Ni-CGO composites by Almar et al. [139] found that

good connectivity between ceramic and metal networks enhances the stability of the electrode at 800 °C. Modifying the microstructure of the nickel ceramic composite can improve the durability of the cell. Skarmoutsos et al. [140] demonstrated that a 40 vol% Ni/8YSZ anode cermet with 40 vol% porosity experienced only 8% conductivity decrease after 1000 h at 1000 °C. However, one with 20 vol% porosity experienced 21% decrease, which correlated to an increase in average diameter of nickel particle from 1.56 µm to 3.11 µm observed in optical images. This was attributed the large pore-size to nickel-particle-size ratio for the 20 vol% porous cermet, which provided more free volume for nickel agglomeration.

Addition of TiO_2 has also been reported to stabilise Ni nanoparticles. Tiwari and Basu found [141] adding 4% TiO_2 to Ni -YSZ anode-supported cell maintained a power density of 400 mW cm^{-2} under annealing and redox cycling for 94 h and attributed this stability to the interaction between Ni-TiO_2 through the transfer of electron from Ni to vacant oxygen site in TiO_x. Also, impregnating a layer of oxide particles around NiO in the cermets has been shown to inhibit the sintering of the later Ni particles in the cermet. Jiang et al. [142] reported that impregnating samaria-doped ceria (SDC) nanoparticles around 100 nm in a Ni-YSZ cermet eliminated the Ni agglomerates larger than 2 µm originally observed in the Ni-YSZ cermet after the fuel cell testing. It has also been also shown in studies that coating on the nickel particles, especially ceria nanocoating, can effectively suppress nickel coarsening [143][62].

The interfacial energy between nickel and the ceramic phase plays a role in determining the nickel stability. At the TPB, the Young-Laplace equation can be applied to relate the contact angle θ from the surface and interfacial tensions γ between nickel and the electrolyte phase.

$$\gamma_{electrolyte} = \gamma_{Ni/electrolyte} + \gamma_{Ni} cos\theta \qquad (2.4)$$

Modification on the wetting angle between the nickel and the ceramic can influence the Ni coarsening. A phase field model by Jiao and Shikazono [138], which simulates nickel coarsening in FIB-SEM 3-D reconstruction of Ni-YSZ electrodes, shows that decreasing the wetting angle of Ni on YSZ surface resulted in less isolated Ni. Experimentally, alternating lamellae of porous Ni and YSZ with a layer thickness of 200 nm prepared with different crystallographic orientation revealed that the formation of a lowest-energy interface in the Ni-YSZ system at a reduction temperature at 800 °C leads to good thermal stability of the cermet. No apparent evolution of microstructure, nickel in particular, was observed after aging at 900 °C for 300 h [144].

Kishimoto et al. [145] showed that TiO_2 doping of YSZ can suppress nickel agglomeration when the nickel particles have an average diameter of 800 nm. The average nickel particle size per unit area observed in back-scattered electron images were 3.842 on an YSZ substrate but decreased to 3.480 on a TiO_2 doped YSZ substrate. Meanwhile, a lower contact angle θ was also observed for TiO_2 doped YSZ substrate. The surface modification lowered the $\gamma_{Ni/YSZ}$ interfacial energy, which then reduced the contact angle and the equilibrium nickel particle size.

Structural manipulation on the interface between the nickel and the more rigid ceramic phase has been shown to enhance the stability of nanoscale electrodes. A nano-heterogeneously structured Ni-YSZ electrode developed by Kim et al.[146], with 10 – 30 nm nano-sized Ni and YSZ coating on 0.3 µm YSZ powders, was stable at 800 °C for 550 h of operation with a cell voltage of 0.8 V under a load current of 1 A cm^{-2}. The grain growth of nickel was inhibited by the neighbouring nano-sized YSZ in the mixture. Kim later demonstrated durability of the anode made of the nanocomposite with only nickel nano-

coating on YSZ for over 530 h [147]. This electrode made by micron-sized YSZ with nano-sized nickel coating showed stable electrical conductivity at about 1300 S cm^{-1} after 20 thermal cycling from 800 °C to room temperature [148] as shown in Figure 2.5. Itoh et al. investigated sintering nickel with 20 wt% coarse YSZ power and 80 wt% fine YSZ power and showed a steady overpotential of the anode up to 5000 h [149]. SEM images reproduced in Figure 2.6 suggested fine YSZ bridged around nickel particles, locking them in place. The fine YSZ particles formed a network in-between the coarse YSZ particles to maintain structural stability. This fine YSZ network also preserves the porosity of the anode in reducing atmospheres, with less than 1% decrease in porosity after dwelling at 1273K as compared to 20% for the reference anode. Particle size was also shown to play a role in determining the electrical conductivity. The anode with 80 wt% coarse YSZ showed a stable conductivity of 700 S cm^{-1} over 300 h in the dual-size structure in Figure 2.6.

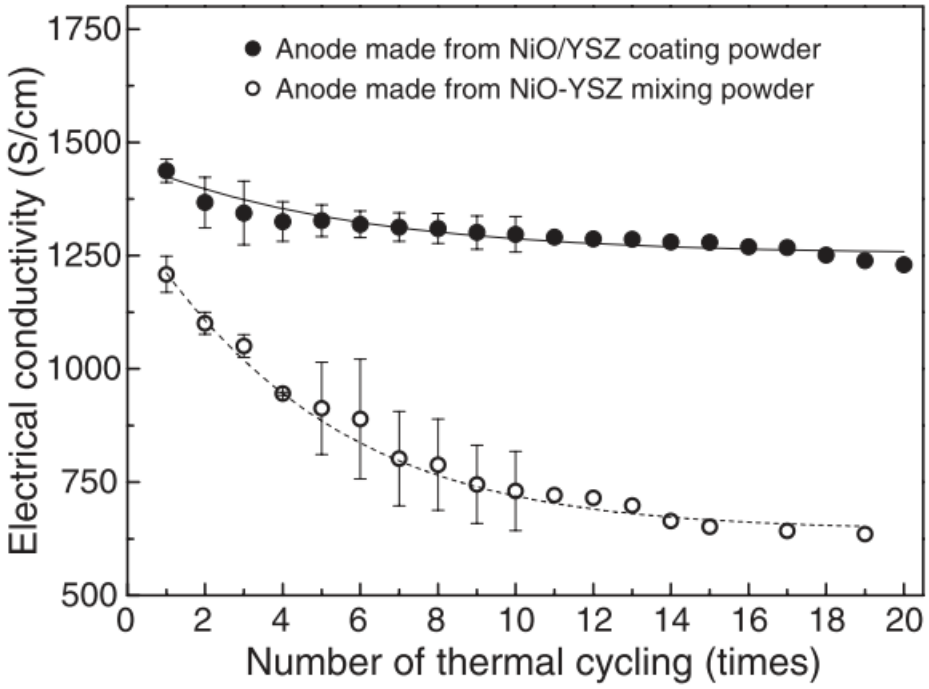


Figure 2.5 Electrical conductivity of the nickel nano-coating anode synthesized by Pechini process and the conventional Ni-YSZ anode after thermal cycling [148].

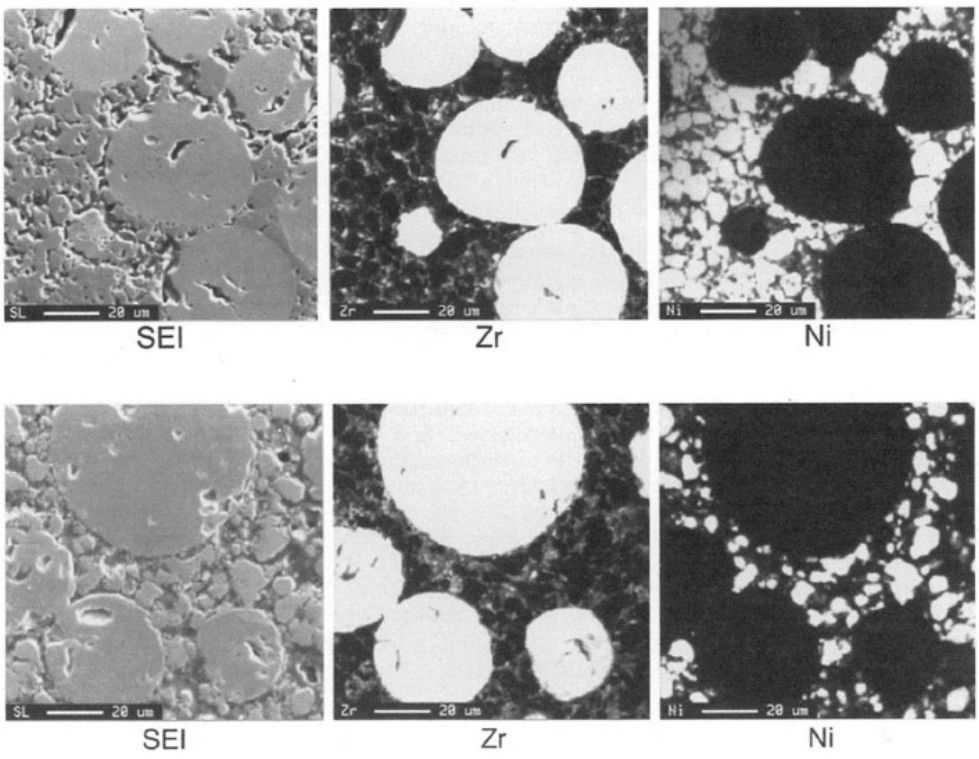


Figure 2.6 Secondary electron images on the cross section of a sintered Ni-YSZ anode before reduction (top row) and after reduction (bottom row) showed large zirconia particles about 20 μm in diameter and small nickel particles about 1 μm in diameter surrounded by a fine zirconia framework [149].

2.5 Conclusions

Various fabrication routes have been used to produce nanostructured Ni-based electrodes. Solution impregnation has been the most popular amongst the research community due to the capability to incorporate a wide range of materials at a relatively low temperature. Tape casting and screen printing are common in industrial practice due to their cost effectiveness.

Fabrication of the nanocomposite powders for ink formulation is challenging but progress has been made based on the co-precipitation and hydrothermal methods.

Nickel coarsening takes place through mainly surface diffusion and is accelerated by the evaporation and condensation of volatile Ni species, mainly $Ni(OH)_2$, in humidified atmosphere. Atomically, the surface diffusion follows Fick's Law. Nevertheless, the rate of coarsening is often modelled by Arrhenius equations to describe the trend of particle growth.

Nickel coarsening causes both a reduction in TPB density and in nickel connectivity. The two microstructural changes will lead to a decrease in electrochemical reaction rate and electrical conductivity, which affects current collection. Coarsening is expected to be worse in nanostructured electrodes because the high surface energy of nanoparticles leads to a high tendency to agglomerate.

The attempts to suppress nickel coarsening in the Ni-based SOFC electrodes include, increasing the rigid ceramic volume in the cermet, introducing a coating layer on Ni, doping to change the wetting angles and structural modification on the Ni and ceramic phase. All methods show encouraging results in improving stability of Ni-based electrodes. However, the literature on enhancing the stability of nanoscale Ni-based electrodes is limited.

3 Methodology

This chapter details the characterisation methods used in this study, especially focused ion beam (FIB)- scanning electron microscopy (SEM) and electrochemical impedance spectroscopy (EIS). FIB-SEM imaging is used to reconstruct the 3-D structure of nickel electrodes before and after high temperature aging. Meanwhile, EIS is used to monitor the polarisation resistance continuously during the aging. Other characterisation methods for measuring powder properties, conductivity and phase information are briefly explained as well.

3.1 Electrochemical Impedance Spectroscopy

3.1.1 Theory

In contrary to DC measurement, AC impedance can separate different physical processes taking place at different characteristic frequencies. In terms of characterising SOFC performance, EIS can reveal ohmic losses, electrochemical kinetics and mass transfer processes. It is hence practical to use AC measurement to identify which physical process in the anode is significantly influenced during the degradation process and model its behaviour.

An AC signal with small magnitude is used to perturb the electrochemical cell and the perturbation at steady state is measured. The EIS measurement was done via frequency response analyser (FRA). The FRA generates a voltage signal to the potentiostat and this

signal adds onto any existing DC bias and applied to the cell in a sum. The resulting current, in reality a voltage signal proportional to the current, is then fed back to the analyser and integrated over several single periods to yield the real and imaginary part of the impedance [150]. The impedance plot with the real part against the imaginary part is called the Nyquist plot.

In this study symmetrical cells, with two identical electrodes on a solid electrolyte in a single atmosphere, are used for EIS measurement. Two-electrode measurement was used with four probes on the symmetrical cell. The working electrode is where the current passes and the counter electrode completes the current path. The reference electrode holds a constant potential during testing to serve as a reference for the potential measurement. In a two-electrode set up, the current leads and sense leads are connected at the same contact points [151]. The working and the sensor electrodes are combined as one and so are the reference and counter electrodes. Between the sensor electrode and the reference electrode, the voltage drop across the whole cell is measured. The EIS measurement was carried out under OCV, with zero bias. The realistic operating voltage for SOFC is 0.7 V, for optimal electrical efficiency and power density. Due to the difficulties and inaccuracies of three-electrode measurement in SOFCs [152], two-electrode measurement with symmetrical cells at OCV is a less error-prone and easy-to-implement set up, which also gives reliable indication of the electrode performance.

Typically for a SOFC electrode, the Nyquist plot of EIS response is similar to the spectrum in Figure 3.1. The high frequency intercept is from the ohmic resistance of the contact interfaces and the resistance of the electrolyte which happens at a high frequency outside the measurable range under this test condition. The total impedance over a limited range of frequency (normally 1M – 0.01 Hz), is associated with the electrode process as pointed

out in Figure 3.1. In the electrode, two physical processes are happening at different relaxation frequencies, the charge transfer (activation polarisation) at high frequencies and the gas diffusion (concentration polarisation) at low frequency. To interpret the impedance spectrum, an equivalent circuit model is built to quantify the physical processes. An R-CPE component as shown in the inset of Figure 3.1 is very frequently used for SOFC electrode process, when depressed semicircles are seen.

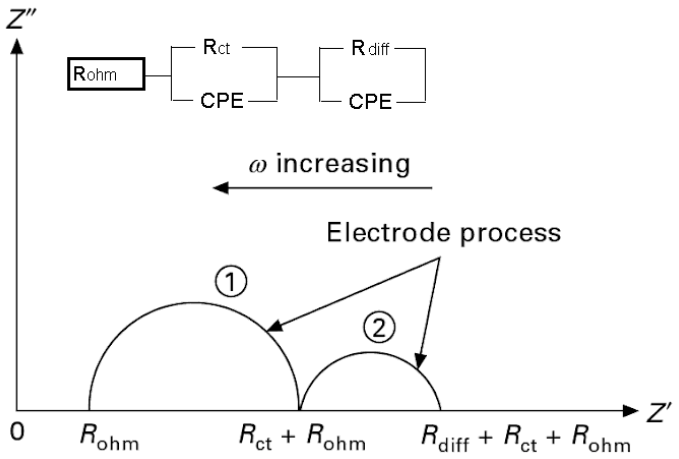


Figure 3.1 An example of a cathode-supported thin-film electrolyte cell with platinum as the counter electrode. Modified from [150].

The equation for the constant phase element (CPE) is

$$Z = \frac{1}{Q(j\omega)^n} \qquad (3.1)$$

where Q is the capacitance with the unit of F when the exponential term $n = 1$ and Q and n are correlated. ω is the angular frequency. When $n \neq 1$, the system is influenced by surface homogeneity, or distributed time constants for reactions [153].

The effective capacitance C_{eff} can be calculated from CPE and the resistance R in the R-CPE pair as explained in Equation 3.2

$$C_{eff} = \left[QR^{(1-n)}\right]^{\frac{1}{n}} \qquad (3.2)$$

A Gerischer element [154]is often used in describing the behaviour of a mixed-ionic-and-electronic conductor (MIEC) as

$$Z = \frac{R}{\sqrt{1+j\omega\tau}} \qquad (3.3)$$

where τ is the characteristic time for the reaction.

3.1.2 Rig Design

In SOFC EIS measurements, the gas flow and current collection in the set-up requires careful design to avoid artefact response outside the electrode. Two rig designs were used in this study and the first one with a closed chamber is shown in Figure 3.2. The body of the cell housing (grey in the figure) is made from pyrophyllite machinable ceramic and consists of two parts that are compressively spring-loaded to clamp the cell between the current collector grids. The symmetrical cell is placed inside a pyrophyllite sample holder. Inside the holders are two platinum meshes connected with platinum leads on each sides of the cell to serve as current collectors. The lower part of the housing receives fuel gas through a central circular aperture and then distributes it to the outer circumference of the housing through a lateral channel. To reach the cell electrodes the fuel diffuses through the annular gap (approximately 10 mm wide) between the two parts of the housing.

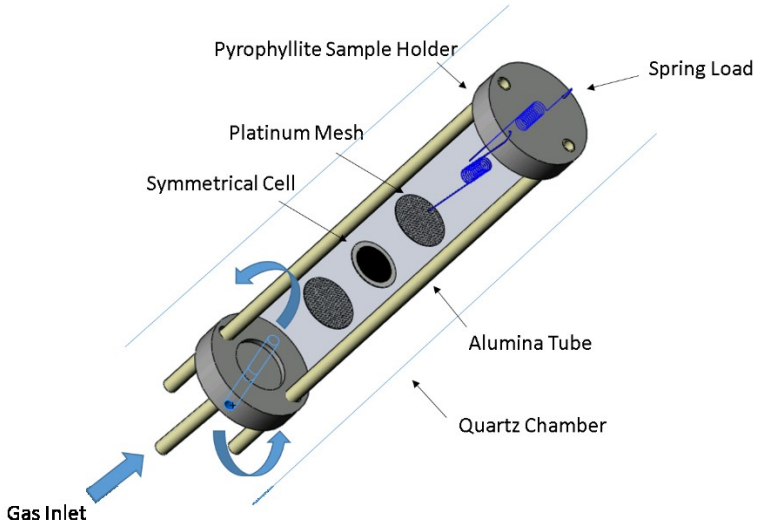


Figure 3.2 The closed-chamber rig design for symmetrical cell measurement. The symmetrical cell sits inside a pyrophyllite sample holder which is clamped by springs.

The advantages of this design are that the cells are mechanically protected, and it is very stable during long-term measurement. The platinum meshes are only mechanically pressed onto the electrodes, so the microstructure of the electrode's top surface is preserved for examination after the measurement. However, the design undesirably creates a thick gas diffusion layer on top of the electrodes. Because of the slow lateral diffusion of the inlet gas, the gas stagnant layer created this way can be as thick as a few mm. A gas stagnant layer found by Primdahl and Mogensen is about 1mm thick in a three-electrode set-up with nickel felt current collectors [23]. As a result, in this rig a polarisation resistance was observed between 1 – 10 Hz caused by this gas stagnant layer outside the electrode and was approximately 1 Ω cm^2. The polarisation resistance is termed 'gas conversion resistance' as first reported by Primdahl and Mogensen [21]. Similar polarisation responses were also observed by Song et al.[155] and Bertei et al.[156] in the same rig design. This artefact response can potentially overshadow the electrode response, especially when the electrode

shows high performance with low polarisation resistance. Additionally, the aperture of the platinum mesh is large in the 0.1 mm range in comparison to the feature size of the electrode (10 – 100 nm). The higher mesh spacing will increase the conductivity required for the electrode measurement proportionally.

To improve the cumbersome gas access and stringent conductivity requirement, a design with open gas flow was made. This design as shown in Figure 3.3 allows easy gas access to the electrode and better current collection. The inlet gas now blows sideways directly to the edge of the symmetrical cells vertically fixed on an alumina platform. While it is still a single gas atmosphere design, which can be managed by a single mass flow controller, the flow rate of the gas around the symmetrical cell is accelerated as compared to the closed-chamber design in Figure 3.2. The gas conversion impedance is greatly reduced.



Figure 3.3 The open gas flow rig design for SOFC measurement. The symmetrical cell sits on a groove in a cylindrical alumina platform. The inlet gas blows directly at the edge of the symmetrical cell.

The current collection is made by porous nickel paste (for above 650 °C) or silver paste (for 650 °C or below) with platinum leads. The paste should be sufficiently adhesive to the

electrode surface and is able to withstand the high temperature. A cross-sectional SEM image of the interface between the silver paste and the Ni-YSZ electrode polished by ion beam is shown in Figure 3.4. The silver paste consists of percolating particles and pores of 1 µm in size, while the Ni and YSZ inside the electrode are of 10 – 100 nm. The aperture size of the paste is 100 times smaller than the platinum mesh, and therefore a better current collection is made without too much compromise in gas access. The reduced pore size in the current collection layer, to some extent, causes a gas access issue but it is outweighed by the benefit of open gas access after removing the parts needed for mechanically compressing the mesh.

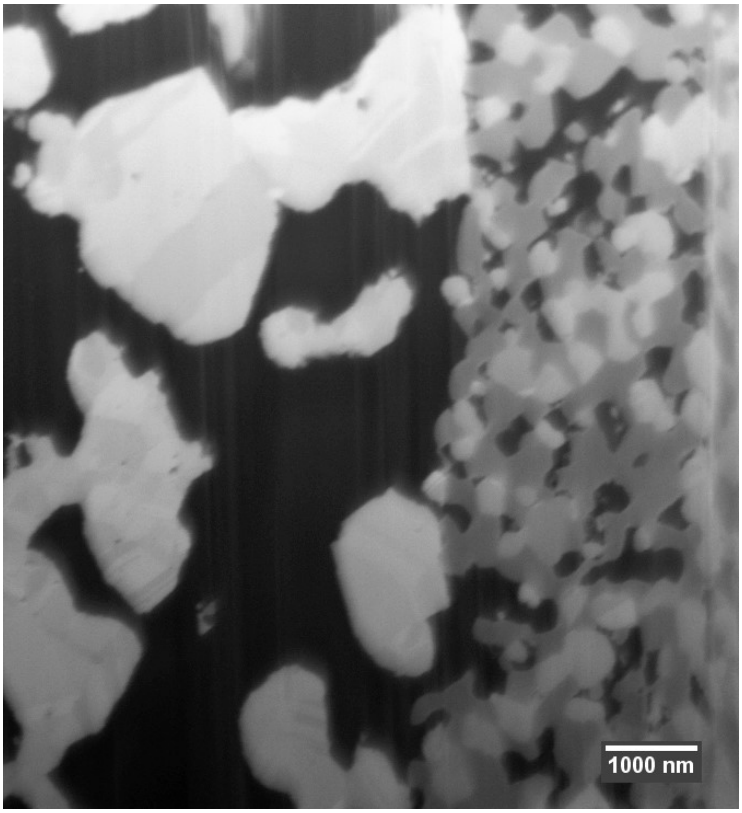


Figure 3.4 Cross-sectional SEM image of the interface between the silver paste and the porous Ni-YSZ electrode. On the left of the image is the silver paste (white) and pore (black), and on the right of the image is the Ni-YSZ electrode.

3.1.3 Transmission Line Model

A transmission line model (TLM) is often used to describe the behaviour of porous electrodes [157]. The TLM used in this study has been detailed in the work of Bertei et al. [158] and its schematics is shown in Figure 3.5. The charge-transfer reactions at the TPBs are described by the Butler-Volmer equations and the gas transport in the pores of the electrode is assumed negligible.

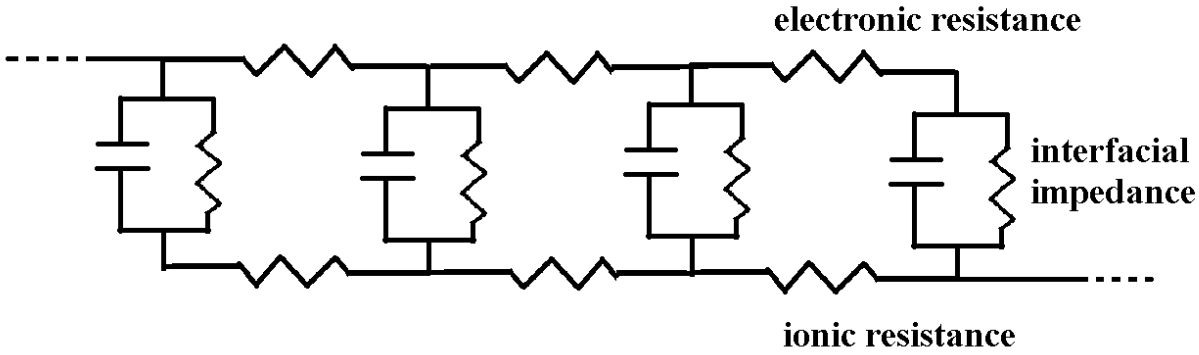


Figure 3.5 schematics of a transmission line used in this study with parallel lines representing the electronic conductor and the ionic conductor respectively.

The impedance for the distributed charge-transfer at the TPBs within the electrode is obtained from the conservation equations of electronic and ionic current as depicted in Figure 3.5 and Equation 3.4 along the thickness of the electrode.

$$\begin{cases} \frac{d\Delta i_e}{dx} = -\Delta i_{TPB}^{F} - \Delta i_{TPB}^{C} \\ \frac{d\Delta i_o}{dx} = \Delta i_{TPB}^{F} + \Delta i_{TPB}^{C} \\ x = 0: \Delta i_e = \Delta I,\ \Delta i_O = 0 \\ x = L_{an}: \Delta i_e = 0,\ \Delta i_O = \Delta I \end{cases} \tag{3.4}$$

i^{F}_{TPB} is the faradaic exchange current across the TPBs and i^{C}_{TPB} the capacitive exchange current. At the electrode/current collector interface $x = 0$, the electronic current i_e is total current I and there is no ionic current i_o. At the electrode/electrolyte interface $x = L_{an}$ is the reverse.

The Adler-Lane-Steele(ALS) model for simulating MIEC response in SOFC electrode is used as well [159]. The ALS model is analogous to the TLM model described above, with conservation equations of oxygen flux. The exchange reaction takes place at the DPBs instead of the TPBs.

3.1.4 Distribution of Relaxation Times

The distribution of relaxation times (DRT) is a useful alternative for interpreting the EIS data to facilitate the deconvolution of different processes. It extracts characteristic distribution of EIS time scales by fitting the measured data Z at the frequency range to a model impedance Z_{DRT} in Equation 3.5.

$$Z_{DRT}(f) = R_{\infty} + \int_0^{\infty} \frac{g(\tau)}{1+i2\pi f\tau}\, d\tau \qquad (3.5)$$

Where R_{∞} is the ohmic resistance and $g(\tau)$ is a suitable function which describes the time relaxation characteristic of the electrochemical system. The DRT model is composed of an ohmic resistance and the sum of infinitely series of parallel R-C pairs. Finding the relaxation time function $g(\tau)$ from Z is mathematically complex and is explained in details by Wan et al. [160]. After the transformation from $Z(f)$ with respect to frequency to $g(\tau)$ with respect to time, the polarisation processes at different characteristic relaxation time are revealed as

more separate peaks. Integration with relaxation time to obtain the area of a peak will give the polarisation resistance corresponding to that peak. As shown in Figure 3.6, the DRT curves shows distinct three peaks for the EIS measurement for the Ni-YSZ electrode. In the Nyquist plot, the high frequency responses between 100 Hz to 10000 Hz overlap.

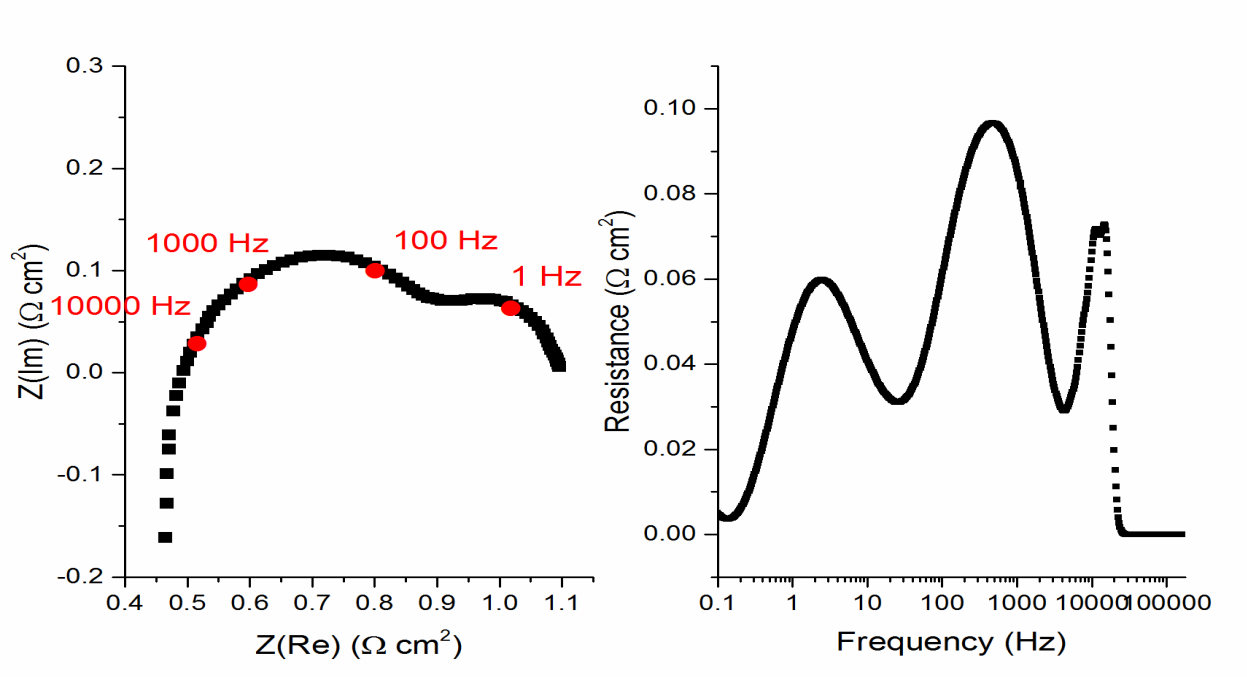


Figure 3.6 The Nyquist plot of a Ni-YSZ electrode at 800 °C in humidified 5% H2- N2 (on the left) and its corresponding DRT plot (on the right).

3.2 Focused Ion Beam- Scanning Electron Microscopy

3.2.1 Theory

The FIB-SEM system is dual beam, combining both a high-resolution SEM and a second column with an ion source of gallium (Ga). FIB uses highly focused Ga^+ beam to scan and cut the substrate surface in a vacuum chamber. The bombardment of the ions on the surface transfers the kinetic

energy to the electrons and atoms of the solid samples. Consequently, the surface is being milled by physical sputtering of neutral and ionised substrate atoms, whereby the surface atoms are ejected when the kinetic energy transferred is larger than the surface binding energy of the material. Meanwhile, the electron emission enables imaging of the surface, but also adversely causes charging of the sample [161]. To etch a desired shape, the beam is scanned over the substrate in programmed positions.

In the dual beam FIB-SEM system, the SOFC sample is tilted as indicated in Figure 3.7. The two beams are aligned at the point of interest and have a coincident angle of 54°. A trench is first dug out by the FIB gun in front of the target volume to expose the cross section of the volume of interest for electron imaging.

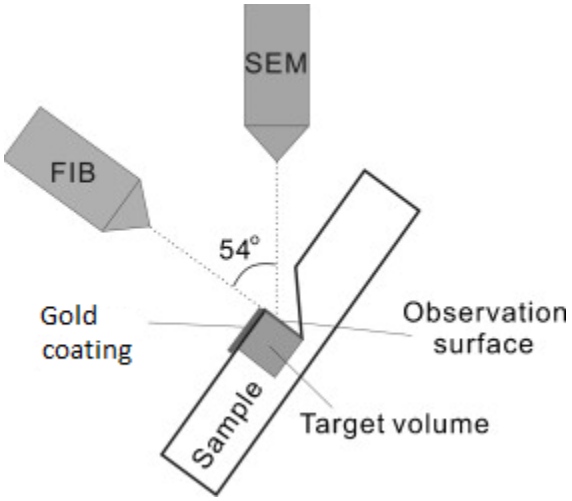


Figure 3.7 Schematic of the FIB-SEM set up for imaging SOFC electrode. Modified from [162].

Two types of electrons emitted from the specimen are used for imaging the SOFC electrode, the secondary electrons and the back-scattered electrons. When the electrons from the emitter strike the surface, they are scattered within certain volume under the surface of impact as shown in Figure 3.8. Within the top 5 – 50 nm, secondary electrons (SE) are generated and below that from 50 – 300 nm are the backscattered electrons (BSE). The two types of electron are collected by different

detectors positioned separately located in the vacuum chamber. The contrasts in electron images arise from the different numbers of electrons collected at each location of the specimen.

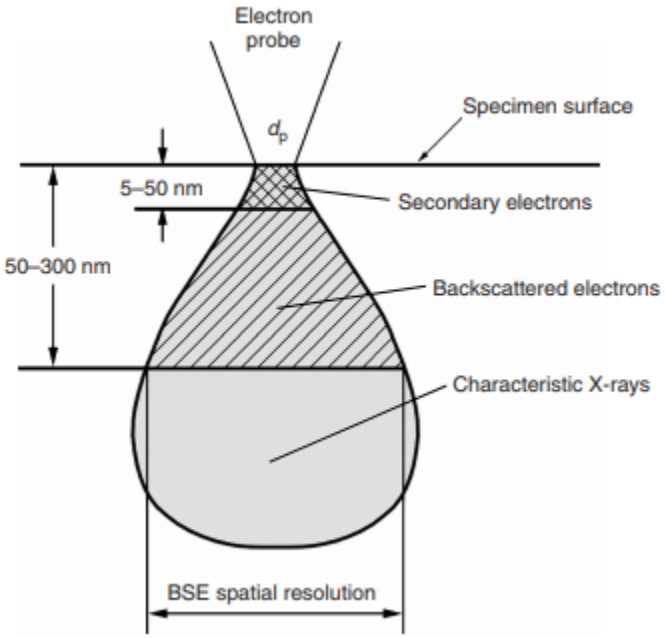


Figure 3.8 The interaction zone of electrons and the specimen under the surface of impact [163].

SEs, as the products of inelastic scattering with small interaction volume, have a higher resolution than BSEs. SEs have signals for topographic information because the trajectory effects are significant in SEs [164]. The trajectory effects originate from the variation on the specimen surface with reference to the detector. An easy pathway from a specific surface to the detector will render the surface to appear brighter and vice versa. In addition to the trajectory effects directly related to the surface contours, the edges or inclined surfaces in the specimen will also appear brighter because more electrons can escape from the edge than a flat surface.

BSEs are produced by elastic scattering and have an energy level close to the incident electrons. While SEs reveal mainly topographic information, the BSEs are mainly affected by the atomic number of the atoms at the site of interest. The backscatter coefficient, which is the ratio of BSEs

to incident electrons, increases with the atomic number of the specimen area and therefore the area with higher atomic numbers will appear brighter. The backscatter coefficient also depends on the orientation of crystallographic planes with respect to the direction of the incident electrons. The atomic packing density along a specific crystallographic plane influences the penetration depth of the electron beam and consequently the backscatter coefficient. The deeper the penetration is, the lower the backscatter coefficient will be.

It is worth noting that the detectors do not distinguish between SEs and BSEs. The common detector is the Everhart-Thornley (E-T) detector. The E-T detector is normally located sideways in the chamber as shown in Figure 3.9. When the detector is positively charged, it attracts signal electrons, mainly SEs because they have low energy of $3 - 5$ eV and are largely deflected by the scattering. To collect the BSEs, either the ET is switched to be negatively charged to exclude electrons less than 50 eV, which are the low energy SEs or another BSE detector located directly above the specimen is used as the BSEs follow more direct paths as a result of elastic scattering. A small number of BSEs are collected in SE signal collection setting and so are SEs in BSE signal collection setting. Moreover, the SEs are slightly influenced by the chemical composition and so are the BSEs by topography. It is hence sometimes possible to extract compositional information in SE signals and topographic information in BSE signals.

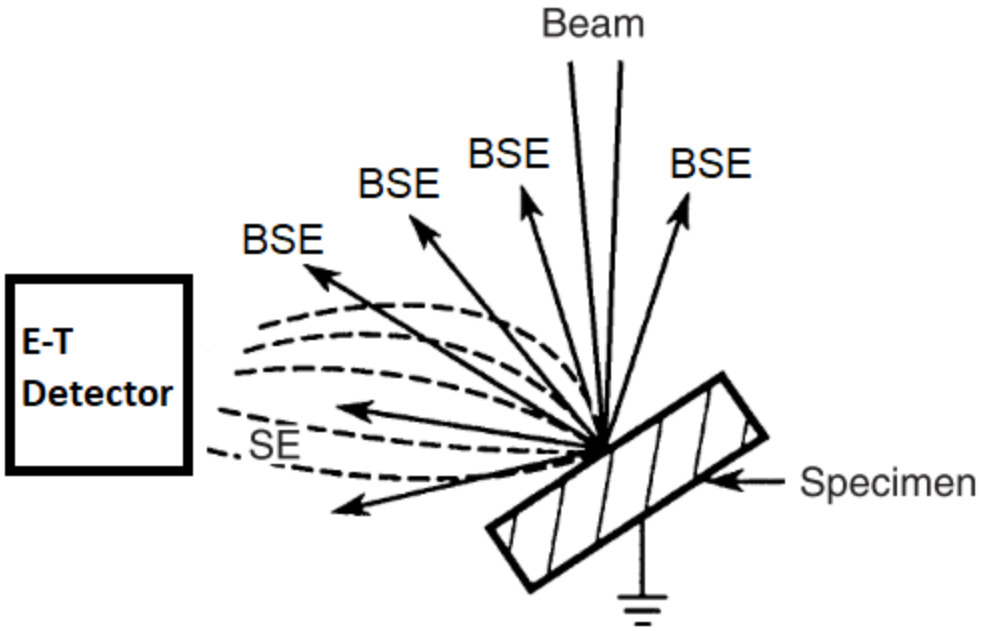


Figure 3.9 Schematics showing the electron collection by an E-T detector. Modified from [164].

In the Zeiss Auriga Dual Beam FIB-SEM system in this study, two types of detectors are used, the in-lens detector and the energy selective backscattered (EsB) detector. The in-lens detector collects mainly SEs along the path of the incident beam and located above the objective lens as shown in Figure 3.10. The detection efficiency of in-lens detector is determined by the electric field of the electrostatic lens. The EsB detector is an annular shaped in-column detector located above the in-lens detector. It detects mainly high-energy BSEs as the low-energy SEs are deflected by the filtering grid.

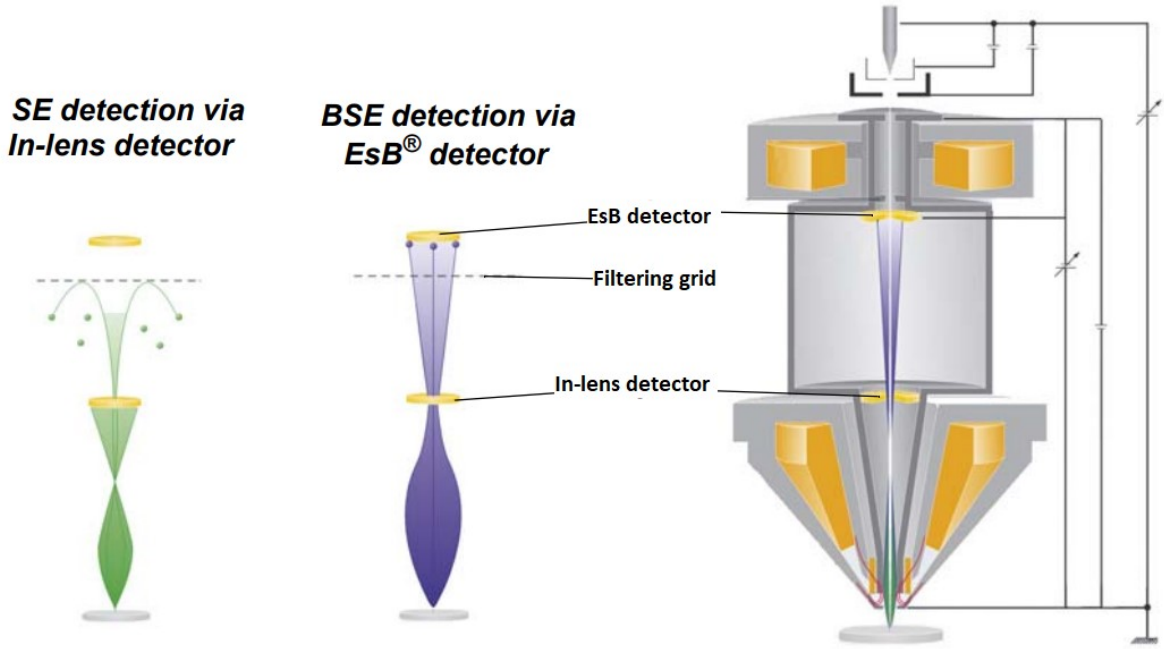


Figure 3.10 Operations and positions of the in-lens and BsE detectors in the Zeiss Auriga Dual Beam system. Modified from [165].

The accelerating voltage in the SEM determines the beam energy and consequently affects the quality of the image. Joy and Joy [166] performed a Monte Carlo simulation of the electron trajectories in the specimen to that the higher accelerating voltage and hence a higher beam energy leads to a larger interaction volume in the specimen as shown in Figure 3.11. While a high accelerating voltage can probe deeper into the bulk of the specimen, a lower accelerating voltage focuses more on the interaction near the surface. A low accelerating voltage is preferred for detecting fine surface features, including both chemical composition and topographic information. The low energy of the incident electrons also reduce the charge-up, edge effect and surface damage by electron beam [167].

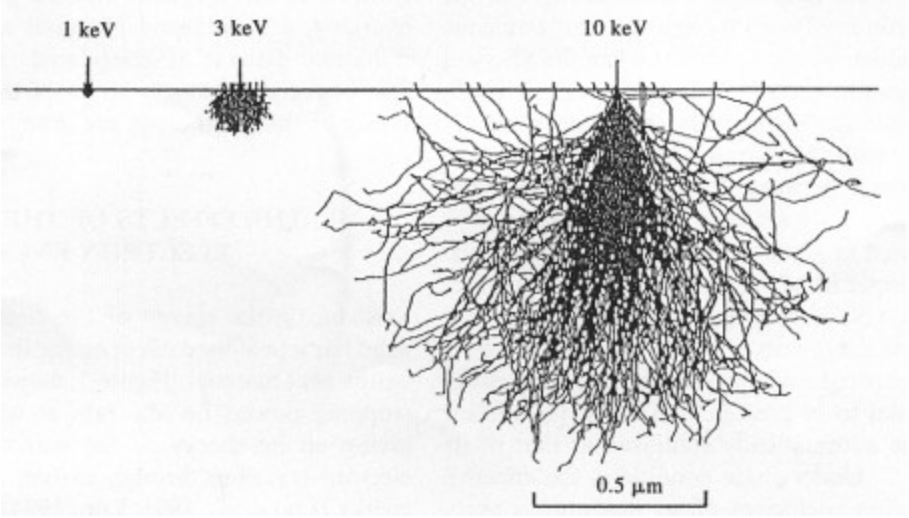


Figure 3.11 Interaction volume of electrons in carbon at 1, 3 and 10 keV energy beams from Monte Carlo simulation [168].

For FIB milling, the spot size increases with the beam current [169]. The ion beam current is a measure of the rate of ion delivery on the specimen with respect to time and hence a low current should be chosen for fine milling. For cross section milling, a protective metallic layer is often deposited onto the specimen to reduce the undesirable effect of 'curtaining' or 'waterfalling' as shown in the porous Ni-YSZ specimen in Figure 3.12. The sputtering rate of the ion beam is sensitive to local changes in surface topography and curtaining is very easy underneath a surface defect (pore or crack) [170]. The metallic protective coating helps to smooth the surface to reduce this artefact and increase the conductivity for SEM imaging.

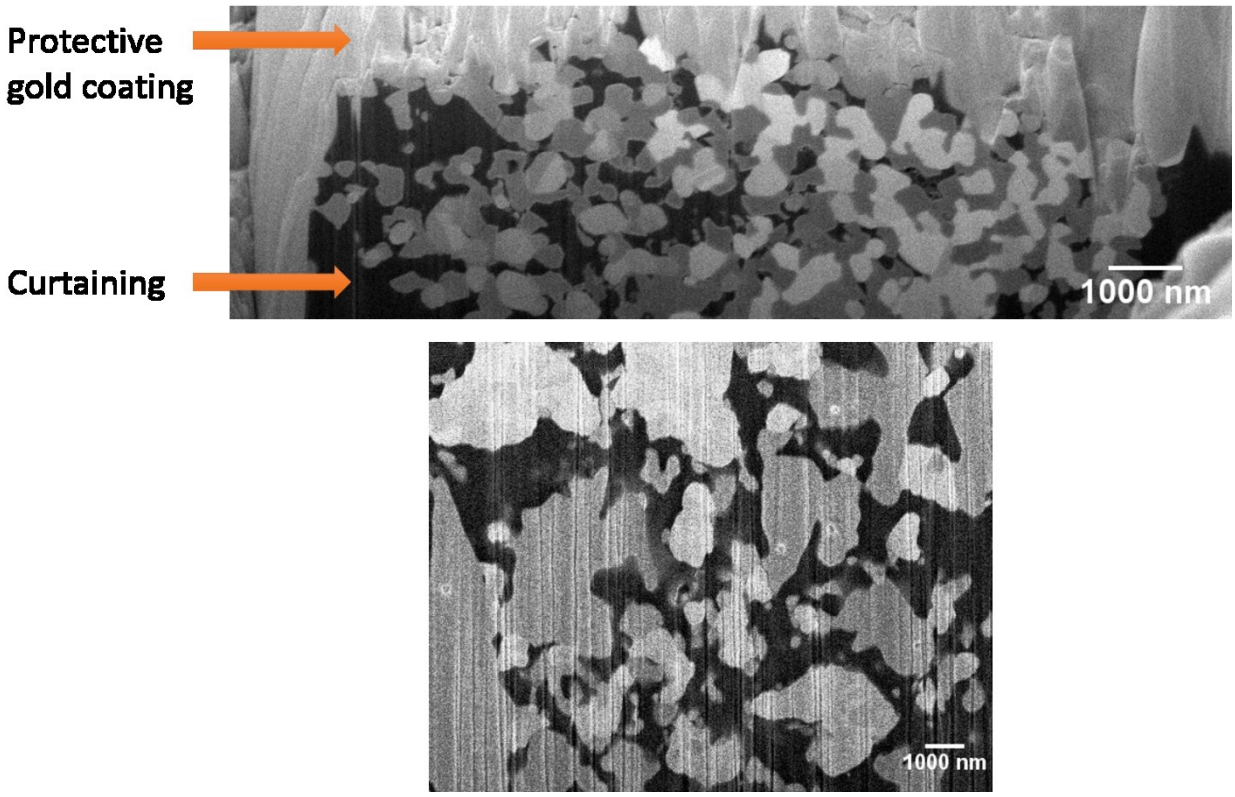


Figure 3.12 SEM image on top of the cross-sectional area of a porous Ni-YSZ electrode after FIB milling, showing the protective gold coating and the curtaining effect. The SEM image below shows a stronger effect of curtaining of a poorly milled cross section.

3.2.2 Sample Preparation

The symmetrical cells of the electrode of interest are vacuum impregnated with epoxy resin (Struers). The vacuum was set at 0.9 bar for 11 h to cure the resin. The resin-impregnated cell was then cut in parallel lines by high speed diamond saw (Accutom-50 Struers) at a small feed speed of 0.01 mm s^{-1} and rotation speed of 300 rpm, to ensure a smooth cut. Each slice of the cell after cutting is about 2 – 5 mm in thickness. The slice was then placed onto an adhesive carbon tape, with the cross section of the cell exposed for imaging (Figure 3.13),

and top surface of the slice was coated with a protective layer of gold by plasma spraying. The sides of the slides were painted with silver to complete the conductive coating.

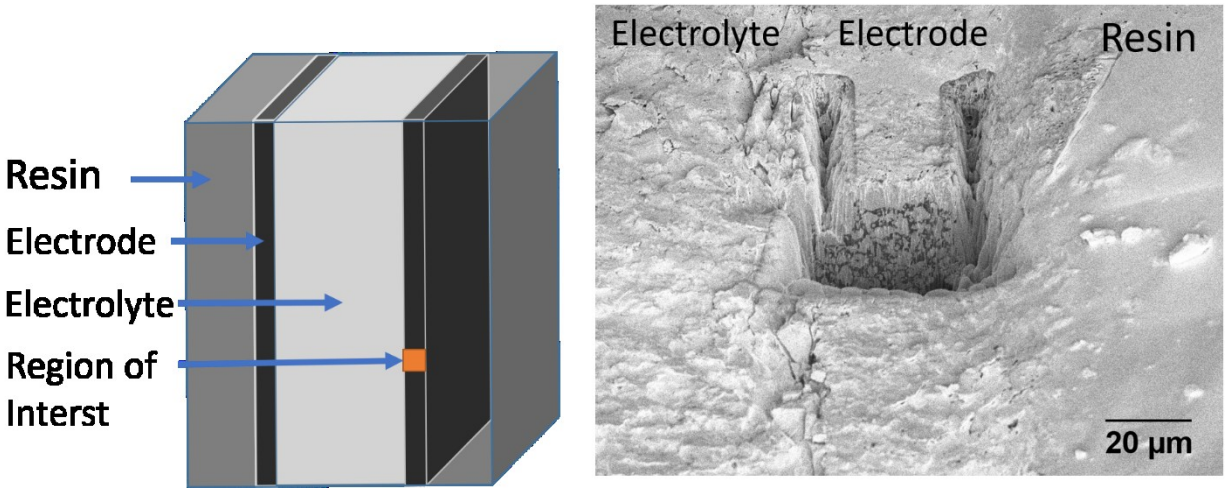


Figure 3.13 Schematics of the whole specimen for FIB-SEM imaging (left) and a SEM image of the specimen after the U-shape trench is dug out before imaging.

3.2.3 Milling and Imaging

After the alignment of the FIB beam, the SEM beam and the region of interest as shown in Figure 3.7, a U-shape volume was first removed in front of the region of interest. The FIB milling current was high when milling the U-shape trench, 5 – 10 nA for fast coarse milling. As shown in Figure 3.13, the 20 µm U-shape trench was removed to expose the cross section of the electrode and also allow easy disposal of the subsequent materials removed during the slice-and-view process. When the trench is not sufficiently large, the materials removed in the later stage will tend to re-deposit onto the surface and cover the electrode surface with grey dust.

After the trench was complete, the milling current was reduced to 120 pA, which corresponds to 20 nm slice size per milling cycle (based on silicon as the standard material) and the milling depth set to 10 µm. The first few milling cycles were expected to polish the rough surface caused by the previous coarse milling. After a smooth surface had been observed, a SEM image was taken on the electrode's cross section after each FIB milling cycle in the slice-and-view mode.

A low accelerating voltage of 1.5 kV was used for imaging because the phase contrast on the 2-D surface milled by FIB is the main concern. For the porous Ni-YSZ electrode, in-lens detector for SE signals was used for imaging, for the best resolution and contrast. The resin-filled pores appear the darkest, followed by YSZ and lastly Ni the brightest. For the porous Ni-CGO electrode, BsE detector for BSE signals was used for imaging. The resin-filled pores appear darkest again, but the Ni appears grey and the CGO appears to be the brightest.

3.2.4 Image Processing

For SOC applications, many studies have quantified the TPB density by 3-D reconstruction of the electrode microstructure using FIB-SEM [193] and X-ray tomography [194][195]. 3-D parameters, including the TPB density, are extracted from the reconstructed 3-D volume of the selected region.

The images were first de-noised by an edge-preserving smoothing filter and then the slices aligned in a stack. The alignment is done by an Iterative Closest Point algorithm that minimises the root mean square distance between the corresponding points on the

consecutive images. After that depending on how severe the curating effect is, a Fourier transform filter may be applied to remove the vertical stripes in the images.

The brightness and contrast were then adjusted by examining the grayscale histogram of the images in order to achieve the best distinction between the peaks representing the three different phases (Ni, the ceramic phase and pore). A non-local mean filter was applied to the images for smoothing and de-noising, which computed the average of all the pixels weighted by the similarity between the pixel to the target pixel [171]. The brightness gradient along the depth of the milling (the y-axis of the images) caused by shadowing of the imaging electrons deeper down the trench is also corrected by an in-house programme. The top region is dimmed, and the bottom region is brightened according to the linear regression of the brightness along y-axis. After the alignment and image correction, the 3-D image stack was segmented by Trainable Weka Segmentation which combines the machine learning algorithms with the selected image features for pixel-based segmentations [172]. The few pixels at the interfaces of the darkest phase and the brightest phase unavoidably appear grey and are mistaken as the third phase by the segmentation algorithm. Hence, one or two pixels of the grey phase is corroded and replaced by the pore phase to remove this interface artefact. This will undesirably alter the microstructure slightly but removing this interfacial artefact by increasing the resolution during SEM imaging will increase the scanning time and consequently reduce the sampling volume. There is always a balance between the image resolution and the sampling volume which needs to be considered in FIB-SEM imaging.

The sources of errors in the image processing are from both the image segmentation and the sampling volume. The image segmentation is dependent on the phase input selection for training and therefore, each training can produce slightly different segmentation result.

It is worth repeating the segmentation process for each image stack and calculate the random error associated with the input selections. Additionally, it is worth mentioning that the FIB-SEM sampling volume of approximately 500 μm^3 is 9 order of magnitude smaller than the actual volume approximately 150×10^9 μm^3 of the electrode. The sampling volume, due to its limited size, may not be large enough to be representative of the whole electrode. A quick analysis was done using the MATLAB plugin TauFactor[173] to check the representativeness of each 3D volume by tracing the volume fraction of each phase as the sampling size increases. An example is shown in Figure 3.14. The sampling volume is regarded as representative if the trends of phase volume fractions converge quickly, which is true for the case in Figure 3.14.

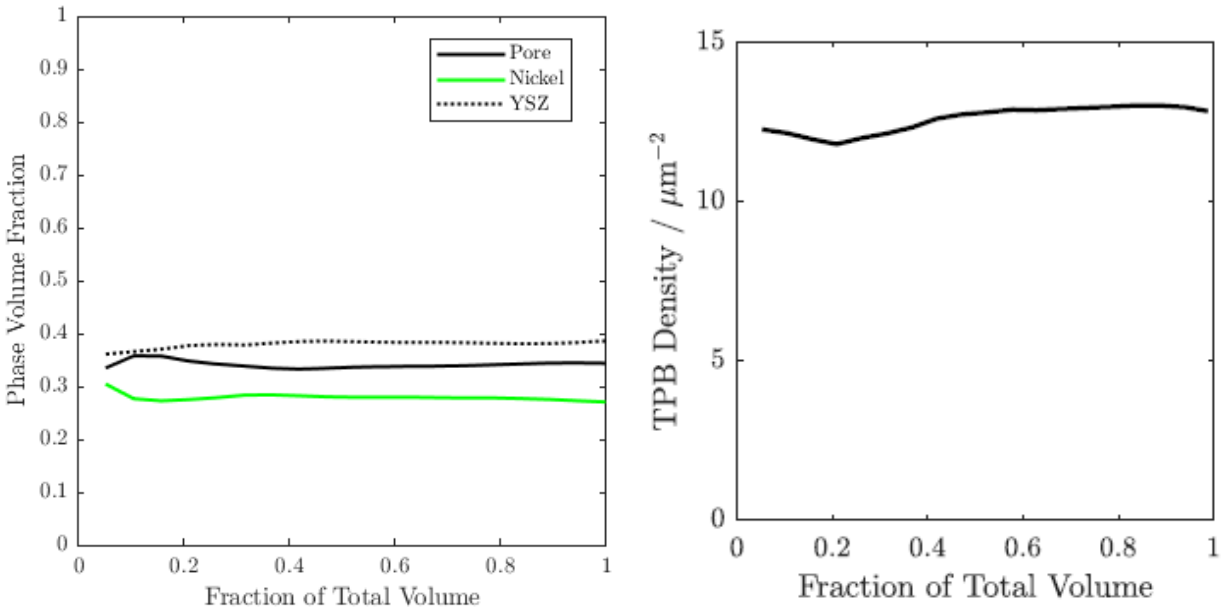


Figure 3.14 An example of the representative volume check done on the FIB-SEM 3D volume with a porous Ni-YSZ electrode. The volume fractions (on the left) are calculated from a fraction of the sampling volume to the whole sampling volume and converge after 0.2. Similarly, the TPB density converges after 0.4.

However, the errors arise from sample-to-sample variations are not accounted for in this thesis due to the time constrains in obtaining FIB-SEM image stacks from two or more electrodes fabricated and aged in the same manner.

3.3 Other Characterisation Methods

3.3.1 Brunauer-Emmett-Teller Surface Area and t-Plot

Surface properties of powders are measured by its adsorption and desorption isotherms of N_2. The adsorption and desorption of nitrogen gas molecules on a solid surface is used to measure the surface area by the Brunauer-Emmett-Teller (BET) theory and the influence of pores by the t-plot method.

Based on the BET model, the adsorbed molecules in one layer can act as adsorption sites for molecules in the next layer, at any pressure below the saturation vapour pressure P_o. The main assumptions of the BET theory are, 1) the material surface is homogeneous with no preferential sorption areas; 2) inter-molecular interactions are negligible; 3) the uppermost layer is in equilibrium with no net change in the number of adsorbed molecules at a given vapour pressure; 4) the rate of adsorption is limited by kinetics and hence the adsorption energy is assumed the same for all molecular layers and 5) no further adsorption beyond saturation pressure [174].

BET surface area calculation was done on the range of relative pressure between 0.04 and 0.12 where monolayer adsorption takes place using Equation 3.6 [175],

$$\frac{1}{v\left(\frac{P_O}{P}-1\right)} = \frac{1}{v_m C} + \frac{C-1}{v_m C}\left(\frac{P}{P_O}\right) \qquad (3.6)$$

where v is the volume of gas adsorbed at the relative pressure $\frac{P}{P_O}$ and v_m is the volume adsorbed in the monolayer. C is a constant related to the binding energy, which is also termed the BET constant.

A linear plot of $\frac{1}{v\left(\frac{P_O}{P}-1\right)}$ against $\left(\frac{P}{P_O}\right)$ will give a slope $S = \frac{C-1}{v_m C}$ and an intercept of $i = \frac{1}{v_m C}$. The monolayer volume v_m can therefore be calculated from S and i, and the specific surface area S_{BET} is determined by

$$S_{BET} = \frac{v_m N A}{V_g\, m} \qquad (3.7)$$

Where N is the Avogadro's number and A is the cross-sectional surface area of a single adsorbed gas molecule (16.2 Å for N_2). m is the mass of the material used in the measurement and V_g represents the volume of one mole of gas under standard temperature and pressure (STP), which is 22400 cm^3 for nitrogen gas.

The adsorption isotherms of gases on solids can be classified into five types as shown in Figure 3.15 as described by Brunauer, Deming, Deming an Teller [176]. The Type I isotherm indicates the amount of gas increases with increasing pressure till the saturation is reached after a monolayer coverage. For the Type II isotherm, after the levelling at the monolayer saturation, the amount adsorbed starts to grow again at higher pressure where multilayer adsorption takes place. Type III occurs where there is strong adsorbate-adsorbate interactions and the adsorption becomes easier after some adsorbate nucleates on the surface. Type IV and V occurs for multilayer adsorption in porous solid. They are similar to type II and III initially but eventually the adsorbed layer fills up the pores.

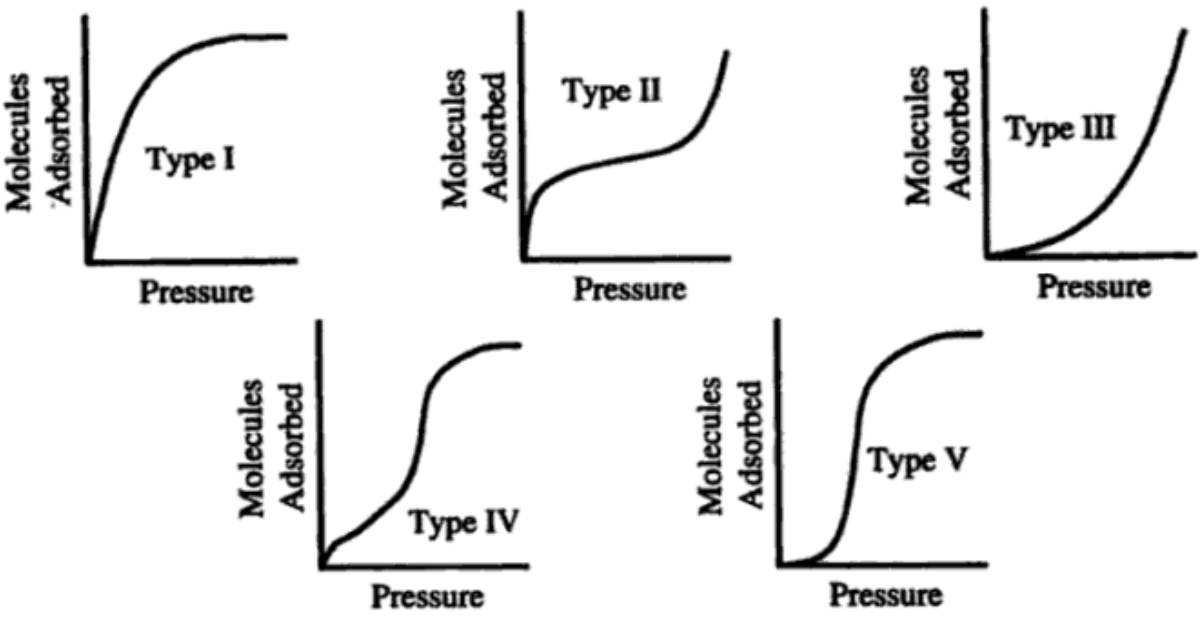


Figure 3.15 The five types of adsorption isotherm [175].

The statistical thickness of the adsorbed gas t is calculated by comparing the adsorbed volume to a standard silica reference. Using the thickness-plot (t-plot), the external surface area outside the pores was derived from the slope of v and t [177].

The thickness t of the adsorbed film in Å is obtained by the de Boer equation [178][179], which is based on nitrogen sorption at 77 K on non-porous adsorbents like siliceous materials.

$$t = \left[\frac{13.99}{\log\left(\frac{P_o}{P}\right)+0.034}\right]^{\frac{1}{2}} \qquad (3.8)$$

For a standard type II isotherm of a non-porous sample, the plot of t against relative pressure is a linear line passing through the origin. The slope s in this case can be converted to the specific surface area S_t by

$$S_t = 15.47\, s \qquad (3.9)$$

For non-porous materials, S_t is in good agreement with S_{BET} as determined by the BET theory. The presence of micropores (< 20 Å) will increase the update of gas at low relative pressures and hence extrapolating the curve to the molecule adsorbed axis (the y-axis) will give a positive intercept i_t [180]. The micropore volume V_{mp} in cm^3 can be calculated from i_t by

$$V_{mp} = 0.001547\, i_t \qquad (3.10)$$

The internal surface area, i.e. the surface area inside the micropores, is derived from the slope of the linear line of adsorption volume against t. The external surface area is then the difference between the S_{BET} and the internal surface area.

3.3.2 Laser Diffraction Particle Sizing

The laser diffraction method is used to measure particle size distribution by measuring the angular variation in intensity of light scattered as the laser beam passes through a dispersed particulate sample. The larger the particles, the smaller the scattering angles. The angular scattering intensity data is then analysed to calculate the volume equivalent sphere diameter based on the Mie theory of light scattering [181].

The volume weighted mean diameter $D_{4,3}$ is calculated from the diameter of each particulate D by

$$D_{4,3} = \frac{\sum_1^n D_i^4}{\sum_1^n D_i^3} \qquad (3.11)$$

3.3.3 X-ray Diffraction and Rietveld Refinement

X-ray powder diffraction (XRD) gives a set of Bragg's peaks, some overlapped and superimposed on a smooth and slowly varying background. Rietveld refinement is a complex multi-parameter curve fitting method to derive phase information from the XRD pattern. The model function is defined by the crystal structure, including the atomic coordinates, thermal displacements and site occupancies, combined with the experimental factor, such as peak profile broadening and etc. [182]. To obtain good signal-to-noise ratio, an angular step size below 0.02 ° and time per step above 15 s is used for the scanning. The adjustable parameters for the model function are refined by a least-squares minimisation of the weighted differences between the observed and calculated intensities.

Quantitative analysis via Rietveld refinement for powders with more than one phase is based on the following equation [183].

$$\mathrm{W_p} = \frac{S(ZMV)}{\sum_1^n S_i(ZMV)_i} \qquad (3.12)$$

Where S is the Rietveld scale factor, Z is the number of formula units per unit cell, M is the mass of the formula unit and V is the volume of the unit cell. The weight fraction W_p of the target phase can then be derived after successful refinement.

3.3.4 Van Der Pauw Conductivity

For a flat sample, the in-plane conductivity can be measured by the van der Pauw method. The flat electrode cast on the electrolyte substrate was measured by a four-point probe as shown in Figure 3.16 by applying a small DC current.

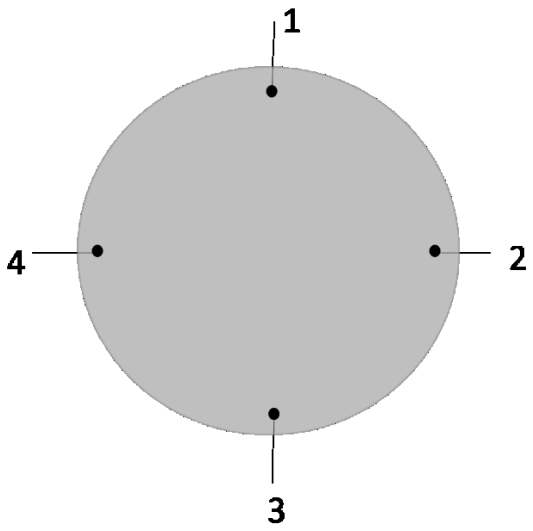


Figure 3.16 Van der Pauw DC measurement was carried out by four point contacts on the electrode plane. A small current of 0.01A was passed through probe 1 and probe 3 while the potential was measured between probe 2 and probe 4. A repeated measurement was done by swapping 1 and 3 and swapping 2 and 4. R_1 represents the resistance averaged from these two measurements. Similarly, R_2 is calculated from the two measurements with current passing through probe 2 and 4 and the potential measured between 1 and 3.

The in-plane conductivity σ is calculated by the measured resistances R_1 and R_2 and the known thickness d of the electrode by Equation 3.13.

$$e^{-(\pi d\sigma R_1)} + e^{-(\pi d\sigma R_2)} = 1 \qquad (3.13)$$

3.4 Summary

The microstructural information obtained by FIB-SEM and the electrochemical measurement by EIS are complementary to each other in understanding the electrode properties and different microstructures and during the degradation process. Powder characterisation and gas adsorption not only provides guidance for the electrode processing, but also predicts some microstructural characteristics of the resultant electrode.

4 Nickel Impregnated Scandia-Stabilised Zirconia Electrode

This chapter investigates the stability of nickel-impregnated scandia-stabilised zirconia composite electrodes during isothermal annealing at temperatures from 600 to 950°C in a humidified hydrogen atmosphere (3 vol % water vapour). The impact of the nickel coarsening during isothermal annealing is explored using a physical model of electrode performance which relates the macroscopic electrochemical performance to measurable microstructural parameters.

4.1 Experimental

The ScSZ scaffold was prepared by sintering ScSZ powder mixed with carbon black as a pore former. 80 wt% ScSZ (fuelcellmaterials Sc10SZ-TC, surface area 8.9 $m^2 g^{-1}$) and 20 wt% carbon black (Alfa Aesar, surface area 75 $m^2 g^{-1}$) were mixed with ethylcelulose-N7 (Hercules) binder, anhydrous terpineol (Aldrich) solvent and dispersant using a magnetic stirrer to form a homogeneous paste. The paste was milled in a triple roll mill to break up small agglomerates. The ScSZ scaffold ink was tape cast onto an 8 mol% YSZ substrate (fuelcellmaterials YSZ-2.0, 20 mm in diameter and 0.28 mm in thickness). The cast scaffolds were dried at 70 °C for 24 hours, heated at 1 °C min^{-1} to 500 °C and held for two hours to burn off the carbon black and then heated at 3 °C min^{-1} to 1250 °C for a two-hour sintering. The sintered ScSZ scaffolds were then impregnated with 2 M nickel (II) nitrate solution in

ethanol. 2 µL nitrate solution was infiltrated at each impregnation cycle and the nitrate solution was decomposed at 550 °C for 1 hour [64]. Each cell underwent 12 impregnation cycles until the nickel loading reached approximately 40 wt% in the electrode as deduced from the increase in weight after reduction. The average thickness of a scaffold was 10 µm as determined from SEM measurements on specimen cross sections and its diameter 14 mm.

Symmetrical cells with Ni-impregnated ScSZ electrodes and YSZ electrolyte fabricated via the route described above were loaded into an electrochemical test station for electrochemical impedance measurements at 650 °C, 800 °C or 950 °C under open circuit conditions. The test rig is shown schematically in Figure 3.2. The symmetrical cells were heated up in a protective nitrogen atmosphere to the test temperature and then reduced in-situ in the test atmosphere of humidified 5 vol% hydrogen and 95 vol% nitrogen at a flow rate of 100 ml min^{-1} unless specified otherwise. Water vapour was introduced into the gas flow by bubbling the gas supply through deionised water at room temperature. A 0.02 V amplitude sinusoidal voltage was applied in the two-electrode measurement set-up over the frequency range 10 MHz to 0.1Hz. Current collection was made using Pt grids with 100 mesh size (aperture 149 µm) made from wire of 0.076 mm in diameter unless specified otherwise. The ASR was obtained by multiplying half the measured resistance by the area (circle 14mm in diameter) of a single electrode.

Van der Pauw sheet resistance for the electrode was also measured as a function of exposure time. Symmetrical cells were exposed to wet 5 vol% hydrogen and 95 vol% nitrogen at a flow rate of 100 ml min^{-1} for 10 minutes at the test temperature to reduce nickel oxide to nickel and was subsequently cooled at 5 ^{o}C min^{-1} to room temperature. The cells were placed in the measurement rig with a probe spacing of 6 mm and heated at a rate of 5 ^{o}C min^{-1} back to the reduction temperature for van der Pauw measurement. The conductivity of the

electrode was calculated using the average measured thickness of 10 µm and assuming that the conductivity does not vary through the thickness.

Microstructures of the Ni-ScSZ anode were examined by secondary electron images using a LEO Gemini 1525 Field Emission Gun Scanning Electron Microscope (FEG-SEM) and FIB-SEM slice-and-view cross-sectional imaging using Zeiss Auriga Cross Beam. The images were processed by Matlab to measure the particle size distributions of nickel in the electrode.

The EIS results were analysed by equivalent circuit fitting using ZView with R-CPE components.

4.2 Results and Discussion

4.2.1 Electrode Electronic Conductivity

The van der Pauw conductivity measurement at elevated temperatures in Figure 4.1 revealed a rapid initial decrease in the Ni-impregnated ScSZ electrode in-plane conductivity before reaching a steady value. Jung et al [184] have shown that application of the van der Pauw method to electrodes impregnated with copper nitrate can be potentially unreliable due to the formation of a copper-rich surface layer during drying. This can produce a high conductivity surface layer on the electrode after reduction which distorts the measured apparent conductivity of the full depth of the electrode. This possibility should be borne in mind with the present results, though the microstructures presented later show no evidence of such a surface layer.

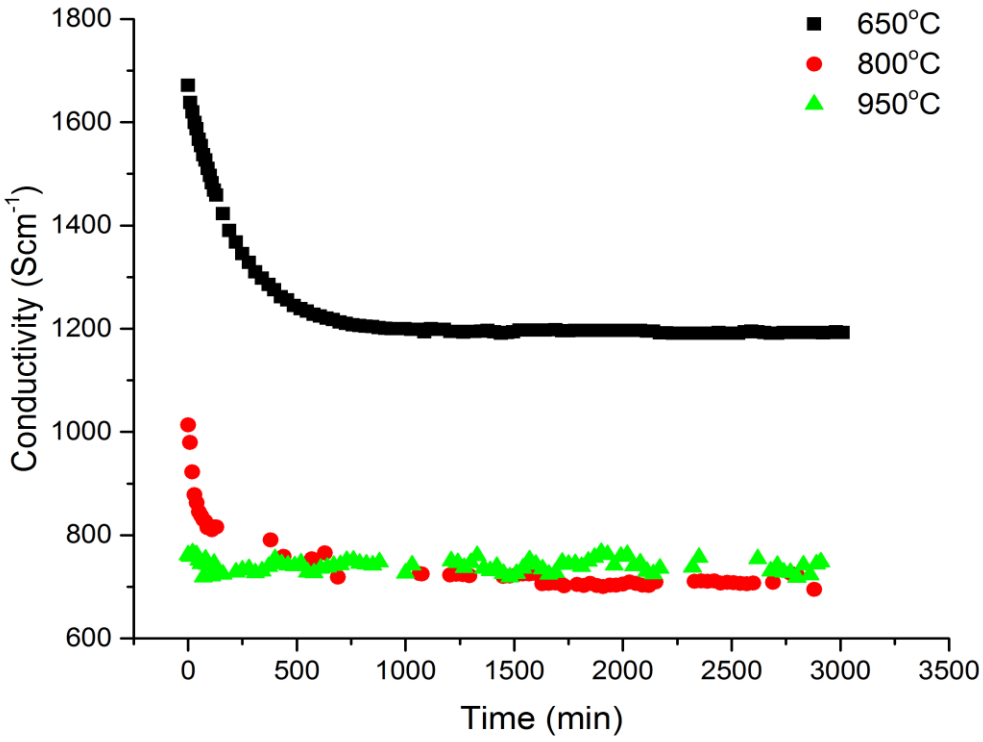


Figure 4.1 In-plane conductivities of the Ni-impregnated ScSZ electrode were measured with time as the electrodes were being annealed isothermally in humidified 5% H_2-95% N_2.

At 650 °C, the in-plane conductivity of the electrode decreased from 1670 S cm^{-1} to 1200 S cm^{-1} within the first 1000 min of annealing, reaching a plateau of 1200 S cm^{-1} afterwards. The rapid conductivity decrease in the first 1000 min of annealing was also observed in the electrode annealed at 800 °C, for which the conductivity decreased from 1010 S cm^{-1} to 700 S cm^{-1}. At 950 °C, the conductivity remained relatively constant at 750 S cm^{-1} throughout the 3000 min of annealing. The absence of an initial conductivity drop in this case was probably due to the heat treatment prior to the measurement. Any rapid initial degradation probably happened during the slow cooling and heating before the van der Pauw measurement. Different reduction temperatures may result in different nickel distribution

and morphology in the electrode. Literature revealed once the reduction temperature goes above 800 °C, the reduction is achieved within seconds, as compared to the long induction time (up to 2000 s) at 500 °C [185]. High reduction temperature tends to give a continuous layer of reduced Ni. NiO reduced at 950 °C is likely to form better connected Ni than at 800 °C. This may lead to the plateau conductivity at 950 °C being comparable to the conductivity measured at 800 °C.

The conductivities of nickel, ScSZ and YSZ vary with temperature T according to the equations below. The conductivity of YSZ pellet was measured using a symmetrical cell with platinum electrode in air.

$$\sigma_{ScSZ}(T) = 0.46 \cdot [6.5 \cdot 10^2 \exp(-\frac{9250}{T})] \text{ [S cm}^{-1}\text{] [158]} \qquad (4.1)$$

$$\sigma_{YSZ}(T) = \frac{4.55 \cdot 10^5}{T} \exp(\frac{-10220}{T}) \text{ [S cm}^{-1}\text{]} \qquad (4.2)$$

$$\sigma_{Ni}(T) = \frac{1.47 \cdot 10^5}{[1 + 0.0069(T - 298)]} \text{ [S cm}^{-1}\text{] [186]} \qquad (4.3)$$

At the annealing temperatures, the conductivity of nickel is 10^6 to 10^7 times the conductivity of ScSZ or YSZ. In the 4-point probe arrangement, the current flow could possibly extend into the YSZ substrate at elevated temperatures the electrode is more than 10 times thinner than the electrolyte. However, even with the increased conductivity at high temperatures, the substrate resistance is estimated to be five to six orders of magnitude higher than that of the Ni-ScSZ electrode. The contribution from the substrate is hence negligible and the measurements represent the true conductivities of the electrodes, averaged over the depth of the electrode. From Equation 4.3 the conductivity of nickel at 800 °C is 2.3×10^4 S cm^{-1}

whereas the long-term steady conductivity of the sample aged at 800 °C is approximately 700 S cm^{-1}. This is only 3% of the bulk value and indicates that the nickel network is not well-connected despite its high volume fraction and favourable location on the internal surfaces of the porous zirconia scaffold. The rapid initial reduction in conductivity is therefore likely to reflect the microstructural change of the nickel within the electrode over time. Klemensø et al. [127] also observed a severe initial degradation for nickel impregnated YSZ anode at 650 °C, though on a time-scale of 24 h, and attributed the degradation to nickel sintering by surface diffusion.

4.2.2 Electrochemical Impedance Spectroscopy

Three capacitive processes were observed at 650 °C in addition to the ohmic series resistance as shown in Figure 4.2. The small capacitive process at high frequency was assigned to the transfer of oxygen ions across the interface between the YSZ electrolyte and the ScSZ electrode [158][187][188]. The process at 10^2-10^3 Hz was assigned to the electrochemical reaction [189]–[192]. The large low frequency response at 1-10 Hz is most likely a gas conversion impedance due to the test rig geometry, and is caused by diffusion of gas molecules from the flowing gas stream into, and out of, the electrode compartments of the cell test chamber [21], [23]. The different contributions are shown as an equivalent circuit model in the inset and their assignments are discussed later.

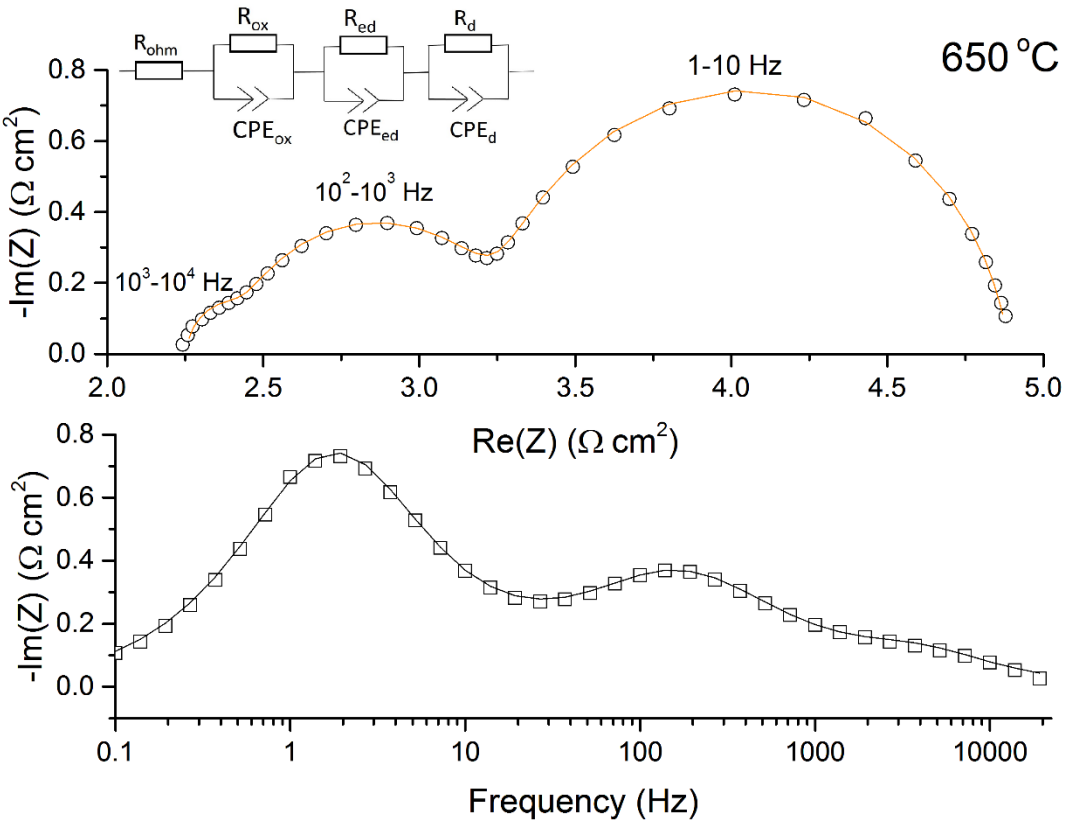


Figure 4.2 Nyquist plot and Bode plot for a symmetrical infiltrated cell aged at 650 °C for 30 min. The dots represent the experimental data and the solid lines represent the equivalent circuit fitting. The equivalent circuit model is shown in the inset.

When the annealing temperature was increased to 800 °C or 950 °C, the oxygen transfer resistance could not be distinguished in the impedance spectra as shown in Figure 4.3. The medium frequency contribution assigned to the electrochemical reaction became much smaller and the low frequency diffusion contribution was dominant.

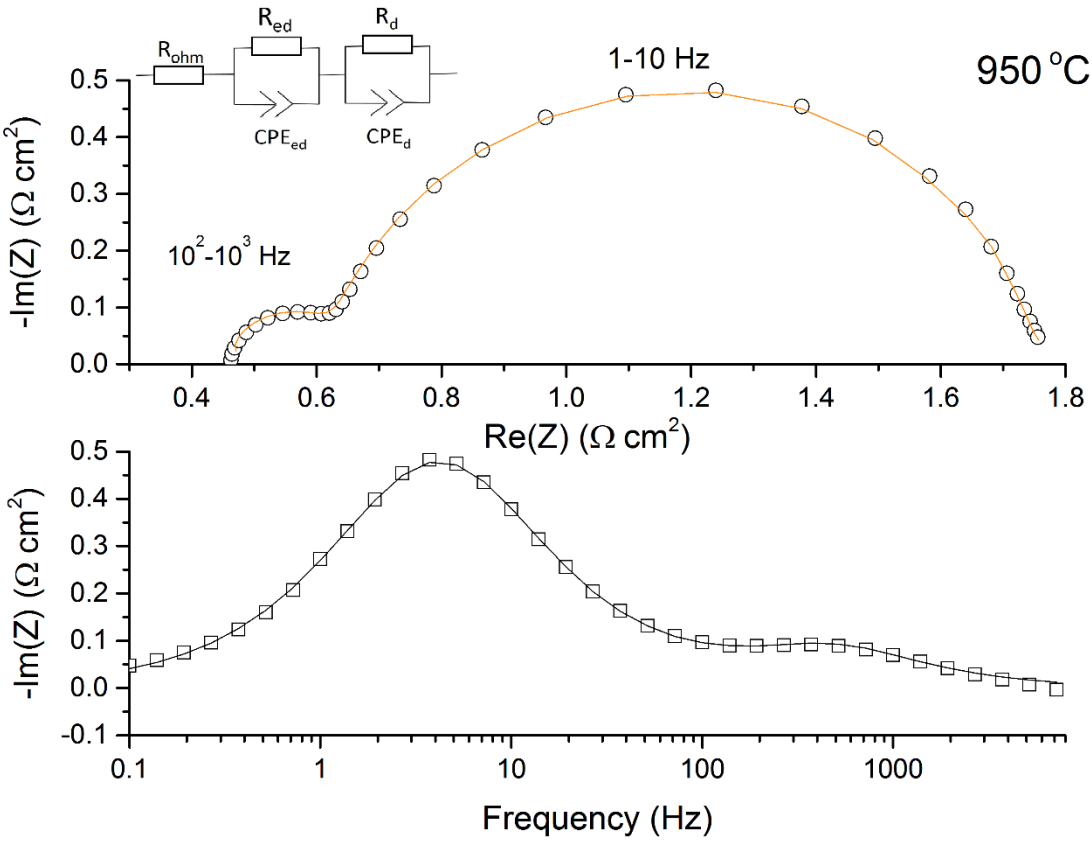


Figure 4.3 Nyquist plot and Bode plot for a symmetrical infiltrated cell aged at 950 °C for 70 min

The following section describes the variation of ohmic resistance, electrochemical reaction resistance and diffusion resistance with time as the electrodes were aged at the different test temperatures.

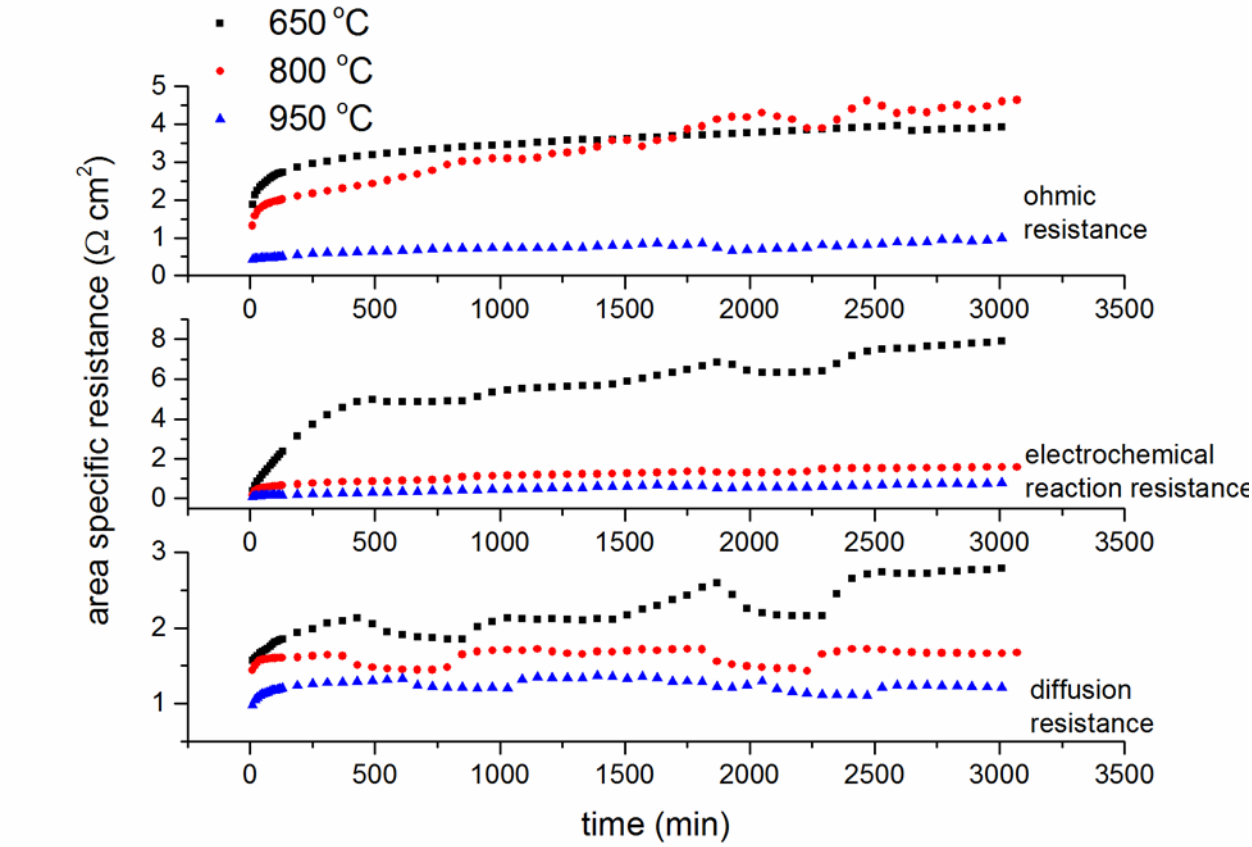


Figure 4.4 The area specific resistance contributions as a function of time at different annealing temperatures. The measurement was made at 10 min intervals during the first 120 min and then at 60 min interval thereafter.

Figure 4.4 shows the time evolution of the ASR from the different contributions at the isothermal annealing temperature of 650 °C, 800 °C and 950 °C. Note that for 800 °C and 950 °C the transfer resistance contribution is included in the ohmic series resistance as it cannot be distinguished as a separate component. All the contributions tend to show an initial increase over the first 1000 min of annealing, followed by a more gradual increase at longer times. Figure 4.5 summarises the change in ASR contributions in the two stages.

The ASR evolution for the diffusion contribution in Figure 4.4 exhibits a periodic fluctuation, which is seen to a lesser degree in the electrochemical reaction contribution. These fluctuations were found to be due to variation from 3.0% to 3.7% in the water content of the inlet gas caused by changes in room temperature (24 °C to 28 °C). As discussed later, these fluctuations are consistent with the influence of water vapour pressure on the individual contributions to the ASR in the model used to interpret the data.

It is interesting that all three contributions to the ASR show a similar qualitative evolution, which is particularly unexpected for the ohmic contribution. Furthermore, the magnitude of the ohmic contribution is significantly greater than expected from the electrolyte pellet. (The ASR plotted in the figure is for unit area of a single electrode and therefore has a contribution from half the thickness the electrolyte pellet.) For example, at 800 °C the measured initial ohmic ASR is 1.32 Ω cm^2 whereas that expected from the YSZ electrolyte pellet (using Equation 4.2) is 0.45 Ω cm^2. This suggests that there was a problem with current collection from the electrode to the platinum grids that became worse as the in-plane resistance of the electrode decreased, as shown in Figure 4.1. Such an in-plane resistance can reduce the active area of the electrode as the electrode electronic conductivity decreases and therefore influences all the contributions to the ASR. However, in this case, the measured lateral conductivity of the electrodes is sufficiently high that transfer of electrons to the platinum grid wires should not be a problem for the grid size used. This probably indicates that the current collector grids were not making good uniform contact on the electrode surface so that the current collection points were separated by larger distances than the grid aperture size. An alternative explanation is that the measured lateral conductivity of the electrode is dominated by a nickel-rich surface layer and the through-thickness conductivity of the electrode is poor and degrades with time. However this is not supported by the observed nickel distribution in the electrodes that is described later.

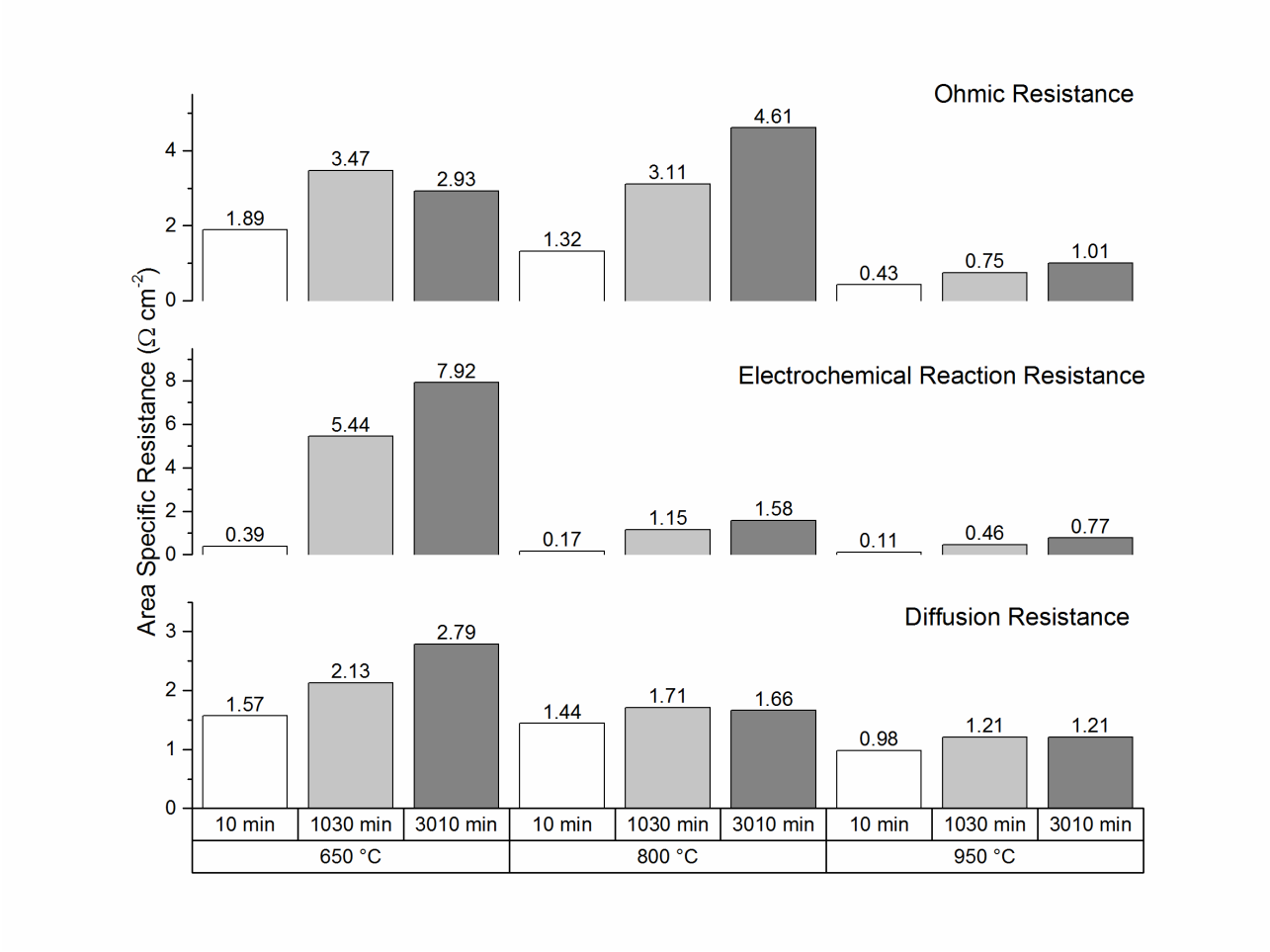


Figure 4.5 Ohmic resistance, electrochemical reaction resistance and diffusion resistance of the infiltrated electrode at 10 min, 1030 min and 3010 min of annealing.

In order to demonstrate the influence of lateral current collection, similar symmetrical cells were fabricated with a layer of silver paint applied on top of the electrode before inserting in the test rig in order to improve current collection. Electrochemical impedance measurements were then carried out at 650 °C in both 5 vol% H_2 and 95 vol% H_2. The evolution of the ASR contributions for these cells is presented in Figure 4.6. These results show that the ohmic component is now much more stable (Figure 4.7). Nevertheless, there is still some residual increase with time over the initial 1030 min which could indicate a small contribution from the through thickness electronic conduction in the electrode. In

contrast, the electrochemical reaction contribution still displays a marked increase with time, indicating its inherent sensitivity to microstructure changes in the electrode. The diffusion and electrochemical reaction contributions again show the periodic fluctuations caused by humidity changes. The diffusion contribution shows no increasing trend with time but is reduced considerably by an increase in hydrogen partial pressure. Although the electrochemical reaction resistance also decreases with increase in hydrogen concentration, it still demonstrated an initial stage of rapid increase with exposure time. Figure 4.7 summarises the values for the three resistances at the end of 1010 minutes and 3010 minutes of annealing and again illustrates the relatively small change in ohmic and diffusion resistances as compared to the change in electrochemical reaction resistance. Nickel coarsening brings about two degradation effects: i) a loss in nickel percolation, and ii) a reduction in triple phase boundary length. The ASR data in Figure 4.6 hence confirm that the increase in ohmic and diffusion resistance seen in Figure 4.5, is a result of percolation (conductivity) loss while the increase in electrochemical reaction resistance seen in both figures is caused by loss of both percolation and TPB density, i.e. a loss of active TPB density.

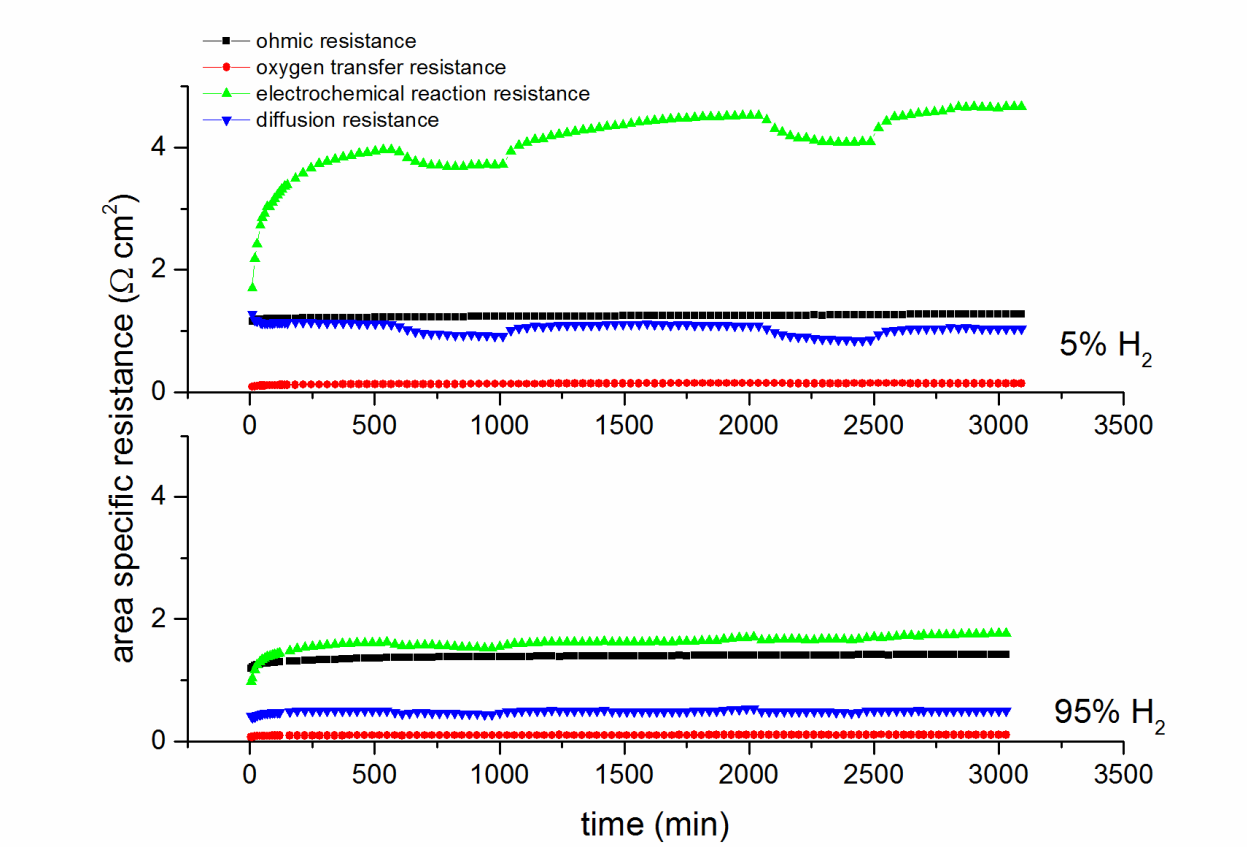


Figure 4.6 The time evolution of the contributions to ASR from the ohmic, oxygen ion transjer, electrochemical reaction and the gas diffusion processes. Measurement was made at 650 °C in two gas compositions 1) humidified 5% H_2 and 95% N_2 (above), 2) humidified 95% H_2 and 5% N_2 (below), with a flow rate of 100 ml min^{-1}. Silver paint was applied onto the surface of the electrodes in addition to the Pt mesh contact to improve current collection.

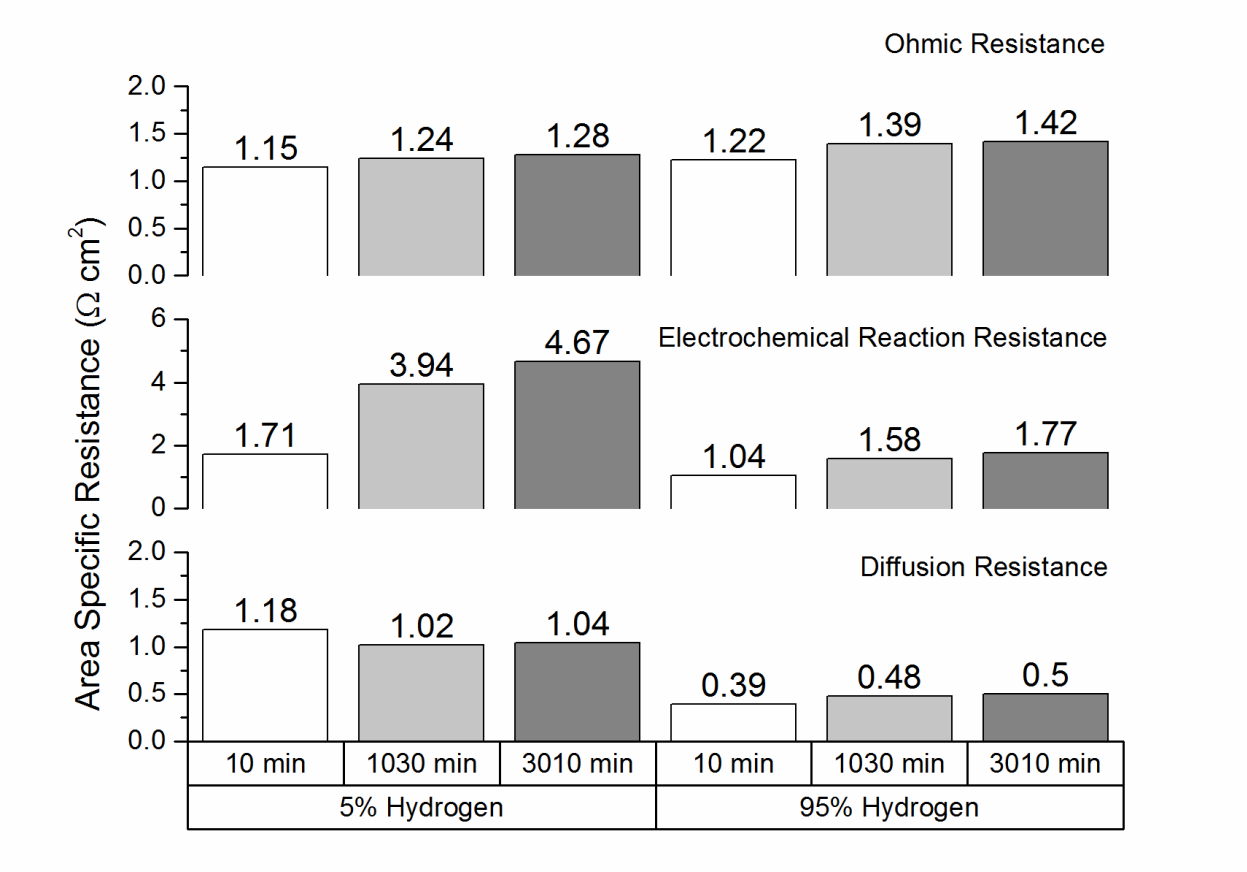


Figure 4.7 Values of the three contributions to the ASR at 10 min, 1050 min and 3010 min at 650 ˚C with a silver paint coating on the cell to improve current collection.

Increasing the hydrogen molar fraction from 5% to 95% reduced both the electrochemical reaction resistance and the diffusion resistance by a factor of approximately 2 (see Figure 4.7 and Figure 4.8), confirming that these two contributions are dependent on gas composition.

In order to support the identification of the different contributions to the ASR, experiments were carried out, on electrodes with silver paste as additional current collector, in which flow rate, temperature and hydrogen concentration were changed. In the following example the specimen had been annealed for 3010 min at 650 °C in an atmosphere of humidified 5%

H_2 and 95% N_2 before the impedance measurement to reduce the complicating effects of time dependent changes on the cell performance. The results are shown in Figure 4.8.

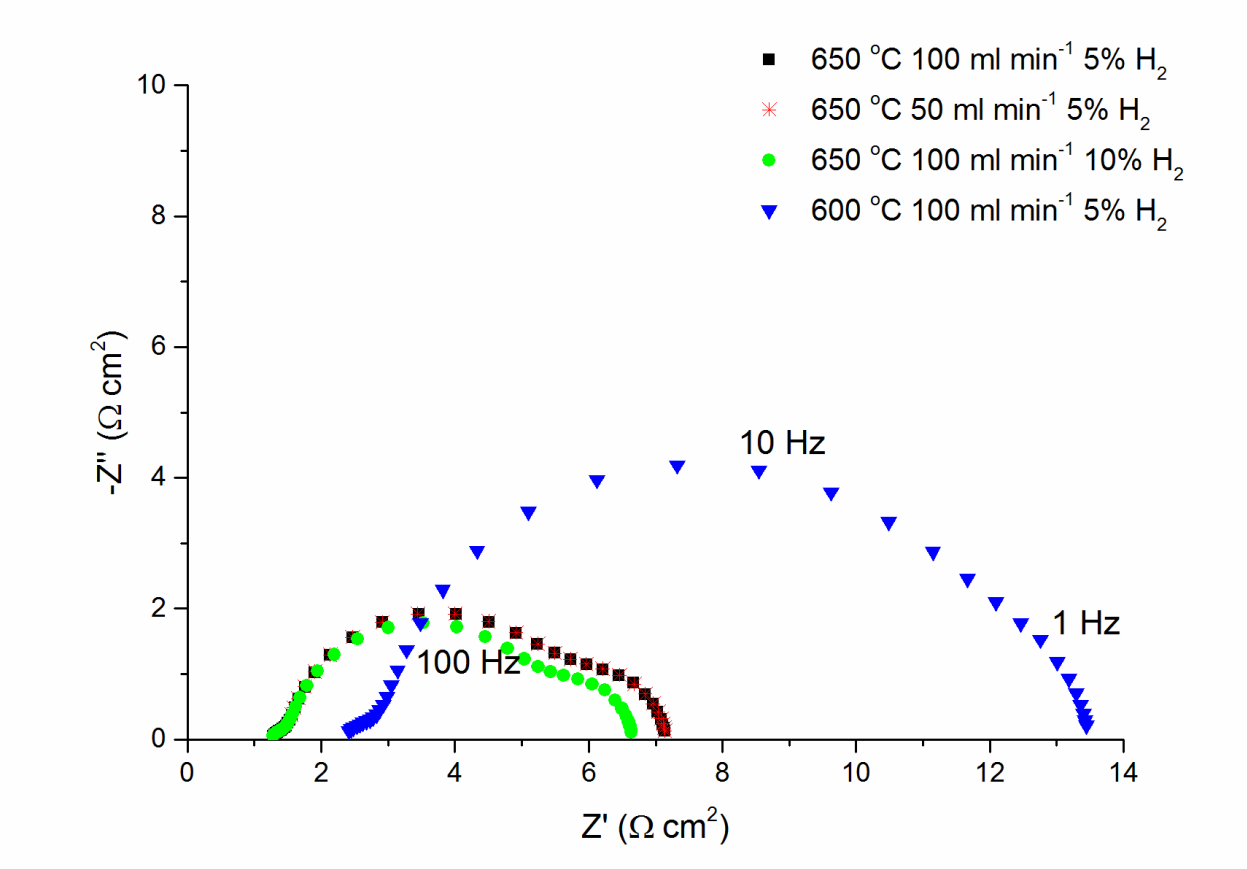


Figure 4.8 Nyquist plots for a symmetrical cell, with silver paint current collection, measured at different temperatures, fuel gas composition and gas flow rate (indicated in the legend).

Decreasing the flow rate of the fuel gas from 100 ml min^{-1} to 50 ml min^{-1} had no detectable influence on any of the contributions to the ASR. Due to the test rig configuration shown in Figure 3.2, changes to gas mass transport outside the test housing are not expected to influence conditions inside the housing because of the relatively long diffusion path between the two parts of the housing. Increasing the hydrogen content from 5 vol% to 10 vol% in the gas supply decreased both the medium frequency and low frequency contributions. The electrochemical reaction resistance at medium frequencies decreased because a higher

hydrogen activity is available at the triple phase boundary reaction sites. Similarly, a higher hydrogen molar fraction in the gas outside the housing provides a greater driving force for diffusion into the cell chamber. When the measurement temperature was decreased from 650 °C to 600 °C, all four resistance values increased, but especially the medium frequency contribution assigned to the electrochemical reaction.

4.2.3 Microstructure Characterisation

The microstructure of the nickel-impregnated ScSZ electrode was examined before and after isothermal annealing for 50 h. The morphology of the nickel and ScSZ phases are identified from the SEM images.

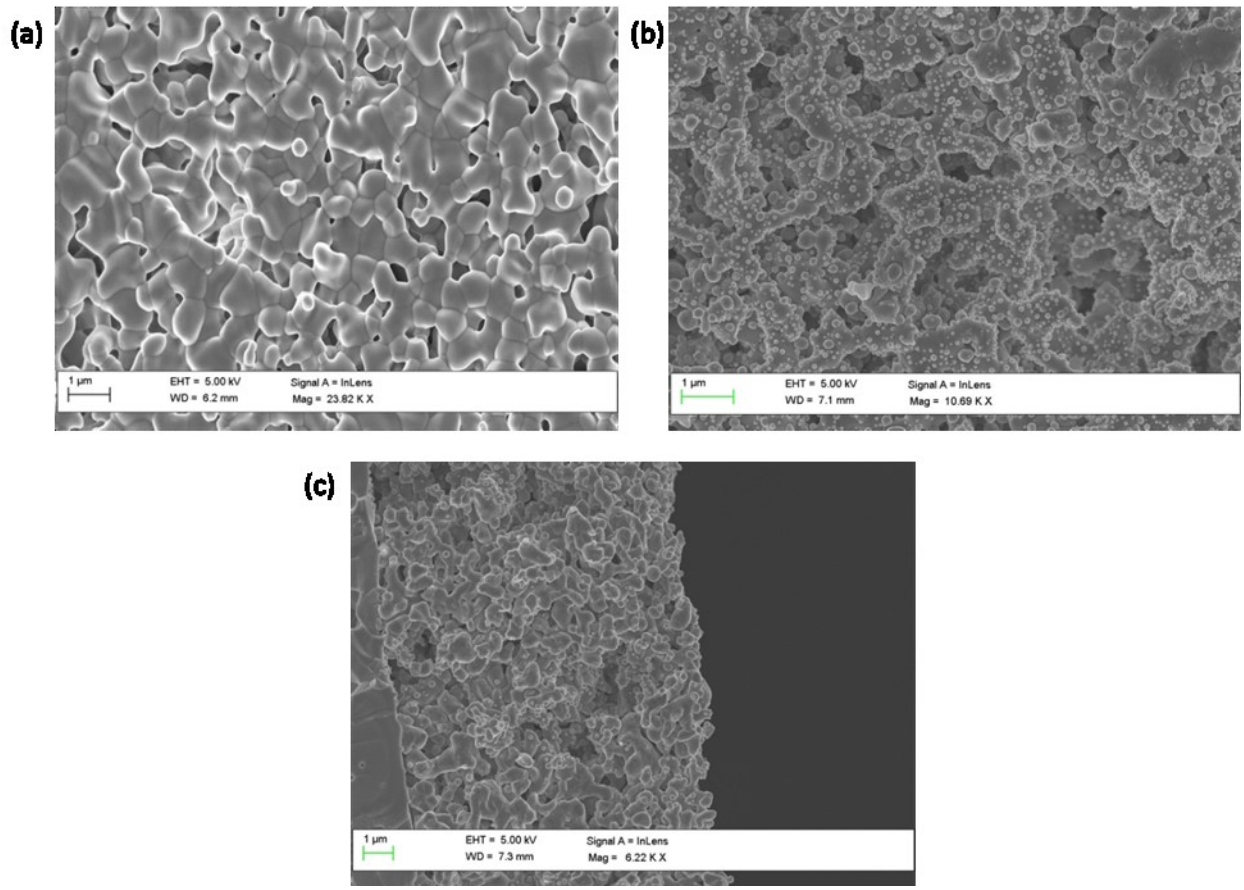


Figure 4.9 SEM micrographs of a) the ScSZ porous scaffold after sintering, b) the ScSZ scaffold after impregnating with nickel, c) the fracture cross section of nickel-ScSZ electrode after being reduced at 950 °C and held for 3010 min.

The microstructure observations revealed that the ScSZ after sintering formed an interconnecting porous scaffold as shown in Figure 4.9a. After infiltration and reduction, the nickel particles were homogeneously distributed onto the ScSZ surface as nanometer-size spheres facing the open pores (Figure 4.9b). The thickness of the scaffold is approximately 10 µm and the nickel particles are distributed throughout the whole scaffold as shown in Figure 4.9c.

The FIB-SEM image in Figure 4.10 confirmed that nickel particles were distributed over the entire ScSZ porous backbone. There is no indication of a nickel-rich surface region that would have distorted the conductivity measurements. The ScSZ grains are generally faceted whereas the nickel particles are spheroidal. This distinctive morphological difference between the two phases enables the identification of nickel particles from the secondary electron images. The microstructures of the electrodes aged for 30 min and for 3010 min are compared in Figure 4.11.

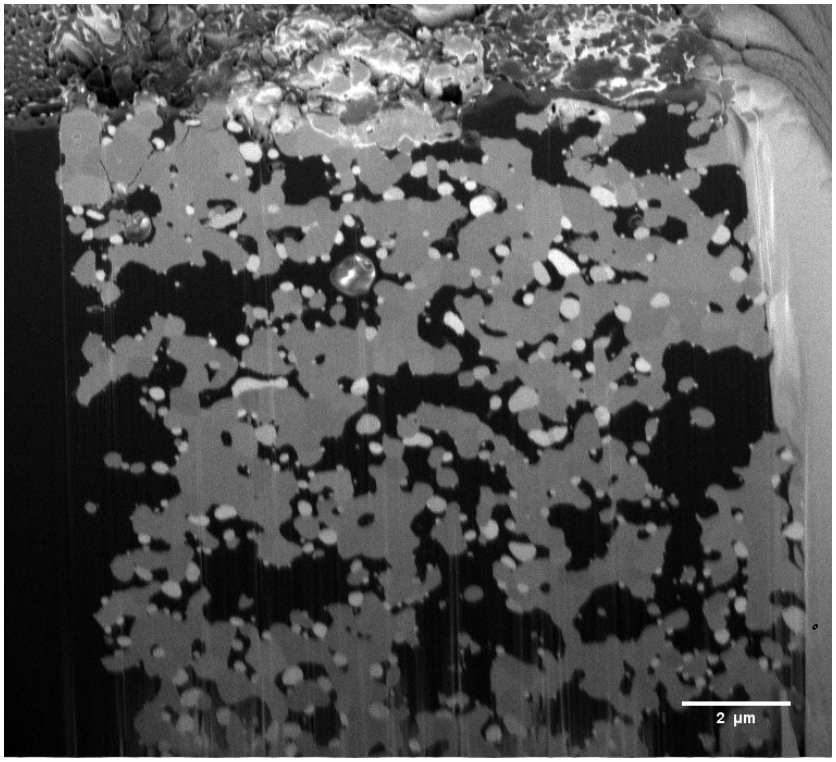
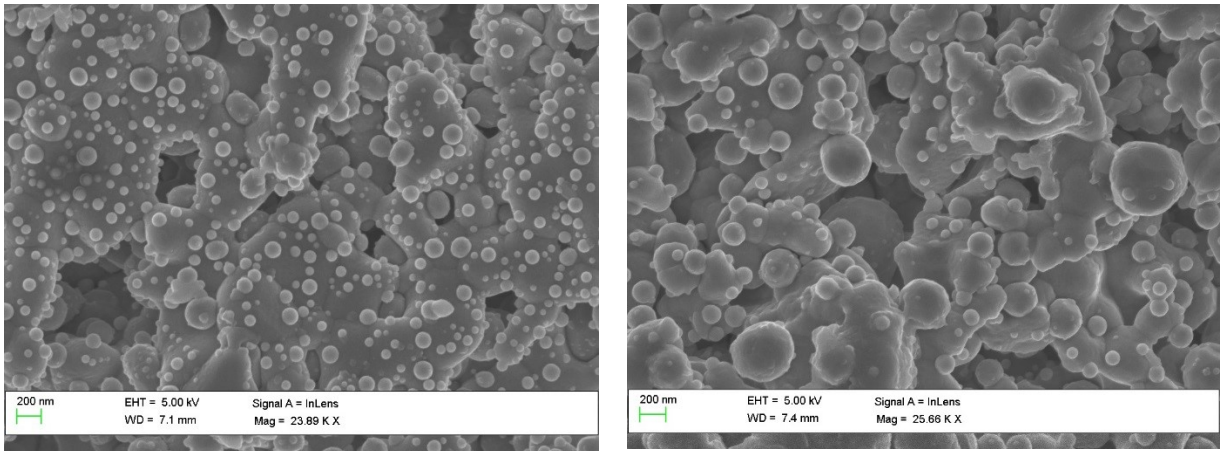


Figure 4.10 The secondary electron cross-sectional image of the image sliced and polished by focused ion beam shows three different phases with different colour contrast. The darkest phase is the epoxy resin that fills the pores. The brightest phase is nickel, which appears as nearly spherical particles. The grey phase in-between is ScSZ, forming a support network. The electrode has been reduced and aged at 950 °C in wet 5% hydrogen and 95% nitrogen for 30 min.

As shown in Figure 4.11 a2) and b2), the circular nickel particles were identified and the radii of the circles measured using MATLAB. The particle size distributions of nickel at the beginning (30 min) of annealing and the end (3010 min) are presented in Figure 4.12. The frequency is weighted by the diameter of the particle, so that the frequency distribution can be directly related to the TPB length.

a1) b1)



a2) b2)

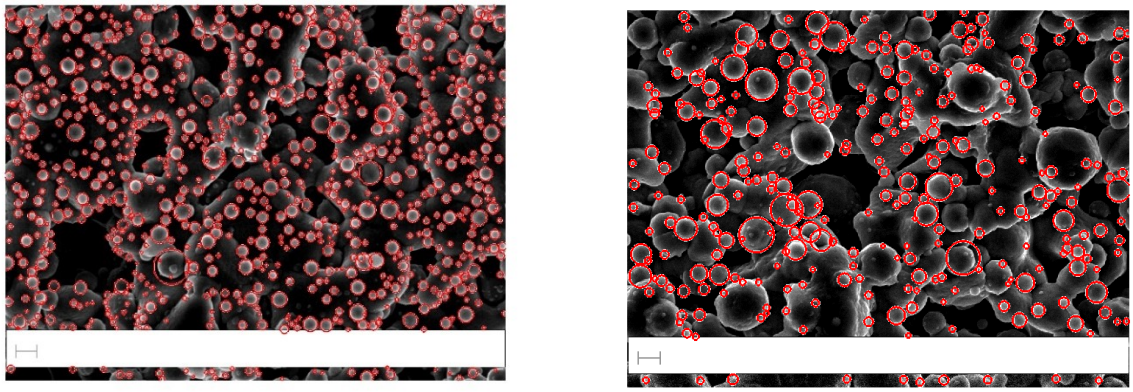


Figure 4.11 Secondary electron images of an electrode reduced and aged at 950 °C for 30 min a1) and 3010 min b1). The images were processed for image analysis by enhancing the contrast and edge threshold level to emphasise the circular objects (nickel particles) in a2) and b2).

An increase in particle size with the annealing time is clear in Figure 4.12. The fine nickel particles with a particle size less than 40 nm disappeared after 3010 min of ageing and some particles grew to above 200 nm in diameter. The number of spherical particle detected decreased from 850 at 10 min to 294 at 3010 min while the total volume of the spheres were conserved. The particle size distribution indicated both an increase in average particle size and a decrease in the number of particles.

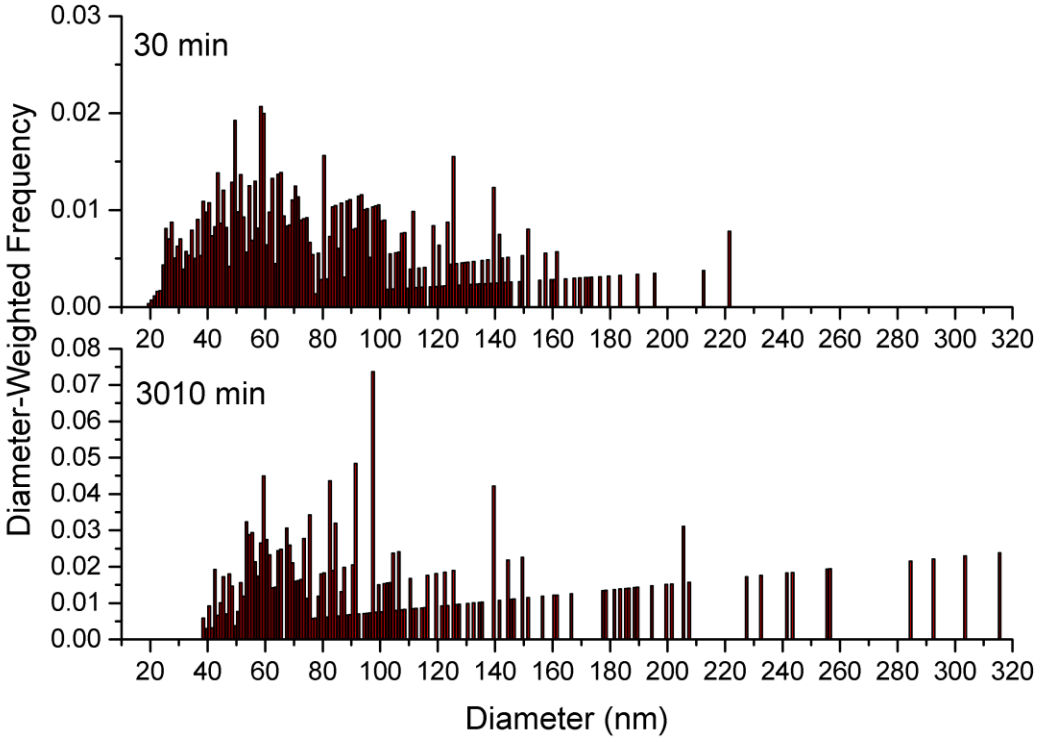


Figure 4.12 The diameter-weighted particle size distributions of nickel in the infiltrated electrode after 30 min (above) and 3010 min (below) of annealing

4.2.4 Physical Model of Electrode ASR

The 1D distributed model developed by Bertei et al. [158] was used to interpret the degradation in the nickel impregnated ScSZ electrode semi-quantitatively. The model treats the electrode microstructure as a continuum with a key parameter being the effective TPB length per unit volume of the electrode. Other microstructure parameters in the model that influence the contribution from the electrochemical reaction to a lesser degree are the area of the Ni/ScSZ interface per unit volume, the conductivity factor for the ionic conducting network (defined as the conductivity of the network compared with the conductivity of the dense ionic conductor) and the electrode thickness. The degradation due to nickel coarsening can be quantified by two time-dependent parameters: 1) decreasing active anode area due to increasing electronic current collection resistance; and 2) decreasing active TPB density.

The model makes the following simplifying assumptions.

i. the effective electronic conductivity is much larger than the effective ionic conductivity in the electrode;
ii. within the active area, the microstructural properties are uniform;
iii. the electrochemical TPB reaction obeys Butler-Volmer kinetics.

Figure 4.13 illustrates the contact, in the absence of silver coating, between the electrode and the Pt mesh current collector, and also the area of the electrode between two contact points. The inactive region, in which the nickel connection towards the neighbouring current collector is cut off, enlarges as nickel coarsening breaks up the percolation.

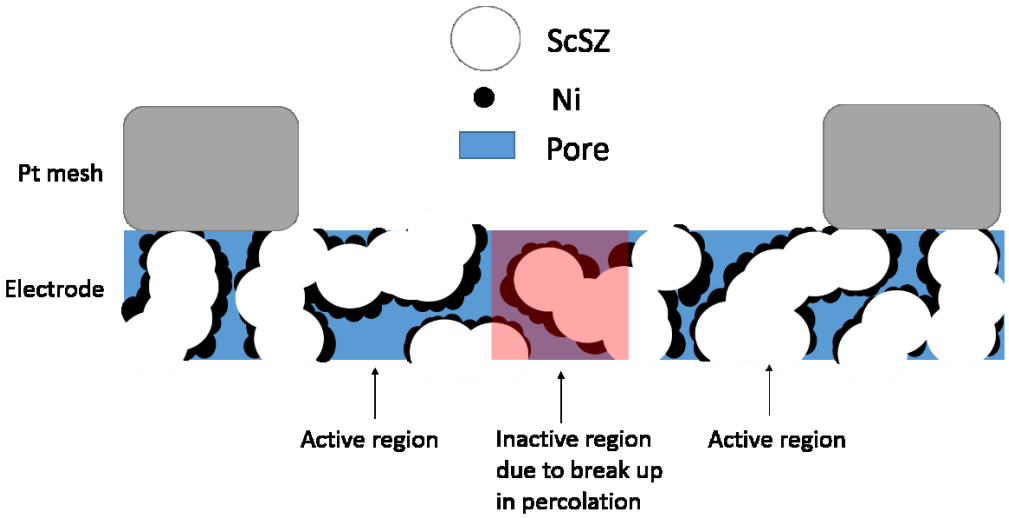


Figure 4.13 Schematic of the electrode microstructure between two Pt mesh contact points (no additional silver current collection) showing the inactive regions due to break up in percolation of the nickel network upon degradation (note: figure not drawn to scale). Electrochemical reaction takes place at the percolating triple phase boundaries and the electrons released from hydrogen oxidation flow along the nickel path (in black) to the Pt mesh current collector.

The impedance spectra obtained during annealing of the specimens without the silver current collection were analysed according to the following steps.

1) The oxygen transfer resistance was determined (using parameter values established previously for a similar ScSZ scaffold [158]) and compared with the experimental data to decouple it from the ohmic series resistance. At 650 °C the initial ASR contribution from oxygen transfer was measured to be 0.13 Ω cm^2 in the present experiments, in good agreement with the value of 0.14 Ω cm^2 from the model parameters. At the higher temperatures (at which this contribution could not be separated experimentally) the model predictions are 0.009 Ω cm^2 at 800 °C and 0.0012 Ω cm^2 at 900 °C. Therefore at these temperatures this contribution is

negligible and the ohmic resistance is dominated by the electrolyte and current collection resistances.

2) The measured ohmic resistance was then compared with the initial ohmic resistance to calculate the time-dependent active area fraction assuming in all cases that the initial active area fraction is 100 %. The result is shown in Figure 4.14 indicating that the active area fraction exhibited a rapid decrease over the first 1000 min of annealing and then slowed down afterwards.

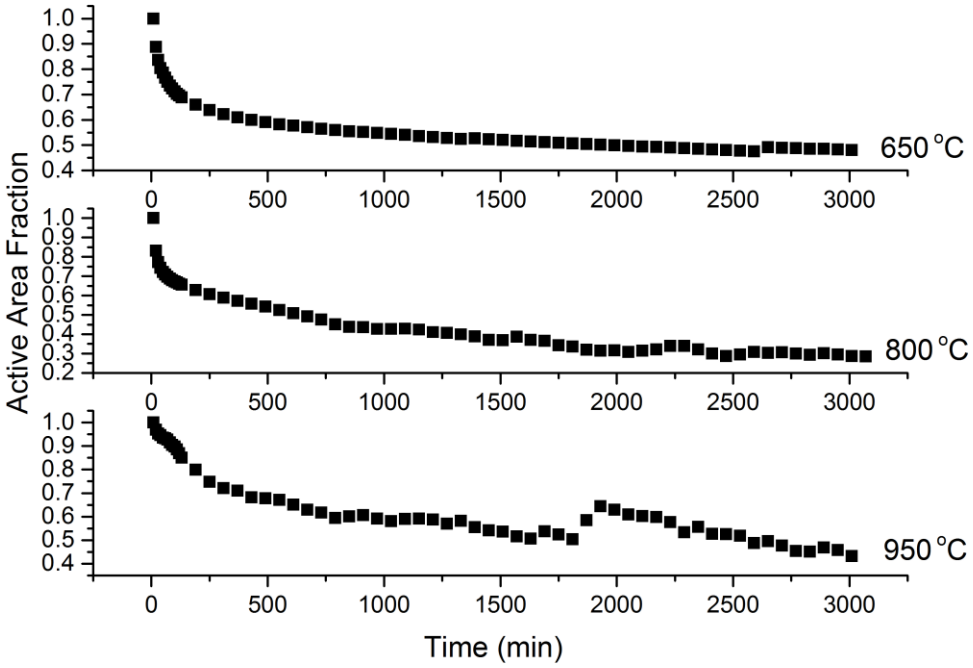


Figure 4.14 The time evolution of active area fraction of electrodes at 650 ‘C, 800 ‘C and 950 ‘C.

3) Measurements of room temperature changes during the annealing were used to determine the water vapour pressure variation with time, assuming equilibrium in the water bubbler. Using this, the periodic fluctuation in the electrochemical reaction resistance due to water molar change was corrected to a common water vapour

concentration of 3% assuming that the exchange current density is proportional to $y_{H2O}^{0.52}$ where y indicates mole fraction as specified for the exchange current density in the model [193]. The variation in percolating TPB density was thus separated from the variation in active area fraction as shown in Figure 4.15. The active TPB density was then estimated from the model using the values for the exchange current density per unit length of TPB and the effective ionic conductivity of ScSZ at each temperature, as established previously when applying the model to similar Ni-infiltrated ScSZ electrodes [158].

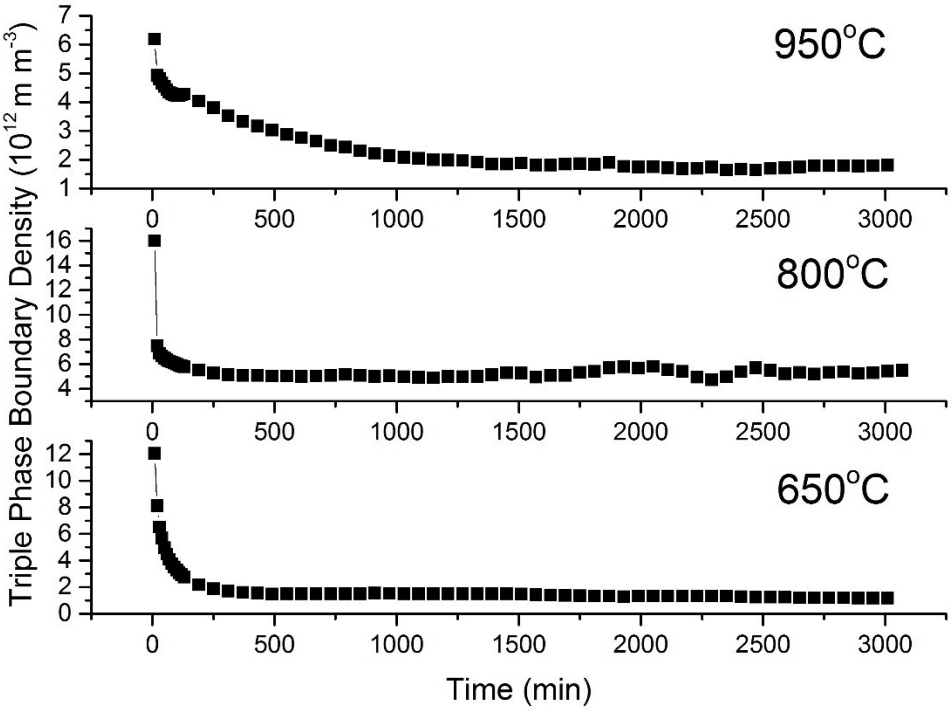


Figure 4.15 The evolution of active triple phase boundary densities with annealing time at 950 ‘C, 800 ‘C and 650 ‘C derived from the electrode model.

The active TPB densities in Figure 4.15 showed a sharp decrease over the first 1000 min of annealing. A plateau was reached after the initial degradation. At 950 °C and 650 °C, the

plateau TPB density was approximately 1.8×10^{12} m^{-2} and 1.2×10^{12} m^{-2} respectively. However, there is not a smooth trend with annealing temperature. Surprisingly, the highest plateau density of 5.5×10^{12} m^{-2} was found at 800 °C. This is believed to be due to the different reduction temperatures giving different initial nickel microstructures that also evolve differently. The initial TPB densities of the nickel-impregnated electrodes are similar in magnitude to the TPB densities measured by FIB-SEM tomography in Ni-impregnated gadolinium-doped ceria scaffold electrodes [60].

For the experiments in which a silver paste current collector was used, the effective area fraction was assumed to be 1 independent of ageing time since the effect of percolation breakup is mitigated. The expected electrochemical reaction resistance at different annealing stages with the silver current collector were predicted by assuming the same evolution of TPB density shown in Figure 4.15 at 650 °C with 5 vol% hydrogen. The predicted values are compared with the measured values (Figure 4.6) as shown in Table 4.1. The predicted and measured effects are in reasonable agreement except for the 10 minute data. The discrepancy at this stage is probably due to sensitivity of the early ageing results to reproducibility in reduction procedure and initial heating to test temperature.

Table 4.1 Comparison between the model predicted electrochemical reaction ASR and the measured ASR at 650 ‘C with silver paste in moist (3 vol% water vapour) 5 vol% hydrogen-nitrogen

	Predicted ASR (Ω cm^2)	Measured ASR (Ω cm^2)
Electrochemical Reaction at 10 min	0.61	1.71
Electrochemical Reaction at 1030 min	3.84	3.94
Electrochemical Reaction at 3010 min	4.80	4.67

Models have also been published to estimate the TPB density of infiltrated electrodes a priori. Reszka et al. [194] presented a model of the microstructure of infiltrated electrodes that considers the total and active TPB lengths as functions of infiltrated particle size, scaffold porosity and pore size and volume fraction of infiltrate. For the current materials the initial infiltrated particle size is approximately 100 nm, scaffold porosity is 50%, the scaffold particle (grain) size is 0.5 µm, the scaffold pore size is approximately 1 µm, and the volume fraction of nickel is 20%. According to their model the active TPB density is not very sensitive to the scaffold pore size and is approximately 0.8 unit^{-2} (where a unit is the infiltrated particle size) for 20 vol %. infiltrate loading. This corresponds to a TPB density of 800×10^{12} m^{-2}, which is much greater than the value estimated from the electrochemical model and probably reflects the fact that the a priori model for the infiltrated microstructure is not sufficiently close to reality. Bertei et al. [195] present a similar model which predicts a percolating TPB density equal to approximately 50 d_s^2, (where d_s is the scaffold particle

size and is 5 times the infiltrated particle size as in the present experiments) and in the present case corresponds to a connected TPB density of 8×10^{12} m^{-2}. This latter value is of a similar order of magnitude to the total TPB density of 18×10^{12} m^{-2} measured by tomography in similar electrodes with a doped ceria scaffold infiltrated by nickel [60] and the connected TPB densities estimated in the current specimens before the isothermal annealing (Figure 4.15).

4.3 Conclusions

In this chapter, an early rapid degradation in the ASR of nickel-impregnated ScSZ electrodes was observed and correlated with changes in the electrode microstructure. The in-plane conductivity of the electrodes was also observed to decrease significantly with exposure time. Electrochemical impedance spectroscopy revealed four contributions to the overall ASR of the symmetrical cells: a series resistance from the electrolyte support; a small high frequency contribution from transfer of oxygen ions from the electrode to the electrolyte; a medium frequency contribution from the electrochemical reaction; and a low frequency contribution from gas diffusion into the test chamber. The increase in ohmic resistance revealed an issue with current collection when using platinum mesh current collectors that caused all contributions to increase in a similar way. This showed that disruption of the percolating nickel pathways in the electrodes decreased their effective active area. This was confirmed in experiments in which a silver layer was applied on top of the electrode to improve current collection.

The microstructure images showed that nickel particles coarsened after annealing in wet hydrogen. The degradation due to nickel coarsening was described by two time-dependent parameters, 1) decreasing effective electrode area as a result of percolation break-up and 2) decreasing active triple phase boundary density. A previously published physical model was used to extract the active electrode area fraction and the active triple phase boundary densities in the active regions from electrochemical impedance spectra. Both parameters reduced sharply during the initial stage of annealing and then stabilised to reasonably steady values. Decoupling the active TPB density from the active anode area fraction verified that the major degradation associated with nickel coarsening in the impregnated electrode takes place at a relatively short time-scale (1000 min) as compared to the desired operational life time of solid oxide fuel cells in most applications (40,000 h or more).

5 Fabrication of Nanoscale Nickel Yttria-Stabilised Zirconia Electrode from Nanocomposite Powder

Though impregnation is a versatile tool and widely used in laboratory for fabricating nano-scale SOC electrodes, it has not yet been scaled up to mass production. In the case of Ni-impregnated electrode, the nickel sitting on the scaffold has much free volume for movement. This inherent structural feature may not be beneficial in the long term to preserve nickel nanoparticles. The conventional power-mixing and co-sintering fabrication route is likely to be better suited for reducing the free volume for nickel movement.

Here a different, potentially commercially viable, approach to producing a nano-structured Ni-YSZ electrode with both nano- and micron-sized porosity for gas access is investigated. Hydrothermal synthesis is used to produce an intimate mixture of NiO and YSZ precursors that can be subsequently processed into a powder containing agglomerates of a NiO-YSZ nanocomposite mixture. On reduction of the NiO to Ni, fine pores are created within the agglomerates giving gas access to the internal surface of the agglomerates. The agglomerates also produce an electrode microstructure with larger pores to allow gas to access the outer surface of each agglomerate. Thus, inside the agglomerates are nanoparticles of NiO and YSZ, while in-between the agglomerates is micron-sized pore space. This chapter describes the processing of the NiO-YSZ nano-composite particles, followed by an investigation of the electrochemical performance and microstructural features of the resulting electrodes.

5.1 Experimental

5.1.1 Nanoparticle Synthesis

The nanoparticles used in this study were synthesised in a continuous hydrothermal reactor at pilot plant scale at University College London by Dr. Chris Starkey. Details of the process are given in [196]. An aqueous salt mixture (Ni nitrate, yttrium nitrate and zirconyl nitrate) with hydrogen peroxide oxidising agent was fed to the reactor at concentrations consistent with the target composition of the eventual electrode. Independent streams of deionised water and aqueous potassium hydroxide were also employed to cause hydrolysis and precipitation. The reactor operated at 24.1 MPa and 450 °C. The process is similar to co-precipitation, but in the reactor hydrolysis and precipitation are very fast. As a result, the cations in the two feeds remain intimately mixed during hydrolysis and the intimate mixing is preserved in the precipitate. The precipitate was recovered by centrifugation, washed in deionised water to remove anions and again centrifuged. At this stage the product was in the form of an aqueous slurry. The particle size as synthesized is typically 5 nm as reported in [196].

5.1.2 Fabrication of the Electrode

The nanopowder synthesized by the continuous hydrothermal flow route was freeze-dried for 5 days in a FreeZone 4.5 Liter Console Freeze Dry System in order to prevent the formation of hard agglomerates. The as-dried powder was calcined at 700 °C for 30 min to remove any physi-sorbed and chemi-sorbed water and decompose any remaining nitrate

impurities (see later thermal analysis). The calcined powder was then dispersed in ethanol and milled in a planetary ball mill for 30 h at 300 rpm to reduce the size of soft agglomerates. The milled powder was then made into electrodes on YSZ substrate as detailed in Chapter 4.1. The electrodes were sintered at 1300 °C for 2 h.

5.1.3 Powder Characterisation

The particle size of the powder was measured after ultrasonic dispersion in de-ionised water by laser scattering using a Malvern Mastersizer 3000. The nitrogen adsorption and desorption isotherms were obtained at 77 K using a Micromeritics TriStar II and the specific surface area calculated by BET theory. Thermogravimetric analysis (TGA) and differential scanning calorimetry (DSC) on the as-dried composite powder were conducted using a Netszch Jupiter thermal analyser at a heating rate of 10 °C min^{-1} in air from room temperature to 950 °C. A sample of the as-dried composite powder was also uniaxially and then isostatically pressed into a green cuboid pellet. The sintering dilatometry of the green pellet was measured using a Netzsch 402E dilatometer in air at a heating rate of 5 °C min^{-1} from room temperature to 1500 °C.

5.1.4 Electrode Characterisation

XRD of the Ni-YSZ electrode was done using a Bruker D2 diffractometer with Cu Kα radiation at a step size of 0.016 °. High-resolution SEM images of the Ni-YSZ electrode and the NiO-YSZ powder were taken using a LEO Gemini 1525 SEM. The sequential FIB cross

section SEM images of the resin-impregnated electrode were taken using a Zeiss Auriga Cross Beam FIB-SEM. The pixel size of each FIB-SEM image was 16.4 nm and the thickness of each slice was 20 nm. The contrast of the different phases in the images was enhanced, and the noise reduced, using ImageJ and Avizo. Segmentation was carried out using Trainable Weka Segmentation [172]. Phase sizes were determined using the linear intercept method in three orthogonal directions on the 3-D reconstruction with a proportionality constant of 1.56 [197]. 3-D reconstruction was done using Avizo and data extraction from the 3-D volume using MATLAB and the TauFactor plug-in [173].

The in-plane conductivity of the electrode was measured by the van der Pauw method with a square array probe spacing of 6 mm at room temperature in air. The average electrode thickness was measured to be 15 µm, the value then used in the conductivity calculation. The EIS data were measured in an in-house rig (Figure 3.3) on the symmetrical cells. The cell was fixed vertically in a groove in an alumina platform at the front of the gas flow channel and current collection was made using porous Ni paste and a platinum wire pick-up. The electrode was reduced for 60 min at 800 °C in humidified 5% H_2 – 95% N_2 at a flow rate of 100 ml min^{-1} and the impedance spectra were measured from 1 MHz to 0.1 Hz under open circuit condition in a two-electrode set-up. Humidification was introduced by passing the test gas through a water bubbler at room temperature which gives a water vapour content of approximately 3 vol %.

5.2 Results and Discussion

5.2.1 NiO-YSZ Nanocomposite Powder Characterisation

The particle size distribution after freeze-drying has a volume weighted mean particle diameter of 49 µm, indicating the formation of large soft agglomerates. The BET surface area was calculated to be 189 ± 1 m^2 g^{-1}, which is significantly larger than the value of 4-8 m^2 g^{-1} typical of commercial NiO-YSZ powder.

To stabilize such high surface area nanopowders in an ink, large amounts of dispersant and solvent are required [198]. This undesirably lowers the solid loading of the ink and causes difficulties to sinter the cast ink to a sufficient density. Initial attempts to make an ink from the freeze-dried powder failed because, when the ink had an appropriate rheology for casting, it was too dilute and the layer cracked upon drying and firing. Therefore, a calcination step was introduced to purposely reduce the surface area, and additionally to remove chemisorbed water and residual nitrates from the freeze-dried powder.

TGA and DSC analysis of the freeze-dried powder is shown in Figure 5.1b. The mass decreased as the temperature increased until reaching a plateau of 83% at approximately 700 °C. The DSC shows two endothermic peaks, one at 100 °C and the other at 290 °C, which are likely caused by the loss of physiosorbed and chemisorbed water. From the results in Figure 5.1b, a suitable calcination temperature for the freeze-dried powder was chosen to be 700 °C.

Constant heating rate dilatometry of the pressed pellet from the as-dried powder is shown in Figure 5.1a. The shrinkage rate has a minor peak at 290 °C and a much larger one at 1320 °C. The minor peak correlates with the endothermic change at the same temperature

in Figure 5.1b, implying the loss of chemisorbed water leads to a small degree of shrinkage. The fastest shrinkage takes place at about 1300 °C and hence this was considered to be a suitable sintering temperature for the electrode.

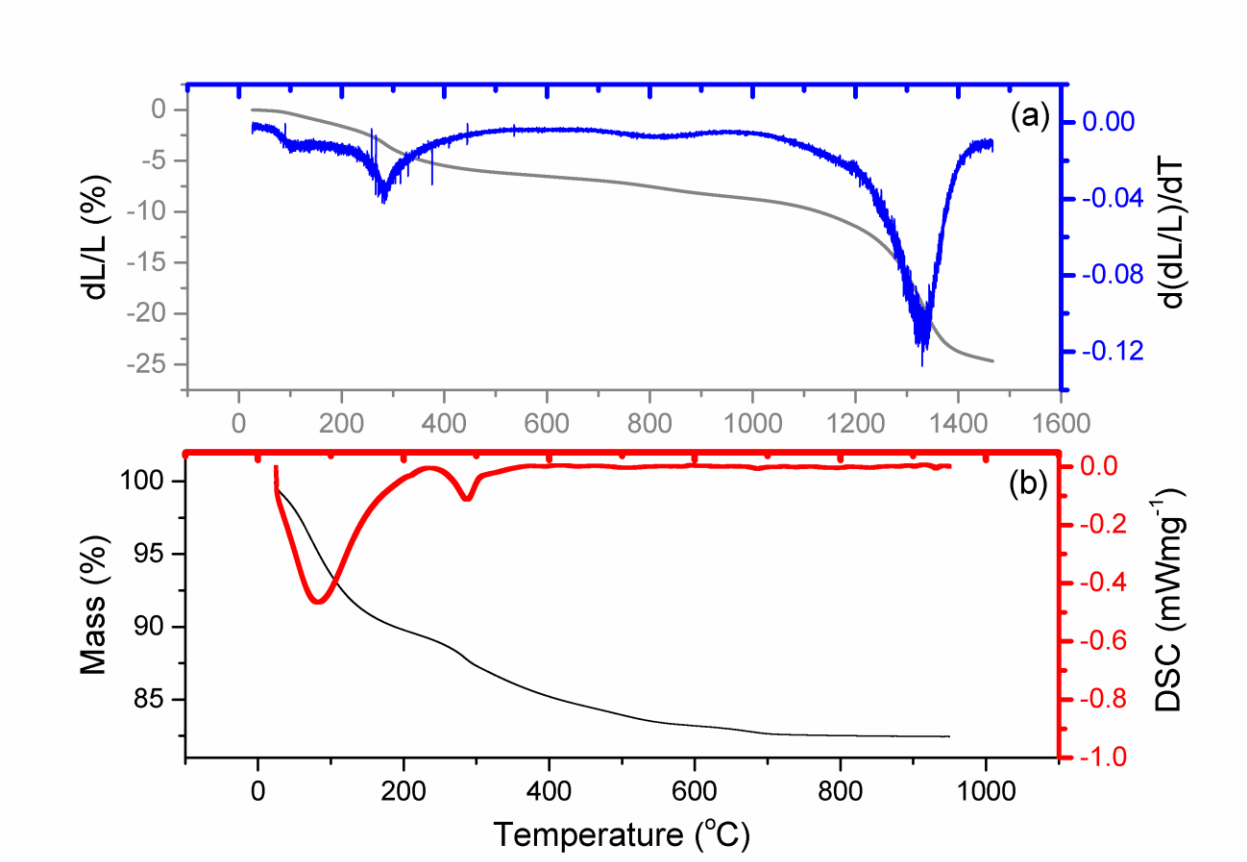


Figure 5.1 Thermal properties of the NiO-YSZ powder. (a) dilatometry of the freeze-dried NiO-YSZ green pellet: linear shrinkage and shrinkage rate vs. temperature (b) DSC and TGA of the freeze-dried NiO-YSZ powder from room temperature to 950 °C

Both the particle size distribution and adsorption-desorption isotherm were measured again after calcination and ball milling. The particle size distribution (Figure 5.2a) exhibited a major peak between 2 and 3 µm and a minor peak at 10 - 20 µm. The mean particle size was decreased by more than 10 times by the milling. The nitrogen adsorption-desorption isotherm (Figure 5.2b) for the calcined and milled powder displays a type II isotherm with

evidence of micro-pores (< 2nm). The total BET surface area is 51.3 ± 0.2 m^2 g^{-1} and the t-plot method determined that the micro-pore area is 22.7 m^2 g^{-1} and external surface area is 28.6 m^2 g^{-1}.

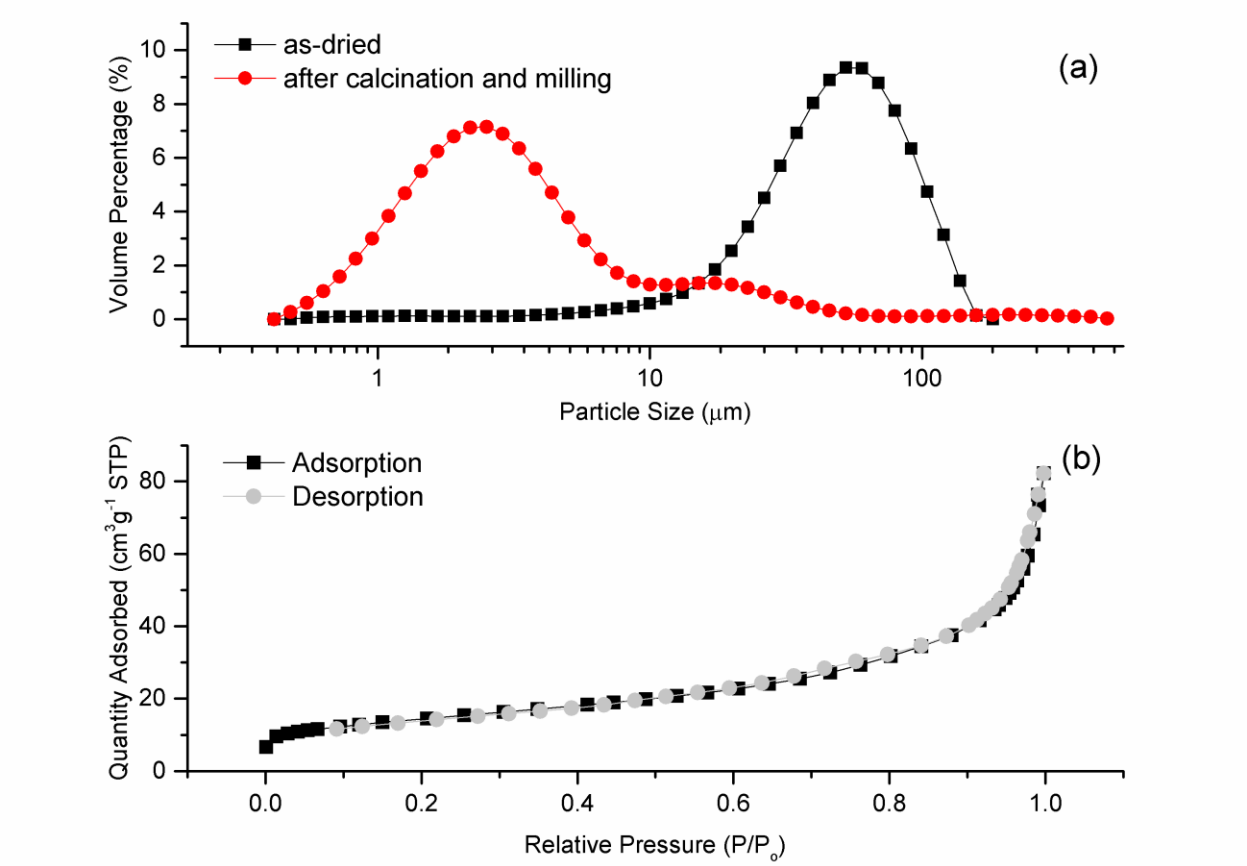


Figure 5.2 NiO-YSZ powder size distribution and surface area measurements. (a)The particle size distribution measured by laser scattering as-dried and after calcination and milling. (b) Adsorption and desorption isotherm of N_2 at 77 K of the NiO-YSZ nano-composite powder after calcination and ball milling.

After calcination, the structure of the nano-composite agglomerates was examined by SEM and an example is shown in Figure 5.3. The agglomerate is approximately 1 μm in diameter, irregular in shape and consists of many fine primary particles less than 100 nm in size. The pores in-between the fine particles are also less than 100 nm. The NiO and YSZ

nanoparticles formed loosely-bonded micron-sized agglomerates, which are suitable for processing into a castable ink.

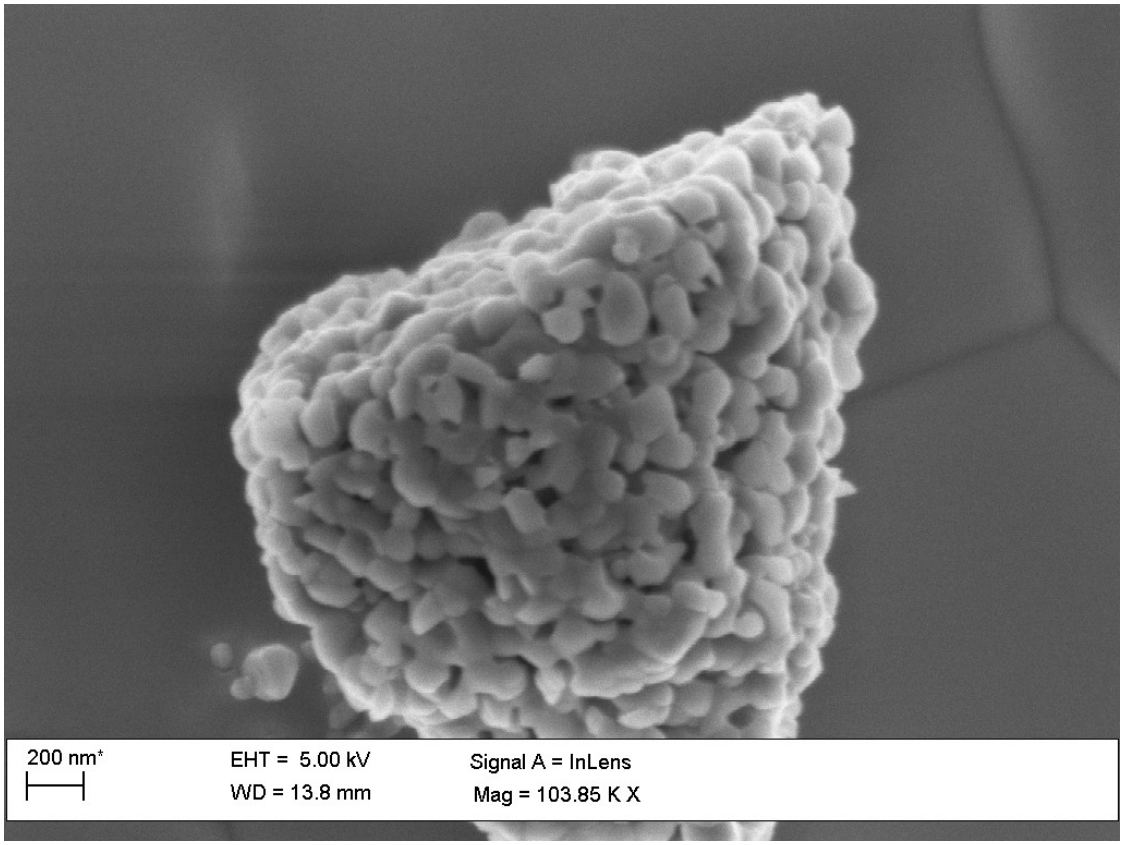


Figure 5.3 SEM image of a typical agglomerate particle of the NiO-YSZ nano-composite powder after calcination.

5.2.2 Ni-YSZ Nano-Composite Electrode Physical Characterisation

X-ray diffractometry of the sintered and reduced nano-composite electrode (Figure 5.4b) confirmed its constituents as 8 mol% YSZ and Ni, with no other phases detected. Using Rietveld refinement, the weight fractions of the two phases were determined to be 40.6 ± 0.3 wt% for Ni and 59.4 ± 0.3 wt% for YSZ. The nickel content in the electrode was also

measured by mass changes following reduction and re-oxidation of a sintered pellet and found to be 41.7 ± 0.2 wt%, in good agreement with the X-ray analysis.

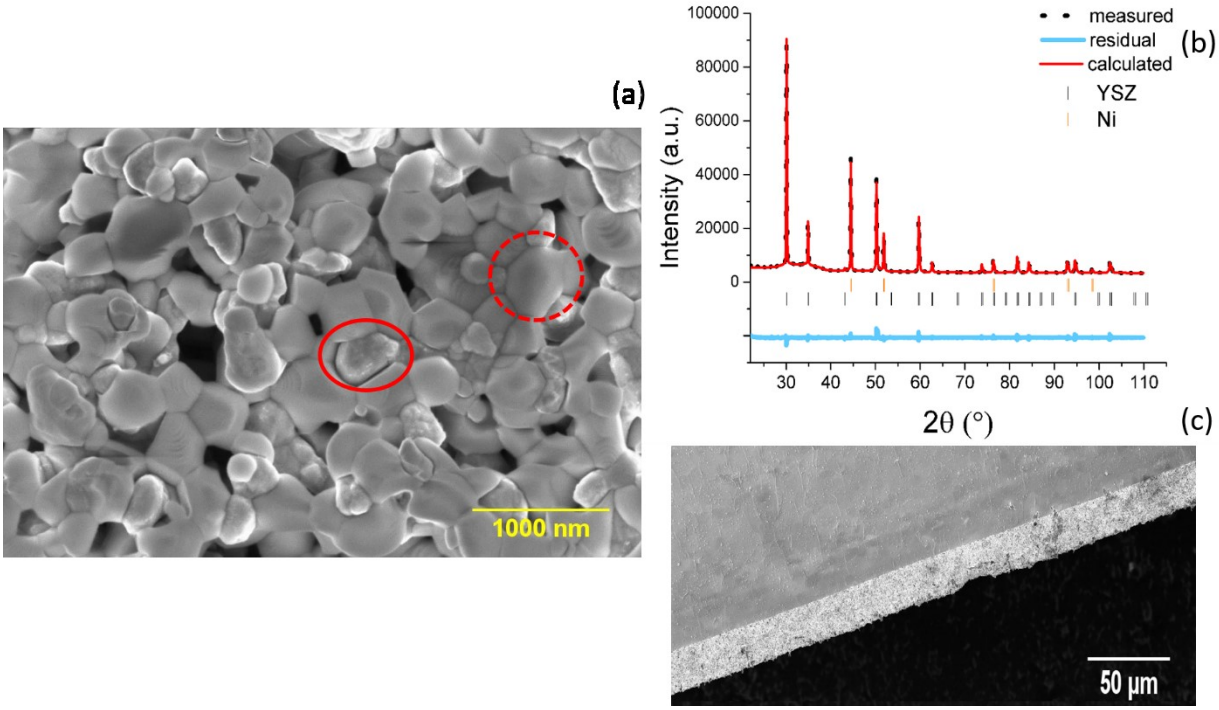


Figure 5.4 Morphology and composition of the Ni-YSZ electrode (a) SEM image of the top surface of the Ni-YSZ electrode. The particle circled in dotted line is YSZ and the particle circled in solid line is Ni. (b) XRD pattern and Rietveld refinement of the Ni-YSZ electrode c) SEM cross section of the Ni-YSZ electrode on the YSZ substrate.

The SEM image of the top surface of the Ni-YSZ electrode is shown in Figure 5.4a. The particle sizes of Ni, YSZ and pores are all in the 100 nm range. Nickel particles tend to have extra porosity nearby due to the volume shrinkage during NiO reduction, as seen in the region circled in solid line in Figure 5.4a. The nickel particles appear to be more rounded with rough surfaces and the YSZ particles more faceted with smooth surfaces (e.g. in the region circled in dotted line). From the cross section in Figure 5.4c, the electrode thickness was measured to be 15 µm and is uniform.

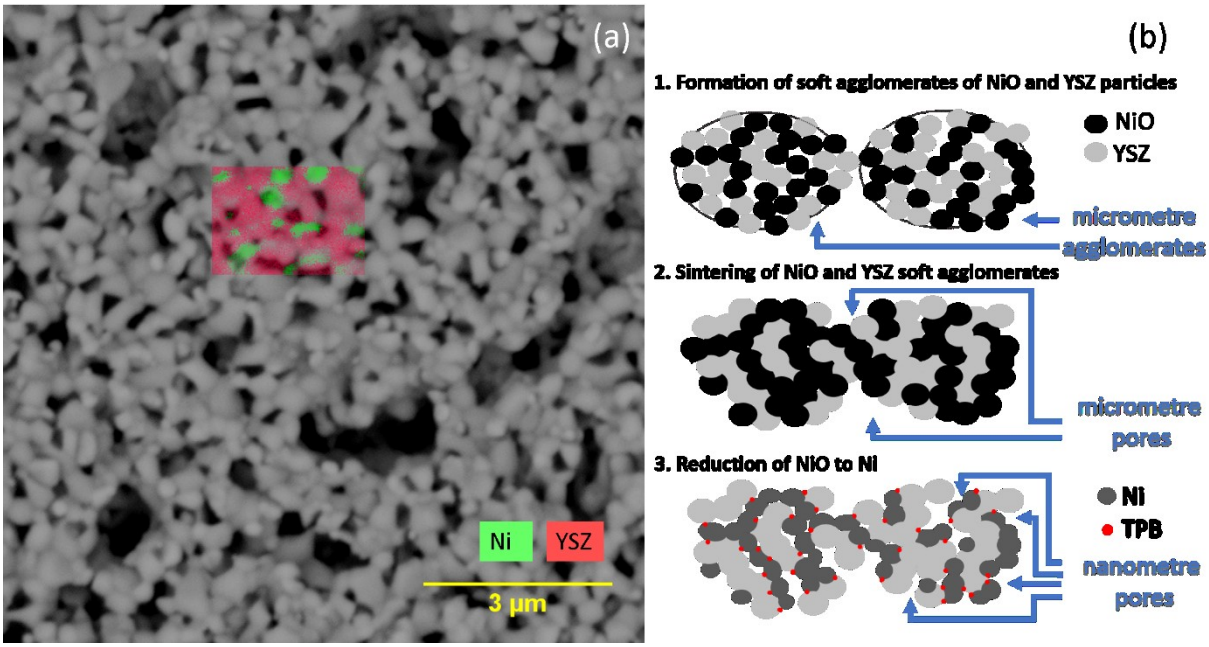


Figure 5.5 The dual porosity microstructure (a) EDX mapping on the top surface of the Ni-YSZ electrode combined with back-scattered electron image. The green region represents where Ni is detected and red region, Zr. (b) schematic showing the evolution of the microstructure in the fabrication route after 1) calcination and ball milling 2) sintering and 3) reduction.

The energy-dispersive X-ray (EDX) mapping in Figure 5.5a shows the location of Ni and Zr. The two phases in the mapped region are intimately mixed primary particles with fine porosity between them. Additionally, Figure 5.5a shows pores with two different length scales. One type of pore is nanometre in size, which was also observed in Figure 5.4a. The other type is micrometre in size. While the nano-sized pores are formed by the volume shrinkage when nano-sized NiO is reduced to Ni, the micron-sized pores are formed during the sintering of the NiO-YSZ cast layer between the soft agglomerates as illustrated in Figure 5.5b. This dual porosity microstructure allows both fast gas diffusion through the

micrometre pores and a large number of electrochemical reaction sites in the nano-porous denser regions.

An image stack of 300 consecutive 2-D FIB-SEM slice-and-view images was analysed quantitatively, resulting in a reconstructed volume measuring 10.45 µm × 5.29 µm × 5.98 µm as shown in

Figure *5.6*a.

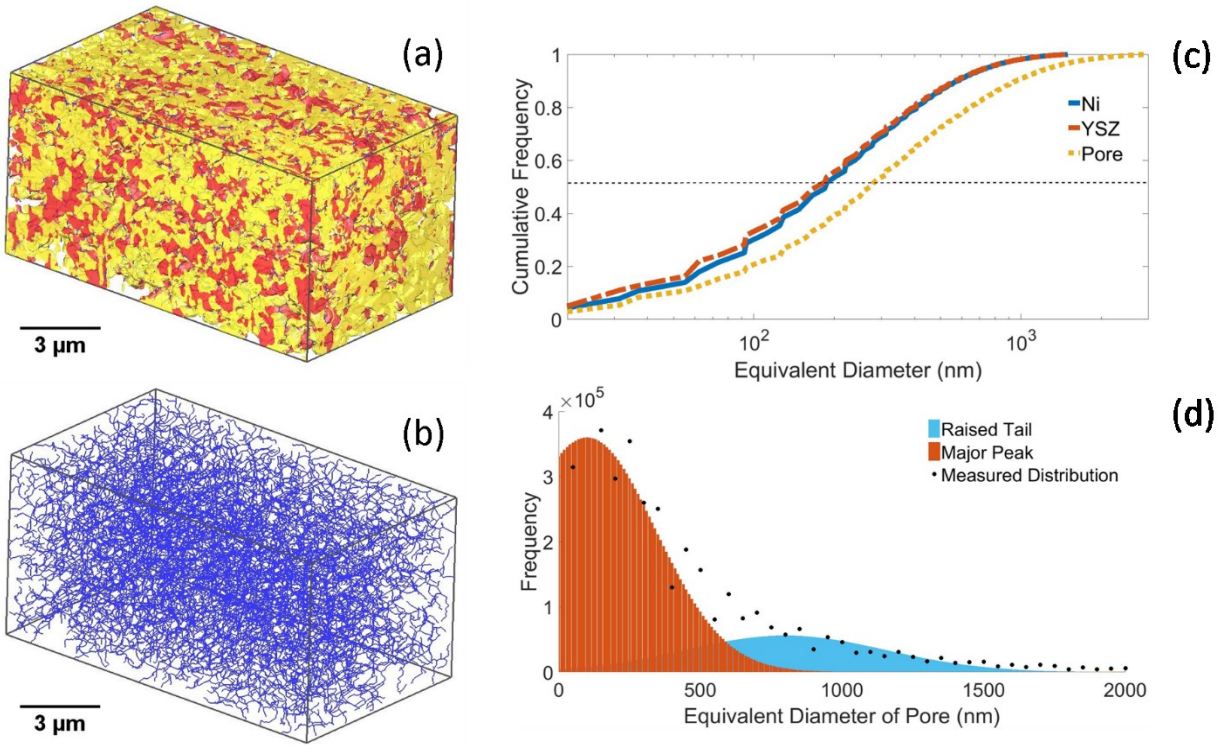


Figure 5.6 3-D reconstruction from FIB-SEM image sequence. (a) 3-D reconstructed volume of the Ni-YSZ electrode. The red region represents Ni and the yellow region YSZ. Porosity is represented as transparent hollow space. (b) Percolated TPB network inside the 3-D reconstructed volume. (c) Cumulative frequency curves for the equivalent diameter for the three phases, Ni, YSZ and pores measured from the 3-D reconstructed volume. The average particle sizes are determined from the 50th percentile (indicated by the dotted line). (d) Frequency distribution of the pore size, showing a major peak at approximately 200 nm and a raised tail at 1000 nm.

From the 3-D reconstruction, the percolated (active) TPB densities were measured as described in [199], by counting the points neighbouring pixels of three different phases and applying a smooth factor, and shown in

Figure *5.6*b. The total TPB density was calculated to be 36.2 μm^{-2} and the percolated TPB density was calculated to be 11.1 μm^{-2}. Literature values of TPB densities of other Ni-based cermet electrodes are summarised in Table 5.1. The percolated TPB density in this electrode is approximately 3 times the values reported for typical conventional Ni-YSZ electrodes and is comparable to the high TPB electrode made by impregnation.

Table 5.1 TPB densities of Ni-based porous cermet electrode

Materials	Fabrication	Active TPB (μm^{-2})	All TPB (μm^{-2})	Source
Ni-YSZ	screen printing of commercial power or ink	2.49		[200]
		8.15	12.99	[201]
		1.66	2.56	[162]
		~3.97	3.97	[135]
	pressed pellet of NiO-YSZ	5.39	10.58	[202]
	colloidal deposition technique	4.28		[203]
	phase inversion technique	6.40		[204]
Ni-CGO	Impregnation	N/A (no percolating Ni)	18.4	[60]
Ni-ScSZ	19 times impregnation	19.77		[156]

The particle sizes, indicated by their equivalent diameters, of the three phases are determined quantitatively from the cumulative frequency curve (

Figure *5.6*c) as 180 nm for Ni, 170 nm for YSZ and 310 nm for pores. In

Figure *5.6*c, 99% of Ni and YSZ "particles" are found to be less than 1 µm in diameter. The pore size frequency distribution is plotted in

Figure *5.6*d. The majority of the pores are 100-500 nm in diameter, but a noticeable raised tail at 1000 nm confirmed the presence of a number of micron-sized pores.

5.2.3 Electrochemical Characterisation and Modelling

The in-plane conductivity of the Ni-YSZ electrode was 1390 S cm^{-1} at room temperature, which is mainly the electrical conductivity of the nickel phase. The room temperature conductivity of pure Ni is approximately 1.4×10^5 S cm^{-1} [205] and hence the relative conductivity of the Ni in the electrode is 0.010. Hong et al. [206] reported that the electrical conductivity of conventional Ni-YSZ cermets varied from 500 S cm^{-1} to 14000 S cm^{-1} depending on the processing conditions and Ni content. The electrical conductivity of the Ni-YSZ cermet in this study is hence considered satisfactory for the electrode function with the nickel paste current collector used in the electrochemical experiments.

An impedance spectrum at 800 °C in humidified 5% H_2- N_2 is shown in Figure 5.7a and the total polarisation resistance is 0.56 Ω cm^2. Two different processes can be seen from the two distinctive peaks in the frequency plot in Figure 5.7b, one at a low peak frequency of 4 Hz and another at a higher peak frequency of 400 Hz. The high frequency response is related to the electrochemical reaction taking place at the TPBs. The low frequency response is associated with either the gas diffusion through the current collector, or a stagnant boundary layer between the current collector and the bulk flowing gas [19]. The diffusion

length l_d of this response is calculated from its characteristic frequency f_d according to Equation 5.1 [207]. The effective binary diffusion coefficient D_{eff} between H_2O and N_2 is 8.91 $\times 10^{-5}$ m^2 s^{-1} at 800 °C is calculated based on 50% porosity of the current collector and Fuller et al. equation [208].

$$l_d = \sqrt{\frac{D_{eff}}{2\pi f_d}} \qquad (5.1)$$

The diffusion length was found to be 1.9 mm which is similar in magnitude to the thickness of the stagnant layer reported by Primdahl and Mogensen [209]. Hence it was concluded that the low frequency response is most likely associated with diffusion in the stagnant gas layer outside the electrode.

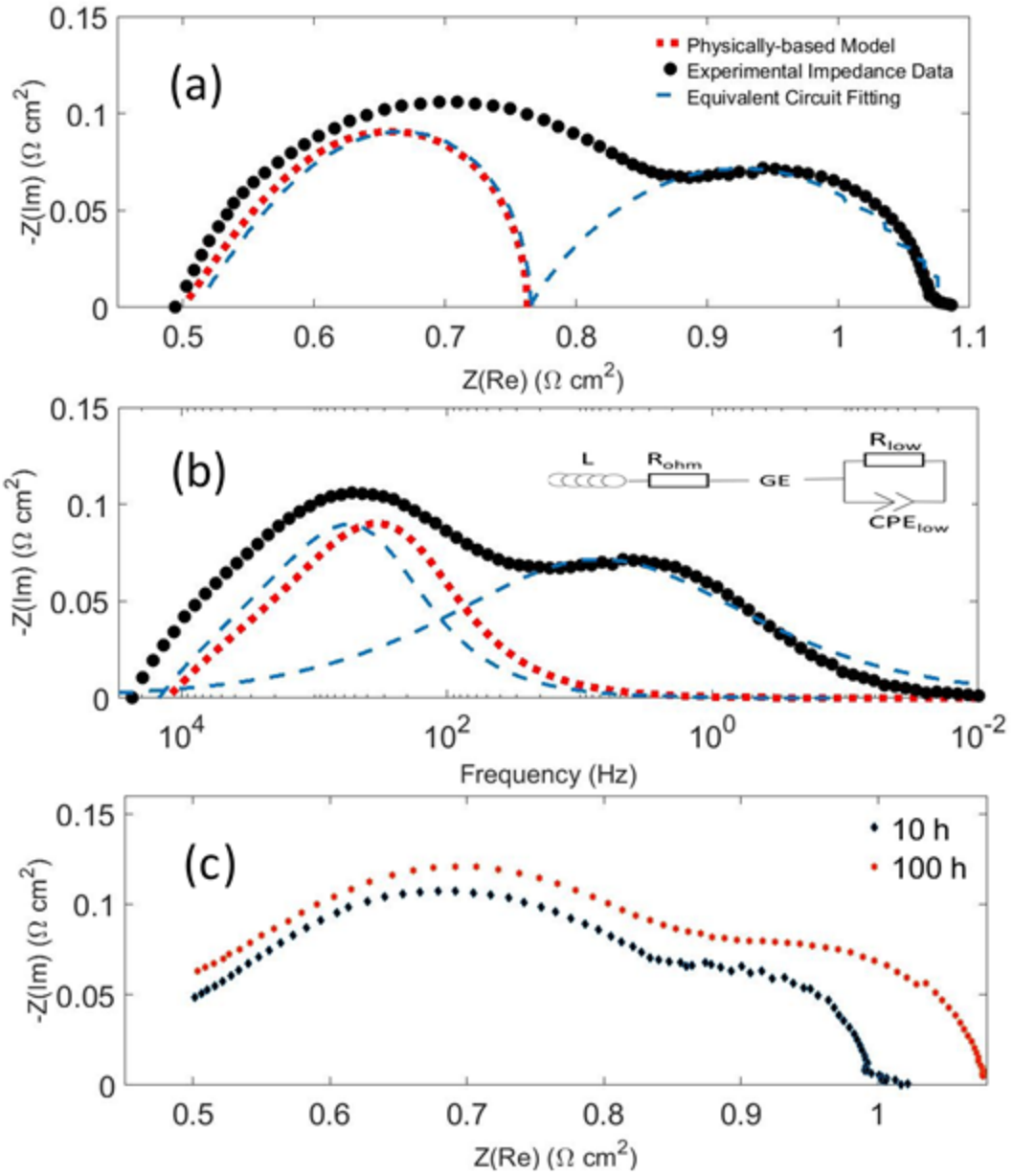


Figure 5.7 Impedance spectra of the nano-composite electrode after being exposed to humidified 5% H_2-N_2 for 60 min at 800 °C and at open circuit, measured from 10 kHz to 0.01 Hz. (a) Nyquist plot compared with the equivalent circuit model (inset) fitting and the physically-based model simulation (b) the Bode plot of the imaginary component (c) the Nyquist plot after ageing for 10 h and for 100 h in humidified 5% H_2-N_2.

A 1-D transmission line physically-based model reported by Bertei et al.[158], similar to that developed by Costamagna et al. [210] and by Paasch et al. [211] was applied to simulate the electrochemical reaction response at the TPBs. In this model the impedance is given by

$$Z = L(\rho_1 + \rho_2)\frac{\cosh(\Gamma) + \Omega[2 + \Gamma\sinh(\Gamma) - 2\cosh(\Gamma)]}{\Gamma\sinh(\Gamma)} \qquad (5.2)$$

$$\text{with } \Omega = \frac{\rho_1\rho_2}{(\rho_1+\rho_2)^2} \text{ and } \Gamma = \sqrt{i_o^v f L^2(\rho_1+\rho_2) + j\omega c^v L^2(\rho_1+\rho_2)}$$

In these equations Z is the complex impedance, L the thickness of the electrode, ρ_1 the effective electronic resistivity and ρ_2 the effective ionic resistivity. The inverse of the effective resistivities, that is, the effective conductivity of Ni σ_{1eff} and effective conductivity of YSZ σ_{2eff} are obtained from the intrinsic conductivity of each phase σ_1 and σ_2 multiplied by their relative conductivities σ_{1R} and σ_{2R} which are controlled by the microstructures of the electronic and ionic phases in the electrode. i_o^v is the exchange current density per unit volume of electrode, f the Faraday constant divided by temperature and universal gas constant, ω the angular frequency and c^v the interface capacitance between Ni and YSZ per unit volume of electrode. The volume specific exchange current density is calculated by multiplying the exchange current density per unit length of TPB i_{oTPB} and the percolating TPB density n_{TPB}. Similarly, the specific interface capacitance is calculated by multiplying the area specific double layer capacitance between Ni and YSZ $C_{Ni/YSZ}$ with the interfacial area of Ni and YSZ per unit volume $A_{Ni/YSZ}$. The microstructural parameters used in this simulation were obtained from the 3-D image reconstruction and are summarised in Table 5.2.

Table 5.2 Physical and microstructural parameters used in the Transmission Line Model of the nano-composite Ni-YSZ electrode

Parameter [unit]	Value	Source
L [m]	15×10^{-6}	cross section SEM
σ_1 [S m^{-1}]	2.32×10^{6}	[186]
σ_{1R} [-]	0.05 ± 0.01	FIB-SEM
σ_2 [S m^{-1}]	3.10	[212]
σ_{2R} [-]	0.08 ± 0.02	FIB-SEM
i_{oTPB} [A m^{-1}]	5.28×10^{-5}	[213]
n_{TPB} [m m^{-3}]	11.1×10^{12}	FIB-SEM
$C_{Ni/YSZ}$ [F m^{-2}]	1.22	[214]
$A_{Ni/YSZ}$ [m^2 m^{-3}]	4.1×10^{6}	FIB-SEM

The exchange current density i_{oTPB} was calculated based on the experimental work of Bieberle et al. [213] and summarized by Kanno et al. [215] as Equation 5.3.

$$i_{oTPB} = 0.0013\, {p_{H2}}^{0.11}\, {p_{H2O}}^{0.67}\, \exp\left(-\frac{0.849 \times 10^5}{RT}\right) \quad (5.3)$$

The exchange current density varies with partial pressures (in units of Pa) of H_2 (p_{H2}) and H_2O (p_{H2O}), as well as the temperature T. In this study, the impedance measurement was carried out in 5% H_2 and 3% H_2O.

The Nyquist and Bode plots in Figure 5.7a and b were also fitted with an equivalent circuit with an inductor, a series resistance, a finite-length Gerischer element and a R-CPE element for the low frequency response. The Gerischer element represents the electrochemical reaction polarisation process in the electrode as expected from the transmission line model.

The equivalent circuit Gerischer element response and the response simulated by the physically-based model, using the microstructural parameters obtained from FIB-SEM 3-D reconstruction, are seen to be in good agreement. The area specific resistance of the electrochemical reaction for the simulation and the equivalent circuit fitting are both 0.26 Ω cm^2, which is better than the ASR of 0.36 Ω cm^2 reported in Chapter 2.1 of a similar nanostructured electrode.

In a real operating SOFC, both the H_2 and H_2O pressures vary with fuel utilisation and are much higher than in the present experiments (50% H_2 and 50% H_2O for example) and consequently the exchange current density will be greater. The predicted electrochemical ASR from the physically-based model with 50% H_2- 50% H_2O is 0.086 Ω cm^2 at 800 °C. This is approximately half of the value, 0.15 Ω cm^2, regarded as a requirement in commercial applications.

A degradation test was carried out by aging the cell in humidified 5% H_2- N_2 at 800 °C for 10 h and 100 h. The impedance spectra after aging are shown in Figure 5.7c and were fitted using the same equivalent circuit. The electrochemical reaction ASR was thus found to be 0.25 Ω cm^2 after 10 h and 0.29 Ω cm^2 after 100 h. This degradation is low in comparison with the rapid degradation observed in nanoscale impregnated Ni-cermet electrodes [156], [212], [127], [132], [216]. The stability of this electrode and its microstructural evolution during high temperature aging will be the subject of the next chapter.

5.3 Conclusions

Fabrication of a nano-scale Ni-YSZ electrode has been achieved by hydrothermally synthesising NiO/YSZ nano-composite particles. Calcination and ball-milling of the freeze-dried slurry from the hydrothermal reactor generates micron-size soft agglomerates of the nanoparticles which are suitable for incorporating into an ink to produce an electrode. The optimal sintering temperature of this nano-composite powder was 1300 °C.

In the nano-composite Ni-YSZ electrode, the Ni particles have an average size of 180 nm and the YSZ 170 nm. The microstructure has porosity at two length scales. There are micron-size denser regions (corresponding to the agglomerates in the milled powder) with internal pores approximately 310 nm in diameter. Separating the denser regions are larger pores approximately 1 µm in diameter. This nano-composite electrode has a Ni loading of 41 wt % and a high percolated TPB density of 11.1 μm^{-2}.

The room temperature in-plane conductivity of the nano-composite Ni-YSZ electrode was 1390 S cm^{-1} and the electrochemical reaction polarisation resistance measured at 800 °C in humidified 5% H_2- N_2 was 0.26 Ω cm^2. The measured impedance response was in excellent agreement with a simulation using a transmission line model and microstructural parameters measured by 3-D tomography of the electrode. From the simulation, an electrochemical reaction ASR of 0.086 Ω cm^2 at 800 °C is predicted in 50% H_2-50% H_2O.

6 Microstructural Evolution of the Nanostructured Co-sintered Nickle Yttria-Stabilised-Zirconia Cermet Electrode

Nanomaterials have attracted attention in SOC electrode engineering for the improvement of electrochemical activity. However, the durability of nanomaterials during the high temperature operations of SOCs is still questionable. Particle coarsening is aggravated by the high surface energy of nanoparticles and undesirably the triple phase boundary and active interface decrease more rapidly. In this chapter, a nanostructured Ni-YSZ electrode is fabricated by formulating mixed nanoparticles of NiO and YSZ into an ink and tape casting. The polarisation resistance of the nanostructured Ni-YSZ electrode is measured while it is being aged at 800 °C in humidified 3% H_2-N_2. 3-D reconstructions of the electrode microstructure after 1 h and 100 h of aging by FIB-SEM are compared to identify the structural changes in nanoscale Ni, YSZ and pore. The microstructural evolution is related to the polarisation resistance by electrochemical modelling. Finally, the enhanced stability of this nanostructured Ni-YSZ electrode is explained by the coarsening behaviours from the 3-D reconstruction.

6.1 Experimental

The nanostructured Ni-YSZ cermet electrodes were fabricated from nanocomposite powder synthesized by CHFS using tape casting as detailed in Chapter 5.1. The cells used in this chapter are fabricated in the same way as those used in Chapter 5. The EIS and van der Pauw measurements were also detailed in Chapter 5.1 but now the EIS measurements were carried out continuously as the cells were being aged at 800 °C. An equivalent circuit model was fitted onto the EIS spectra using Zview and the corresponding distribution of relaxation time graphs were computed based on a Tikhonov regularization with Gaussian function discretization and a regularization parameter of 10^{-2} using the Matlab Plug-in developed by Wan et al.[160]

FIB-SEM 3-D tomography was done on the Ni-YSZ electrode as detailed in Chapter 3.2 and 4.1. The network of each phase is separated into individual particles using a watershed algorithm and the Equivalent Spherical Diameter (D_s) for each particle and the Equivalent Circular Diameter (D_c) for the necks between particles were calculated in Avizo.

6.2 Results and Discussion

The nanostructured Ni-YSZ electrode consists of micron-sized clusters of intermixed Ni and YSZ nanoparticles. The Ni and YSZ particles are of the same length scale, from a few 10's nm to a few 100's nm. The porous clusters of nanoscale Ni and YSZ have neighbouring micron-sized pores as illustrated in the Figure 6.1.

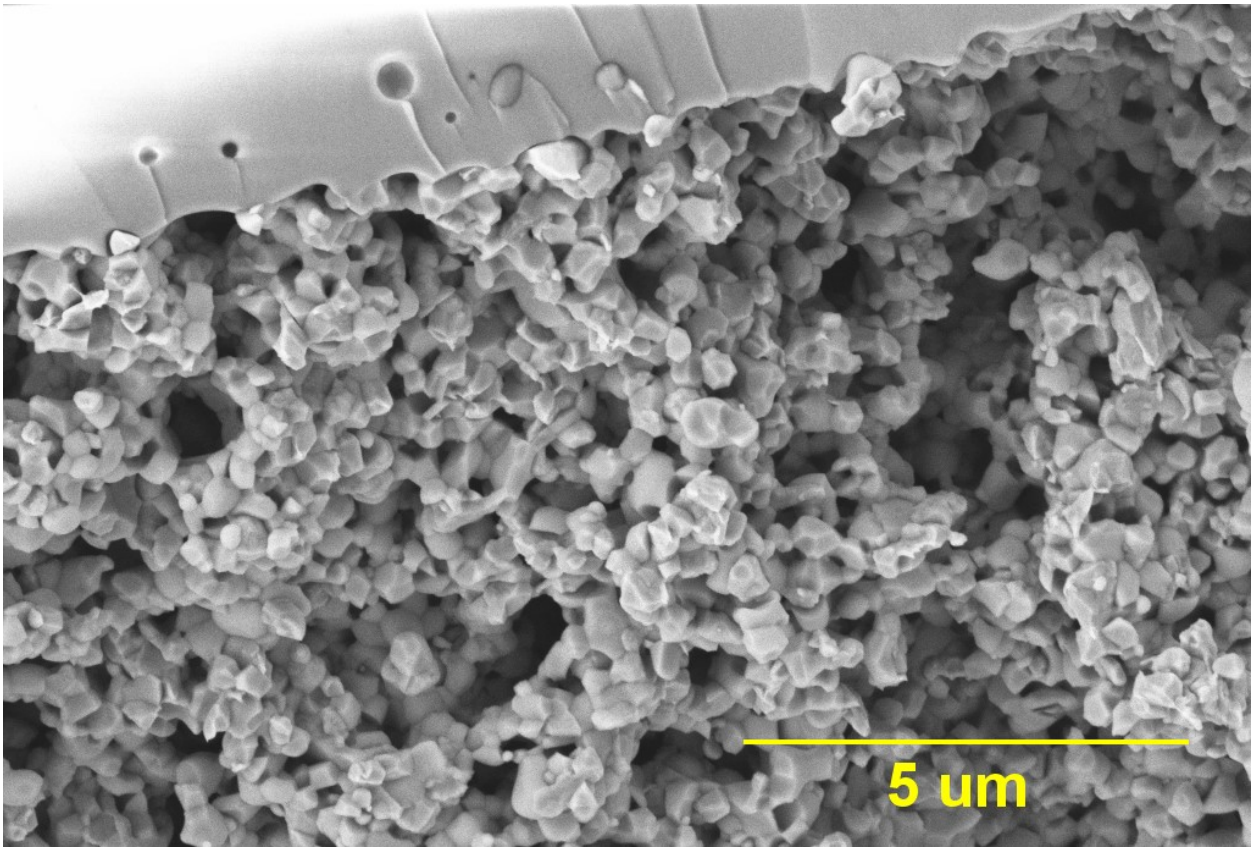


Figure 6.1 Cross-sectional SEM image of the nanostructured Ni-YSZ after 60 min of reduction and aging at 800 °C. The region includes micron-sized clusters of intertwined nanoscale Ni and YSZ network and pores in-between the clusters.

During aging, the total polarisation resistance of the electrode increased from 0.47 Ω cm^2 at 14 min to 1.01 Ω cm^2 at 2010 min and then decreased to 0.87 Ω cm^2 at 6100 min as shown in Figure 6.2. The high frequency intercept on the Nyquist plot in Figure 6.2 is the ohmic resistance from the YSZ electrolyte and the contact resistance of the current collector. The DRT graphs in Figure 6.2 shows the presence of three different polarisation processes. At the high frequency 10 kHz, the peak of the polarisation process R_{high} is partially distorted by the inductive response but in general does not change significantly with aging. The medium frequency response between 100 to 1000 Hz R_{med}, has a pronounced increase from

the beginning of aging till 2010 min and then decreases from 2010 to 6100 min. The low frequency response between 1 to 10 Hz R_{low}, remains relatively constant during aging. High temperature aging of the electrode hence mainly affects the polarisation process R_{med} between 100 to 1000 Hz.

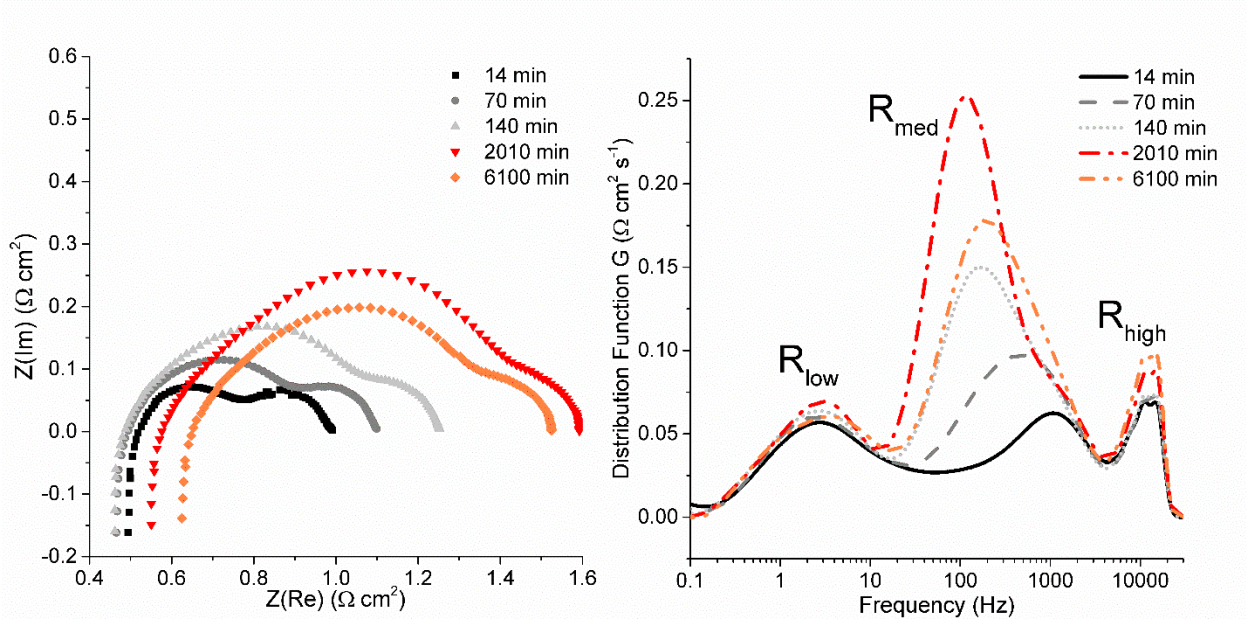


Figure 6.2 The Nyquist plots of the impedance of the symmetrical cell with nano-composite electrodes at 800 °C under open circuit voltage (left) at different aging time and their corresponding distributions of relaxation times (right).

To determine the physical processes responsible for each polarisation resistance, after the cell was aged for 100 h and became was stable at 800 °C, the hydrogen content of the inlet gas was changed. In Figure 6.3a, the low frequency ASR R_{low} decreased as the hydrogen content increased from 5% to 95%, but the medium frequency ASR R_{med} increased instead. The high frequency response R_{high} remained unchanged with gas composition. As the temperature decreased from 800 °C to 700 °C in 5% humidified H_2 in Figure 6.3b, R_{low}

remained constant. Both R_{med} and R_{high} increased with decreasing temperature, with R_{med} increasing more significantly.

The low frequency response R_{low}, sensitive to gas composition but not to temperature, is attributed to the gas diffusion through gas boundary layer on top of the electrode, which was also observed in similar set-ups [156][20][217]. The high frequency response R_{high}, sensitive to temperature but not to gas composition, is associated with the oxygen ion transfer across the electrode and the electrolyte interface. Unfortunately, due to the interference of the inductive signal at high frequency, it is not possible to accurately quantify R_{high} from the DRT in Figure 6.3b. Nevertheless, R_{high} is significantly lower than the other two polarisation resistances and plays only a minor part in the total ASR. The medium frequency response R_{med} is sensitive to both gas composition and the temperature. The increase in R_{med} with hydrogen partial pressure is likely to be caused by the competitive adsorption equilibrium of H_2, H_2O and O on Ni surfaces at the TPBs [218]. The activation energy for R_{med} is calculated in the Arrhenius plot in Figure 6.3c as 1.20 eV, which is similar to the activation energy reported for the electrochemical reaction at TPBs [219][220]. Hence, R_{med} is the polarisation process influence by the microstructural properties of the Ni-YSZ electrode and significant in determining the electrochemical ASR. The impedance spectra were fitted by the equivalent circuit shown in Figure 6.3d, with two R-CPE for the high and low frequency responses and a Gerischer element for the medium frequency response caused by the electrochemical reaction (Fitting result in Table 6.1). Some studies have found that in certain Ni-YSZ electrode, the Gerischer element gave a better fitting than the more commonly used R-CPE component [221][222][158]. The Gerischer element has been widely used in modelling mixed ionic and electronic conductor (MIEC), and explained fully by the Adler-Lane-Steele Model [159] or the TLM model detailed in Chapter 5.2.3. A Gerischer element is suitable for modelling the EIS response of a diffusion process coupled

to a electrochemical reaction [223]. In this work, the unique structure of micrometre cluster of ionic conductor YSZ and electronic conductor Ni leads to an EIS response similar to a MIEC and is well-modelled by a Gerischer element.

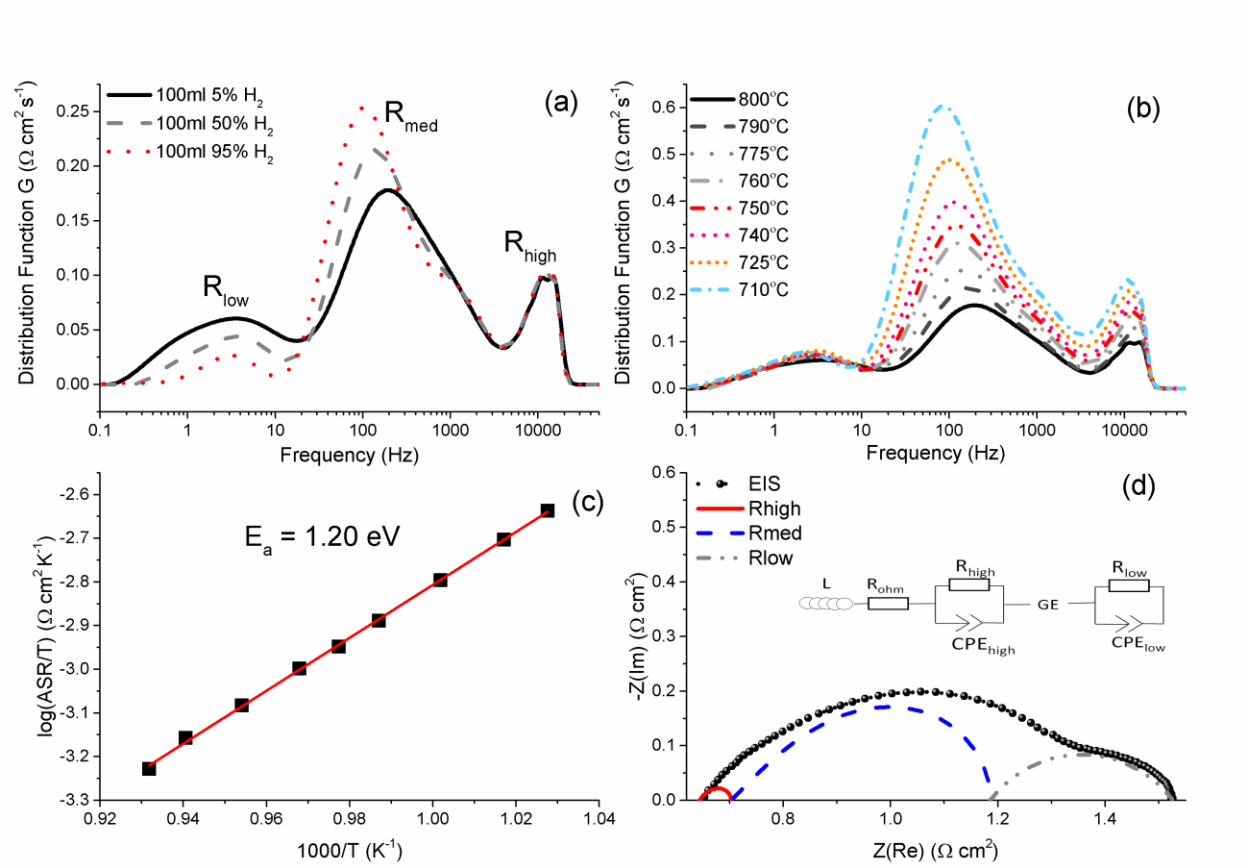


Figure 6.3 DRT of the EIS measurement with varying hydrogen partial pressure (a) and at different temperatures. The Arrhenius plot of the medium-frequency response R_{med} is plotted and its activation energy calculated (c). The impedance spectrum of the symmetrical cell aged for 6100 min at 800 °C in humidified 5% H_2-N_2 in fitted with complex nonlinear least square (CNLS) fitting with the equivalent circuit in the inset (d).

Table 6.1 Values from complex nonlinear least square (CNLS) fitting on the impedance spectrum in Figure 6.3d with the equivalent circuit of two R-CPEs and one Gerischer.

	High Frequency	**Medium Frequency**	**Low Frequency**
Resistance (R)	0.10	0.48	0.34
Capacitance (F)	2×10^{-4}	2×10^{-3}	5×10^{-2}
CPE n exponential	1	N.A.	0.5

Two additional electrodes E1 and E100 were aged at 800 for 1 h and 100 h correspondingly and their room temperature in-plane conductivities were measured as 1400 S cm^{-1} and 180 S cm^{-1}. The decrease in the conductivity by almost one order of magnitude indicated significant change in the Ni network. To monitor the degradation behaviour with time, the variations of % H_2-N_2 for 60 h and another for 600 h are shown in Figure 6.4. During the initial stage of aging, the electrochemical ASR R_{med} increased from 0.17 **Ω** cm^2, to 0.76 **Ω** cm^2 in the first 10 h. However, R_{med} decreased gradually afterwards. The long-term aging shows that after the gradual decrease till approximately 200 h, R_{med} stabilised at 0.15 **Ω** cm^2. The electrodes demonstrated interesting degradation behaviour with a peak ASR at 10 h and a stable ASR in the long run. 3-D microstructure of electrodes E1 and E100 were reconstructed by FIB-SEM as shown in Figure 6.4 to investigate the microstructural changes.

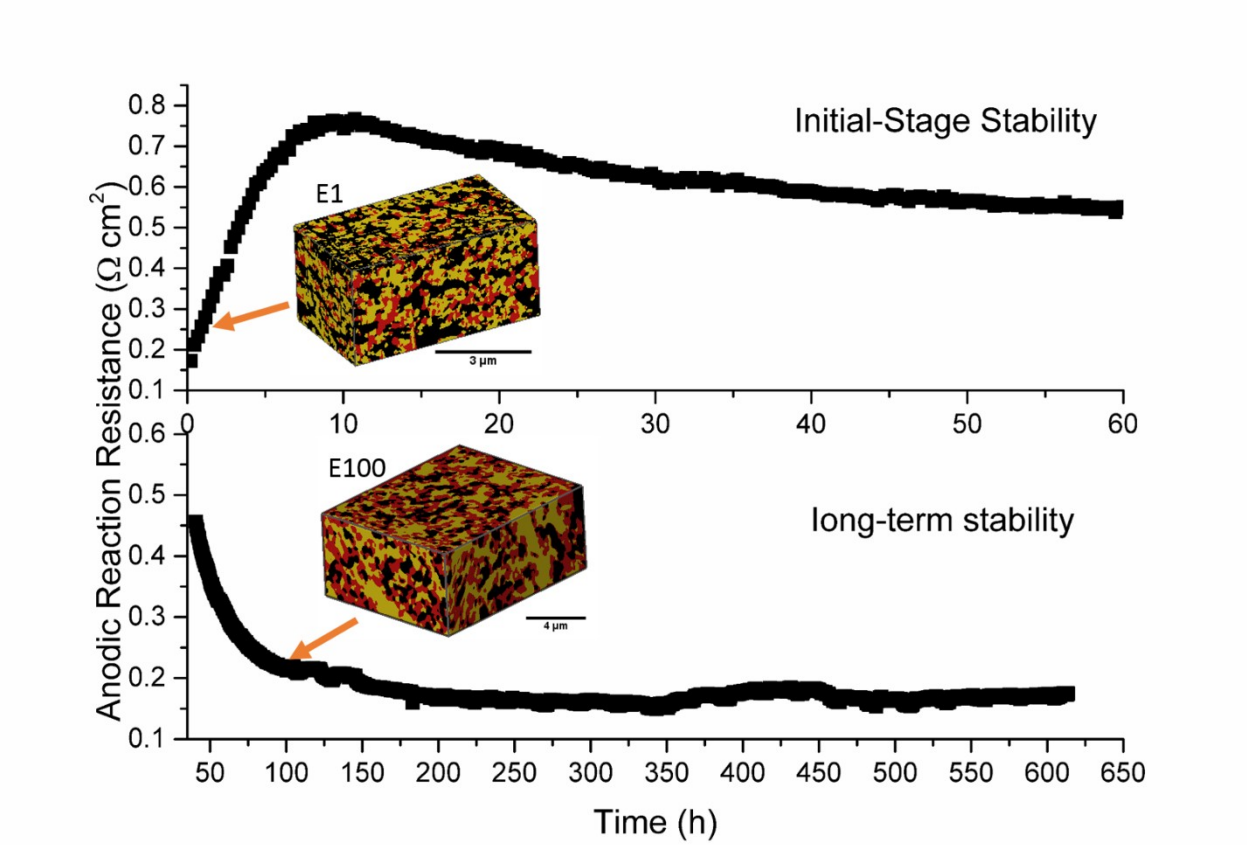


Figure 6.4 The ASR for R_{med} with time for an electrode aged in the short term for 60 h and another aged in the long term for 600 h. The FIB-SEM reconstructions of E1 and E100 electrodes correspond to the high temperature aging time indicated by the arrow.

The FIB-SEM reconstructions of E1 and E100 reveal the difference of particle size distributions of the Ni, YSZ and pore. In Figure 6.5, the peak of the Ni particle diameter distribution has shifted from approximately 50 nm to 400 nm after aging. The distribution curve becomes broader after aging. For the YSZ diameter distribution, the major peak at 50 nm lowers and the minor peak at 300 nm becomes more prominent and shifts towards 400 nm. The pore diameter distribution peak at 50 nm reduces significantly after aging, indicating the disappearance of very fine pores. The distribution curve for pores with a peak at 400 nm, however, has no noticeable change after aging. The neck diameter distributions

in Figure 6.6 show that the Ni neck size is larger for E100, but both the YSZ and pore neck size stay relatively constant. Therefore, both the Ni and YSZ particles coarsened during the high temperature aging as shown in Figure 6.5, but the extent of coarsening is less in YSZ.

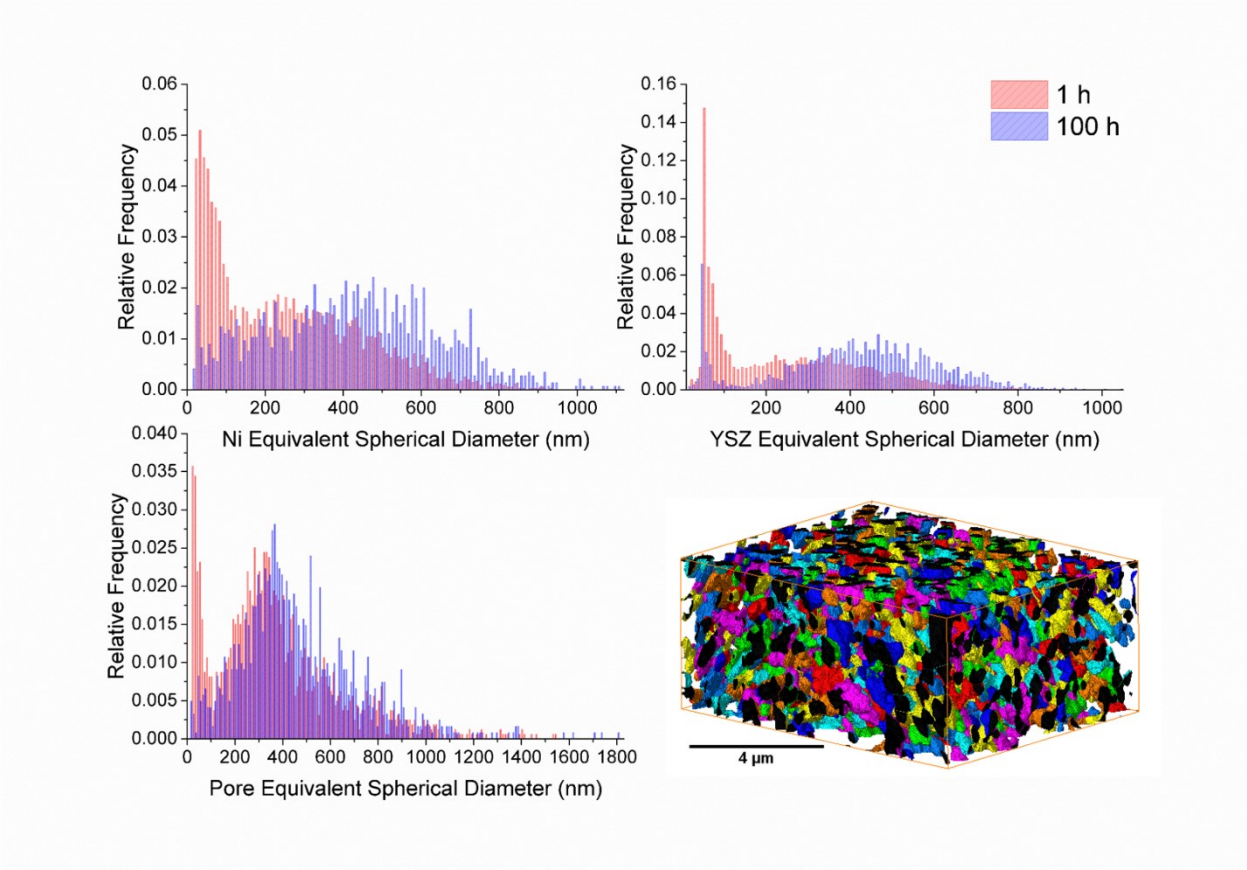


Figure 6.5 Distribution of the particles' equivalent spherical diameters for Ni, YSZ and Pore, with the particles identified by the watershed algorithm. The 3-D volume illustrates the particles identified in the Ni network in E100. Each particle is represented by a different colour to its neighbouring particles.

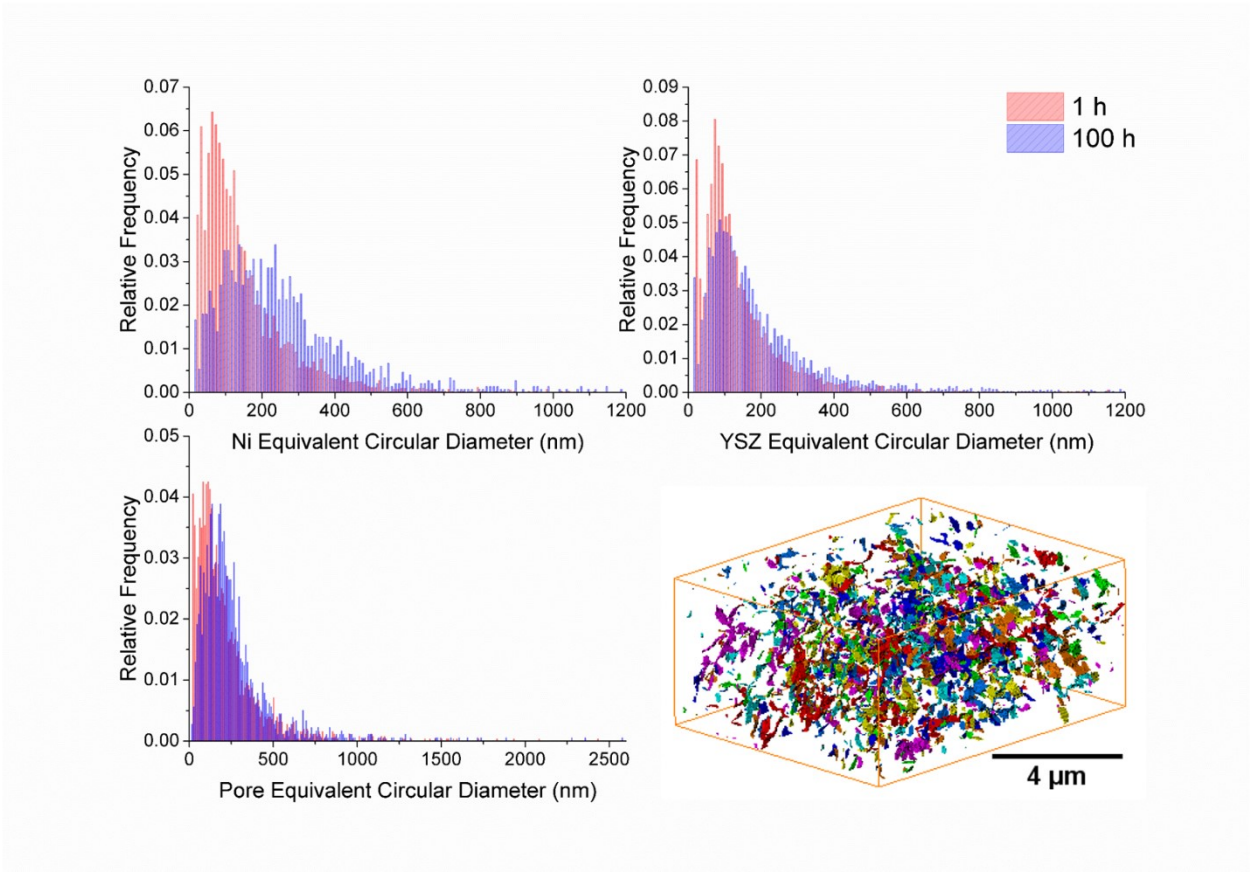


Figure 6.6 Distribution of the neck diameter for the three networks, Ni, YSZ and pore in E1 after 1h aging and E100 after 100 h aging. The necks are the areas shared by neighbouring particles. The 3-D volume visualises the necks, indicated by different colours, in the Ni network in E100.

The general consensus in the fuel cell community is that coarsening of Ni and YSZ are undesirable as it reduces the TPB density of the electrode[224][44]. However, the study by San Pang Jiang on Ni-8 mol% YSZ with an initial size of 0.36 µm, suggested that some extent of coarsening at an appropriate temperature in fact reduced both the electrode ohmic resistance and the polarisation resistance due to improved particle contact [225], though their coarsening temperature was 1300 °C, much higher than the temperature in our study. Ni coarsening has been frequently reported in the literature while YSZ has been regarded

as a stable support structure. However, in this nanostructured electrode, sintering of YSZ was observed at a relatively low temperature of 800 °C qualitatively in Figure 6.4 and quantitatively in Figure 6.5. The initial particle diameter of YSZ of 50 nm is very small and consequently the nanometer size results in high surface energy and a tendency to coarsen at a relatively low temperature.

Table 6.2 Microstructural parameters and electrochemical resistance for electrodes E1 after 1 h of aging and E100 after 100 h of aging.

	E1	E100
Percolated TPB density (μm^{-2})	13 ± 2	10.0 ± 0.3
Ni-Pore interfacial area (μm^{-1})	1.8 ± 0.2	0.4 ± 0.1
Ni-YSZ interfacial area (μm^{-1})	3.8 ± 0.5	3.0 ± 0.3
YSZ-Pore interfacial area (μm^{-1})	2.8 ± 0.2	3.2 ± 0.3
Tortuosity of Pore	3.0 ± 0.1	3.5 ± 0.3
Tortuosity of Ni	5.5 ± 0.1	9.5 ± 0.5
Tortuosity of YSZ	4.5 ± 0.3	2.8 ± 0.3
Volume Fraction of Pore	0.40 ± 0.01	0.36 ± 0.02
Volume Fraction of Ni	0.27 ± 0.01	0.29 ± 0.02
Volume Fraction of YSZ	0.32 ± 0.01	0.34 ± 0.05
Measured R_{med} (Ω cm^2)	0.26	0.20
Predicted R_a (Ω cm^2)	0.22 ± 0.02	0.20 ± 0.01

The microstructural parameters of E1 and E100 are compared in Table 6.2. Error estimation was done by calculating the standard errors from the image stacks of the same sample regions segmented with three different input selections during machine learning

segmentation. The percolated TPB density, decreased from 15.8 to 10.0 μm^{-2} after aging. However, the TPB density is still considered high even though it reduced by 37 %. The interfacial area between Ni and the other two phases decreased, especially the Ni-Pore interfacial area which decreased by 3 times. This suggested Ni has coarsened during the high temperature aging. The increase of YSZ-pore interfacial area from 3.0 to 3.5 μm^{-1} indicated the Ni coarsening is more significant than YSZ, as Ni coarsening exposed more surface area of YSZ to pore space than the YSZ surface reduction due to its own sintering. Meanwhile, the small extent of Ni-YSZ interfacial area decrease implies the interaction between the two phases during microstructural re-arrangement resulted in a relatively constant contact area. While the tortuosity of Ni increased after aging, the tortuosity of YSZ halved instead. Sintering in Ni led to break up in Ni network but sintering in YSZ led to enhanced connectivity. The pore network remained relatively unchanged. However, the reduction of volume fraction of pore suggests the electrodes densified after aging.

In a porous Ni-YSZ electrode, the electrochemical reactions take place at TPBs. Electron transport along Ni is fast and as the pore structure has not changed with time, the transport of gaseous species is not much influenced by high temperature aging. It is hence likely that the diffusion of oxygen ions in the YSZ network is a significant factor. The electrochemical reaction resistance R_a (corresponding to the experimentally measured R_{med})was simulated from the microstructural parameters obtained by FIB-SEM in Table 6.2 , by a physically-based model modified from the work of Paasch et al. [226].

The exchange current density per unit volume is the multiple of the exchange current density per unit length of triple phase boundary (TPB) i^o_{TPB} and the length of TPB per unit volume n_{TPB} in the TPB electrode. The effective ionic resistivity can be written as the

reciprocal of the effective ionic conductivity σ_{ion}. Hence, the DC area specific resistance R_a is expressed in Equation 6.1.

$$\frac{1}{R_a} = \left(\frac{zF}{RT}(i^o_{TPB} n_{TPB})\sigma_{ion}\right)^{\frac{1}{2}} \qquad (6.1)$$

The model assumes the thickness of the electrode is larger than the characteristic active depth. In Equation 6.1, i^o_{TPB} is taken as 5.28×10^{-5} A m^{-1} [102] at 800 °C in this testing atmosphere. The term (i^o_{TPB} n_{TPB}) is associated with the electrochemical reaction. The ionic conductivity of YSZ σ_{ion} is responsible for the diffusion and is calculated by the intrinsic YSZ conductivity 0.031 S cm^{-1} at 800 °C, corrected by its tortuosity and 33% volume fraction in the electrodes. The predicted R_a had excellent agreement with the measured R_{med} as shown in Table 6.2.

Because both the TPB density and the tortuosity of the YSZ network change during high temperature aging in this nanostructured electrode, the variation of the electrochemical ASR with time is a result of the two effects combined. During the first 10 h of aging, the decrease in TPB density was dominant as nickel nanoparticles coarsened rapidly and hence an initial rapid increase in R_{med} was observed. Afterwards, the effect of YSZ nanoparticle sintering took over and the improvement in effective ionic conductivity led to a gradual decrease in R_{med}.

The microstructure of E100 is analysed further in Figure 6.7 with both 2-D image with phase contrast and 3-D reconstructed volume. The contact angles between Ni and YSZ measured in Figure 6.7a range from 100 ° to 150 °. Most of the bright nickel particles are surrounded by the grey YSZ phase, with fractions of the edge exposing to pore. This is more evident in Figure 6.7b, where the Ni network is contained within the YSZ network. In Figure 6.7b, the sintering of Ni appears to be hindered when the easily accessible pore space

in the nanoscale YSZ network is filled and the Ni reached bottle-necks of the YSZ framework and formed high contact angles.

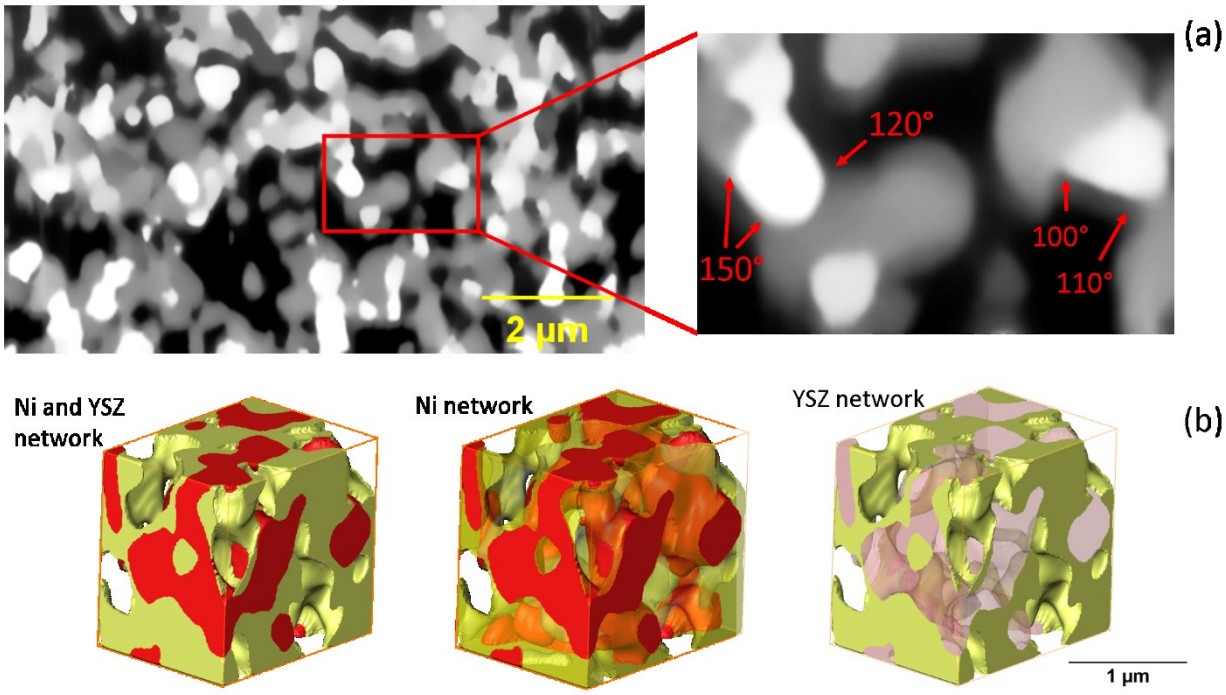


Figure 6.7 The morphology of the electrode E100 after 100 h of aging. The FIB-SEM image in (a) shows nickel as the bright phase, YSZ as the grey phase and pore as the dark phase. The contact angles between Ni and YSZ at TPBs within the region reframed in red are measured. The 3-D reconstruction of a selected region in the electrode is shown in (b), with the nickel network in red and YSZ network in yellow. The first 3-D image on the left shows both phases, while the second image shows primarily the Ni network (with the YSZ phase made translucent) and the third image the YSZ network.

Constant interfacial surface area between Ni and YSZ under operation, reported by Huber et al.[227], suggested the YSZ backbone inhibits the Ni sintering in the cermet. Similar constraint effects were also observed in other Ni-YSZ thermal cycling and annealing studies [148][149][228][125]. In this nanostructured Ni-YSZ electrode, the constraining effect of YSZ

network to Ni sintering is prominent in the closely-packed clusters with the Ni and YSZ of the same nanometer length scale. This morphology stabilised Ni in the long term and maintains the nanoscale features, which explained why R_{med} eventually reached a low plateau of 0.15 Ω cm^2 in Figure 6.4.

6.3 Conclusions

The ASR of nano-structured Ni-YSZ electrodes, with micron-sized clusters where nanoscale Ni and YSZ network entangled, were measured using impedance spectroscopy at 800 °C in humidified 5% H_2- N_2 during annealing. Three physical processes with different relaxation times were observed and the response at 100 Hz, with an activation energy of 1.20 eV, was associated with the electrochemical reaction in the nano-structured electrode. The electrochemical reaction resistance varied significantly with time, increasing rapidly from 0.17 to 0.76 Ω cm^2 in the first 10 h, but decreasing to 0.15 Ω cm^2 at 200 h. Afterwards, the electrochemical reaction resistance stayed constant at 0.15 Ω cm^2 to 600 h.

3-D reconstruction of FIB-SEM image stacks from two electrodes E1 and E100, aged for 1 h and for 100 h correspondingly was built to extract microstructural information. The percolated TPB density was lower at 10.0 µm^{-2} for E100 than 15.8 µm^{-2} for E1. The Ni-YSZ and Ni-pore interfacial areas both reduced as a result of 100 h aging but the YSZ pore interfacial area increased slightly. The YSZ tortuosity also decreased from 4.34 to 2.44. Particle diameter distributions showed both the Ni and YSZ became bigger from 50 nm to a few 100 nm but the pore structure remained relatively unchanged. The strong correlation between the electrochemical reaction ASR and the microstructural parameters in a physical

model suggests that the TPB density and effective ionic conductivity are the two determining factors for the performance of this nanostructured electrode. In E100, Ni was also found to form high contact angles with the YSZ surface at the bottlenecks of the nanoscale YSZ network. The coarsening of Ni is slowed down by the constraints in the more stable YSZ network during long-term aging.

This chapter demonstrated the encouraging durability of this nano-structured Ni-YSZ electrode with both Ni and YSZ particles in 10-100 nm scale. The 3-D analysis in line with electrochemical measurement highlights the potential to minimise Ni coarsening by microstructural engineering.

7 Co-sintered Nanoscale Nickel Gadolinia-Doped-Ceria Electrode

In this chapter, nanostructured Ni-CGO electrodes co-sintered from nano-composite particles are fabricated, characterised and investigated for degradation under annealing. The electrode was aged at 800 °C in humidified 5% H_2-N_2 while the impedance spectra were recorded continuously. The initial and post-test microstructures were imaged by FIB-SEM and 3-D reconstruction was carried out to extract structural information, for example TPB and DPB densities. The focus is to understand how the microstructural changes during annealing influence the polarisation resistance of the nanostructured Ni-CGO electrode.

7.1 Experimental

The composite powders of NiO and CGO were synthesized via CHFS by Dr. Paul Boldrin [101]. The nanocomposite particles were washed thoroughly and dried in air. The dried particles were calcined at 600 °C for 2 h and then ball milled for 24 h at 300 rpm. The electrodes were made as detailed in Chapter 5.1.2 with a sintering temperature of 1300 °C and a sintering duration of 2 h. The heating rate was set to a low value of 1 °C min^{-1} and a dwell time of 1 h is set at 800 °C to avoid cracking caused by rapid shrinkage. The particle size distribution, nitrogen adsorption and desorption isotherms and thermal analysis for the as-dried powder and the XRD analysis for the as-calcined powder were also detailed in Chapter 5.1.3.

One batch of symmetrical cells of the electrode as sintered were reduced in humidified 5% H_2-N_2 with a flow rate of 100 ml min^{-1} at 650 °C and aged at 800 °C for 180 h till the impedance spectra under open circuit conditions in a two-electrode set-up remained unchanged with time. The H_2 partial pressures were then varied from 5% to 95% and the temperature from 800 °C to 700 °C to record the impedance spectra in the different test environments. The other batch of symmetrical cells were also reduced in-situ at 800 °C and then monitored by impedance spectroscopy to trace the trend of degradation during isothermal annealing. The distributions of relaxation times were calculated by the Tikhonov regularization with Gaussian function descretisation based on the programme developed by Wan et al.[160]. The regularization parameter was set as 10^{-2}. SEM images were taken at an accelerating voltage of 5 kV. FIB-SEM imaging and 3-D reconstruction were carried out as detailed in Chapter 3.2 and 6.1.

7.2 Results and Discussion

The as-dried composite powders were measured by dilatometry and DSC/TGA to determine the thermal properties. The shrinkage rate in Figure 7.1a shows the onset of sintering starts as early as 290 °C. The sintering at 290 °C corresponds to the endothermic peak observed in DSC in Figure 7.1b. At this temperature, the chemisorbed water on the powder as a result of the hydrothermal flow synthesis evaporated and caused a shrinkage and mass reduction. Between 500 to 1000 °C, there is a gradual shrinkage over a large temperature range. The major sintering takes place at 1300 °C, though the sintering process spans over a wide temperature range of approximately 400 °C as shown in Figure 7.1a. The sintering of NiO-CGO happens continuously over the temperature range between 200 to 1500 °C

instead of being triggered by a specific temperature. Hence, to avoid cracking due to the continuous shrinkage, the heating rate must be sufficiently low when the composite powders are being sintered. In Figure 7.1b, the mass of the composite powder decreases during heating and stabilises at 600 °C. To completely remove the residual water and nitrates, the as-dried NiO-CGO powder was calcined at 600 °C.

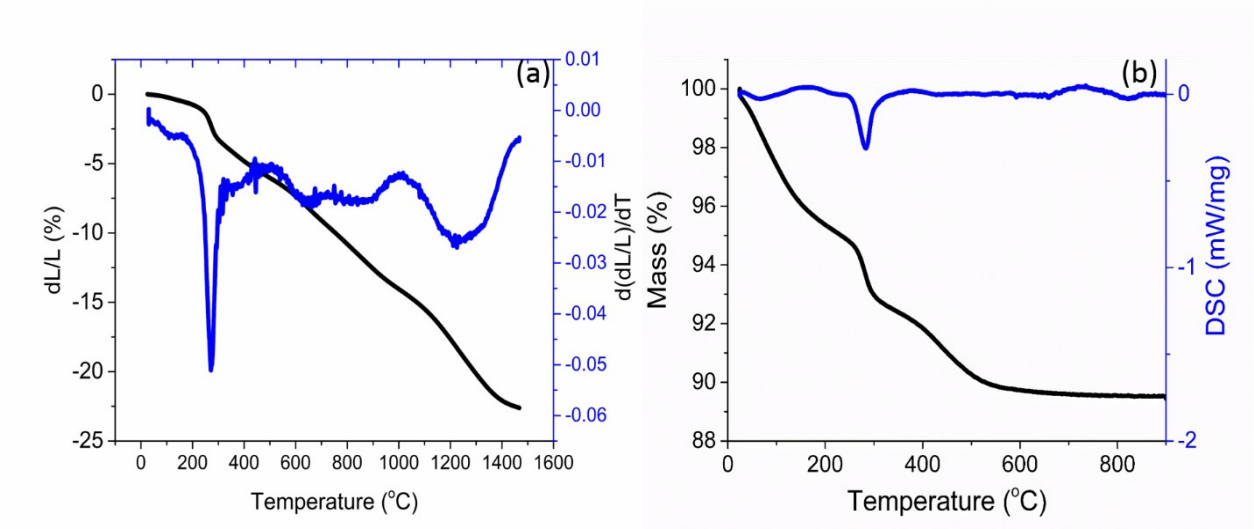
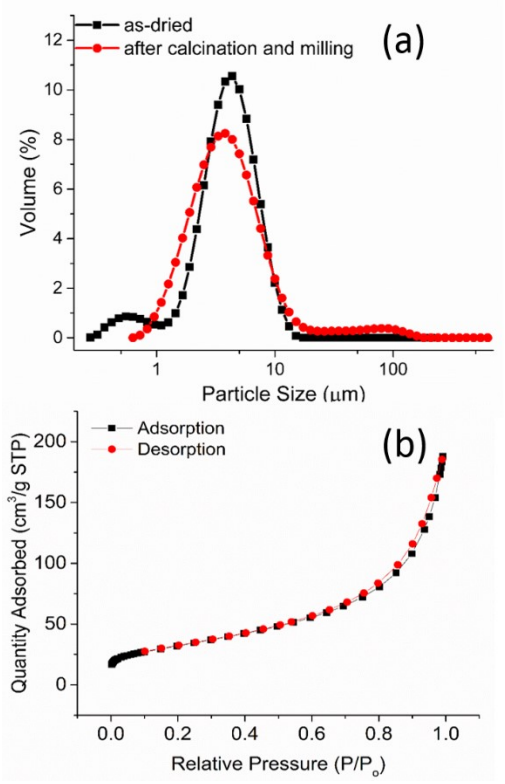


Figure 7.1 thermal properties of the composite NiO-CGO powder. The sintering behaviour is shown in (a) the shrinkage and rate of shrinkage during constant-rate heating measured in dilatometer of a pressed green pellet using the as-dried powder. The mass change and the endothermic reaction were shown in (b) by DSC and TGA.

As the calcination causes some degree of agglomeration, the calcined powder was ball milled for a day to break up the large agglomerates. The particle size distribution of the final powder is similar to the initial as-dried powder as shown in Figure 7.2a, with the majority of the particles falling within 1-10 µm in diameter. The volume weighted mean diameter for the particles are 7 µm for both the as-dried and after-calcination-and-milling powders. The surface area of the powder was calculated from the isotherms in Figure 7.2b by the BET

theory as 111.2 m^2 g^{-1}. The t-plot method determines that 8.8 m^2 g^{-1} of the surface area is from the internal surface of micropores (< 2nm). The BET surface area for the as-dried powder was 158.7 m^2 g^{-1} and hence the calcination treatment has decreased the specific surface area by 30%. Despite the surface area reduction, the surface area of the final Ni-CGO powder is still very large as compared to the typically 10 m^2 g^{-1} commercial powders and the reported values for high-surface-area Ni-CGO powders [139][229][230]. After calcination and milling, the initial nanopowders in aqueous slurry, which were 1-10 nm in diameter, have formed agglomerates in Figure 7.2c. Each 'particle' in the final powder is a micrometer-scale composite agglomerate of the NiO and CGO nanoparticles.



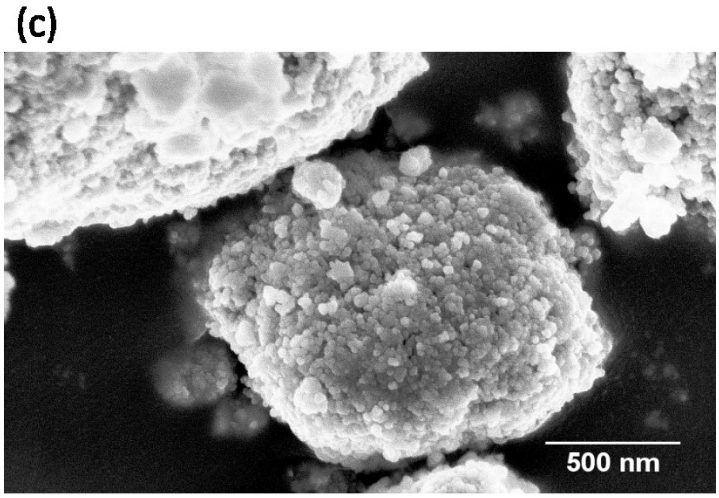


Figure 7.2 particle size and surface area measurement. The volume-weighted particle size distributions (in diameter) in (a) are plotted for the initial powders as-dried and the final powders after calcination and ball milling. The adsorption and desorption isotherms on N_2 for the final powder is plotted in (b). The SEM image in (c) shows a typical particle of the final powder sprinkled on the conductive carbon tape.

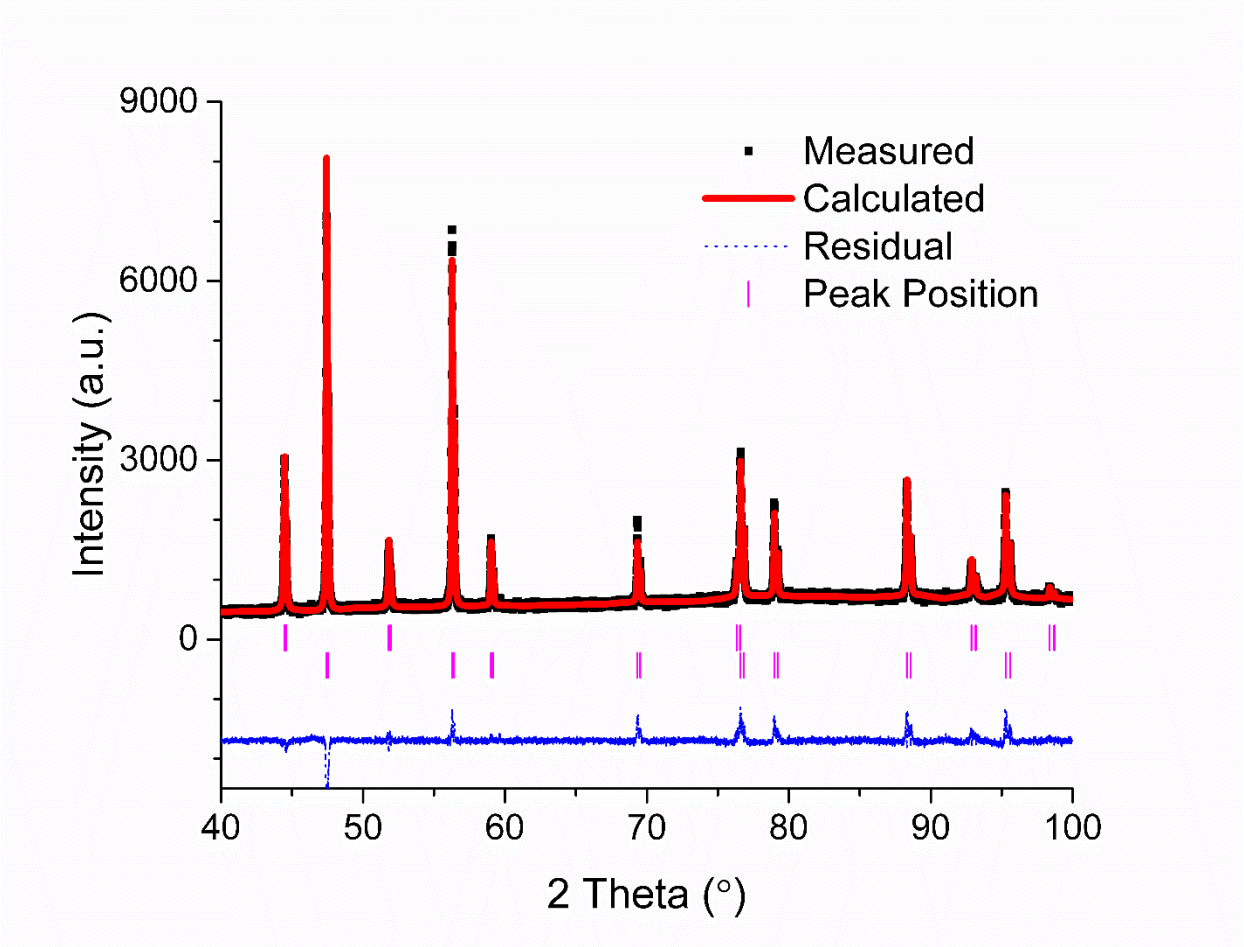


Figure 7.3 The XRD pattern corresponds to the Ni-CGO electrode cast on a YSZ substrate after the electrode was sintered at 1300 °C and reduced at 800 °C. The Bragg reflections belong to Ni (Cubic) marked in the first row of peak positions and $Ce_{0.9}Gd_{0.1}O_{1.95}$ *(Cubic) in the second row. The measured data are drawn with black dots, the calculated profiles in red lines and the difference between the two in blue lines.*

The micrometre particles comprising intermixed NiO and CGO finer particles (10 nm) are then formulated into an ink, cast, sintered and reduced to Ni-CGO electrodes on YSZ electrolytes. The Ni loading of the final powder was measured as 28.8 wt% by the mass change of a sintered pellet in the oxidised state with NiO and reduced state with Ni. Rietveld refinement was also done on the XRD pattern of the final electrode with Ni and

$Ce_{0.90}Gd_{0.1}O_{1.95}$ (CGO10) (Figure 7.3) and reported a Ni loading of 29.9 wt%, close to the value determined by mass measurement. The cross section of the electrode was imaged by FIB-SEM in a series of consecutive slices and Figure 7.4a is an example of an image slice. The image stack was segmented based on the phase contrast between Ni, CGO and pore as shown in Figure 7.4a and assembled into a 3-D volume of the porous Ni-CGO electrode as shown in Figure 7.4b. From the 3-D volume, it is confirmed that Ni and CGO in the porous electrode are interpenetrating to each other and the 'particles' are mostly in the scale of a few 100 nm. Within the reconstructed volume, the percolating DPB and non-percolating DPB can be extracted as illustrated in Figure 7.4b.

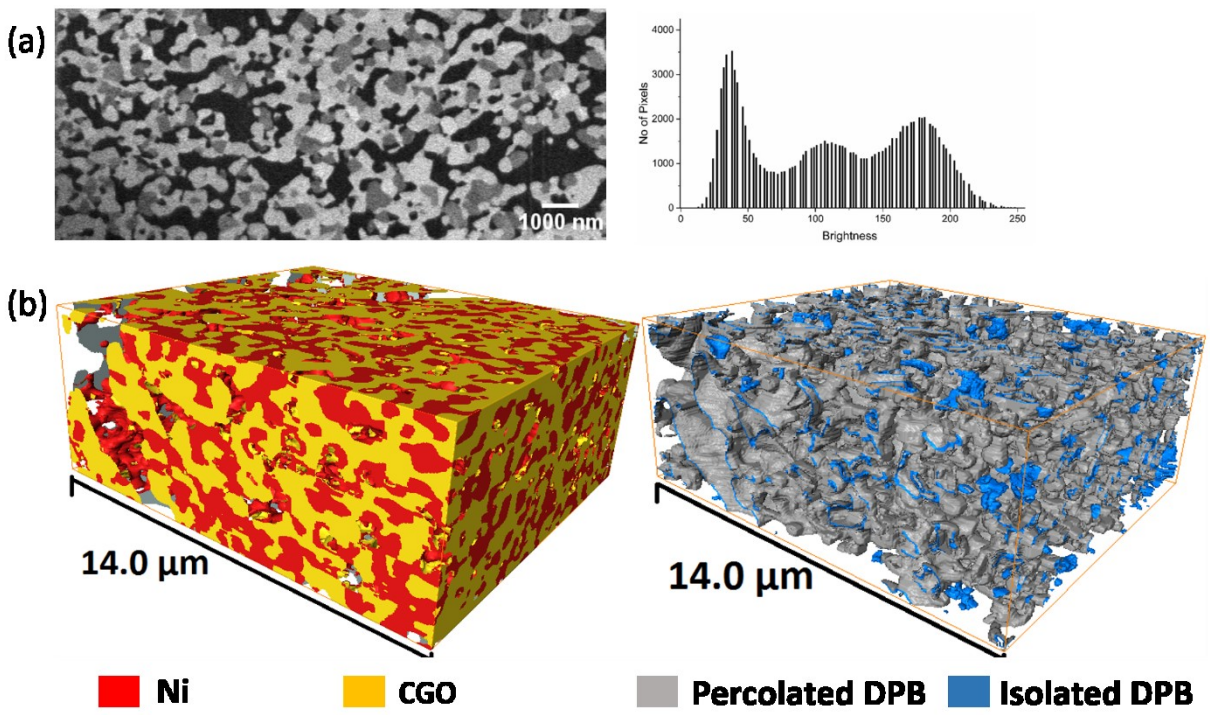


Figure 7.4 FIB-SEM 3-D reconstruction of the porous Ni-CGO electrode. The original FIB-SEM image taken by back-scattered electrons in (a) shows the phase contrast for Ni, CGO and the resin-filled pore. The CGO appears to be very bright, followed by Ni and lastly the resin is the darkest. The image histogram indicates three distinct peaks for the three phases. The consecutive images following (a) were collected and the image stack was reconstructed to the 3-D structure of the electrode in (b). The reconstructed volume on the left shows the intertwined Ni (in red) and CGO (in yellow) in the porous structure. The volume on the right shows the interface between CGO and pore, i.e. the DPBs. The grey network represents percolated DPBs. The blue parts are the DPBs disconnected from the network and become inactive.

The conductivity of the electrode was measured at room temperature by four-point van der Pauw measurement to be 103 S cm^{-1}, which is satisfactory as a fuel cell electrode. A typical Nyquist plot of the symmetrical cells of the Ni-CGO electrode is presented in Figure 7.5d.

The DRT graphs in Figure 7.5a and b show how the impedance varies with different gas compositions and temperatures. Two physical processes were identified in Figure 7.5a, one at 0.2 Hz and another at 6 Hz. The higher frequency response at 6 Hz shows a major peak and a broad shoulder at high frequencies. This peak shape is typical for a Gerischer-type response, where diffusion of oxygen ions and electrochemical reaction at the surface are coupled. In Figure 7.5a, the polarisation resistance R_{low} of the low frequency response at 0.2 Hz decreases significantly as the H_2 partial pressure increases, while R_{high} of the higher frequency response at 6 Hz only decreases slightly. The low frequency response is very likely associated with gas diffusion processes. When the temperature decreases in Figure 7.5b, both R_{low} and R_{high} increase. The activation energy of the two processes are determined in Figure 7.5c. The activation energy is 1.03 eV for the high frequency process and 0.50 eV for the low frequency process. In the literature, the activation energy for electrochemical reaction in Ni-CGO electrode is generally 1-2 eV as reported in [133][231][232]. Hence the high frequency process is likely related to the electrochemical reaction taking place at the DPBs and TPBs based on its activation energy and the Gerischer type behavior often observed in CGO as a MIEC [233][234]. The low frequency process with a relatively low activation energy and high sensitivity to gas composition is very likely related to gas diffusion and other gaseous phase processes. Possible explanations for the origin of this process are as follows.

i) Gas diffusion in the pores. When the pore size is in nanometer scale, Knudsen diffusion is expected to play a role inside the electrode, instead of the bulk diffusion. The gas diffusion in the pore has been observed in Ni-ceria infiltrated Nb-doped $SrTiO_3$ electrode below 100 Hz [235] showing a weak temperature dependence and also in anode-supported cells with a Ni-ScYSZ electrode [193].

ii) Gas conversion/diffusion impedance. The gas diffusion in the stagnant layer on top of the electrode can contribute to polarisation. This is significant with a low gas flow rate[21] and dependent on the test set-up. Previous studies on Ni-CGO electrodes have reported the observation of the gas conversion impedance at low frequency (0.1-1 Hz)[236][237]. However, the gas conversion impedance should show very small activation energy.

In Figure 7.5d, the impedance spectrum of the symmetrical cell was fitted with an equivalent circuit, with a Gerischer element for the high frequency response associated with charge transfer and a R-CPE component for the low frequency response associated with mass transport.

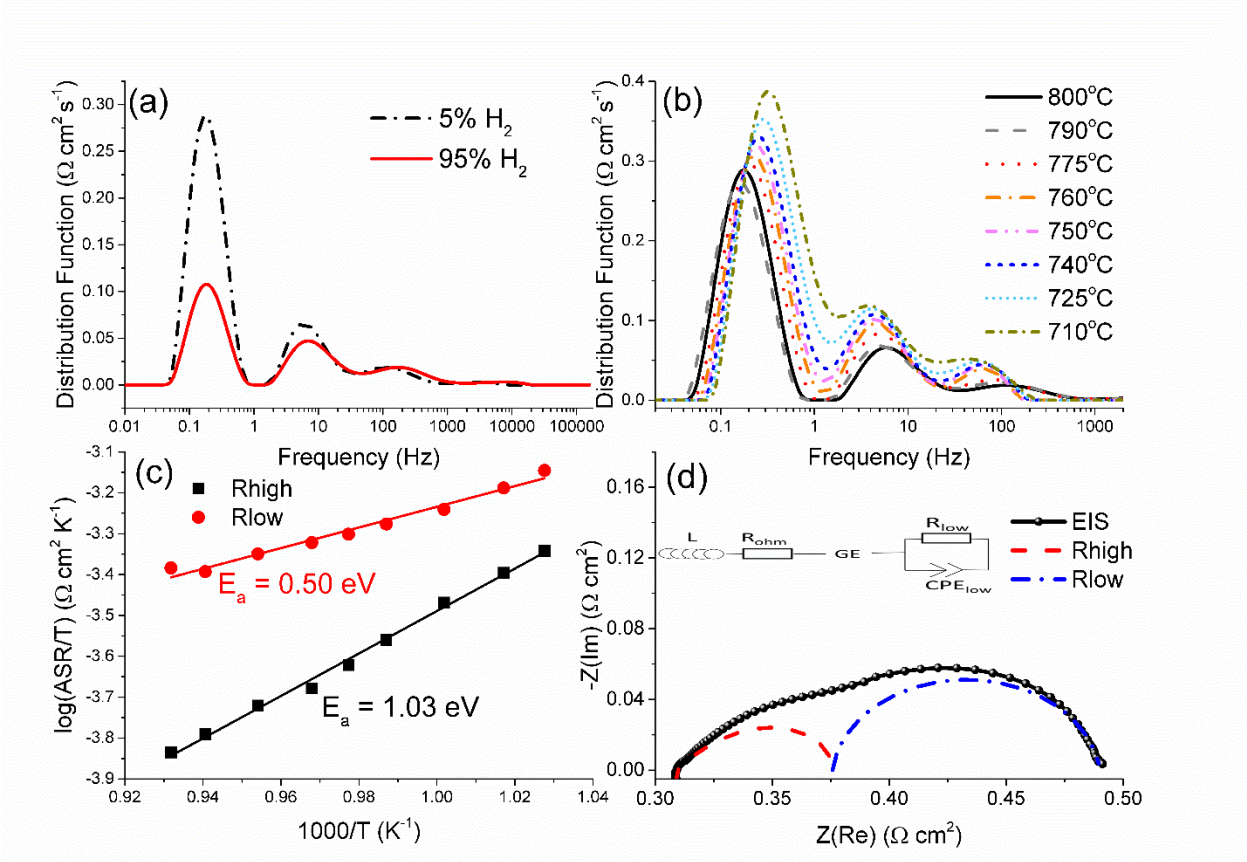


Figure 7.5 Impedance spectra and the corresponding DRT graphs of the symmetrical cells under open circuit conditions at a flow rate of 100 ml min^{-1}. In (a), at 800 °C, the H_2 partial pressure was changed from 5% to 95% and the DRT graphs were plotted accordingly. The temperature of the measurement furnace was varied between 800 °C to 700 °C in humidified 5% H_2-N_2 and the corresponding DRTs plotted in (b). The Arrhenius plot derived from (b) is plotted in (c) and the activation energy of the two different processes taking place at different characteristic frequencies, one between 0.1 and 0.5 Hz as R_{low} and the other between 2 and 10 Hz as R_{high}. In (d), an impedance spectrum (Nyquist plot) at 800 °C in humidified 5% H_2-N_2 is plotted together with the equivalent circuit model (ECM) fitting. The equivalent circuit is shown in the inset in (d).

The symmetrical cell was reduced-in situ and annealed at 800 °C in humidified 5% H_2-N_2 while the impedance spectra were being monitored continuously in Figure 7.6. The low frequency resistance R_{low} varies between 0.12 to 0.13 Ω cm^2. The periodic variation of R_{low} is caused by the water vapour pressure variation during the day because of room temperature fluctuation. Despite this periodic fluctuation, R_{low} remained unaffected by the annealing with time throughout the 4000 min. In contrast, R_{high} is approximately half of R_{low} and experienced a rapid increase in the first 500 min of aging. After the early-stage increase from 0.04 to 0.08 Ω cm^2 in the first 500 min, R_{high} stayed constant at 0.08 Ω cm^2 till 4000 min. Similar trends of polarisation resistances were also shown for the symmetrical cell reduced at 650 °C and annealed at 800 °C in Figure 7.7. After the transient degradation in the first 10 h of aging, the Ni-CGO electrode showed excellent stability during high temperature annealing.

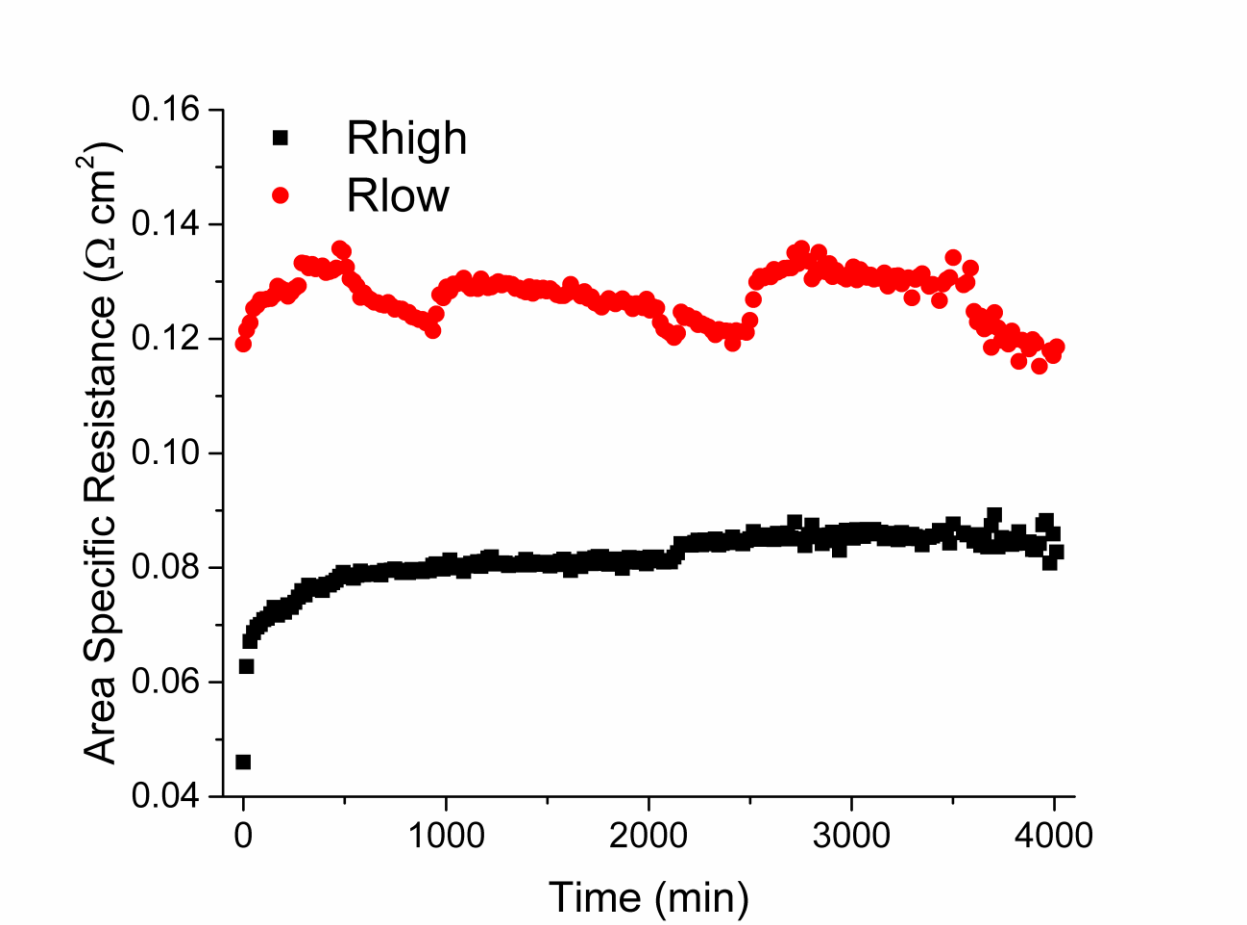


Figure 7.6 Variation of the polarisation resistances at high frequency and low frequency during annealing at 800 °C.

Degradation of the electrode reduced at 650 °C and annealed at 800 °C is shown in Figure 7.7. The polarisation resistances at both the low and high frequencies are much larger than the symmetrical cell reduced at 800 °C in Figure 7.6. The reduction temperature of NiO in the cermet influences the diameters of Ni particles and hence the microstructure of the composite [122]. The influences of the reduction temperatures on the electrochemical performance require ongoing investigations and is beyond the scope of discussion. However, the trends of the polarisation resistance during annealing are similar. The high frequency resistance R_{high} experiences a rapid increase during the first 200 min of annealing and reaches

a plateau of 0.15 Ω cm^2 which is maintained till the end of 10500 min (one week) annealing test. The low frequency resistance R_{low} shows the periodic fluctuation caused by the water vapour pressure variation along with the daily temperature variation. Again, the strong coupling of the water vapour pressure and R_{low} suggests that it may not only be a pure gas diffusion phenomenon, but also a thermally-activation physical or electrochemical reaction involving water vapour. One possibility is that this polarisation process is associated with the electrochemical reactions at the nanoscale pores, where gas access is more restricted and hence is highly sensitive to the water vapour pressure in the gas chamber. The R_{low} also experiences a gentle increase at the early stage of annealing, possibly due to some structural rearrangement in Ni as the temperature is raised to 800 °C, but eventually reaching a relatively constant value of 0.40 Ω cm^2, as the mean value of the daily fluctuations.

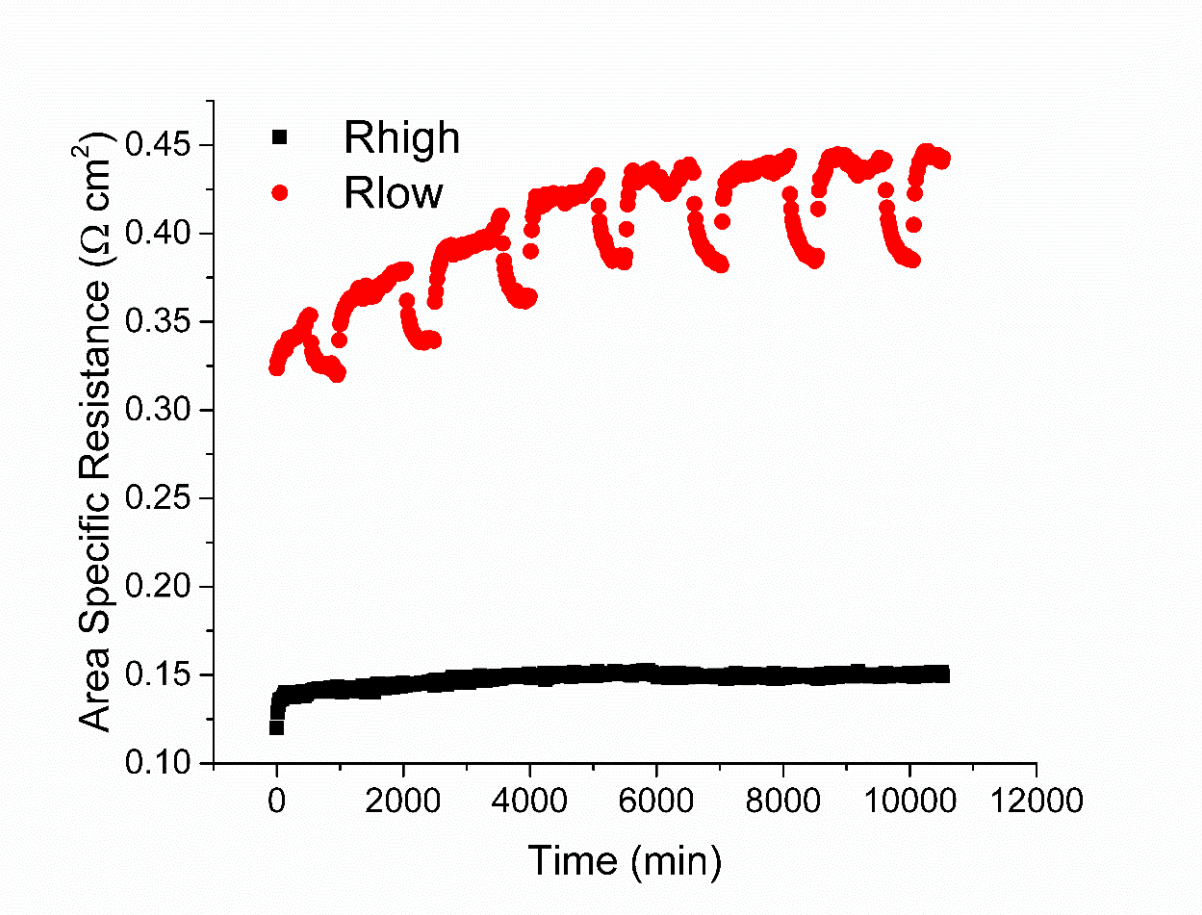


Figure 7.7 The variations of the polarisation resistances at high and low characteristic frequencies with the annealing time is depicted here. The symmetrical cell was reduced at 650 °C for 1 h and heated up to 800 °C for the annealing and impedance measurements in humidified 5% H_2-N_2.

SEM images of two Ni-CGO electrodes aged for 60 min and 4000 min were compared in Figure 7.8. The cross section of the 60-min aged electrode in Figure 7.8a shows distinct morphologic difference between Ni and CGO. The CGO grains appear faceted while the Ni grains appear rounded. Ni grains appear to be sitting in a cavity due to small pore space around them created by the shrinkage when NiO is reduced to Ni. Very fine Ni particles below 10 nm were also present in the cross-sectional images. Those particles are below the

detection limit of the FIB-SEM imaging in Figure 7.4. The EDX mapping on the top surface confirmed that the Ni and CGO networks are intertwined with each other. In Figure 7.8b, the very fine Ni grains are no longer observed after 4000 min of aging. In the dense region captured in the first image on the left in Figure 7.8b, the particles are a few 100 nm in diameter. Morphology difference between the Ni and CGO grains becomes less noticeable. This is very likely to be caused by the Ni growth at 800 °C filling up the small pore space around them. The next two images in Figure 7.8b show the coarsened nickel particles in the porous region. The coarsened Ni particles have grown to 500 - 1000 nm in diameter and remained attached to the dense region. The limited free space in the dense region has resulted in the tendency for the coarsened Ni to bulge out into the neighbouring open pore space.

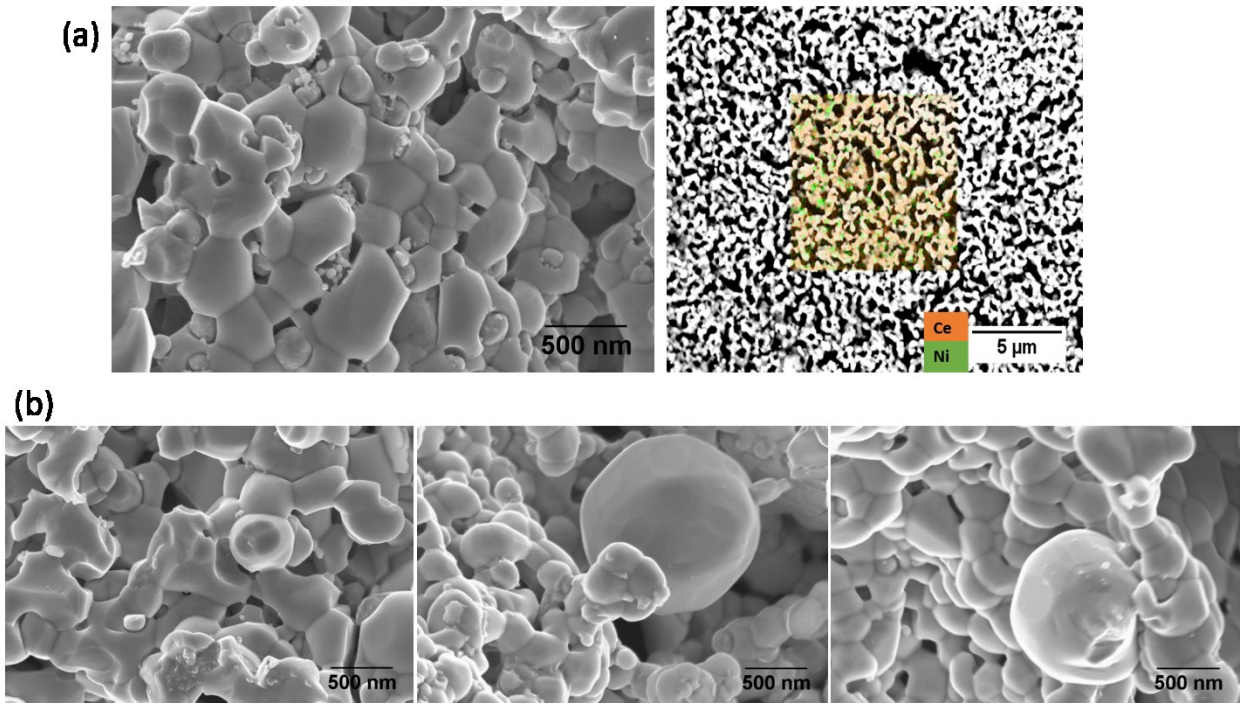


Figure 7.8 SEM images of the electrode after 60 min and 4000 min of annealing at 800 °C in humidified 5% H_2-N_2. The almost pristine electrode with 60 min annealing and in-situ reduction is presented in (a). The image on the left is the cross section of the electrode and on the right is the top surface of the electrode with EDX mapping, where orange indicates Ce and green indicates Ni. In (b) are the cross-sectional images for the electrode with 4000 min annealing and in-situ reduction.

FIB-SEM 3-D tomography was again used to reconstruct the 3-D volume for the porous Ni-CGO electrode after 4000 min of annealing. The active TPB networks in Figure 7.9a for the 60-min aged electrode and 4000-min aged electrode reveal that the reduction of TPB densities is mainly caused by break-up of the TPB network. The density of blue lines in many localised regions have not shown drastic change qualitatively. However, it is noticeable that some regions in the 4000-min electrode are deprived of the blue lines while in the 60-min electrode, the blue lines run through the whole volume. Figure 7.9b shows

that the Ni particles are mostly 100 nm and the CGO particles 50 nm. Though Ni coarsening was apparent in the qualitative observation in Figure 7.8b, the coarsened particles do not reach a substantial number statistically. In Figure 7.9b, there are slight increases for Ni particles about 500 nm after 4000 min of aging, but the increase is of minimal significance. The CGO particle size distribution is not significantly affected by the aging either. The CGO network stays relatively rigid during annealing.

The coarsened Ni particles in this nanoscale Ni-CGO electrode lead to the disconnection of certain regions of TPB networks. Because the number of coarsened Ni particles are relatively small in comparison to the total number of Ni nanoparticles, the TPB density in the well-connected regions has remained relatively unchanged after annealing in Figure 7.9a.

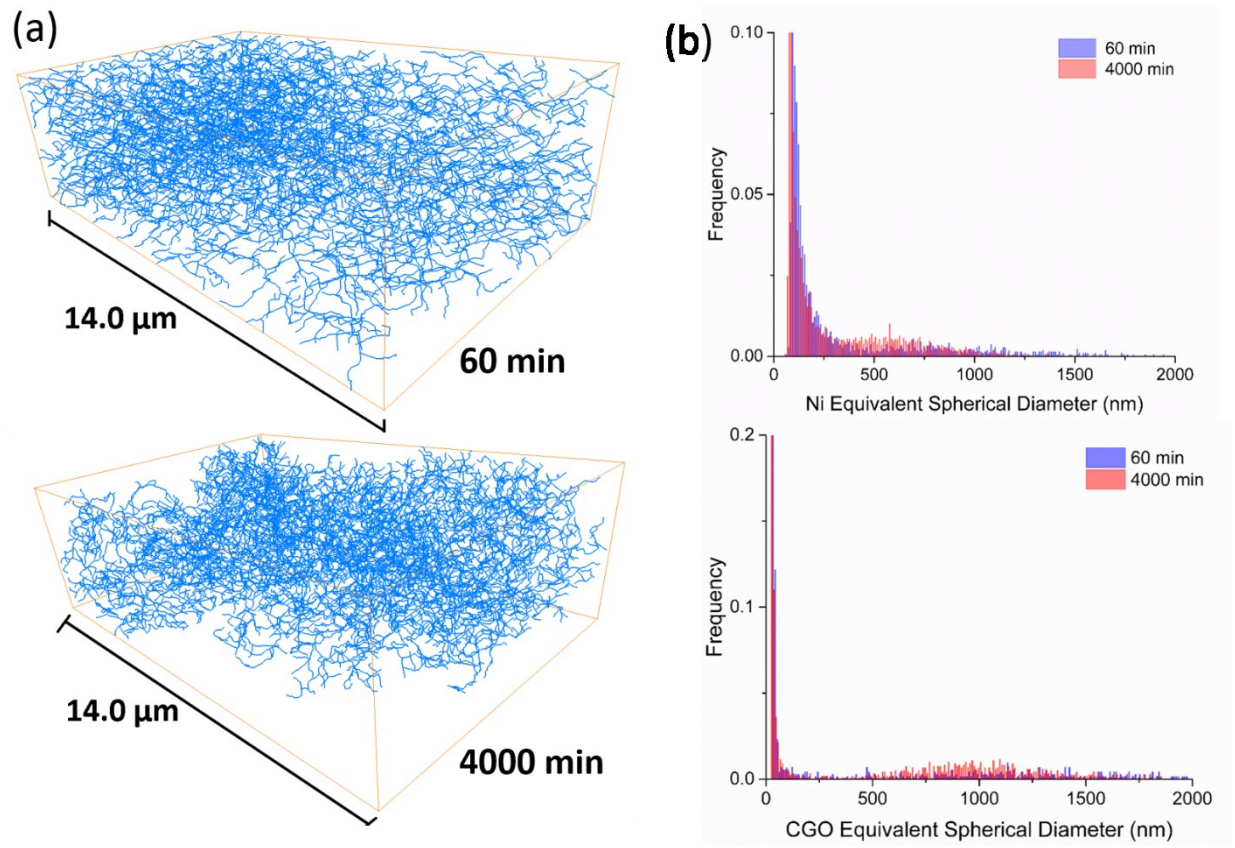


Figure 7.9 Microstructural comparisons between the electrodes aged for 60 min and for 4000 min at 800 °C. The active TPB network in the 3-D volume is shown in (a) as the blue lines and the particle diameter distributions of Ni and CGO for the two reconstructed volumes are shown in (b).

The microstructural parameters extracted from the 3-D reconstruction of the two electrodes E60 aged for 60 min and E4000 aged for 4000 min are summarised in Table 7.1. The total TPB densities of the two electrodes are comparable, but the active TPB density has reduced by 3 times in E4000 as compared to E60. This confirmed the qualitative observation in the TPB networks in Figure 7.9a that Ni coarsening mainly causes disconnection of certain regions of TPBs. Specific interfacial area between Ni and pore has increased and between Ni and CGO decreased because of Ni coarsening. However, the specific interfacial area

between CGO and pore, which is the DPB density, remained relatively constant. Tortuosity of the CGO and pores are not largely affected by the annealing, but the Ni tortuosity is 58% larger in E4000 than in E60. While Ni coarsening has occurred in the porous composite electrode, the CGO structure is relatively unaffected by high temperature annealing.

Table 7.1 Microstructural parameters of the 3-D reconstruction for the electrodes aged for 60 and 4000 min

Sample	**4000 min aged**	**60 min aged**
volume of analysis (μm^3)	788	1086
total TPB density (μm^{-2})	16 ± 2	14 ± 1
active TPB density (μm^{-2})	2.7 ± 0.1	8.5 ± 0.5
Ni-Pore interfacial area (μm^{-1})	1.1 ± 0.1	0.8 ± 0.1
Ni-CGO interfacial area (μm^{-1})	2.5 ± 0.3	3.0 ± 0.5
CGO-Pore interfacial area (μm^{-1})	1.8 ± 0.2	1.9 ± 0.3
tortuosity of Pore	3.6 ± 0.1	3.8 ± 0.1
tortuosity of Ni	10.2 ± 0.6	6.9 ± 0.3
tortuosity of CGO	2.4 ± 0.2	2.2 ± 0.1
volume fraction of Pore	0.24 ± 0.02	0.26 ± 0.02
volume fraction of Ni	0.20 ± 0.01	0.24 ± 0.02
volume fraction of CGO	0.57 ± 0.05	0.50 ± 0.03

With the microstructural parameters in Table 7.1, the electrochemical performance can be modelled by the Adler-Lane-Steele (ALS) model[159] in Equation 7.1 and 7.2, with some modification to include the effect of TPBs.

$$R_{chem} = \left(\frac{RT}{2F^2}\right)\sqrt{\frac{\tau f_o}{V_{CGO}C_o^2 a D^* k^*}} \qquad (7.1)$$

$$t_{chem} = \frac{V_{CGO}}{a}\frac{C_v}{C_o}\frac{1}{Ak_o} \qquad (7.2)$$

R_{chem} is the polarisation resistance and t_{chem} is the characteristic relaxation time. R is the gas constant, T the temperature and F the Faraday's constant. τ is the tortuosity of the CGO and f_o the jump correlation factor for oxygen diffusion. f_o is approximated to 0.7 with diffusion via free vacancies [238]. V_{CGO} is the volume fraction of CGO, which was determined by FIB-SEM as 50%. A is the thermodynamic factor and for CGO, it is 2. a is the DPB density, which is approximately 1.9×10^4 cm^{-1} for this nanoscale Ni-CGO electrode. C_o is the concentration of oxygen sites and C_v the concentration of vacancies. D* is the oxygen tracer diffusion coefficient, previously measured by secondary ion mass spectrometer (SIMS) as 6×10^{-8} $cm^2 s^{-1}$ at 800 °C [239].

k_o is the intrinsic surface exchange coefficient of the material and k* is the tracer surface exchange coefficient. Neglecting any tracer correlation effect, the two coefficients are identical. Based on a study on samarium-doped-ceria (SDC) [240], the surface exchange coefficient k* is approximately 2×10^{-5} cm s^{-1} at 800 °C and 10^{-15} atm pO_2 in H_2- H_2O mixture. In this Ni-CGO material, the surface reaction can take place through two parallel routes, either on the CGO surface or at the TPBs. Hence, the TPB reactions are considered as add-on effects, explained in Equation 7.3, to the DPB reactions already accounted for in the ALS model.

$$k_{TPB} = \frac{i_{TPB}^o n_{TPB}}{2FaC_o} \qquad (7.3)$$

The add-on effect on the surface exchange coefficient at TPBs, k_{TPB}, is calculated from the TPB exchange current density. Due to the limited literature about exchange current density at Ni-CGO-pore boundary, the TPB exchange current density i^o_{TPB} was taken from experiments on a Ni-YSZ pattern electrode by Bieberle and Gaukler [241], as 5.28×10^{-7} A cm^{-1} at 800 °C. n_{TPB} is the active TPB density, which is 8.4×10^8 cm^{-2}. The k_{TPB} is calculated to be 1.5×10^{-6} cm s^{-1}.

Therefore, the k* and ko in Equation 7.1 and 7.2 are replaced by k_{eff}, which is the sum of k_{TPB} and k*, to account for the surface reactions at both the TPBs and DPBs. R_{chem} is calculated as 0.085 Ω cm^2 , in good agreement with the measured polarisation resistance of R_{high} in Figure 7.6 and t_{chem} 0.016 s, which is approximately 9 Hz, close to the characteristic frequency for the high frequency response reported in Figure 7.5. Hence, the high frequency response is suggested to be associated with the surface reaction and oxygen ion bulk diffusion in the Ni-CGO electrode, giving a Gerischer-type response in the impedance spectra.

It is also worth noting that the add-on k_{TPB} from the model is one order of magnitude lower than the k* for CGO. The contribution of TPBs to the electrochemical reaction is much less significant than the DPBs in the Ni-CGO electrode. This also explains why, despite the drastic change in Ni morphology during the high temperature annealing, the electrodes remained relatively stable as indicated by the polarisation resistances in Figure 7.6. However, the influence of TPB reactions may be significant during the very early stage of aging where a very high TPB density and very fine nickel particles (~ 10 nm) were present. The rapid initial degradation is likely a result of coarsening of Ni nanoparticles. The roles of TPBs and DPBs were also investigated in [242], which pointed out that varying the TPB density while holding the DPB density constant in metal-SDC pattern electrodes does not influence the electrochemical reaction resistance. Hence, in this nanoscale Ni-CGO electrode, where

both Ni and CGO are mainly 50 – 100 nm in diameter, the electrochemical reactions take place predominantly at the DPBs.

Finally, the electrode after 4000 min aging is examined closely in Figure 7.10. Ni agglomeration is noticeable in Figure 7.10a, where the Ni phase has extended into the pore space and grown to 1 µm in size. In the electrode with approximately 30 vol% porosity, the coarsened Ni tends to grow into the sub-micron sized larger pores (the porous regions shown in Figure 7.8b) after filling in the 10-100 nm small cavities they are originally located in. However, encouragingly in Figure 7.10b, many Ni particles are still sitting in the 10-100 nm small cavities and not bulging out into the open pore space. One important characteristic of those Ni particles constrained in the small pores is that the cavities they are sitting in have openings with convex corners. The contact angle between the Ni and CGO at the edge of the openings are larger than 90 °. As the wettability between metal and oxide is poor [243], the convex corners effectively inhibit the Ni coarsening by imposing a geometrical constraint. In contrast, the agglomerated Ni particles in Figure 7.10a are originating from a cavity with concave corners where the contact angle between the Ni and CGO at the edges is smaller than 90 °, which is energetically unfavourable. In the nanoscale Ni-CGO electrode, the structural relationship between Ni and CGO networks is hence important in determining the stability of the electrode.

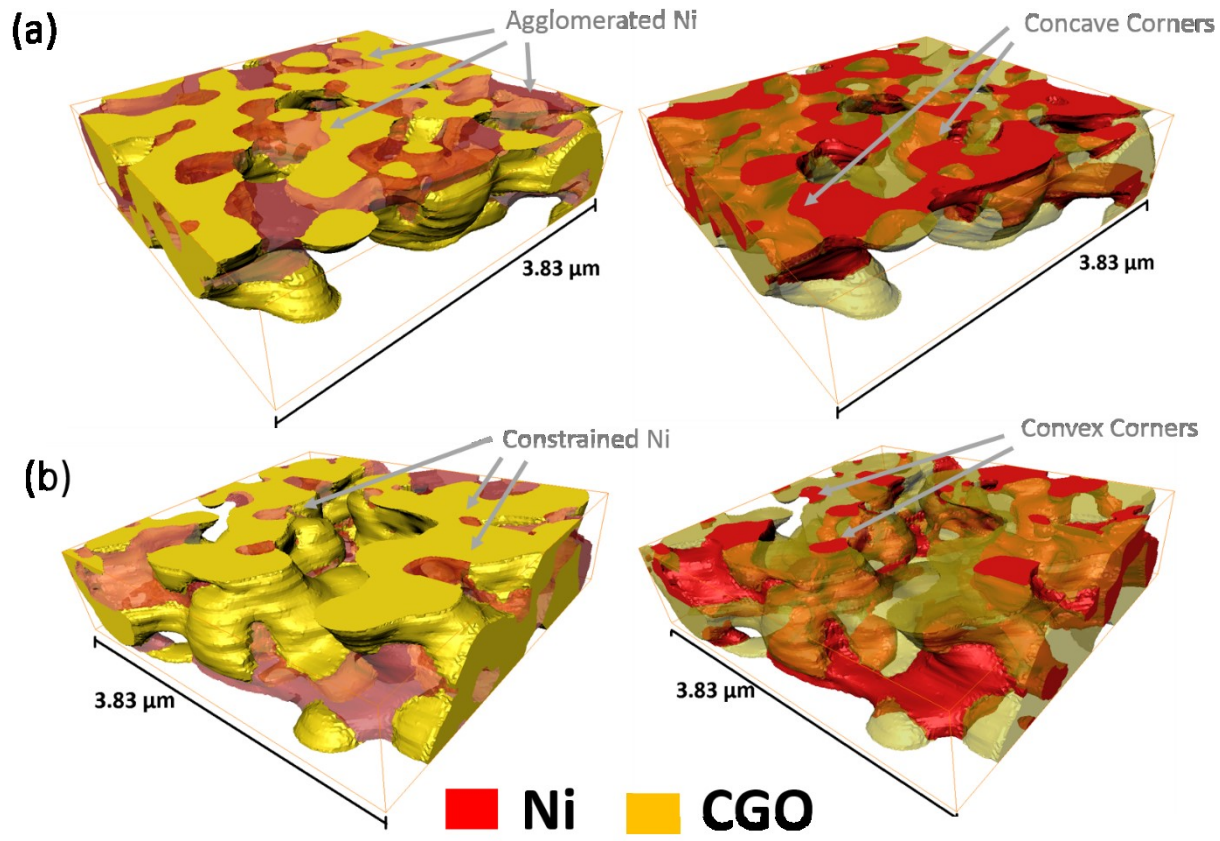


Figure 7.10 Magnified views of the electrode aged for 4000 min at 800 °C in humidified 5% H_2-N_2. Nickel is presented in red and CGO in yellow. In the images on the left, Ni was made translucent to highlight the CGO network structure and vice versa for the images on the right. On one side of the zoom-in region (a), Ni coarsening is appreciable and a few agglomerated particles are labelled. On the other side of the region (b), Ni coarsening is much less severe and many Ni particles remained very fine.

7.3 Conclusions

A high stability nanostructured Ni-CGO electrode has been fabricated by co-sintering NiO and CGO in the form of nanocomposite powders produced by hydrothermal flow reaction. The nanocomposite powders require heat treatment at 600 °C to remove residual water and nitrate and a slow heating rate is required to avoid excessive shrinkage during sintering. The powders have a high BET surface area of 111.2 $m^2 g^{-1}$.

The electrodes sintered at 1300 °C and reduced at 800 °C, with approximately 30 wt% Ni loading, were measured by impedance spectroscopy at 800 °C in humidified 5% H_2-N_2 under OCV. Two polarisation processes were observed at 0.2 Hz and 6 Hz. The higher and lower frequency resistances have activation energies of 1.03 eV and 0.50 eV respectively. Based on the activation energy and the characteristic relaxation time and resistance simulated from the modified ALS model of the electrode impedance, the higher frequency response is associated with the electrochemical reactions at the TPBs and DPBs.

Annealing at 800 °C indicated that the nanostructured Ni-CGO electrodes are stable at high temperature and showed a long-term total polarisation resistance of 0.20 Ω cm^2. SEM images of the cross section of the electrodes showed Ni particles have coarsened during annealing, grown to micrometer larger particle bulging into the open pore space. FIB-SEM 3-D reconstruction on two electrodes aged for 60 min and 4000 min respectively showed that the active TPB density has decreased from 8.4 to 2.7 μm^{-2}, which is related to a loss in TPB connectivity as a result of Ni coarsening. However, the DPB density remained relatively constant, which is responsible for the stable electrochemical performance under high temperature annealing. The particle size distributions of Ni and CGO have major peak at 100 nm and 50 nm for both 60 min-aged and 4000 min-aged electrodes. Statistically, the

number of coarsened Ni particles are not significant. Constraint effect to Ni movement is imposed by the CGO network when the Ni is held in cavities with convex-cornered openings, where the contact angles between Ni and CGO are larger than 90°. The CGO network is therefore the key to the stability of the co-sintered nanostructured Ni-CGO electrode.

8 Conclusion

Nanostructured nickel cermet electrodes demonstrate excellent electrochemical performance for SOFC and SOEC applications. Three types of microstructures are investigated in this thesis as illustrated in Figure 8.1. The Ni nanoparticles in the impregnated electrode in Figure 8.1a is sitting on the surface of the ScSZ scaffold while the Ni nanoparticles in the co-sintered electrode is partially enclosed by the YSZ or CGO network in Figure 8.1b and c. In the impregnated electrode, the ScSZ particles are of 1 µm in scale much larger than the impregnated Ni, but in the co-sintered electrode, the YSZ and CGO particles are of 10 – 100 nm in scale, comparable to the size of the Ni.

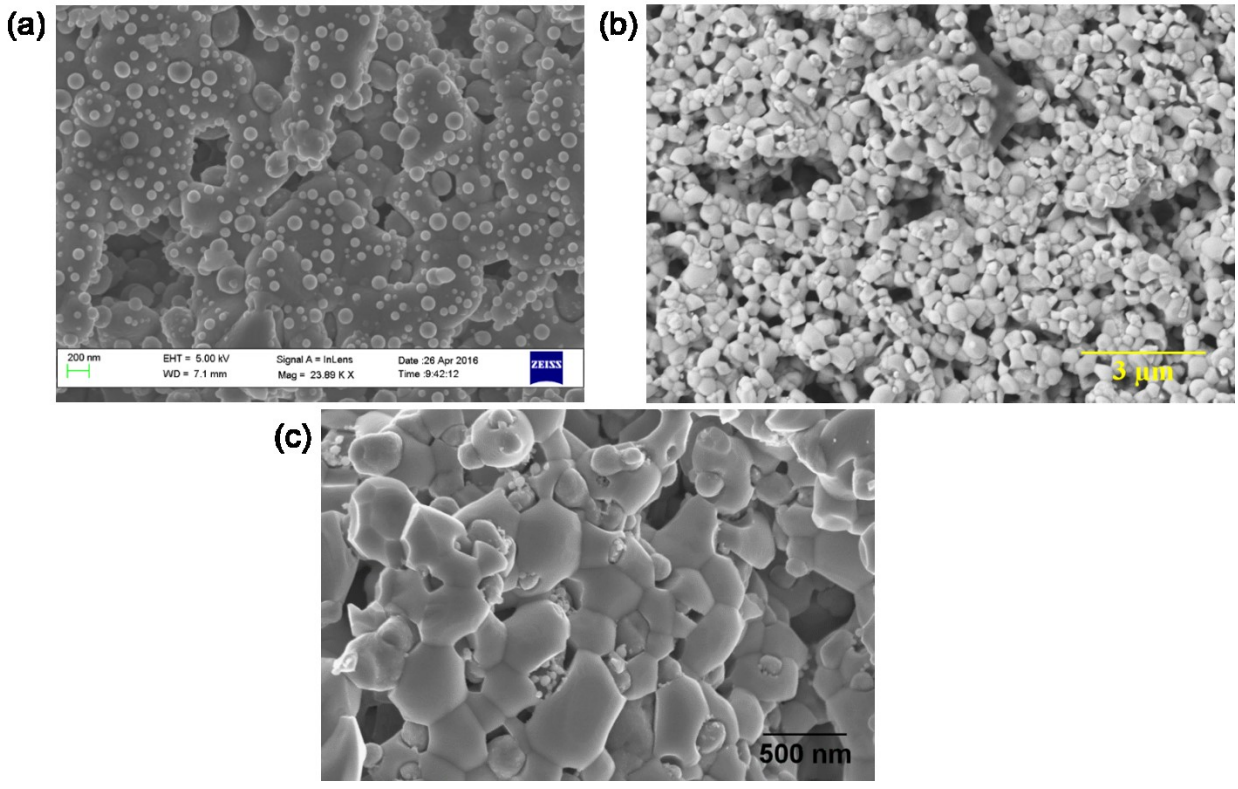


Figure 8.1 SEM images of the three types of microstructures investigated a) nickel-impregnated ScSZ, b) co-sintered Ni-YSZ nanocomposite powder and c) co-sintered Ni-CGO nanocomposite powder.

At 800 °C in 3% H_2O-5% H_2-N_2, the Ni-impregnated ScSZ electrode exhibited an electrochemical reaction ASR of 0.17 Ω cm^2 and the co-sintered Ni-YSZ also 0.17 Ω cm^2 at OCV. The co-sintered Ni-CGO electrode demonstrated a total polarisation resistance of 0.16 Ω cm^2. Despite the different microstructure, all three types of nanostructured electrodes as-reduced showed low polarisation resistance. Using AC impedance, different polarisation processes were observed in the electrode response. For the zirconia-based electrodes, the ionic transfer process between the electrode and the electrolyte generated a polarisation at high frequency. The polarisation at medium frequency range is associated with the electrochemical reaction at the TPBs. At the low frequency (approximately 1 – 10 Hz) is an artefact response of gas conversion impedance resulting from the gas stagnant layer on top of the electrode. For the ceria-based electrode, due to the MIEC property of CGO, the analysis on EIS is more complicated. In the higher frequency range, a Gerischer response was observed, which is associated with the electrochemical reactions occurring primarily on the CGO surface. The response at lower frequency between 1 – 0.1 Hz is both thermally activated and affected by gas composition and hence the origin of this response needs further investigations.

The degradation behaviours of the three nanoscale electrodes are compared in Figure 8.2. A rapid degradation was observed in the time scale of 10 h for nanostructured electrodes. The rapid increase in electrochemical ASR was most prominent in the Ni-impregnated ScSZ electrode as the ASR increased by an order of magnitude, which was attributed to rapid coarsening of Ni nanoparticles. The electrochemical reaction ASR for co-sintered Ni-YSZ electrode firstly increased from 0.17 to 0.76 Ω cm^2 as a result of nickel coarsening but then decreased back to 0.15 Ω cm^2 due to the sintering of YSZ nanoparticles which increased the ionic conductivity of the electrode. In the co-sintered Ni-CGO electrode, the initial increase in the total polarisation resistance was observed due to Ni coarsening but later the ASR

stayed constant during annealing despite the decreasing TPB density. The electrochemical reactions at the DPBs are more significant than those at the TPBs and therefore a relatively stable CGO network led to stable ASR. For the 50 h aging comparison in Figure 8.2, the polarisation resistance of the three electrodes start off from very similar initial values as-reduced. Both resistances for the Ni-impregnated ScSZ electrodes and the co-sintered Ni-YSZ electrodes then shoot up by 5 times during the first 10 h, but for the co-sintered Ni-YSZ electrodes the performance improved afterwards, while the Ni-impregnated ScSZ continued to degrade. The electrochemical resistance of co-sintered Ni-CGO electrode remained relatively low and stable over the whole duration, in comparison.

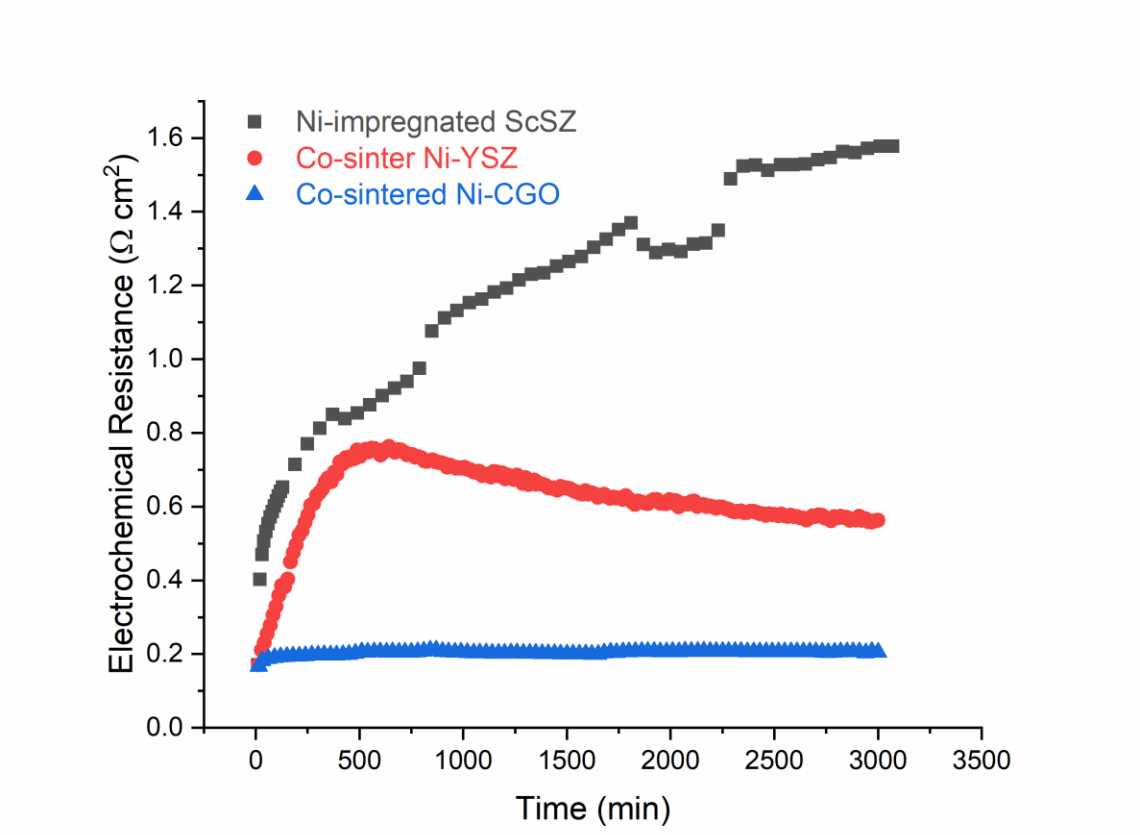


Figure 8.2 Trends of the electrochemical polarisation resistances of the three different electrodes during aging at 800 °C in humidified 5% H_2 – N_2.

Evidence of nickel coarsening was seen in post-test analysis by both 2-D images and 3-D reconstruction. Shifts towards larger particle diameter in the Ni were observed in both the impregnated and co-sintered Ni cermet electrodes. However, the rate of degradation was higher in the nickel impregnated ScSZ electrode, where the nickel nanoparticles speckled on the surface of ScSZ scaffold. The co-sintered Ni-YSZ and Ni-CGO electrodes are both relatively stable towards high temperature annealing in humid hydrogen atmospheres in the time scale of 100 h. The interpenetrating networks between the nanoscale ceramic phase (CGO or YSZ) and nanoscale Ni play a role in minimising nickel coarsening. In the impregnated structure, the open space around Ni gave rise to fast kinetics of coarsening as suggested by the rapid degradation in ASR. The co-sintered electrodes form entangled networks of Ni, pore and YSZ/CGO on the nanometre scale and large contact angles between the Ni and YSZ/CGO. The large contact angles and limited free pore space slowed down the Ni coarsening and preserved the nanostructure (100 nm) of the electrodes.

The extent of Ni coarsening also affects the TPB densities as shown in Figure 8.3. Both the co-sintered Ni-CGO electrodes and the Ni-impregnated ScSZ electrodes experience an approximately 3x decrease in TPB density after aging. Despite the decrease in TPB density, Ni-CGO electrodes still maintain good performance due to the relatively stable DPB density but the performance of Ni-impregnated ScSZ electrodes deteriorated drastically. Encouragingly, the TPB density of co-sintered Ni-YSZ electrodes only decrease by ~17 %. This is due to mitigation on Ni coarsening by the YSZ network. The relatively stable ceramic phase can mitigate Ni coarsening when they form interpenetrating networks and are of comparable length scale.

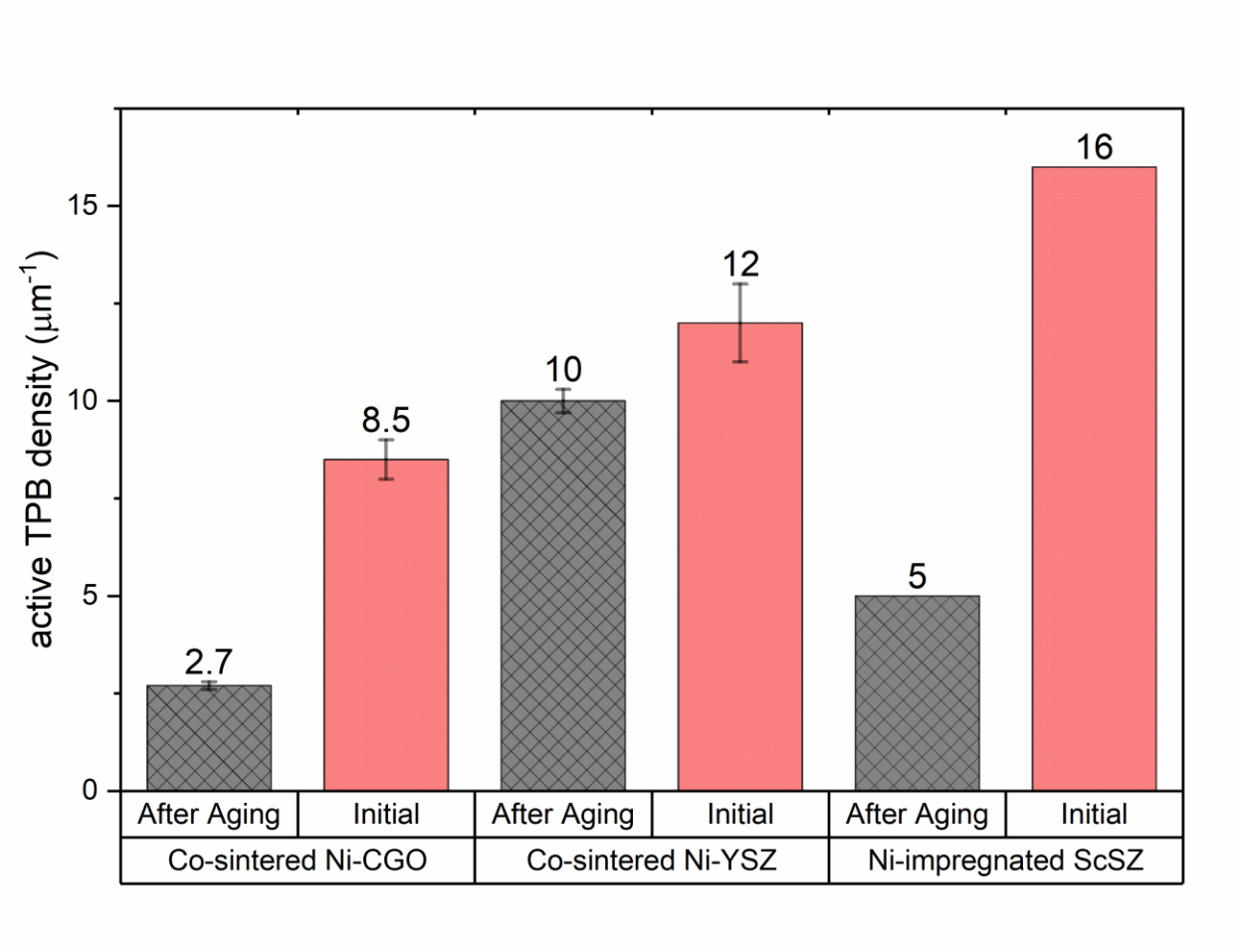


Figure 8.3 The active (percolated) TPB densities of the three electrode as-reduced and after aging. The TPB densities for co-sintered electrodes are measured from FIB-SEM 3D reconstructions and for Ni-impregnated ScSZ electrodes are calculated from the electrochemical polarisation resistances using the physical TLM model.

Considerable sintering was observed in YSZ in the nanoscale Ni-YSZ electrode investigated in Chapter 6, which was evident from the decrease in YSZ tortuosity, a shift towards larger particle sizes and the reduction in the volume fraction of pore. However, the nanoscale CGO network did not experience an apparent shift towards larger particle size and hence it was concluded in Chapter 7 that there was no observable sintering in CGO. However, the dilatometry results in air (Figure 5.1 and Figure 7.1) show that CGO sinters more easily at 800 °C. This contradiction may be caused by the small sampling volumes of FIB-SEM

tomography. As the FIB-SEM region is much smaller than the actual volume of the electrode, it may not be able to capture microstructural gradients at a larger length scale (e.g. 10 µm) in the electrodes even when the sampling volume is deemed homogeneous in the representative volume check. Apart from the possible error from small sampling volume, the sintering of the ceramic phase can be influenced by the microstructure of the porous electrode, as the microstructure is very different from a dense green pellet of NiO-CGO or NiO-YSZ used in dilatometry. The sintering rate is also dependent on the surface diffusion rate given the particular curvature in the microstructure and number of particle-particle contacts. Hence, it is possible that the nanoscale YSZ sinters more easily than CGO in the porous composites.

Finally, the study has correlated the microstructural parameters extracted from FIB-SEM 3-D reconstruction of the electrodes to the ASR from the EIS analysis before and after the aging of the Ni cermet electrodes. It was demonstrated the established electrochemical models can accurately predict the impedance response of SOFC electrodes from its microstructural parameters and reversely, the impedance response reflects changes in SOFC microstructure during degradation. The combination of FIB-SEM and EIS is a powerful tool for characterising SOFC electrode degradation.

9 Future Work

In this study only two-electrode measurements at OCV were conducted. A three-electrode measurement where the DC current fluxes are introduced between the working and counter electrodes is closer to the actual operating condition of SOFC electrodes. Jiao and Shikazono [244] reported that the electrochemical polarisation increased the local humidity at TPBs and decreased surface tension of Ni. The wettability of Ni on YSZ was enhanced under polarisation in the Ni film anode sputtered on YSZ substrate. Hence, it is possible that electrochemical polarisation in the cell influences the kinetics and mechanism of nickel coarsening. Future degradation tests of the nanostructured electrodes in the study should be monitored by EIS with three-electrode measurement to account for the effect of current on Ni morphology evolution.

The electrochemical models applied in this study account for the ionic conducting phase and the electronic conducting phase, but not the effect of pores. Most of the modelling work has focused on the gas flow behaviour in the gas channel outside the SOFC electrodes [245]. When the pores in the electrodes are also scaled down to nanometre range, the gas diffusion in the electrodes' pores may become dominant and Knudsen diffusion kicks in when pore diameter is comparable to the mean free path of gas molecules [19]. In the case of nanostructured porous SOFC electrodes, the gas diffusion inside the porous media needs to be accounted for in the model, for example the 'Dusty Gas Model'. It is worth developing an electrochemical model which incorporates the gas diffusion in electrode when simulating the impedance response from the microstructural data.

To understand the fundamental properties of nickel coarsening in a cermet structure, patterned electrodes will give the most direct indications of microstructural evolution as compared to the actual SOFC electrodes. It has been qualitatively found in this study that the contact angles and structural relationship between the Ni and the YSZ networks influence the kinetics of nickel coarsening. Future experiments will be designed to understand this interaction and quantify the relevant parameters in more details by using pattern electrodes. The contact angles between the Ni and YSZ are modified in the pattern electrode to investigate its influence in nickel coarsening at the operating temperatures of SOFCs.

Ultimately, X-ray nanotomography is available to non-destructively trace the microstructural evolution of nickel nanoparticles inside the actual SOFC electrodes. It has been demonstrated by De Angelis et al.[117] and Kennouche et al. [246] that using X-ray imaging can follow the time evolution of the same sample volume under high temperature aging. In this study using FIB-SEM, only the global microstructural parameters such as the TPB density, tortuosity of phases etc. are analysed. With X-ray nanotomography, the local phenomenon which can provide direct evidence of the nickel coarsening mechanisms will be obtained.

10 Publications and Presentations

- Chen J, Ruiz-Trejo E., Atkinson A., Brandon NP, 2017, Microstructural and Electrochemical Characterisation of Degradation in Nickel Impregnated Scandia-Stabilised Zirconia Electrode during Isothermal Annealing, ECS Transaction, Vol: 78, Pages 1125-1137, doi: 10.1149/07801.1125ecst
- Chen J, Bertei A, Ruiz-Trejo E, Atkinson A, Brandon NP, 2017, Characterization of Degradation in Nickel Impregnated Scandia-Stabilize Zirconia Electrodes during Isothermal Annealing, *JOURNAL OF THE ELECTROCHEMICAL SOCIETY*, Vol: 164, Pages: F935-F943, doi: 10.1149/2.0821709jes

- 5-8th July 2016, European Fuel Cell Forum 2016, Poster Presentation

  Time-dependent Degradation of Nickel-infiltrated ScSZ Anodes

  Jingyi Chen, Xin Wang, Enrique Ruiz-Trejo, Alan Atkinson, Nigel P Brandon
- 12- 14th December 2016, H2FC Supergen Research Conference 2016, Oral Presentation

  Using Electrochemical Impedance Spectroscopy to Measure Microstructural Degradation in Nickel-impregnated Scandia-Stabilised-Zirconia Electrode

  Jingyi Chen, Antonio Bertei, Enrique Ruiz-Trejo, Alan Atkinson, Nigel P Brandon
- 24-28th July 2017, The 15th Solid Oxide Fuel Cell Symposium 2017, Oral Presentation

  Microstructural and Electrochemical Characterisation of Degradation in Nickel Impregnated ScSZ Electrode

  Jingyi Chen, Antonio Bertei, Enrique Ruiz-Trejo, Alan Atkinson, Nigel P Brandon

- 11-13 Dec 2017, H2FC Supergen Research Conference 2017, Oral Presentation

  Fabrication of Nano-porous Nickel Yttria-Stabilised Zirconia Anode

  Jingyi Chen, Chris Starkey, Paul Boldrin, Alan Atkinson, Nigel P Brandon

- 3-6 July 2018, European Fuel Cell Forum 2018, Oral Presentation

  Nano-composite Nickel Yttria-Stabilised Zirconia Anode

  Jingyi Chen, Chris Starkey, Alan Atkinson, Nigel P Brandon

11 Bibliography

[1] A. Haryanto, S. Fernando, N. Murali, and S. Adhikari, "Current Status of Hydrogen Production Techniques by Steam Reforming of Ethanol: A Review," *Energy & Fuels*, vol. 19, no. 5, pp. 2098–2106, Sep. 2005.

[2] F. Mueller-Langer, E. Tzimas, M. Kaltschmitt, and S. Peteves, "Techno-economic assessment of hydrogen production processes for the hydrogen economy for the short and medium term," *Int. J. Hydrogen Energy*, vol. 32, no. 16, pp. 3797–3810, 2007.

[3] S. . Singhal, "Advances in solid oxide fuel cell technology," *Solid State Ionics*, vol. 135, no. 1, pp. 305–313, 2000.

[4] N. Q. Minh, "Solid oxide fuel cell technology - Features and applications," *Solid State Ionics*, vol. 174, no. 1–4, pp. 271–277, 2004.

[5] M. Ni, M. K. H. Leung, and D. Y. C. Leung, "Technological development of hydrogen production by solid oxide electrolyzer cell (SOEC)," *Int. J. Hydrogen Energy*, vol. 33, no. 9, pp. 2337–2354, 2008.

[6] H. Tu and U. Stimming, "Advances, aging mechanisms and lifetime in solid-oxide fuel cells," *J. Power Sources*, vol. 127, no. 1–2, pp. 284–293, Mar. 2004.

[7] R. M. Ormerod, "Solid oxide fuel cells," *Chem. Soc. Rev.*, vol. 32, no. 1, pp. 17–28, 2003.

[8] S. C. Singhal, "Solid-Oxide Fuel Cells," in *Fuel Cells*, Hoboken, NJ, USA: John Wiley & Sons, Inc., 2007, pp. 135–160.

[9] S. M. Jamil, M. H. D. Othman, M. A. Rahman, J. Jaafar, A. F. Ismail, and K. Li, "Recent fabrication techniques for micro-tubular solid oxide fuel cell support: A review," *J. Eur. Ceram. Soc.*, vol. 35, no. 1, pp. 1–22, 2015.

[10] C. Hatchwell, N. . Sammes, I. W. . Brown, and K. Kendall, "Current collectors for a novel tubular design of solid oxide fuel cell," *J. Power Sources*, vol. 77, no. 1, pp. 64–68, 1999.

[11] C. Hiraiwa, K. Okuno, H. Tawarayama, M. Majima, J. Nishimura, and H. Tsuchida, "Application of Ni Porous Metal to Solid Oxide Fuel Cells," no. 83, pp. 59–65, 2016.

[12] S. Zha, C. Xia, and G. Meng, "Calculation of the emf of solid oxide fuel cells," *J. Appl. Electrochem.*, vol. 31, pp. 93–98, 2001.

[13] I. Pilatowsky, R. J. Romero, C. A. Isaza, S. A. Gamboa, P. J. Sebastian, and W. Rivera, "Thermodynamics of Fuel Cells," 2011, pp. 25–36.

[14] V. M. Janardhanan and O. Deutschmann, "Modeling of Solid-Oxide Fuel Cells," *Zeitschrift für Phys. Chemie*, vol. 221, no. 4, pp. 443–478, 2007.

[15] J. Larminie and A. Dicks, "Operational Fuel Cell Voltages," in *Fuel Cell Systems Explained*, West Sussex, England: John Wiley & Sons, Ltd,., 2013, pp. 45–66.

[16] T. Suzuki, Z. Hasan, Y. Funahashi, T. Yamaguchi, Y. Fujishiro, and M. Awano, "Impact of anode microstructure on solid oxide fuel cells," *Science (80-.).*, vol. 325, no. 5942, pp. 852–855, Aug. 2009.

[17] W. Lehnert, J. Meusinger, and F. Thom, "Modelling of gas transport phenomena in SOFC anodes," *J. Power Sources*, vol. 87, no. 1, pp. 57–63, 2000.

[18] M. Ni, M. K. H. Leung, and D. Y. C. Leung, "Parametric study of solid oxide fuel cell performance," *Energy Convers. Manag.*, vol. 48, no. 5, pp. 1525–1535, 2007.

[19] W. G. Bessler, "Gas Concentration Impedance of Solid Oxide Fuel Cell Anodes," *J. Electrochem. Soc.*, vol. 153, no. 8, p. A1492, 2006.

[20] S. Primdahl and M. Mogensen, "Gas Diffusion Impedance in Characterization of Solid Oxide Fuel Cell Anodes," *J. Electrochem. Soc.*, vol. 146, no. 8, pp. 2827–2833, 1999.

[21] S. Primdahl and M. Mogensen, "Gas Conversion Impedance: A Test Geometry Effect in Characterization of Solid Oxide Fuel Cell Anodes," *J. Electrochem. Soc.*, vol. 145, no. 7, p. 2431, 1998.

[22] A. Hauch and M. B. Mogensen, *Advances in Medium and High Temperature Solid Oxide Fuel Cell Technology*, vol. 574. Cham: Springer International Publishing, 2017.

[23] S. Primdahl and M. Mogensen, "Gas Diffusion Impedance in Characterization of Solid Oxide Fuel Cell Anodes," *J. Electrochem. Soc.*, vol. 146, no. 8, p. 2827, 1999.

[24] E. Kim, "South Korea becomes fuel cell leader," *Electric Light & Power*, pp. 1–5, 2018.

[25] D. R. Baker, "Bloom Energy , Silicon Valley fuel-cell unicorn , has a high-powered IPO," *San Francisco Chronicle*, pp. 25–27, 2018.

[26] M. Gandiglio, A. Lanzini, and M. Santarelli, "Large Stationary Solid Oxide Fuel Cell (SOFC) Power Plants," in *Modeling, Design, Construction, and Operation of Power Generators with Solid Oxide Fuel Cells: From Single Cell to Complete Power System*, J. Kupecki, Ed. Cham: Springer International Publishing, 2018, pp. 233–261.

[27] N. H. Menzler, D. Sebold, and O. Guillon, "Post-test characterization of a solid oxide fuel cell stack operated for more than 30,000 hours: The cell," *J. Power Sources*, vol. 374, no. August 2017, pp. 69–76, 2018.

[28] A. Choudhury, H. Chandra, and A. Arora, "Application of solid oxide fuel cell technology for power generation - A review," *Renew. Sustain. Energy Rev.*, vol. 20, pp. 430–442, 2013.

[29] J. Rechberger, M. Reissig, and V. Lawlor, "SOFC EV range extender systems for biofuels," in *Der Antrieb von morgen 2018*, 2018, pp. 51–61.

[30] E. D. Wachsman and K. T. Lee, "Lowering the Temperature of Solid Oxide Fuel Cells," *Science (80-.).*, vol. 334, no. 6058, pp. 935–939, 2011.

[31] E. Richardson, "Unlocking the Potential of Hydrogen in a Decarbonised Energy System,"

Renewable Energy World, 2017.

[32] C. Phil, "Ceres 2018 Result: strategic partners enable a step change in commercial growth," 2018. [Online]. Available: http://www.cerespower.com/news/latest-news/ceres-2018-results/. [Accessed: 12-Mar-2019].

[33] M. Sedighizadeh and A. Rezazadeh, "Comparison between Batteries and Fuel Cells for Photovoltaic System Backup," *Reactions*, vol. 26, no. December, pp. 295–299, 2007.

[34] Z. Dimitrova and F. Maréchal, "Environomic design for electric vehicles with an integrated solid oxide fuel cell (SOFC) unit as a range extender," *Renew. Energy*, vol. 112, pp. 124–142, 2017.

[35] J. Fenn and M. Raskino, *Mastering the Hype Cycle: How to Choose the Right Innovation at the Right Time*. Harvard Business Review Press, 2008.

[36] N. Behling and M. C. Williams, "Solid Oxide Fuel Cells: Opportunities for Economic Growth in Japan," *ECS Trans.*, vol. 78, no. 1, pp. 299–308, May 2017.

[37] D. Craig, "Fuel cell technology," *UK Engineering and Physical Sciences Research Council*, Mar-2018. [Online]. Available: https://epsrc.ukri.org/research/ourportfolio/researchareas/fuelcells/#.

[38] M. Wei, S. J. Smith, and M. D. Sohn, "Experience curve development and cost reduction disaggregation for fuel cell markets in Japan and the US," *Appl. Energy*, vol. 191, pp. 346–357, 2017.

[39] W. Eric, "Fuel Cell Industry Financials in 2018: Bloom's IPO and aftermath, SFC Energy on the edge of profits, red ink abounds," *Greentech Media*, 2018. [Online]. Available: https://www.greentechmedia.com/articles/read/stationary-fuel-cell-industry-financials-2018-in-brief#gs.13lmcb. [Accessed: 12-Mar-2019].

[40] S. Satyapal, "Hydrogen and Fuel Cell Overview," in *DLA Worldwide Energy Conference*,

2017.

[41] N. P. Brandon, S. Skinner, and B. C. H. Steele, "Recent Advances in Materials for Fuel Cells," *Annu. Rev. Mater. Res.*, vol. 33, no. 1, pp. 183–213, 2003.

[42] J. Kurtz, H. Dinh, C. Ainscough, and G. Saur, "Fuel Cell Technology Status : Degradation," 2015.

[43] H. Yokokawa, H. Tu, B. Iwanschitz, and A. Mai, "Fundamental mechanisms limiting solid oxide fuel cell durability," *J. Power Sources*, vol. 182, no. 2, pp. 400–412, 2008.

[44] B. Shri Prakash, S. Senthil Kumar, and S. T. Aruna, "Properties and development of Ni/YSZ as an anode material in solid oxide fuel cell: A review," *Renew. Sustain. Energy Rev.*, vol. 36, pp. 149–179, 2014.

[45] S. . Aruna, M. Muthuraman, and K. . Patil, "Synthesis and properties of Ni-YSZ cermet: anode material for solid oxide fuel cells," *Solid State Ionics*, vol. 111, no. 1–2, pp. 45–51, 1998.

[46] J. Fergus, R. Hui, X. Li, D. P. Wilkinson, and J. Zhang, *Solid Oxide Fuel Cells: Materials Properties and Performance*. CRC Press, 2016.

[47] A. L. Dicks, "Hydrogen generation from natural gas for the fuel cell systems of tomorrow," *J. Power Sources*, vol. 61, no. 1–2, pp. 113–124, 1996.

[48] R. Doshi, "Development of Solid-Oxide Fuel Cells That Operate at 500°C," *J. Electrochem. Soc.*, vol. 146, no. 4, p. 1273, 1999.

[49] M. Mogensen, N. M. Sammes, and G. A. Tompsett, "Physical, chemical and electrochemical properties of pure and doped ceria," *Solid State Ionics*, vol. 129, no. 1, pp. 63–94, 2000.

[50] S. Tao and J. T. S. Irvine, "Discovery and characterization of novel oxide anodes for solid oxide fuel cells," *Chem. Rec.*, vol. 4, no. 2, pp. 83–95, 2004.

[51] B. Steele, "Appraisal of Ce1−yGdyO2−y/2 electrolytes for IT-SOFC operation at 500°C," *Solid State Ionics*, vol. 129, no. 1–4, pp. 95–110, Apr. 2000.

[52] Y. D. Zhen, A. I. Y. Tok, S. P. Jiang, and F. Y. C. Boey, "Fabrication and performance of gadolinia-doped ceria-based intermediate-temperature solid oxide fuel cells," *J. Power Sources*, vol. 178, no. 1, pp. 69–74, 2008.

[53] C. Fu, S. H. Chan, Q. Liu, X. Ge, and G. Pasciak, "Fabrication and evaluation of Ni-GDC composite anode prepared by aqueous-based tape casting method for low-temperature solid oxide fuel cell," *Int. J. Hydrogen Energy*, vol. 35, no. 1, pp. 301–307, 2010.

[54] D. Lee *et al.*, "Direct methane solid oxide fuel cells based on catalytic partial oxidation enabling complete coking tolerance of Ni-based anodes," *J. Power Sources*, vol. 345, pp. 30–40, 2017.

[55] C. Haering, A. Roosen, H. Schichl, and M. Schnöller, "Degradation of the electrical conductivity in stabilised zirconia system Part II: Scandia-stabilised zirconia," *Solid State Ionics*, vol. 176, no. 3–4, pp. 261–268, 2005.

[56] K. Huang, J.-H. Wan, and J. B. Goodenough, "Increasing Power Density of LSGM-Based Solid Oxide Fuel Cells Using New Anode Materials," *J. Electrochem. Soc.*, vol. 148, no. 7, p. A788, 2001.

[57] R. J. Gorte, S. Park, J. M. Vohs, and C. Wang, "Anodes for Direct Oxidation of Dry Hydrocarbons in a Solid-Oxide Fuel Cell," *Adv. Mater.*, vol. 12, no. 19, pp. 1465–1469, 2000.

[58] Z. Zhan, "An Octane-Fueled Solid Oxide Fuel Cell," *Science (80-.).*, vol. 308, no. 5723, pp. 844–847, May 2005.

[59] F. Gao, H. Zhao, X. Li, Y. Cheng, X. Zhou, and F. Cui, "Preparation and electrical properties of yttrium-doped strontium titanate with B-site deficiency," *J. Power Sources*,

vol. 185, no. 1, pp. 26–31, 2008.

[60] M. Kishimoto, M. Lomberg, E. Ruiz-Trejo, and N. P. Brandon, "Enhanced triple-phase boundary density in infiltrated electrodes for solid oxide fuel cells demonstrated by high-resolution tomography," *J. Power Sources*, vol. 266, pp. 291–295, 2014.

[61] V. M. Janardhanan, V. Heuveline, and O. Deutschmann, "Three-phase boundary length in solid-oxide fuel cells: A mathematical model," *J. Power Sources*, vol. 178, no. 1, pp. 368–372, 2008.

[62] H. Kurokawa, T. Z. Sholklapper, C. P. Jacobson, L. C. De Jonghe, and S. J. Visco, "Ceria Nanocoating for Sulfur Tolerant Ni-Based Anodes of Solid Oxide Fuel Cells," *Electrochem. Solid-State Lett.*, vol. 10, no. 9, p. B135, 2007.

[63] H. Tagawa, D. Simwonis, F. Tietz, and D. Stover, "Nickel coarsening in annealed Ni / 8YSZ anode substrates for solid oxide fuel cells," vol. 132, pp. 241–251, 2000.

[64] E. Ruiz-Trejo, A. Atkinson, and N. P. Brandon, "Metallizing porous scaffolds as an alternative fabrication method for solid oxide fuel cell anodes," *J. Power Sources*, vol. 280, pp. 81–89, 2015.

[65] S. P. Jiang, S. Zhang, Y. Da Zhen, and W. Wang, "Fabrication and performance of impregn[1] S. P. Jiang, S. Zhang, Y. Da Zhen, W. Wang, J. Am. Ceram. Soc. 2005, 88, 1779.ated Ni anodes of solid oxide fuel cells," *J. Am. Ceram. Soc.*, vol. 88, no. 7, pp. 1779–1785, 2005.

[66] P. I. Cowin, C. T. G. Petit, R. Lan, J. T. S. Irvine, and S. Tao, "Recent progress in the development of anode materials for solid oxide fuel cells," *Adv. Energy Mater.*, vol. 1, no. 3, pp. 314–332, 2011.

[67] S. P. Jiang, "Nanoscale and nano-structured electrodes of solid oxide fuel cells by infiltration: Advances and challenges," *Int. J. Hydrogen Energy*, vol. 37, no. 1, pp. 449–470,

Jan. 2012.

[68] S. Park, J. M. Vohs, and R. J. Gorte, "Direct oxidation of hydrocarbons in a solid-oxide fuel cell," *Nature*, vol. 404, no. 6775, pp. 265–267, 2000.

[69] X. Liu, X. Meng, D. Han, H. Wu, F. Zeng, and Z. Zhan, "Impregnated nickel anodes for reduced-temperature solid oxide fuel cells based on thin electrolytes of doped LaGaO3," *J. Power Sources*, vol. 222, pp. 92–96, 2013.

[70] S. P. Jiang, W. Wang, and Y. D. Zhen, "Performance and electrode behaviour of nano-YSZ impregnated nickel anodes used in solid oxide fuel cells," *J. Power Sources*, vol. 147, no. 1–2, pp. 1–7, Sep. 2005.

[71] H. Kim, C. Lu, W. L. Worrell, J. M. Vohs, and R. J. Gorte, "Cu-Ni Cermet Anodes for Direct Oxidation of Methane in Solid-Oxide Fuel Cells," *J. Electrochem. Soc.*, vol. 149, p. A247, 2002.

[72] G. Kim *et al.*, "Investigation of the structural and catalytic requirements for high-performance SOFC anodes formed by infiltration of LSCM," *Electrochem. Solid-State Lett.*, vol. 12, no. 3, pp. B48--B52, 2009.

[73] A. N. Busawon, D. Sarantaridis, and A. Atkinson, "Ni infiltration as a possible solution to the redox problem of SOFC anodes," *Electrochem. Solid-State Lett.*, vol. 11, pp. B186–B189, 2008.

[74] K. Haberko, M. Jasinski, P. Pasierb, M. Radecka, and M. Rekas, "Structural and electrical properties of Ni – YSZ cermet materials," *J. Power Sources*, vol. 195, no. 17, pp. 5527–5533, 2010.

[75] A. Babaei, S. P. Jiang, and J. Li, "Electrocatalytic Promotion of Palladium Nanoparticles on Hydrogen Oxidation on Ni/GDC Anodes of SOFCs via Spillover," *J. Electrochem. Soc.*, vol. 156, p. B1022, 2009.

[76] R. J. Gorte, R. Wilson, J. M. Vohs, T.-S. Oh, and Y. Cheng, "An Investigation of LSF-YSZ Conductive Scaffolds for Infiltrated SOFC Cathodes," *J. Electrochem. Soc.*, vol. 164, no. 6, pp. F525–F529, 2017.

[77] M. Rahmanipour, Y. Cheng, T. M. Onn, A. Donazzi, J. M. Vohs, and R. J. Gorte, "Modification of LSF-YSZ Composite Cathodes by Atomic Layer Deposition," *J. Electrochem. Soc.*, vol. 164, no. 7, pp. F879–F884, Jun. 2017.

[78] R. J. Gorte, "Cost-effective Manufacturing and Morphological Stabilization of Nanostructured Cathodes for Commercial SOFCs," Pittsburgh, PA, and Morgantown, WV (United States), Jul. 2018.

[79] Z. Gao, H. Wang, S. Barnett, E. Miller, Q. Liu, and D. Senn, " Tape Casting of High-Performance Low-Temperature Solid Oxide Cells with Thin La 0.8 Sr 0.2 Ga 0.8 Mg 0.2 O 3−δ Electrolytes and Impregnated Nano Anodes ," *ACS Appl. Mater. Interfaces*, vol. 9, no. 8, pp. 7115–7124, 2017.

[80] J. D. Nicholas and S. A. Barnett, "Measurements and Modeling of Sm[sub 0.5]Sr[sub 0.5]CoO[sub 3−x]–Ce[sub 0.9]Gd[sub 0.1]O[sub 1.95] SOFC Cathodes Produced Using Infiltrate Solution Additives," *J. Electrochem. Soc.*, vol. 157, no. 4, p. B536, 2010.

[81] J. D. Nicholas, L. Wang, A. V. Call, and S. A. Barnett, "Use of the Simple Infiltrated Microstructure Polarization Loss Estimation (SIMPLE) model to describe the performance of nano-composite solid oxide fuel cell cathodes," *Phys. Chem. Chem. Phys.*, vol. 14, no. 44, pp. 15379–15392, 2012.

[82] M. Shah, P. W. Voorhees, and S. A. Barnett, "Time-dependent performance changes in LSCF-infiltrated SOFC cathodes: The role of nano-particle coarsening," *Solid State Ionics*, vol. 187, no. 1, pp. 64–67, 2011.

[83] D. Beckel *et al.*, "Thin films for micro solid oxide fuel cells," *J. Power Sources*, vol. 173, no. 1, pp. 325–345, 2007.

[84] Y. Liu, S. Zha, and M. Liu, "Novel nanostructured electrodes for solid oxide fuel cells fabricated by combustion chemical vapor deposition (CVD)," *Adv. Mater.*, vol. 16, no. 3, pp. 256–260, 2004.

[85] D. Neagu, G. Tsekouras, D. N. Miller, H. Ménard, and J. T. S. Irvine, "In situ growth of nanoparticles through control of non-stoichiometry," *Nat. Chem.*, vol. 5, no. 11, pp. 916–923, 2013.

[86] D. Neagu *et al.*, "Nano-socketed nickel particles with enhanced coking resistance grown in situ by redox exsolution," *Nat. Commun.*, vol. 6, 2015.

[87] O. Kwon *et al.*, "Exsolution trends and co-segregation aspects of self-grown catalyst nanoparticles in perovskites," *Nat. Commun.*, vol. 8, no. May, pp. 1–7, 2017.

[88] J. H. Myung, D. Neagu, D. N. Miller, and J. T. S. Irvine, "Switching on electrocatalytic activity in solid oxide cells," *Nature*, vol. 537, no. 7621, pp. 528–531, 2016.

[89] C. Sun and U. Stimming, "Recent anode advances in solid oxide fuel cells," *J. Power Sources*, vol. 171, no. 2, pp. 247–260, 2007.

[90] F. Tietz, H. Buchkremer, and D. Sto, "Components manufacturing for solid oxide fuel cells," vol. 153, pp. 373–381, 2002.

[91] C. Xia, F. Chen, and M. Liu, "Reduced-Temperature Solid Oxide Fuel Cells Fabricated by Screen Printing," *Electrochem. Solid-State Lett.*, vol. 4, no. 5, p. A52, 2001.

[92] F. Han *et al.*, "Novel high-performance solid oxide fuel cells with bulk ionic conductance dominated thin-film electrolytes," *J. Power Sources*, vol. 218, pp. 157–162, 2012.

[93] Y. J. Leng, S. H. Chan, K. A. Khor, S. P. Jiang, and P. Cheang, "Effect of characteristics of Y2O3/ZrO2 powders on fabrication of anode-supported solid oxide fuel cells," *J. Power Sources*, vol. 117, no. 1–2, pp. 26–34, May 2003.

[94] K. Sato, G. Okamoto, M. Naito, and H. Abe, "NiO/YSZ nanocomposite particles

synthesized via co-precipitation method for electrochemically active Ni/YSZ anode," *J. Power Sources*, vol. 193, no. 1, pp. 185–188, 2009.

[95] X. Xi, H. Abe, K. Kuruma, R. Harada, A. Shui, and M. Naito, "Novel Co-precipitation method to synthesize NiO-YSZ nanocomposite powder for solid oxide fuel cell," *Adv. Powder Technol.*, vol. 25, no. 2, pp. 490–494, 2014.

[96] J.-H. Song, M.-Y. Park, H. W. Park, and H.-T. Lim, "Single-step Preparation of Nano-homogeneous NiO/YSZ Composite Anode for Solid Oxide Fuel Cells," *Nano-Micro Lett.*, vol. 5, no. 2, pp. 111–116, 2013.

[97] L. Xu *et al.*, "3D Flowerlike r -Nickel Hydroxide with Enhanced Electrochemical Activity Synthesized by Microwave-Assisted Hydrothermal Method," no. 12, pp. 308–316, 2008.

[98] Q. Zhu and B. Fan, "Low temperature sintering of 8YSZ electrolyte film for intermediate temperature solid oxide fuel cells," *Solid State Ionics*, vol. 176, no. 9–10, pp. 889–894, 2005.

[99] K. Yamamoto, T. Hashishin, M. Matsuda, N. Qiu, Z. Tan, and S. Ohara, "High-performance Ni nanocomposite anode fabricated from Gd-doped ceria nanocubes for low-temperature solid-oxide fuel cells," *Nano Energy*, vol. 6, pp. 103–108, 2014.

[100] X. Yao *et al.*, "Hydrothermally synthesized NiO-samarium doped ceria nano-composite as an anode material for intermediate-temperature solid oxide fuel cells," *Int. J. Hydrogen Energy*, vol. 42, no. 34, pp. 22192–22200, 2017.

[101] X. Weng *et al.*, "Highly conductive low nickel content nano-composite dense cermets from nano-powders made via a continuous hydrothermal synthesis route," *Solid State Ionics*, vol. 181, no. 17–18, pp. 827–834, 2010.

[102] a. Bieberle and L. J. Gauckler, "Reaction mechanism of Ni pattern anodes for solid oxide fuel cells," *Solid State Ionics*, vol. 135, pp. 337–345, 2000.

[103] M. Perez, "Gibbs?Thomson effects in phase transformations," *Scr. Mater.*, vol. 52, no. 8,

pp. 709–712, Apr. 2005.

[104] H.-Y. Chen, H.-C. Yu, J. Scott Cronin, J. R. Wilson, S. a. Barnett, and K. Thornton, "Simulation of coarsening in three-phase solid oxide fuel cell anodes," *J. Power Sources*, vol. 196, no. 3, pp. 1333–1337, Feb. 2011.

[105] J. G. Duh, W. S. Chien, and B. S. Chiou, "Wettability in ZrO2-Ni and ZrO2-Cu bonding," *J. Mater. Sci. Lett.*, vol. 8, no. 4, pp. 405–408, 1989.

[106] R. Davis, F. Abdeljawad, J. Lillibridge, and M. Haataja, "Phase wettability and microstructural evolution in solid oxide fuel cell anode materials," *Acta Mater.*, vol. 78, pp. 271–281, 2014.

[107] V. L. K. Lou, "REVIEW - Graphical Displays of the Thermodynamics of High-Temperature Gas-Solid Reactions and Their Application to Oxidation of Metals and Evaporation of Oxides," *J. Am. Ceram. Soc.*, vol. 68, pp. 49–58, 1984.

[108] A. Hagen, R. Barfod, P. V. Hendriksen, Y.-L. Liu, and S. Ramousse, "Degradation of Anode Supported SOFCs as a Function of Temperature and Current Load," *J. Electrochem. Soc.*, vol. 153, no. 6, pp. A1165–A1171, 2006.

[109] A. Gubner, H. Landes, J. Metzger, H. Seeg, and R. Stübner, "Investigations into the degradation of the cermet anode of a solid oxide fuel cell," in *Proc. of the 5th Int. Symp. on Solid Oxide Fuel Cells, Jgg*, 1997, pp. 40–97.

[110] D. G. Ivey, E. Brightman, and N. Brandon, "Structural modifications to nickel cermet anodes in fuel cell environments," *J. Power Sources*, vol. 195, no. 19, pp. 6301–6311, Oct. 2010.

[111] F. El Gabaly, K. F. McCarty, H. Bluhm, and A. H. McDaniel, "Oxidation stages of Ni electrodes in solid oxide fuel cell environments ," *Phys. Chem. Chem. Phys.*, vol. 15, pp. 8334–8341, 2013.

[112] J. . Blakely and H. Mykura, "Studies of vacuum annealed iron surfaces," *Acta Metall.*, vol. 11, pp. 399–404, 1963.

[113] P. S. Maiya and J. M. Blakely, "Surface self-diffusion and surface energy of nickel," *J. Appl. Phys.*, vol. 38, pp. 698–704, 1967.

[114] W. Gale, S. Newcomb, T. Totemeier, and G. Vandervoort, "Metallography," in *Smithells Metals Reference Book*, 2004, pp. 1–87.

[115] J. N. Israelachvili, "Intermolecular and Surface Forces Third Edition," *Intermol. Surf. Forces*, p. 710, 2010.

[116] R. Vassen, D. Simwonis, and D. Stöver, "Modelling of Agglomeration of Ni Particles in Anodes of Solid Oxide Fuel Cells," *J. Mater. Sci.*, vol. 36, pp. 147–151, 2001.

[117] S. De Angelis, P. S. Jørgensen, E. H. R. Tsai, M. Holler, K. Kreka, and J. R. Bowen, "Three dimensional characterization of nickel coarsening in solid oxide cells via ex-situ ptychographic nano-tomography," *J. Power Sources*, vol. 383, no. January, pp. 72–79, 2018.

[118] F. Ebrahimi and H. Li, "Grain growth in electrodeposited nanocrystalline fcc Ni-Fe alloys," *Scr. Mater.*, vol. 55, no. 3, pp. 263–266, 2006.

[119] M. Thuvander, M. Abraham, A. Cerezo, and G. D. W. Smith, "Thermal stability of electrodeposited nanocrystalline nickel and iron–nickel alloys," *Mater. Sci. Technol.*, vol. 17, no. May, pp. 961–970, 2001.

[120] T. S. Li, W. G. Wang, H. Miao, T. Chen, and C. Xu, "Effect of reduction temperature on the electrochemical properties of a Ni/YSZ anode-supported solid oxide fuel cell," *J. Alloys Compd.*, vol. 495, no. 1, pp. 138–143, Apr. 2010.

[121] H. Kishimoto *et al.*, "Agglomeration behavior of nickel particles on YSZ and TiO2-doped YSZ electrolytes," *J. Power Sources*, vol. 199, pp. 174–178, Feb. 2012.

[122] B. Iwanschitz, L. Holzer, A. Mai, and M. Schütze, "Nickel agglomeration in solid oxide fuel cells: The influence of temperature," *Solid State Ionics*, vol. 211, pp. 69–73, Mar. 2012.

[123] J. Sehested, "Sintering of nickel steam-reforming catalysts," *J. Catal.*, vol. 217, no. 2, pp. 417–426, 2003.

[124] J. Sehested, J. A. P. Gelten, I. N. Remediakis, H. Bengaard, and J. K. Nørskov, "Sintering of nickel steam-reforming catalysts: Effects of temperature and steam and hydrogen pressures," *J. Catal.*, vol. 223, no. 2, pp. 432–443, 2004.

[125] L. Holzer *et al.*, "Microstructure degradation of cermet anodes for solid oxide fuel cells: Quantification of nickel grain growth in dry and in humid atmospheres," *J. Power Sources*, vol. 196, no. 3, pp. 1279–1294, Feb. 2011.

[126] G. J. Nelson *et al.*, "Three-dimensional microstructural changes in the Ni-YSZ solid oxide fuel cell anode during operation," *Acta Mater.*, vol. 60, no. 8, pp. 3491–3500, 2012.

[127] T. Klemensø, K. Thydén, M. Chen, and H. J. Wang, "Stability of Ni-yttria stabilized zirconia anodes based on Ni-impregnation," *J. Power Sources*, vol. 195, no. 21, pp. 7295–7301, 2010.

[128] J. Sehested, J. A. P. Gelten, and S. Helveg, "Sintering of nickel catalysts: Effects of time, atmosphere, temperature, nickel-carrier interactions, and dopants," *Appl. Catal. A Gen.*, vol. 309, pp. 237–246, 2006.

[129] D. Kennouche, Y. K. Chen-Wiegart, C. Riscoe, J. Wang, and S. a. Barnett, "Combined electrochemical and X-ray tomography study of the high temperature evolution of Nickel – Yttria Stabilized Zirconia solid oxide fuel cell anodes," *J. Power Sources*, vol. 307, pp. 604–612, Mar. 2016.

[130] D. Simwonis, F. Tietz, and D. Stover, "Nickel coarsening in annealed Ni / 8YSZ anode substrates for solid oxide fuel cells," *Solid State Ionics*, vol. 132, pp. 241–251, 2000.

[131] A. Faes, A. Hessler-Wyser, D. Presvytes, C. G. Vayenas, and J. Van herle, "Nickel-"Zirconia Anode Degradation and Triple Phase Boundary Quantification from Microstructural Analysis," *Fuel Cells*, vol. 9, no. 6, pp. 841–851, Dec. 2009.

[132] Y. Zhou *et al.*, "Long-term stability of metal-supported solid oxide fuel cells employing infiltrated electrodes," *J. Power Sources*, vol. 295, pp. 67–73, Nov. 2015.

[133] U. P. Muecke, S. Graf, U. Rhyner, and L. J. Gauckler, "Microstructure and electrical conductivity of nanocrystalline nickel- and nickel oxide/gadolinia-doped ceria thin films," *Acta Mater.*, vol. 56, no. 4, pp. 677–687, Feb. 2008.

[134] M. Mogensen and S. Skaarup, "Kinetic and geometric aspects of solid oxide fuel cell electrodes," *Solid State Ionics*, vol. 86–88, no. PART 2, pp. 1151–1160, 1996.

[135] J. R. Wilson, J. S. Cronin, and S. A. Barnett, "Linking the microstructure, performance and durability of Ni-yttria-stabilized zirconia solid oxide fuel cell anodes using three-dimensional focused ion beam-scanning electron microscopy imaging," *Scr. Mater.*, vol. 65, no. 2, pp. 67–72, 2011.

[136] K. A. Publishers, "Modelling of the agglomeration of Ni-particles in anodes of solid oxide fuel cells," vol. 6, pp. 147–151, 2001.

[137] J. M. Blakely and H. Mykura, "Surface self diffusion measurements on nickel by the mass transfer method," *Acta Metall.*, vol. 9, pp. 23–31, 1961.

[138] Z. Jiao and N. Shikazono, "Prediction of Nickel Morphological Evolution in Composite Solid Oxide Fuel Cell Anode Using Modified Phase Field Model," *J. Electrochem. Soc.*, vol. 165, no. 2, pp. F55–F63, 2018.

[139] L. Almar *et al.*, "High-temperature long-term stable ordered mesoporous Ni-CGO as an anode for solid oxide fuel cells," *J. Mater. Chem. A*, vol. 1, no. 14, pp. 4531–4538, 2013.

[140] D. Skarmoutsos, F. Tietz, and P. Nikolopoulos, "Structure ± Property Relationships of Ni

/ YSZ and Ni /(YSZ + TiO 2) Cermets," no. 3, pp. 243–248, 2001.

[141] P. Tiwari and S. Basu, "Ni infiltrated YSZ anode stabilization by inducing strong metal support interaction between nickel and titania in solid oxide fuel cell under accelerated testing," *Int. J. Hydrogen Energy*, vol. 38, no. 22, pp. 9494–9499, 2013.

[142] S. P. Jiang, Y. Y. Duan, and J. G. Love, "Fabrication of High-Performance Ni/Y[sub 2]O[sub 3]-ZrO[sub 2] Cermet Anodes of Solid Oxide Fuel Cells by Ion Impregnation," *J. Electrochem. Soc.*, vol. 149, no. 9, p. A1175, 2002.

[143] C. C. Wu, L. Tang, and M. R. De Guire, "Nanocrystalline ceria coatings on solid oxide fuel cell anodes: The role of organic surfactant pretreatments on coating microstructures and sulfur tolerance," *Beilstein J. Nanotechnol.*, vol. 5, no. 1, pp. 1712–1724, 2014.

[144] M. A. Laguna-Bercero and Á. Larrea, "YSZ-induced crystallographic reorientation of Ni particles in Ni-YSZ cermets," *J. Am. Ceram. Soc.*, vol. 90, no. 9, pp. 2954–2960, 2007.

[145] H. Kishimoto *et al.*, "Agglomeration behavior of nickel particles on YSZ electrolyte," *Solid State Ionics*, vol. 225, pp. 65–68, Oct. 2012.

[146] S. D. Kim, H. Moon, S. H. Hyun, J. Moon, J. Kim, and H. W. Lee, "Nano-composite materials for high-performance and durability of solid oxide fuel cells," *J. Power Sources*, vol. 163, no. 1 SPEC. ISS., pp. 392–397, 2006.

[147] S. D. Kim, H. Moon, S. H. Hyun, J. Moon, J. Kim, and H. W. Lee, "Ni-YSZ cermet anode fabricated from NiO-YSZ composite powder for high-performance and durability of solid oxide fuel cells," *Solid State Ionics*, vol. 178, no. 21–22, pp. 1304–1309, 2007.

[148] S. Kim, H. Moon, S. Hyun, J. Moon, J. Kim, and H. Lee, "Performance and durability of Ni-coated YSZ anodes for intermediate temperature solid oxide fuel cells," *Solid State Ionics*, vol. 177, no. 9–10, pp. 931–938, Mar. 2006.

[149] H. Itoh *et al.*, "Configuration and electrical behaviour of Ni-YSZ cermet with novel

microstructure for solid oxide fuel cell anodes," *J. Electrochem. Soc.*, vol. 144, no. 2, pp. 2–6, 1997.

[150] K. Huang and J. B. Goodenough, *Solid Oxide Fuel Cell Technology: Principles, Performance and Operations*. Elsevier Science, 2009.

[151] Metrohm Autolab, "Basic overview of the working principle of a potentiostat/galvanostat (PGSTAT)," *Autolab application note EC08*, 2011. [Online]. Available: https://www.ecochemie.nl/download/Applicationnotes/Autolab_Application_Note_EC08.pdf.

[152] G. J. Offer, P. Shearing, J. I. Golbert, D. J. L. Brett, A. Atkinson, and N. P. Brandon, "Using electrochemical impedance spectroscopy to compensate for errors when measuring polarisation curves during three-electrode measurements of solid oxide fuel cell electrodes," *Electrochim. Acta*, vol. 53, no. 26, pp. 7614–7621, 2008.

[153] M. E. Orazem and B. Tribollet, *Electrochemical Impedance Spectroscopy*. Wiley, 2011.

[154] D. Klotz, *Characterization and Modeling of Electrochemical Energy Conversion Systems by Impedance Techniques*. Karlsruher Institut für Technologie, 2014.

[155] B. Song, E. Ruiz-Trejo, A. Bertei, and N. P. Brandon, "Quantification of the degradation of Ni-YSZ anodes upon redox cycling," *J. Power Sources*, vol. 374, no. August 2017, pp. 61–68, 2018.

[156] A. Bertei *et al.*, "The fractal nature of the three-phase boundary: A heuristic approach to the degradation of nanostructured solid oxide fuel cell anodes," *Nano Energy*, vol. 38, no. May, pp. 526–536, 2017.

[157] M. E. Orazem and B. Tribollet, *Electrochemical Impedance Spectroscopy*. Interscience, 2008.

[158] A. Bertei, E. Ruiz-Trejo, F. Tariq, V. Yufit, A. Atkinson, and N. P. Brandon, "Validation

of a physically-based solid oxide fuel cell anode model combining 3D tomography and impedance spectroscopy," *Int. J. Hydrogen Energy*, vol. 41, no. 47, pp. 22381–22393, 2016.

[159] S. B. Adler, J. A. Lane, and B. C. H. Steele, "Electrode Kinetics of Porous Mixed-Conducting Oxygen Electrodes," *J. Electrochem. Soc.*, vol. 143, no. 11, p. 3554, Feb. 1996.

[160] T. H. Wan, M. Saccoccio, C. Chen, and F. Ciucci, "Influence of the Discretization Methods on the Distribution of Relaxation Times Deconvolution: Implementing Radial Basis Functions with DRTtools," *Electrochim. Acta*, vol. 184, pp. 483–499, 2015.

[161] S. Reyntjens and R. Puers, "A review of focused ion beam applications in microsystem technology," *J. Micromechanics Microengineering*, vol. 11, no. 4, pp. 287–300, 2001.

[162] H. Iwai *et al.*, "Quantification of SOFC anode microstructure based on dual beam FIB-SEM technique," *J. Power Sources*, vol. 195, no. 4, pp. 955–961, 2010.

[163] Y. Leng, *Materials Characterization*. Weinheim, Germany: Wiley-VCH Verlag GmbH & Co. KGaA, 2013.

[164] Y. Leng, *Materials Characterization*. Weinheim, Germany: Wiley-VCH Verlag GmbH & Co. KGaA, 2013.

[165] Carl Zeiss NTH GmbH, "Instruction Manual AURIGA series." Oberkochen, Germany, 2010.

[166] D. C. Joy and C. S. Joy, "Low voltage scanning electron microscopy," *Micron*, vol. 27, no. 3–4, pp. 247–263, 1996.

[167] A. Ul-Hamid, *A Beginners' Guide to Scanning Electron Microscopy*. Springer, 2018.

[168] D. C. Joy and C. S. Joy, "Low voltage scanning electron microscopy," *Micron*, vol. 27, no. 3–4, pp. 247–263, 1996.

[169] A. Sabouri, C. J. Anthony, P. D. Prewett, J. Bowen, and H. Butt, "Effects of current on

early stages of focused ion beam nanomachining," *Mater. Res. Express*, vol. 2, no. 5, pp. 0–8, 2015.

[170] P. R. Munroe, "The application of focused ion beam microscopy in the material sciences," *Mater. Charact.*, vol. 60, no. 1, pp. 2–13, 2009.

[171] A. Buades, B. Coll, and J.-M. Morel, "A Non-Local Algorithm for Image Denoising," in *2005 IEEE Computer Society Conference on Computer Vision and Pattern Recognition (CVPR'05)*, 2005, vol. 2, no. 0, pp. 60–65.

[172] I. Arganda-Carreras *et al.*, "Trainable Weka Segmentation: A machine learning tool for microscopy pixel classification," *Bioinformatics*, vol. 33, no. 15, pp. 2424–2426, 2017.

[173] S. J. Cooper, A. Bertei, P. R. Shearing, J. A. Kilner, and N. P. Brandon, "TauFactor: An open-source application for calculating tortuosity factors from tomographic data," *SoftwareX*, vol. 5, pp. 203–210, 2016.

[174] J. Brame and C. Griggs, "Surface Area Analysis Using the Brunauer-Emmett-Teller (BET) Method," Washington DC, 2016.

[175] S. Brunauer, P. H. Emmett, and E. Teller, "Adsorption of Gases in Multimolecular Layers," *J. Am. Chem. Soc.*, vol. 60, no. 2, pp. 309–319, 1938.

[176] S. Brunauer, L. S. Deming, W. E. Deming, and E. Teller, "On a Theory of the van der Waals Adsorption of Gases," *J. Am. Chem. Soc.*, vol. 62, no. 7, pp. 1723–1732, 1940.

[177] S. Lowell, J. E. Shields, M. A. Thomas, and M. Thommes, *Characterization of Porous Solids and Powders: Surface Area, Pore Size and Density*. Springer Netherlands, 2006.

[178] J. H. de Boer, B. C. Lippens, B. G. Linsen, J. C. P. Broekhoff, A. van den Heuvel, and T. J. Osinga, "The t-curve of multimolecular N_2-adsorption," *J. Colloid Interface Sci.*, vol. 21, no. 4, pp. 405–414, 1966.

[179] B. LIPPENS and J. H. de Boer, "Studies on pore systems in catalysts V. The t method," *J.*

Catal., vol. 4, no. 3, pp. 319–323, Jun. 1965.

[180] S. Lowell, J. E. Shields, M. A. Thomas, and M. Thommes, "Micropore Analysis," in *Characterization of Porous Solids and Powders: Surface Area, Pore Size and Density*, Dordrecht: Springer Netherlands, 2004, pp. 129–156.

[181] Malvern Instruments, "A basic guide to particle characterization," Worcestershire, 2015.

[182] R. B. Von Dreele, "Powder Diffraction: Theory and Practice," The Royal Society of Chemistry, 2008, pp. 266–281.

[183] C. T., J. C. de Lima, and P. B., "The Quantification of Crystalline Phases in Materials: Applications of Rietveld Method," in *Sintering - Methods and Products*, vol. 9, no. 14, V. Shatokha, Ed. InTech, 2012, pp. 2745–2752.

[184] S. Jung, C. Lu, H. He, K. Ahn, R. J. Gorte, and J. M. Vohs, "Influence of composition and Cu impregnation method on the performance of Cu/CeO2/YSZ SOFC anodes," *J. Power Sources*, vol. 154, no. 1, pp. 42–50, 2006.

[185] K. V. Manukyan *et al.*, "Nickel Oxide Reduction by Hydrogen: Kinetics and Structural Transformations," *J. Phys. Chem. C*, vol. 119, no. 28, pp. 16131–16138, 2015.

[186] V. Rudnev, D. Loveless, R. L. Cook, and M. Black, *Handbook of Induction Heating*. CRC Press, 2002.

[187] S. B. Adler, "Mechanism and kinetics of oxygen reduction on porous La Sr CoO electrodes electrodes," *Solid State Ionics*, vol. 111, pp. 125–134, 1998.

[188] A. Häffelin, J. Joos, M. Ender, A. Weber, and E. Ivers-Tiffée, "Time-Dependent 3D Impedance Model of Mixed-Conducting Solid Oxide Fuel Cell Cathodes," *J. Electrochem. Soc.*, vol. 160, no. 8, pp. F867–F876, 2013.

[189] D. Kennouche, Y. Karen Chen-Wiegart, J. Scott Cronin, J. Wang, and S. A. Barnett, "Three-Dimensional Microstructural Evolution of Ni- Yttria-Stabilized Zirconia Solid Oxide

Fuel Cell Anodes At Elevated Temperatures," *J. Electrochem. Soc.*, vol. 160, no. 11, pp. 1293–1304, 2013.

[190] A. Leonide, V. Sonn, A. Weber, and E. Ivers-Tiffée, "Evaluation and Modeling of the Cell Resistance in Anode-Supported Solid Oxide Fuel Cells," *J. Electrochem. Soc.*, vol. 155, no. 1, p. B36, 2008.

[191] H. Zhu, a. Kromp, a. Leonide, E. Ivers-Tiffee, O. Deutschmann, and R. J. Kee, "A Model-Based Interpretation of the Influence of Anode Surface Chemistry on Solid Oxide Fuel Cell Electrochemical Impedance Spectra," *J. Electrochem. Soc.*, vol. 159, no. 7, pp. F255–F266, Jan. 2012.

[192] V. Sonn, A. Leonide, and E. Ivers-Tiffée, "Combined Deconvolution and CNLS Fitting Approach Applied on the Impedance Response of Technical Ni8YSZ Cermet Electrodes," *J. Electrochem. Soc.*, vol. 155, no. 7, p. B675, 2008.

[193] T. Ramos, M. Søgaard, and M. B. Mogensen, "Electrochemical Characterization of Ni/ScYSZ Electrodes as SOFC Anodes," *J. Electrochem. Soc.*, vol. 161, no. 4, pp. 434–444, 2014.

[194] A. J. L. Reszka, R. C. Snyder, and M. D. Gross, "Insights into the Design of SOFC Infiltrated Electrodes with Optimized Active TPB Density via Mechanistic Modeling," *J. Electrochem. Soc.*, vol. 161, no. 12, pp. F1176–F1183, 2014.

[195] A. Bertei, J. G. Pharoah, D. A. W. Gawel, and C. Nicolella, "A Particle-Based Model for Effective Properties in Infiltrated Solid Oxide Fuel Cell Electrodes," *J. Electrochem. Soc.*, vol. 161, no. 12, pp. F1243–F1253, 2014.

[196] X. Weng *et al.*, "Highly conductive low nickel content nano-composite dense cermets from nano-powders made via a continuous hydrothermal synthesis route," *Solid State Ionics*, vol. 181, no. 17–18, pp. 827–834, 2010.

[197] M. I. MENDELSON, "Average Grain Size in Polycrystalline Ceramics," *J. Am. Ceram. Soc.*, vol. 52, no. 8, pp. 443–446, Aug. 1969.

[198] A. Kocjan, M. Logar, and Z. Shen, "The agglomeration, coalescence and sliding of nanoparticles, leading to the rapid sintering of zirconia nanoceramics," *Sci. Rep.*, vol. 7, no. 1, pp. 1–8, 2017.

[199] J. Golbert, C. S. Adjiman, and N. P. Brandon, "Microstructural Modeling of Solid Oxide Fuel Cell Anodes," *Ind. Eng. Chem. Res.*, vol. 47, no. 20, pp. 7693–7699, 2008.

[200] M. Kishimoto, H. Iwai, M. Saito, and H. Yoshida, "Quantitative evaluation of solid oxide fuel cell porous anode microstructure based on focused ion beam and scanning electron microscope technique and prediction of anode overpotentials," *J. Power Sources*, vol. 196, no. 10, pp. 4555–4563, 2011.

[201] P. R. Shearing, Q. Cai, J. I. Golbert, V. Yufit, C. S. Adjiman, and N. P. Brandon, "Microstructural analysis of a solid oxide fuel cell anode using focused ion beam techniques coupled with electrochemical simulation," *J. Power Sources*, vol. 195, no. 15, pp. 4804–4810, 2010.

[202] P. R. Shearing, J. Golbert, R. J. Chater, and N. P. Brandon, "3D reconstruction of SOFC anodes using a focused ion beam lift-out technique," *Chem. Eng. Sci.*, vol. 64, no. 17, pp. 3928–3933, 2009.

[203] J. R. Wilson *et al.*, "Three-dimensional reconstruction of a solid-oxide fuel-cell anode," *Nat. Mater.*, vol. 5, no. 7, pp. 541–544, 2006.

[204] X. Lu *et al.*, "Correlation between triple phase boundary and the microstructure of Solid Oxide Fuel Cell anodes: The role of composition, porosity and Ni densification," *J. Power Sources*, vol. 365, pp. 210–219, 2017.

[205] J. Everhart, *Engineering Properties of Nickel and Nickel Alloys*. Springer US, 2012.

[206] H. S. Hong, U. S. Chae, S. T. Choo, and K. S. Lee, "Microstructure and electrical conductivity of Ni/YSZ and NiO/YSZ composites for high-temperature electrolysis prepared by mechanical alloying," *J. Power Sources*, vol. 149, no. 1–2, pp. 84–89, 2005.

[207] E. Barsoukov and J. R. Macdonald, *Impedance Spectroscopy: Theory, Experiment, and Applications*. Wiley, 2018.

[208] E. N. Fuller, P. D. Schettler, and J. C. Giddings, "A new method for prediction of binary gas-phase diffusion coefficients.," *Ind. Eng. Chem.*, vol. 16, no. 10, p. 551, 1966.

[209] S. Primdahl and M. Mogensen, "Gas Diffusion Impedance in Characterization of Solid Oxide Fuel Cell Anodes," *J. Electrochem. Soc.*, vol. 146, no. 8, pp. 2827–2833, 1999.

[210] P. Costamagna, P. Costa, and V. Antonucci, "Micro-modelling of solid oxide fuel cell electrodes," *Electrochim. Acta*, vol. 43, no. 3–4, pp. 375–394, Jan. 1998.

[211] G. Paasch, K. Micka, and P. Gersdorf, "Theory of the Electrochemical Impedance of Macrohomogeneous Porous-Electrodes," *Electrochim. Acta*, vol. 38, no. 18, pp. 2653–2662, 1993.

[212] J. Chen, A. Bertei, E. Ruiz-Trejo, A. Atkinson, and N. P. Brandon, "Characterization of Degradation in Nickel Impregnated Scandia-Stabilize Zirconia Electrodes during Isothermal Annealing," *J. Electrochem. Soc.*, vol. 164, no. 9, pp. F935–F943, 2017.

[213] A. Bieberle, L. P. Meier, and L. J. Gauckler, "The Electrochemistry of Ni Pattern Anodes Used as Solid Oxide Fuel Cell Model Electrodes," *J. Electrochem. Soc.*, vol. 148, no. 6, p. A646, 2001.

[214] S. Gewies and W. G. Bessler, "Physically Based Impedance Modeling of Ni/YSZ Cermet Anodes," *J. Electrochem. Soc.*, vol. 155, no. 9, p. B937, 2008.

[215] D. Kanno, N. Shikazono, N. Takagi, K. Matsuzaki, and N. Kasagi, "Evaluation of SOFC anode polarization simulation using three-dimensional microstructures reconstructed by FIB

tomography," *Electrochim. Acta*, vol. 56, no. 11, pp. 4015–4021, 2011.

[216] P. Keyvanfar, A. R. Hanifi, P. Sarkar, T. H. Etsell, and V. Birss, "Enhancing the Stability of Infiltrated Ni/YSZ Anodes," *ECS Trans.*, vol. 68, no. 1, pp. 1255–1263, 2015.

[217] J. Chen, A. Bertei, E. Ruiz-trejo, A. Atkinson, and N. P. Brandon, "Characterization of Degradation in Nickel Impregnated Scandia-Stabilize Zirconia Electrodes during Isothermal Annealing," vol. 164, no. 9, pp. 1–10, 2017.

[218] M. Ihara, T. Kusano, and C. Yokoyama, "Competitive Adsorption Reaction Mechanism of Ni/Yttria-Stabilized Zirconia Cermet Anodes in H[sub 2]-H[sub 2]O Solid Oxide Fuel Cells," *J. Electrochem. Soc.*, vol. 148, no. 3, p. A209, 2001.

[219] K. Sato, M. Naito, and H. Abe, "Electrochemical and mechanical properties of solid oxide fuel cell Ni/YSZ anode fabricated from NiO/YSZ composite powder," *Nippon Seramikkusu Kyokai Gakujutsu Ronbunshi/Journal Ceram. Soc. Japan*, vol. 119, no. 1395, pp. 876–883, 2011.

[220] M. Brown, S. Primdahl, and M. Mogensen, "Structure/Performance Relations for Ni/Yttria-Stabilized Zirconia Anodes for Solid Oxide Fuel Cells," *J. Electrochem. Soc.*, vol. 147, no. 2, p. 475, 2000.

[221] B. A. Boukamp, M. Verbraeken, D. H. A. Blank, and P. Holtappels, "SOFC-anodes, proof for a finite-length type Gerischer impedance?," *Solid State Ionics*, vol. 177, no. 26–32 SPEC. ISS., pp. 2539–2541, 2006.

[222] S. H. Jensen, A. Hauch, R. Knibbe, T. Jacobsen, and M. Mogensen, "Modeling Degradation in SOEC Impedance Spectra," *J. Electrochem. Soc.*, vol. 160, no. 3, pp. F244–F250, 2013.

[223] B. A. Boukamp and H. J. M. Bouwmeester, "Interpretation of the Gerischer impedance in solid state ionics," *Solid State Ionics*, vol. 157, no. 1–4, pp. 29–33, 2003.

[224] G. Muller, R. N. Vannie, A. Ringuede, and C. Laberty-Robert, "Reduction of NiO to Ni in

nanocrystalline composite NiO/Ce0.9Gd0.1O2-δporous thin films: Microstructure evolution through in situ impedance spectroscopy," *J. Phys. Chem. C*, vol. 117, no. 32, pp. 16297–16305, 2013.

[225] S. P. Jiang, "A comparative study of fabrication and performance of Ni/3 mol % Y2O3-ZrO2 and Ni/8 mol % Y2O3-ZrO2 cermet electrodes," *J. Electrochem. Soc.*, vol. 150, no. 11, pp. E548–E559, 2003.

[226] G. Paasch, K. Micka, and P. Gersdorf, "Theory of the Electrochemical Impedance of Macrohomogeneous Porous-Electrodes," *Electrochim. Acta*, vol. 38, no. 18, pp. 2653–2662, 1993.

[227] M. Hubert, J. Laurencin, P. Cloetens, B. Morel, D. Montinaro, and F. Lefebvre-Joud, "Impact of Nickel agglomeration on Solid Oxide Cell operated in fuel cell and electrolysis modes," *J. Power Sources*, vol. 397, no. April, pp. 240–251, 2018.

[228] A. Faes, A. Hessler-Wyser, D. Presvytes, C. G. Vayenas, and J. Vanherle, "Nickel-zirconia anode degradation and triple phase boundary quantification from microstructural analysis," *Fuel Cells*, vol. 9, no. 6, pp. 841–851, 2009.

[229] A. Caravaca, S. Picart, M. Aouine, B. Arab-Chapelet, P. Vernoux, and T. Delahaye, "Development of highly nano-dispersed NiO/GDC catalysts from ion exchange resin templates," *Catalysts*, vol. 7, no. 12, pp. 1–7, 2017.

[230] K. Sugihara *et al.*, "A quantitative analysis of influence of Ni particle size of SDC-supported anode on SOFC performance: Effect of particle size of SDC support," *Solid State Ionics*, vol. 262, no. 3, pp. 433–437, 2014.

[231] D. A. Macedo, F. M. L. Figueiredo, C. A. Paskocimas, A. E. Martinelli, R. M. Nascimento, and F. M. B. Marques, "Ni-CGO cermet anodes from nanocomposite powders: Microstructural and electrochemical assessment," *Ceram. Int.*, vol. 40, no. 8 PART B, pp. 13105–13113, 2014.

[232] L. Liu, G. Y. Kim, A. C. Hillier, and A. Chandra, "Microstructural and electrochemical impedance study of nickel-Ce0.9Gd0.1O1.95anodes for solid oxide fuel cells fabricated by ultrasonic spray pyrolysis," *J. Power Sources*, vol. 196, no. 6, pp. 3026–3032, 2011.

[233] J. Nielsen, T. Klemenso, and P. Blennow, "Detailed impedance characterization of a well performing and durable Ni:CGO infiltrated cermet anode for metal-supported solid oxide fuel cells," *J. Power Sources*, vol. 219, pp. 305–316, 2012.

[234] W. Lai and S. M. Haile, "Impedance spectroscopy as a tool for chemical and electrochemical analysis of mixed conductors: A case study of ceria," *J. Am. Ceram. Soc.*, vol. 88, no. 11, pp. 2979–2997, 2005.

[235] A. Mohammed Hussain, J. V. T. Høgh, T. Jacobsen, and N. Bonanos, "Nickel-ceria infiltrated Nb-doped SrTiO3for low temperature SOFC anodes and analysis on gas diffusion impedance," *Int. J. Hydrogen Energy*, vol. 37, no. 5, pp. 4309–4318, 2012.

[236] M. Lomberg, E. Ruiz-Trejo, G. Offer, and N. P. Brandon, "Characterization of Ni-infiltrated GDC electrodes for solid oxide cell applications," *J. Electrochem. Soc.*, vol. 161, no. 9, pp. F899–F905, 2014.

[237] P. V. Aravind, J. P. Ouweltjes, and J. Schoonman, "Diffusion Impedance on Nickel/Gadolinia-Doped Ceria Anodes for Solid Oxide Fuel Cells," *J. Electrochem. Soc.*, vol. 156, no. 12, p. B1417, 2009.

[238] K. Compaan and Y. Haven, "Correlation factors for diffusion in solids," *Trans. Faraday Soc.*, vol. 52, no. 786, p. 786, 1956.

[239] J. A. Lane and J. A. Kilner, "Oxygen surface exchange on gadolinia doped ceria," *Solid State Ionics*, vol. 136–137, pp. 927–932, 2000.

[240] C. B. Gopal and S. M. Haile, "An electrical conductivity relaxation study of oxygen transport in samarium doped ceria," *J. Mater. Chem. A*, vol. 2, no. 7, pp. 2405–2417, 2014.

[241] A. Bieberle and L. J. Gauckler, "Reaction mechanism of Ni pattern anodes for solid oxide fuel cells," vol. 135, pp. 337–345, 2000.

[242] W. C. Chueh, Y. Hao, W. Jung, and S. M. Haile, "High electrochemical activity of the oxide phase in model ceria-Pt and ceria-Ni composite anodes," *Nat. Mater.*, vol. 11, no. 2, pp. 155–161, 2012.

[243] H. Kishimoto *et al.*, "Effect of the oxide substrate on the nickel particle properties," *Solid State Ionics*, vol. 262, pp. 403–406, 2014.

[244] Z. Jiao and N. Shikazono, "Study on Nickel Morphological Change at Active Three-Phase-Boundary in Solid Oxide Fuel Cell Anode Using Patterned Nickel-film Electrode," *ECS Trans.*, vol. 78, no. 1, pp. 1169–1177, May 2017.

[245] W. G. Bessler and S. Gewies, "Gas Concentration Impedance of Solid Oxide Fuel Cell Anodes," *J. Electrochem. Soc.*, vol. 154, no. 6, p. B548, 2007.

[246] D. Kennouche *et al.*, "Observing the microstructural evolution of Ni-Yttria-stabilized zirconia solid oxide fuel cell anodes," *Acta Mater.*, vol. 103, pp. 204–210, 2016.